Nanoparticulate materials for environmental remediation: Adsorption Vs. Advanced oxidation techniques

Niki Hamilton

Nanoparticulate materials for environmental remediation: Adsorption Vs. Advanced oxidation techniques

Niki Hamilton

Supervisor: Dr. Lorraine Gibson

Department of Pure and Applied Chemistry
University of Strathclyde

A thesis submitted to the Department of Pure and Applied Chemistry, University of Strathclyde, in part fulfillment of the regulations for the degree of Doctor of Philosophy (Ph.D.)

October 2018

For my daughter, Poppy.

Born at 11.07 pm on the 26/10/2018, 6lbs 3oz.

Acknowledgements

Abstract

The research presented in this thesis examines the performance of silica-based materials as adsorbents in the remediation of air and water environments alongside conventionally used sorbents. In addition, photocatalytic oxidation (PCO) is investigated as an alternative remediation technique.

The use of mesoporous silica materials, MCM-41 and SBA-15, as sorbents for the removal of volatile organic compounds (VOCs) from indoor air was assessed. SBA-15 was found to possess the best dynamic adsorption capacity; trapping 12.5 ng cm^{-3} of toluene and was shown to perform better as a scavenger sorbent than the commercially available material, Tenax TA.

A mesoporous titanium dioxide (TiO$_2$) photocatalyst was prepared via a surfactant templated, sol-gel synthesis approach. Optimum photocatalytic activity for the degradation of VOCs required five coatings of TiO$_2$ film on glass bead support material. High photocatalytic activity and long-term performance were demonstrated with respect to the degradation of toluene, ethylbenzene and cumene (96 – 100 %). Reaction intermediates and a possible degradation mechanism were successfully identified. Regeneration proved to be a simple process, achieved by cooling down the system.

The aqueous adsorption of pharmaceuticals or nitrobenzene onto powdered activated carbon (PAC) and silica materials; as-synthesised (As-syn) and calcined (Calc) MCM-41, bioinspired silica (Bio-Si) and iron incorporated Bio-Si (Fe Bio-Si) was assessed. The four target pharmaceuticals in the multi-analyte solution were acetaminophen, caffeine, sulfamethoxazole and carbamazepine. Bio-Si and Fe Bio-Si displayed the lowest adsorption capacities, < 0.25 mg g^{-1}, for each pharmaceutical target. The maximum adsorption capacities of PAC and As-syn MCM-41, obtained from the Freundlich model, were 97 and 6 mg g^{-1}, respectively. Nitrobenzene adsorption followed the general pattern: PAC > Calc MCM-41> As-syn MCM-41 > As-syn Bio-Si and Fe Bio-Si > Calc Bio-Si and Fe Bio-Si. Both investigations revealed commercially available PAC to be the dominant sorbent in aqueous adsorption.

Fe Bio-Si, applied as a heterogeneous Fenton catalyst, was shown to be highly effective for the degradation of nitrobenzene exhibiting long-term catalytic activity ~ 95 % and 85 % degradation at pH 3 and 7 respectively, with no loss in performance after 15 successive recycle runs. Furthermore, the catalyst was shown to successfully mineralise pharmaceutical targets at pH 3, reaching 100 % degradation for all compounds after the initial cycle.

Finally, the process of visible-light induced photocatalytic oxidation, using a Fe-TiO$_2$ thin film as a photocatalyst, displayed potential for the degradation of nitrobenzene in aqueous solutions, achieving 49.1 and 54.9 % degradation for 20 and 50 % Fe-TiO$_2$.

Where the mesoporous silica materials failed, in large, to compete with commercially available sorbents, the developed PCO systems, for both indoor air and water treatment, excelled and proved to be very simple yet highly effective techniques that could be easily applied industrially for the efficient degradation of organic pollutants.

Table of Contents

1. Introduction to porous materials

1.1 Definition and classification of porous materials

A solid material that contains cavities, channels or interstices, which are deeper than they are wide, can be regarded as porous.[1] Porous materials have attracted great scientific interest in various applications ranging from catalysis, adsorption, separation and energy storage owing to their high surface area, tuneable pore size, adjustable framework and surface properties. Based on accessibility of an external fluid, pores can be classified into two main kinds: closed pores and open pores.

- Closed Pores – are defined as empty spaces immersed in the bulk material that are completely isolated from each other and the external surface, not allowing the access of water in either liquid or vapour phase. (see Figure 1.1, A) They influence neither transport of liquids nor adsorption of gases in materials but do affect properties such as bulk density, mechanical strength and thermal conductivity. Materials with closed pores are useful in thermal insulation, or as lightweight materials for structural applications.

- Open pores – are defined as pores that have a continuous channel of communication with the external surface of the material. Open pores can be further divided into blind (B), through (C) and interconnected (D) pores. It is the presence of open pores in the framework that generates the large surface areas of porous materials. They enhance the physical and chemical properties of porous materials by allowing the interaction with atoms, ions and molecules; thus, enabling the use of these materials in a large variety of applications.
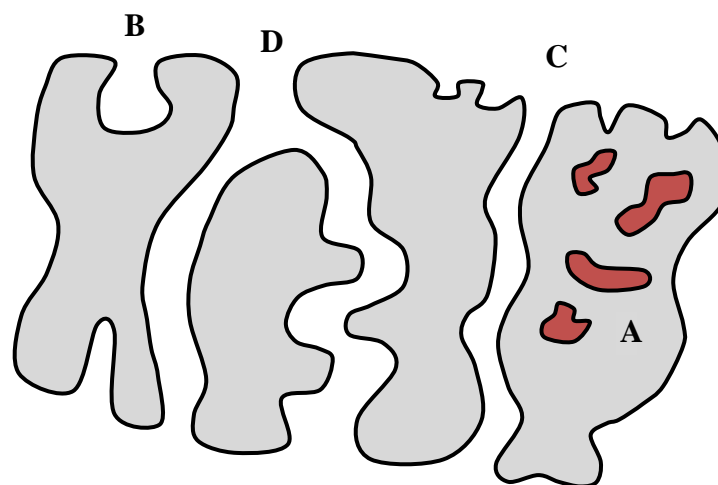
Figure 1.1: Cross section of hypothetical porous particle: A – closed pores; B – blind pores; C – through pores and D – interconnected pores.

Porous materials can also be classified, according to the pore diameter, into three categories described by the International Union of Pure and Applied Chemistry (IUPAC):[1]

Microporous materials with pore diameters less than 2 nm

Mesoporous materials with pore diameters between 2 and 50 nm

Macroporous materials with pore diameters greater than 50 nm

Recently, the science and technology surrounding porous materials has been significantly advanced through the understanding, design and manipulation of pores and consequently these materials have gained increasingly important roles in modern society.

1.2 Background and development of porous silicates

The development of advanced porous materials with channels of tunable dimensions originated with the discovery of microporous zeolites in 1756 by a Swedish mineralogist, Cronstedt.[2] He noted that a natural mineral, upon rapid heating, produced large amounts of steam as a result of the water that had been adsorbed by the material. Based on this observation, he named the class of minerals, zeolites, from the classical Greek words *zeo* meaning to boil and *litho* meaning stone.

Zeolites are crystalline aluminosilicates built from $[SiO_4]^{4-}$ and tetrahedral $[AlO_4]^{5-}$ units with periodic three-dimensional framework structures which contain voids. During the 19th century, the microporous characteristic of natural zeolites and their unique physical adsorption properties were gradually recognised.[3, 4] The production of synthetic zeolites was brought to the attention of many scientists in the 1950s when Breck[5] and researchers at the Union Carbide Company began to synthesis zeolites from reactive aluminosilicate gels prepared from sodium aluminate and sodium silicate solutions. This led directly to the discovery of the first two new synthetic zeolites A and X. These new zeolites exhibited high cation contents and were found to have excellent ion-exchange and gas separation properties. The successful synthesis of zeolites A and X laid the foundation for rapid development in the field of zeolite synthesis research. Even though many new frameworks have been discovered since then, with more than 40 natural and 150 synthetic zeolites reported,[6] these zeolites still hold scientific and industrial importance.

By virtue of their crystalline network, zeolites exhibit an extremely narrow pore size distribution, which allows their successful exploitation for size specific applications in

adsorption, separation and shape-selective catalysis. However, a major drawback of these materials is their limited pore size (<2.5 nm), which prevents their use in size-specific processes involving large molecules. In response to these increasing demands, there has been a growing interest in zeolite pore size expansion from the micropore to mesopore region.

It is well known that dealumination can produce mesopores in zeolites. However, both the pore size and number of pores created depend on the dealumination conditions; consequently, disordered mesopore arrangements are typically produced. Since the 1980s, pillared clays containing mesopores have been well studied.[7, 8] These layered materials are pillared via intercalation of large molecules including polycations (such as alumina oligomers Al_{13}^{7+}) and silicates generating mesopores. Clays include vermiculites, montmorillonites and typical phosphates such as zirconium phosphates. These materials were considered to be future catalysts for heavy oil cracking. Unfortunately, it was later discovered that weak surface activity, easy coke deactivation and low thermal stability made them unsuitable for catalytic cracking. In addition, the pillars are amorphous and irregularly arranged despite the ordered atomic crystals of clays and phosphates, leading to a disordered pore arrangement and non-uniform mesopore sizes. Larger pores are also present in porous glasses and porous gels, synthesised via the sol-gel process. Silica gel is an amorphous material with pores typically larger than 2 nm and is, therefore, considered a mesoporous material. The pore size can eventually reach the macroporous range. Similar to pillared clays, they have disordered pore arrangements and therefore exhibit broad pore size distributions.

1.3 Ordered mesoporous silicates

Ordered mesoporous silicates are a class of materials that share the amorphous characteristics of gels and the ordered porosity of crystalline materials such as zeolites. These periodic materials consist of extended inorganic or inorganic-organic hybrid arrays with exceptional long-range ordering, highly tuneable textural and surface properties and controlled pore size and geometry.

1.3.1 Impact of Mobil publication

Mesoporous silica materials with ordered pore arrangements became a research topic of intense interest in 1992, when Mobil Oil Corporation scientists first reported the synthesis of these materials.[9, 10] They developed a family of mesoporous materials, the M41S series; Mobil composition of matter (MCM-41, MCM-48 and MCM-50) and as well as describing their synthesis they proposed a general 'liquid-crystal templating' mechanism of formation. The discovery of Mobil's M41S mesoporous molecular sieves, was an unanticipated outcome of the application of many years of knowledge and new synthesis techniques. A paper published by Kresge and Roth,[11] two of the authors of the original Mobil publications, in 2013 describes the discovery of mesoporous molecular sieves with a 20 year perspective.

Like many petroleum companies, in the mid-1980s Mobil had a material synthesis programme with the aim of exploring new materials that could selectively convert high molecular weight hydrocarbons into more valuable fuel products. Their efforts focussed on developing pillared layered materials and it transpired that the synthesis conditions applied; high pH, high template concentration and a reactive silica source, were conducive to the formation of the original mesoporous molecular sieve, MCM-41. The most outstanding feature of this synthesis is the template agent used; no longer is the template a single solvated organic molecule or metal ion, as traditionally used in zeolite preparation, but rather the templates are liquid-crystalline, self-assembled surfactant molecular arrays. The discovery and identification of other members of this new class of porous materials, MCM-48 and MCM-50, came several months later as a result of a detailed study relating the effect of surfactant concentration on the silica reagent.

It has been argued that similar materials had been previously developed 20 years earlier. In the early 1970s, a patent produced by Chiola *et al.*[12] recorded a method to synthesise 2D hexagonal mesoporous silica, similar to MCM-41, using cationic surfactants. However, due to the lack of characterisation data these scientists failed to recognise the remarkable features of their product, vaguely describing it as low-bulk density silica. Later this material was synthesised, characterised and compared to MCM-41.[13] It was said to be clear that this material was a predecessor to the mesoporous silica that is synthesised today, even though the importance of this type of material was not recognised then.

In 1990, Yanagisawa *et al.,*[14] also described the synthesis of mesoporous materials, albeit through an alternative pathway. They utilised a cationic surfactant to support the so-called Kanemite layered clay. They clay structure was destroyed in a high-alkalinity solution and a

new mesoporous material was generated, later named folded sheet mesoporous material (FSM-16). Once again, attention was not given as a result of a lack of understanding surrounding the formation mechanism and characterisation data.

It was the publication of the Mobil group's research in Nature[10] that sparked a rapid development in ordered mesoporous materials including new mesostructures, compositions, formation mechanisms and applications, giving rise to a new inorganic research area. The initiation of a significant and ever-expanding number of studies in this research field can be observed by referring to the Science Citation Index (SCI) expanded (Web of Science). By searching 'mesoporous' as the topic subject, the publication numbers each year can be found. Figure 1.2 shows the increasing publication numbers on mesoporous materials and along with citation numbers for the Kresge publication in 1992.[10]

■ Number citations for Kresge et al.

■ Number of publications dealing with mesoporous materials
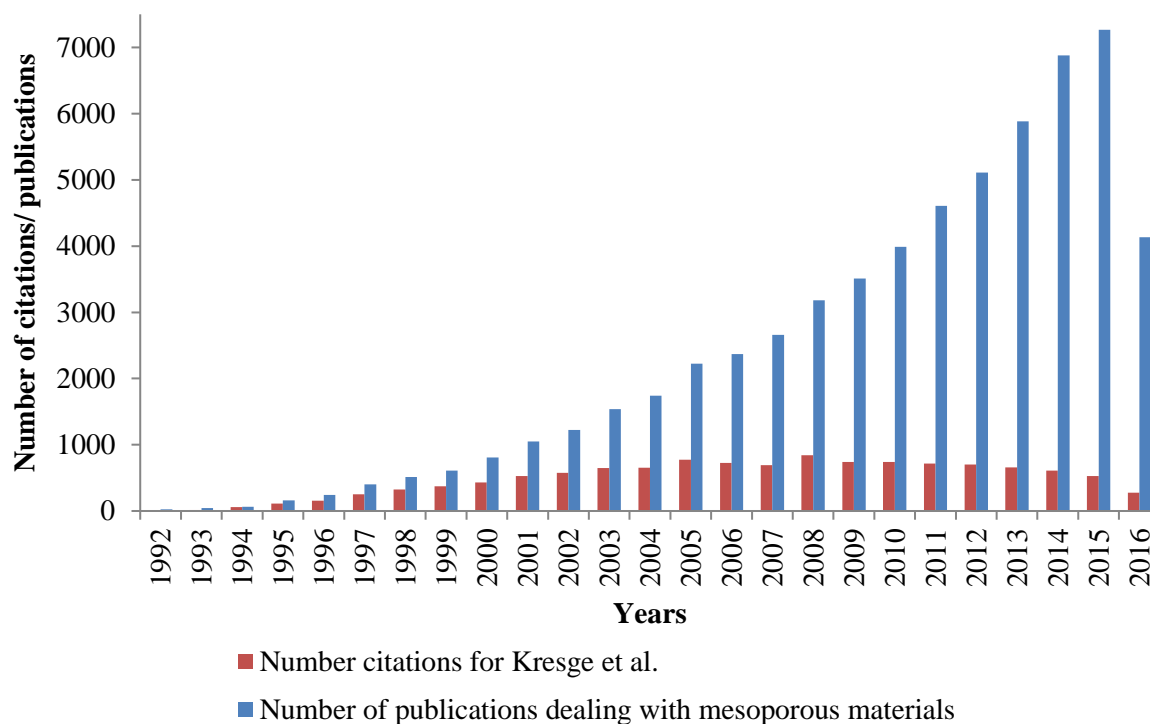
Figure 1.2: Yearly occurrence of the term 'mesoporous' in open literature since 1992 and the number of citations for the Nature article by Kresge *et al*.

From Figure 1.2 it can be seen that the year 1992 marked a quick ascent in the number of publications on mesoporous materials. Simultaneously, the citation numbers of the Kresge *et al*.[10] Nature publication increased steadily for the first 10 years, highlighting the impact of

this publication and its ability to launch a worldwide research effort. To date, over 60,000 papers have been published on these materials, half of these since the beginning of 2011. This enormous expansion of publications and knowledge has resulted in a wide range of new materials, phenomena and concepts which has continued to grow until recent years.

1.3.2 M41S series

The M41S family of materials possess a regular array of uniform mesopores, bridging the gap between microporous zeolites and macroporous materials. Like the microporous zeolites, this class of materials is characterised by very large specific surface areas, ordered pore arrangements and very narrow pore size distributions. Unlike the crystalline zeolites, however, the M41S materials have pore diameters from approx 2 to 20 nm and exhibit amorphous pore walls. Depending on the synthesis conditions used when preparing these materials, three members of the M41S family can be obtained, the main difference being the pore organisation in three-dimensional space: hexagonally ordered MCM-41, bicontinuous cubic MCM-48, and lamellar MCM-50 (see Figure 1.3).
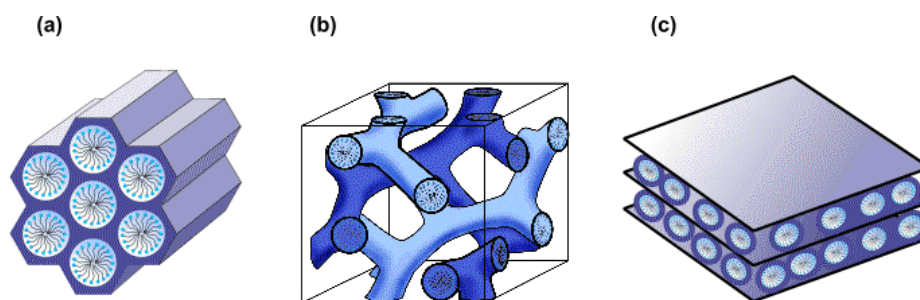
Figure 1.3: Structures of M41S materials – (a) MCM-41 (b) MCM-48 (c) MCM-50.[15]

MCM-41

MCM-41 is a mesoporous material which exhibits a honeycomb structure that is the result of a highly ordered hexagonal array of one-dimensional cylindrical channels. The channels, which constitute the pores, are long, parallel and isolated from each other. MCM-41 has been extensively investigated, more so than other members of the M41S family, which are thermally less stable and more difficult to synthesise.

MCM-48

MCM-48 has two independent networks of mesoporous channels which are intricately interwoven together into a three-dimensional structure with cubic arrangement. [9, 16-18] With the increase in dimension, the three dimensional channel network of MCM-48 was thought to have superior properties to that of the one dimensional channel of MCM-41. The elimination of pore blockage, which produces mass transfer limitations, makes MCM-48 a more desirable material for diffusional and catalytic purposes.[19] However, the number of publications on MCM-48 is much smaller as a consequence of synthesis difficulties. In fact, the MCM-48 structure was only briefly mentioned in the first reports on M41S powders. An accurate synthesis procedure was not published until approximately one year later.[18] The main difference in the synthesis of MCM-48 compared to that of MCM-41 is the surfactant to silica ratio in the synthesis solutions.[20] Huo *et al.*[21] have systematically investigated different surfactants in order to obtain a reliable synthesis of cubic materials.

MCM-50

MCM-50 has a lamellar structure with silicate or aluminosilicate layers separated by surfactant layers. However, the sheet-like structure of this material is not stable after removal of the template. MCM-50 has therefore been given little attention so far, due to its limited stability.

1.3.3 SBA series

Since the first series of M41S materials were reported, a second family of mesoporous materials were prepared by the Stucky group from University of California, Santa Barbara. These materials were named Santa Barbara Amorphous (SBA-x) where x is a number corresponding to a specific pore structure and surfactant.

The SBA series was the first mesoporous silica materials to be synthesised using non-ionic triblock polymers as surfactants and were originally reported in 1998 by Zhao *et al.*[22] The characterisation data showed that SBA-15 had a similar structure to that of MCM-41 in that pores are formed by long cylindrical channels arranged in a hexagonal order. The average pore size was found to be over 15 nm and the pore wall thickness was approximately 4 - 6 nm, which is 2 to 3 times thicker than that of MCM-41, indicating that SBA-15 may have better thermal and hydrothermal stabilities. However, unlike MCM-41 which has parallel, isolated channels; the channels of SBA-15 are connected by a secondary micropore system. This network of micropores surrounding each mesopore is called the corona,[23] which interconnects the mesopores with each other and is responsible for the high surface area of SBA-15. These coexisting pore structures of mesopores and micropores are known as a bimodal pore system[24-26] and materials with this system are expected to be ideal as catalysts and adsorbents.

1.4 Material synthesis

The synthesis of ordered mesoporous molecular sieves combines sol-gel chemistry and the use of molecular surfactant assemblies as framework templates. The procedures appear to be relatively straightforward since the key requirements involved are widely known: a surfactant template, a silica source, a catalyst for the polymerisation of silica and a solvent.

Mesoporous materials can be synthesised under basic or acidic conditions. A general procedure includes several steps. First a homogenous solution is obtained by dissolving the surfactant in water. Inorganic precursors are then added into the solution where they undergo hydrolysis, catalysed by an acid or a base, transformation to a sol then a gel. A hydrothermal treatment is then carried out to induce the complete condensation and solidification. The

resultant product is cooled to room temperature, filtered, washed and dried. The mesoporous material is obtained after removal of the organic template.

The mesoporous structure generated can be controlled by the choice of the surfactant template or changing reaction parameters such as surfactant concentration, pH of the media, the ratio of the components in the reactant mixture, the reaction temperature, the duration of the reaction and the template removal process utilised. As a consequence of the large number of factors affecting the material produced, samples synthesised under similar conditions but from different research groups show distinguishing properties, implying that a complicated combination of simple factors can offer great opportunities in creating different porous textures, even new mesoporous family members. Therefore, fully understanding their roles in the synthesis and formation of mesostructures is imperative in furthering both research and applications of these materials.

1.4.1 Silica precursor

The silica source plays an important role in the synthesis of mesoporous materials by determining the reaction conditions used. Several types of silica precursors can be employed for the synthesis of mesoporous silica materials. The most common are alkoxides, especially tetramethyl orthosilicate (TMOS) or tetraethyl orthosilicate (TEOS) but other alkoxides with longer alkyl chains can also be used.[27] An alternative, cheaper, silica precursor that can be used is sodium silicate[28, 29] or a combination sodium silicate and alkoxides.[30] TEOS is the most studied precursor in the sol-gel process: its low reactivity towards hydrolysis makes it possible to follow and control the reaction more easily.
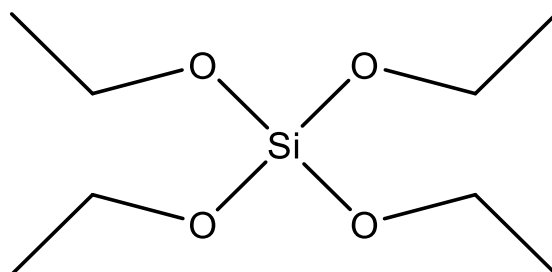
Figure 1.4: Chemical structure of TEOS.

1.4.1.1 Sol-gel chemistry

The methods employed to prepare mesoporous molecular sieves are similar to the ones commonly used for sol-gel derived oxides.[31] Both types of material consist of amorphous frameworks; the main difference is the degree of order since porous sol-gel oxides are completely disordered. The surfactant templating synthesis of the mesoporous molecular sieves provides the ordered arrangement of the mesopores, uniform pore sizes and large surface area. However, it is the sol-gel approach to the synthesis that allows the composition and microstructure of the material to be tailored through the control of the precursor chemistry and processing conditions.

The first step in the sol-gel process is the formation of silanol groups. In aqueous solution this occurs by hydrolysis of the alkoxysilane precursor (Equation 1.1). Hydrolysis is generally catalysed by an acid (HCl) or a base (NaOH, NH$_3$). Additionally, the hydrolysis rate is affected by the nature of the silicon precursor. For example, the more hydrophobic or sterically hindered the precursor is, the slower the hydrolysis rate. Depending on the synthesis conditions, water/alkoxide ratio and the quantity and nature of the catalyst, hydrolysis may be only partial or go to completion, where all the OR groups are replaced by OH groups. In both cases, the silanol formed will undergo self-condensation or condensation with an alkoxysilane molecule producing siloxane bonds (Si-O-Si) and water (Equation 1.2) or alcohol (Equation 1.3).

$$\equiv Si - OR \ + \ H_2O \ \xrightleftharpoons{\text{Hydrolysis}} \ \equiv Si - OH \ + \ ROH \qquad \textbf{Equation 1.1}$$

$$\equiv Si - OH \ + \ HO - Si \equiv \ \xrightleftharpoons{\text{Water Condensation}} \ \equiv Si - O - Si \equiv \ + H_2O \quad \textbf{Equation 1.2}$$

$$\equiv Si - OR \ + \ HO - Si \equiv \ \xrightleftharpoons{\text{Alcohol condensation}} \ \equiv Si - O - Si \equiv \ + ROH \quad \textbf{Equation 1.3}$$
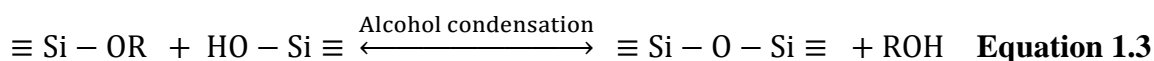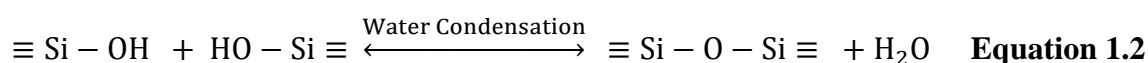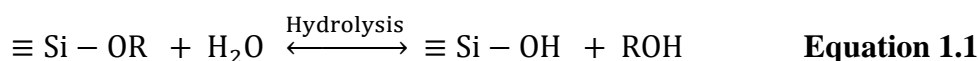
The overall reaction proceeds as a poly-condensation to form soluble higher molecular weight polysilicates. This resulting colloidal dispersion is the *sol*. The polysilicates eventually link together to form a three-dimensional network which spans the container and is usually filled with solvent molecules, called the *gel*, or precipitate as precipitated silica. Sol-gel polymerisation proceeds in several possibly overlapping steps which are

polymerisation to form primary particles, growth of the particles and finally aggregation. Each step depends strongly on pH, temperature, concentration and co-solvent effects.

1.4.1.2 Silica polymerisation pH dependence

The hydrolysis and condensation reactions are influenced strongly by the nature and concentration of the catalysts, resulting in pH dependence. The pH dependence of the polymerisation reaction which has been recognised for colloidal silica-water systems can be employed in the synthesis of silicate-surfactant mesophases. It is possible to synthesise mesoporous silica via acidic or basic routes as shown in Figure 1.5.

Under acidic conditions, between pH 1 and 2, the precipitation of mesoporous material is significantly slower, requiring up to several hours depending on surfactant type. This is a result of the pH being near the isoelectric point of the silicate (pH 2), slowing the condensation rate of silicate species. At very low pH solutions, the silicate species are positively charged and, therefore, the synthesis of mesoporous silica is accelerated, precipitation occurring within minutes at room temperature.[32] The optimum pH value is below 1 therefore strong acids such as HCl are favoured as catalysts. Under these low pH conditions, the polymerisation and cross linkage mechanisms are irreversible meaning that once the gel has formed it is difficult to change the structure of the material.

Under basic conditions, in the pH range of 9.5 – 12.5, the solubility of the silicate increases strongly with pH and the condensed species are likely to be ionised[33] resulting in a rapid templating reaction. The addition of the silica source to the surfactant solution leads to the immediate precipitation of the silica-surfactant composite. Under these high pH conditions, the polymerisation and cross linkage of silicate species are reversible, the structure of the material can be altered by simply adjusting the synthesis conditions, allowing the use of a wide variety of silica precursors such as silica gels and aerogels, sodium silicates or TEOS.

Although more efficient condensation of the silanol groups occurs in mesoporous silica under alkaline conditions,[9, 10, 14] a diverse morphology of mesostructures are achievable under acidic conditions, producing short and long fibres, solid and hollow spheres and films.[34-37]

Hydrolysis:
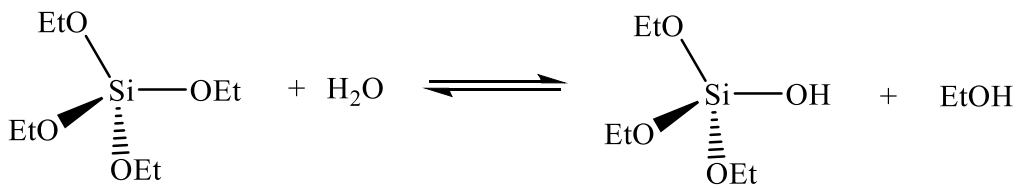
Condensation:

Acidic
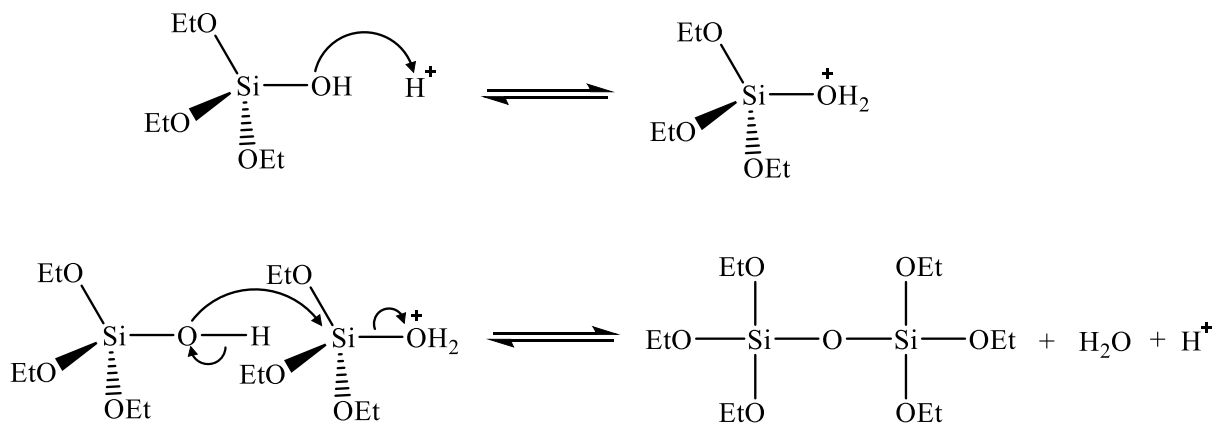
Alkaline
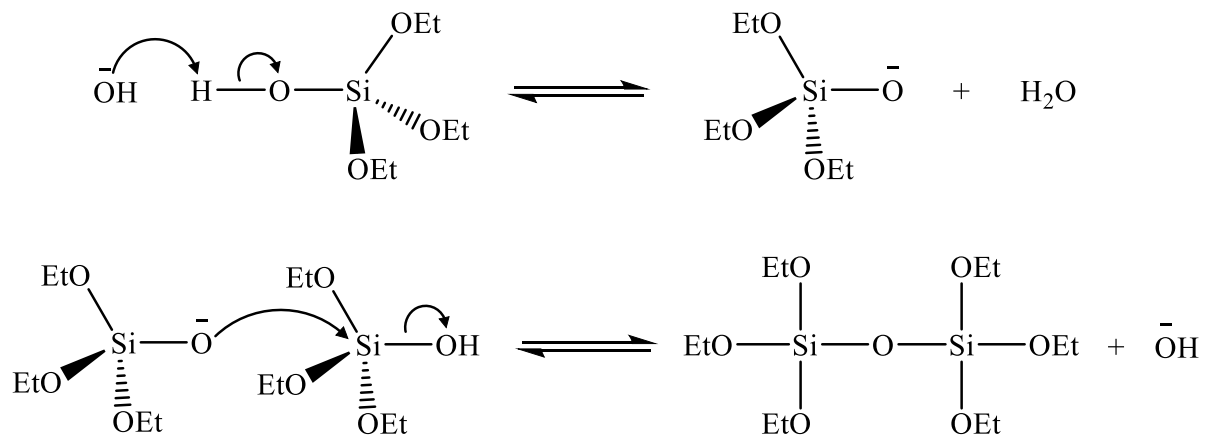
Figure 1.5: Hydrolysis and condensation reaction mechanisms for TEOS under acidic and alkaline conditions.

1.4.2 Role of surfactant

During the synthesis of ordered mesoporous materials, the role of the surfactant template is to act as a structure directing agent that is critical for control of the frameworks.

1.4.2.1 Common surfactant templates

Surfactants are generally amphiphilic molecules with hydrophilic and hydrophobic sections in their structure. They may be classified into four different groups, depending on the nature of the polar head group; anionic, cationic, zwitterionic and non-ionic surfactants.[38] Cetyltrimethylethylammonium bromide (CTAB), a quaternary ammonium salt with long alkyl chain, is a common cationic surfactant used in the synthesis of MCM-41 (Figure 1.6).
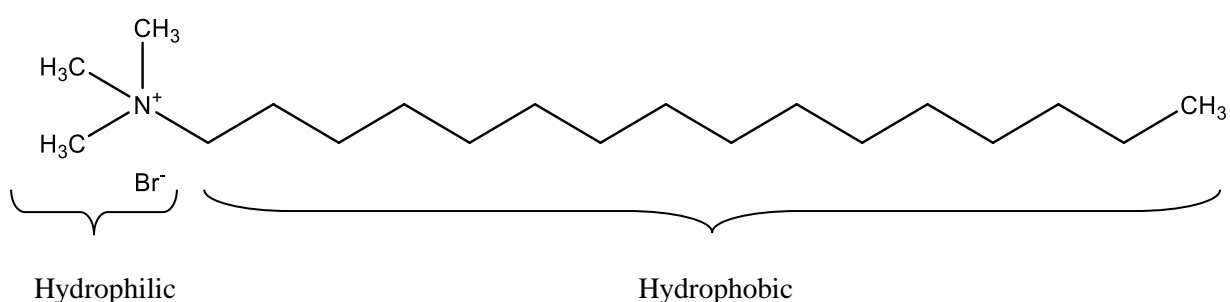
Figure 1.6: Chemical structure for cationic surfactant, CTAB.

In the synthesis of SBA-15 triblock copolymer, P123, is used as surfactant template.[22] This non-ionic triblock copolymer, commercially known as a Pluronic-type surfactant, has the chemical formula, $(EO)_{20}(PO)_{70}(EO)_{20}$, where EO are ethylene oxide groups and PO are propylene oxide groups (Figure 1.7).
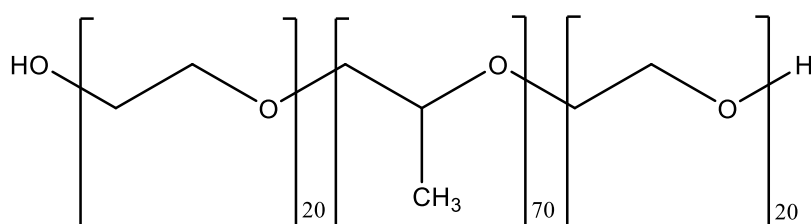
Figure 1.7: Chemical structure for triblock copolymer P123.

1.4.2.2 Behaviour of surfactant molecules in aqueous solution

As a result of their amphiphilic nature, in a simple binary system of water-surfactant, surfactant molecules show a natural tendency to auto-arrange into complex supramolecular arrays. This arrangement minimises the unfavourable interaction of the hydrocarbon tails with water but introduces a competing unfavourable interaction – repulsion of the charged head groups. The balance between these competing factors determines the relative stability of the micelles formed.

The extent of micelle formation, the shape of the micelles and the aggregation of the micelles into liquid crystals depends on surfactant concentration. At very low concentrations the surfactant is present as individual molecules dissolved in solution. When the surfactant concentration is gradually increased, the surfactant molecules aggregate together to form micelles in order to increase the system entropy; this process can be summarised in the following stages:[39]

1. The initial concentration threshold at which individual surfactant molecules aggregate to form small spherical micelles is called the critical micelle concentration (CMC).

2. As the concentration continues to increase these spherical micelles eventually coalesce to form elongated cylindrical micelles when the amount of solvent available between the micelles decreases.

3. The formation of liquid crystalline phases occurs at slightly higher surfactant concentrations. Initially the cylindrical micelles aggregate to form a hexagonal close-packed arrangement, followed by the formation of bicontinuous cubic phase and finally the formation of a lamellar structure.

The close packed micellar arrangements formed in concentrated surfactant-water systems are closely mimicked by those found in surfactant templated silica materials, with the silica material filling the equivalent regions to the water in the structures.

1.4.2.3 Surfactant packing parameter

The particular aggregate shape present in a surfactant aqueous solution depends not only on the given concentration but also on the nature of the surfactant itself such as the size, shape

and charge on the molecule. [40] According to a concept introduced by Israelachvili *et al.*,[41] predications can be made about the arrangement of different surfactant aggregates just above the CMC and thus their corresponding mesophase structures. This concept is known as the packing parameter, g which is expressed in Equation 1.1.

$$g = \frac{V}{a_0 l_c}$$

Equation 1.1

where V is the total volume of the hydrophobic chains plus any co-surfactant organic molecules between the chains, a_0 is the effective head group area and l_c is the critical length of the hydrophobic tail.
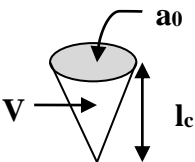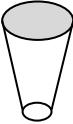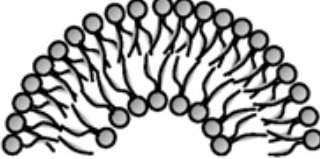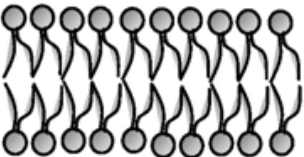
The parameter g depends on the molecular geometry of the surfactant. The number of carbons in the hydrophobic chain,[42] the degree of chain saturation and the size and charge of the polar head group influence the value of g. Additionally reaction conditions such as pH, ionic strength of the solution, co-surfactant effects and temperature will affect V, a_0 and l_c thus highlighting that the packing parameter for a specific surfactant is not a constant but merely an approximation.

Due to variations in size of different types of surfactant tails and head groups, the packing parameter will vary for different types of surfactants. In general terms, surfactants with large head groups provoke large surface curvature and surfactants with a large hydrophobic chain volume and relatively small head groups generate small surface curvature. Therefore, with increasing values of g, the lower the curvature in the surfactant aggregates, which is reflected in the phase transitions observed in the mesostructure.

If the packing parameter is below 1/3, only spherical micelles exist in the solution. If the surfactant concentration is sufficiently high, the spherical micelles organise into arrays, creating mesostructures with cubic ordering. A g value between 1/3 and 1/2 produces cylindrical micelles which assemble into ordered hexagonal mesostructures. Surfactant aggregates form vesicles and flexible bilayers when the packing parameter is between 1/2 and 1, arranging into three dimensional cubic mesostructures. Lastly, when the g value is 1, the surfactants arrange in sheets forming lamellar mesophases.

Table 1.1 summarises the typical g values, demonstrating their use in predicting the structure of the micelle aggregates and therefore the geometry of the final mesophase, as governed by the relative sizes of the surfactant tail and head group.

Table 1.1: Expected aggregate characteristics and mesophase structures in relation to surfactant packing parameter, g.

g	Shape of Cross Section	General Surfactant Type	Expected Aggregate Structure[43]	Expected Mesostructure
<1/3	Cone	Single Chain with large head group	Spherical micelles	Cubic (Pm3n) e.g. SBA-1
1/3 - 1/2	Truncated Cone	Single Chain with small head group	Large cylindrical micelles	Hexagonal e.g. MCM-41, FSM-16
1/2 - 1	Truncated Cone	Double chain with large head group and flexible chains	Vesicles and flexible bilayers	Cubic (Ia3d) e.g. MCM-48
1	Cylinder	Double chain with small head groups or rigid chains	Planar bilayers	Lamellar e.g. MCM-50

V is the total volume of the hydrophobic chains plus any co-surfactant organic molecules between the chains, a_0 is the head group area and l_c is the length of the hydrophobic tail.

By altering the size and shape of the head group of the surfactant relative to the tail volume, the pore shape and connectivity can be tailored, while the overall size of the micelle hydrophobic region generally determines the pore size.[44]

1.4.3 Template removal

When the synthesis procedure is complete and the material has reached a sufficient degree of condensation, the templating molecules are no longer needed and can be removed to open the

porous structure. Since some composite mesophases can contain as much as 45-55 % of organic material by weight,[45] the removal procedure can alter the final properties of the desired materials. For mesoporous materials, the most important requirements for template removal are: efficient removal of the template, short operation time, limited use of hazardous chemical, minimum negative effect on the structure and ideal structural and surface properties of the inorganic framework.

1.4.3.1 Calcination

The most common laboratory template removal method is calcination. In this method, the as-synthesised (mesosilica with template remaining) materials are heated in flowing air,[46] nitrogen or a combination of both nitrogen and oxygen,[9] burning away the organics. Usually, the heating rates required are slow with heating ramps such as 1 °C min^{-1} up to 550 °C, followed by an extended period of heating at a temperature plateau (4 to 8 h).

There have been several investigations into the mechanism of thermal degradation during the calcination process looking at various different surfactant types.[45, 47-49] It was found that materials synthesised using alkytrimethylammonium surfactants showed a stepwise template removal mechanism. The first step of the template decomposition is consistent with the Hoffmann degradation, followed by oxidation and combustion reactions above 250 °C. On the other hand, it has been proposed that most of the block copolymer template is removed from SBA-15 at lower temperatures, in a single oxidation step with higher temperatures associated with the oxidation of a significant proportion of ethylene oxide head group located within the micropores.[50]

Although the templates can be burnt out effectively, such thermal treatment may have negative effects on the mesoporous structure. At very high temperature, partial collapse of the structure may occur and, in contrast, if the temperature is limited to 500 °C, a small quantity of organic fragments may still remain in the mesopores.[48] In addition, calcination of an as-synthesised mesophase containing large amounts of carbonaceous species can leave carbon deposits, or coke, as a contaminant in the porous materials resulting in pore blocking. Generally, when the template is removed by calcination, characteristic features can be observed; the high temperature used invariably leads to a large contraction of the pores (up to 25 %)[51] due to further condensation of the silicate species in the framework and, thus, the ordered mesostructure could be dramatically affected.[52, 53]

1.4.3.2 Solvent extraction

An alternative procedure for the template removal with less destructive effects is solvent extraction.[24, 54, 55] The possibility of the extraction of template molecules depends strongly on the nature of the surfactant-inorganic interactions. The process usually involves the extraction of dried as-synthesised samples in acid solutions, alcohols, neutral salt solution, ammonium acetate or mixtures of these. Hitz *et al.*[55] demonstrated the removal of up to 73 % of the template in MCM-41 sample by extracting with solutions of an acid or salt in ethanol for 1 h at 78 °C. When extracting with acidic ethanol, ionic exchange of the counter cations with acidic protons was achieved. The use of a strong acid or small cations, proved to be more efficient for the extraction of the template in ethanol, suggesting that the size and mobility of the cations in the close packed micellar aggregates is a key factor when determining the extent of extraction. Moreover, it seems that more polar solvents are superior media to dissolve the template ions. Accordingly, it is widely suggested that an ion-exchange mechanism occurs during solvent extraction of M41S-type materials.[45] The presence of cationic species in the extraction liquid for charge balance is therefore required for ion-exchange. Various acidic media are used for surfactant extraction, ethanolic HCl solution being the most commonly employed.[45, 55]

The efficiency of the solvent extraction depends in particular on the strength of the interaction between the organic molecules and the framework. The SBA-type frameworks are considered to be relatively neutral and the resulting framework-surfactant interactions are weak. Such weak interactions are more favourable for surfactant extraction even in the absence of cationic species since counter cations are not needed. Block copolymers can be extracted from SBA-15 using acidic ethanol solution for short times and low temperatures.[23, 24, 56] Hence, extraction might provide an alternative to calcination especially in the case of low thermal stability mesophases.

In the manufacture of ordered mesoporous materials, the surfactant template accounts for a high percentage of the cost with the material comprising of as much as 45-55 % organic template. The use of solvent extraction is, therefore, more desirable with the possibility of recovering the template which can be used in subsequent synthesis reactions.[57] Additionally, it is proposed that the solvent extraction procedure produces materials with improved properties, such as gas transport, when compared to other template removal methods as a result of the pore structures remaining unchanged, in most cases, from the as-synthesised materials.

The efficiency of solvent extraction methods rely on a balance between extraction time and temperature as well as on the composition and concentration of the extraction solution. Therefore a drawback of this process is the possibility of incomplete removal of the template and often long extraction times, or multiple extraction steps, are necessary for successful elimination of the template.[51, 54, 55] This technique also requires the use of high volumes of organic solvent, thereby, failing to meet economic and environmental constraints imposed by large scale applications. Furthermore, the excessive stirring of the suspension during repeat solvent washing steps can reduce particle size as a result of mechanical action.

1.4.3.3 Microwave Digestion

Tian *et al.*[58] adopted a microwave digestion (MWD) procedure to remove surfactants from mesosilica. This was achieved by placing the as-synthesised sample and an appropriate amount of HNO_3 and H_2O_2 in a reactor. The instantaneous high temperature (~200 °C) and pressure (~1.3 M Pa) generated by the microwave radiation facilitated the oxidation of the surfactants by HNO_3 and H_2O_2. Surfactants in the mesopores were completely eliminated.

The advantages of this method of template removal were:

1. Complete removal of the surfactant;
2. The process was relatively quick, taking 3 to 10 min;
3. The framework shrinkage was small (about 10 %), much lower than that from calcination (greater than 20 %);
4. The products possessed highly ordered mesostructures, high surface areas and large pore volume;
5. In contrast to calcination, the MWD technique was easy and effectively removed surfactants without sacrificing the silanols on the silicate pore walls.

The MWD extraction procedure, therefore, provided many benefits over the other extraction methods including fast extraction times, lower structural shrinkage, larger surface area and pore volumes and retention of a higher degree of silanol groups on the surface of the mesosilica.

1.4.4 Functionalisation

The Mobil scientists reported that the surface properties of MCM-41 were close to those of silica gel, as a result of the lack of crystallinity of the pore walls. Consequently, MCM-41 and other mesosilica surfaces feature silanol groups (single or germinal) and siloxane bridges. The presence of silanol groups leads to poor hydrothermal stability but can be advantageous, providing an opportunity to modify the surface via chemical bonding of organic ligands. The large surface of mesoporous materials can be split into two categories: external surface and internal surface. Approximately 90 % of all surface silanol groups are on the internal surface, therefore by carefully choosing the functionalisation approach the mesoporous silica material can be effectively and selectively functionalised with different functional groups.[59-61] Organosilane chemistry offers a large choice of organic functions to graft for modifying surface properties (polarity, hydrophobic/hydrophilic balance) or to bring specific properties to the bulk material (catalytic, magnetic, and optical).

Two main methods have been developed for the synthesis of porous, regular structures with organic functionalities:

1. Post-synthesis grafting onto the pore surface of purely inorganic silica material.
2. Co-condensation of silica with the organosilica precursor.

1.4.4.1 Post-synthesis grafting (PSG)

The process of grafting involves the modification of the inner surfaces of pre-fabricated mesoporous silica structures with organic groups. As previously described, ordered mesoporous silicas have an abundance of unreacted silanol groups (Si-OH) on the pore surfaces, owing to their amorphous structure, which can be exploited through the reaction with organosilane molecules, acting as convenient anchoring points for organic functionalisation.[62-65] This process has three principle objectives: to change the pore wall polarity and adsorption properties using organic groups, to eliminate unreacted silanol groups (passivation) or to introduce specific organic functionality. Common organosilane species used as reactants for the grafting process are chloroorganosilanes $ClSiR_3$, alkyoxyorganosilanes $(R'O)_3SiR$ and silazanes $HN(SiR_3)_2$. Among them chloroorganosilanes are hard to control and give rise to unwanted polymerisation reactions, so the other two

species are preferable. In principle, functionalisation with a variety of organic groups can be achieved in this way by variation of the organic residue R, as shown in Figure 1.8.
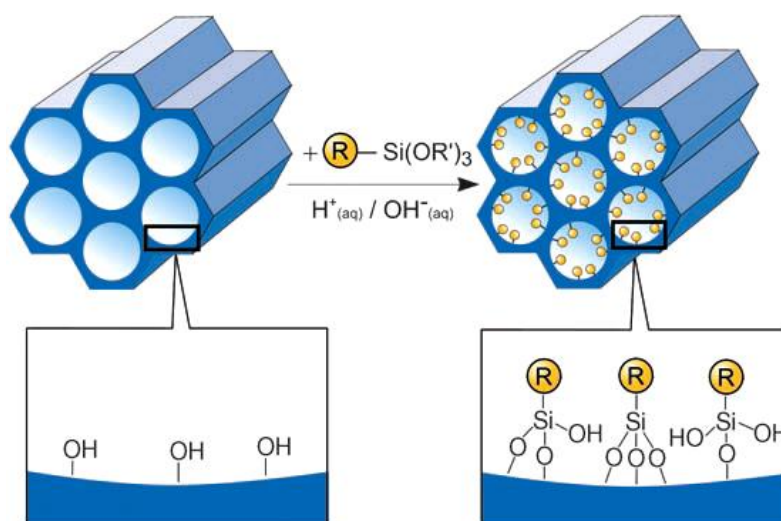
Figure 1.8: Functionalisation of mesoporous silicates by grafting.[15]

An advantage of the PSG process is that it works on a pre-existent structure, thereby usually retaining the mesostructure of the starting phase and lowering the risk of creating a pore-less material. Nevertheless, depending on the size of the organic molecule and the degree of occupation on the pore walls, the grafting process is accompanied by a reduction in the porosity of the organic-inorganic hybrid material. Additionally, the materials obtained by this method can exhibit non-homogenous distribution of the organic groups within the pores and a lower degree of occupation. Grafting molecules are strong, reactive and non-specific, with the tendency to react fast and preferentially with silanol groups near the pore opening, where there is first contact between reactants. Once molecules are grafted, the pore opening size decreases, impairing the diffusion of further molecules into the centre of the pores and confining the remaining reactants near to the external surface.[15, 66] To avoid this problem, two possible solutions could be to start from a mesostructure with large pores to leave enough open space to enable diffusion, or to use less reactive silanes leaving a longer reaction time. Overall, the grafting method is used for low-coverage surface modification, using small amounts of grafting agents, or for specific applications that only require functionalisation near the pore opening.

1.4.4.2 Co-condensation (direct synthesis)

An alternative method to synthesise organically functionalised mesoporous silica phases is the co-condensation method.[67] Co-condensation is a direct synthesis method where tetraalkoxysilanes, $(RO)_4Si$ e.g. TEOS or TMOS condense in the presence of terminal trialkoxyorganosilanes of the type $(R'O)_3SiR$ and a surfactant templating agent.[68, 69] This method leads to the preparation of organically modified mesoporous silicas with organic residues anchored covalently to the pore walls. Since the organic functionalities (R) are usually hydrophobic they tend to intercalate into the hydrophobic region of the surfactant micelles, causing the incorporated functionalities to project into the pores.[70]

By using the condensation method, the organic functionalities are directly incorporated into the silica framework, as shown in Figure 1.9, therefore, pore blockage and shrinkage are not an issue and the organic units are generally more homogenously distributed than in materials synthesised by the grafting method.[15, 60, 66] Additionally co-condensation allows easy control of the final mesoporous silica morphology.[37]
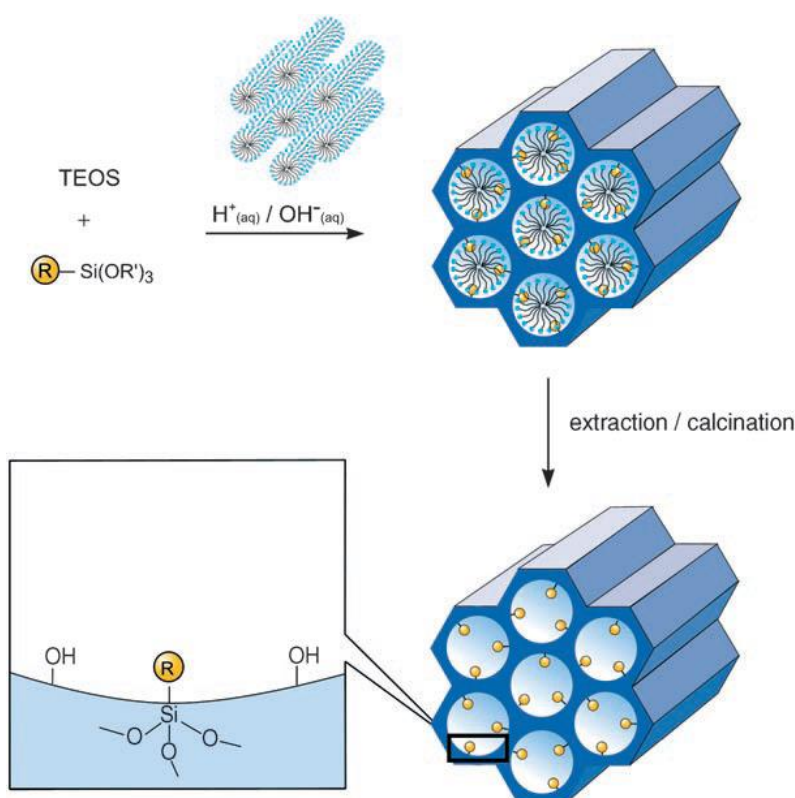
Figure 1.9: Co-condensation between organoalkoxysilanes and tetraalkoxysilanes to synthesise hybrid inorganic-organic mesoporous silicates.[15]

Despite these merits, the direct synthesis method also has some drawbacks. First, the addition of organosilanes can dramatically change the characteristic of the reaction solution. This may result in a change in the mesostructure of the resulting product and often leads to a disordered or non-porous material; the situation worsening with an increase in organosilane concentration. In common synthesis, the percentage of organosilane is typically between 5 and 15 %,[71, 72] a limit is set to 40 % over which an ordered structure no longer exists. Second, a phase separation problem may occur if the organosilane is poorly soluble in the surfactant solution or if its hydrolysis or condensation rates differ greatly from that of TEOS. Furthermore, it has been reported that some of the organic functional groups introduced via the co-condensation method may not be accessible due to the fact they are embedded inside the silica matrix.[73, 74]

Considering all these aspects, co-condensation is a method which can be used, under the appropriate conditions, to obtain materials with few organic groups homogeneously distributed in the structure. Materials produced by this way show interesting catalytic and adsorption properties, different from pure-silica systems. An ideal application could be to use these materials as scaffolds for post- synthetic grafting starting from reactive organic groups introduced during the synthesis.

1.4.5 Synthesis mechanisms

With silica mesoporous materials the general mechanism of formation involves the arrangement of silica around a surfactant template. Depending on the starting block two mechanisms can lead to the formation of these ordered mesostructures. The synthetic route determines not only the final mesostructure but also the macroscopic structure of the materials produced and this is due, in part, to differences in the formation mechanism involved in each route.

1.4.5.1 Initial mechanism proposal

In 1992 Beck *et al.*[9] proposed the liquid crystal templating (LCT) mechanism for the formation of mesoporous materials. A key feature of the LCT mechanism is that the structure is defined by the organisation of surfactant molecules into liquid crystalline mesophases or

micelles which acted as templates for the formation of the structure. Silicate condensation was not considered to be the dominant factor of the mechanism. Accordingly, the final product is a silicate skeleton which contains voids that mimicked the mesophases. The whole process may be summarised into 2 two possible mechanistic pathways as illustrated in Figure 1.10.

1. The liquid crystal mesophases form prior to the addition of the silicate species.
2. The addition of the silicate species to the reaction results in the ordering of the subsequent silicate-encased surfactant micelles into the desired phase i.e. hexagonal mesophase. Therefore, the mesophase formed is structurally and morphologically directed by the existing liquid crystal micelles and/or mesophases.
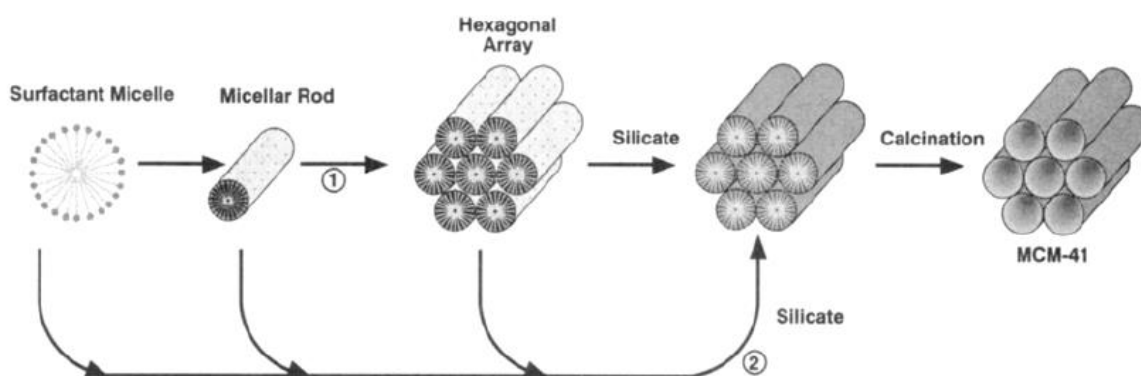
Figure 1.10: Possible mechanistic pathways for the formation of MCM-41: (1) liquid crystal phase initiated and (2) silicate anion initiated.[9]

The support for this templating mechanism is that the structure and pore dimensions of MCM-41 materials are intimately linked to the surfactant chain length, solution chemistry and the existence of other mesophases. Consequently, synthesis pathway (1) did not gain great support in the literature. Cheng *et al.*[75] highlighted the need for a greater than 40 % (CTA)Cl surfactant concentration before the formation of a hexagonal liquid-crystal phase in the surfactant-water system occurred. At lower concentrations, only micelles exist in solution. Knowing that MCM-41 may be formed at surfactant concentrations as low as 1 wt. % with respect to water content,[18] the pathway according to which the hexagonal liquid crystal formed first was questioned. Moreover, in situ ^{14}N-NMR spectra acquired by Chen et al[76] revealed that the hexagonal liquid crystalline phase was not present at any time during MCM-41 formation. It was, therefore, concluded that formation of MCM-41 was more probable via pathway 2.

1.4.5.2 Alternative formation mechanisms

In-depth investigations into the formation process of these materials have been carried out, however all appear to stem from and expand on the original liquid crystal templating mechanism pathways. The process can be refined into two main synthetic routes, characterised by the surfactant concentration in the initial solution: (i) True liquid crystal templating (TLCT) and (ii) Cooperative self-assembly.

True liquid crystal templating

Derived from pathway 1 of the original liquid crystal templating method described by Beck *et al.*[9], the TLCT mechanism takes into account the high surfactant concentrations required for the existence of true liquid crystal mesophase micelles. In TLCT, the concentration of the surfactant is so high (generally greater than 20 wt. %)[77] that micellar liquid crystals are produced without requiring the presence of the inorganic silica precursor. The formed surfactant micelle crystals then serve as templates for the formation of inorganic-organic composites around these crystals after the addition and subsequent condensation of silica precursors in solution. Accordingly, the final product is a silicate framework which contains voids that mimic these micelle arrangements.

Cooperative self-assembly

The concept of the original Beck *et al.*[9] silicate anion initiated mechanism was explained and expanded upon by many researchers, specifically by the research group of Prof. Stucky at the University of California, Santa Barbara,[18, 78-80] and was termed cooperative self-assembly. The cooperative self-assembly mechanism occurs at low surfactant concentrations and it was proposed that interactions between the surfactant and the inorganic precursor were the driving force for the mesoporous material formation. A typical synthesis described using this mechanism involved initially the silica precursor and templating surfactant being combined and the formation of hybrid inorganic-surfactant micelles or aggregates driven by interaction between the species including hydrogen bonding, van der Waals forces and electrostatic attraction. The ordered mesostructured material is finally formed via continuous polymerisation and condensation of silica precursors.

The fundamental condition for this mechanism was that an attractive interaction between the template and silica precursor was produced to ensure the inclusion of the structure directing agent without phase separation taking place. The Stucky group expanded this explanation for

the synthesis mechanism when they introduced the concept of charge density matching.[18, 78, 79, 81] They proposed four primary reaction pathways for the synthesis of mesoporous materials founded on the knowledge of the specific electrostatic interactions linking the inorganic silica precursor (I) and the surfactant head group (S). These can be summarised by two interaction types:

Direct electrostatic interactions (S⁺ I⁻ or S⁻ I⁺)

If the reaction takes place under basic conditions whereby the silica species are present as anions and cationic quaternary ammonium surfactants are used, the synthetic pathway is termed S^+I^-, the prime example of this interaction being the original synthesis of M41S materials. (Figure 1.11, pathway A). The reaction can take place under acidic conditions (below the isoelectric point, pH 2, of the Si-OH bearing inorganic species) whereby the silica species is positively charged when negatively charge surfactants are used such as long-chain alkyl phosphates (S^-I^+, pathway C). The pore size of the mesoporous structure is determined by the surfactant chain length in these reactions. The pore walls are generally smooth and without large defects.

Mediated electrostatic interactions (S⁺X⁻I⁺ or S⁻M⁺I⁻)

It is possible for the reaction to take place in conditions where both the surfactants and the inorganic species are either cationic (acidic media) or anionic (basic media). To create an interaction, the addition of a mediator ion is necessary; pathway B, $S^+X^-I^+$, requires a negatively charged counter ion where $X^- = Cl^-$, Br^- etc and pathway D, $S^-M^+I^-$, a positively charged counter ion where $M^+ = Na^+$, K^+, etc is needed. In these reactions the pore size is dependent not only on the surfactant chain length but also the ion dimensions. The pore walls, as a result of imperfect distribution of counter ions, are sometimes rough with defects presenting.

In 1995 an additional pathway to synthesise mesoporous materials was proposed by Tanev and Pinnavaia[46]; the neutral templating route. This was then extended by Bagshaw *et al.*[82] to include non-ionic surfactants.

Neutral/ non-ionic interactions (S⁰I⁰ / N⁰I⁰ / S⁰(XI)⁰)

This case was based on the use of neutral (S^0: a long chain amine) or non-ionic (N^0: polyethylene oxide or triblock copolymers such as Pluronics) surfactants alongside a neutral

inorganic precursor (S^0I^0 / N^0I^0, pathway E) or ion pair ($S^0(XI)^0$, pathway F). An interaction is supported by hydrogen bonding, dipolar or Van der Waals forces, without effective charges. Pore size is principally dependent on surfactant dimensions, small differences and defects could be due to interposition of water molecule clusters.
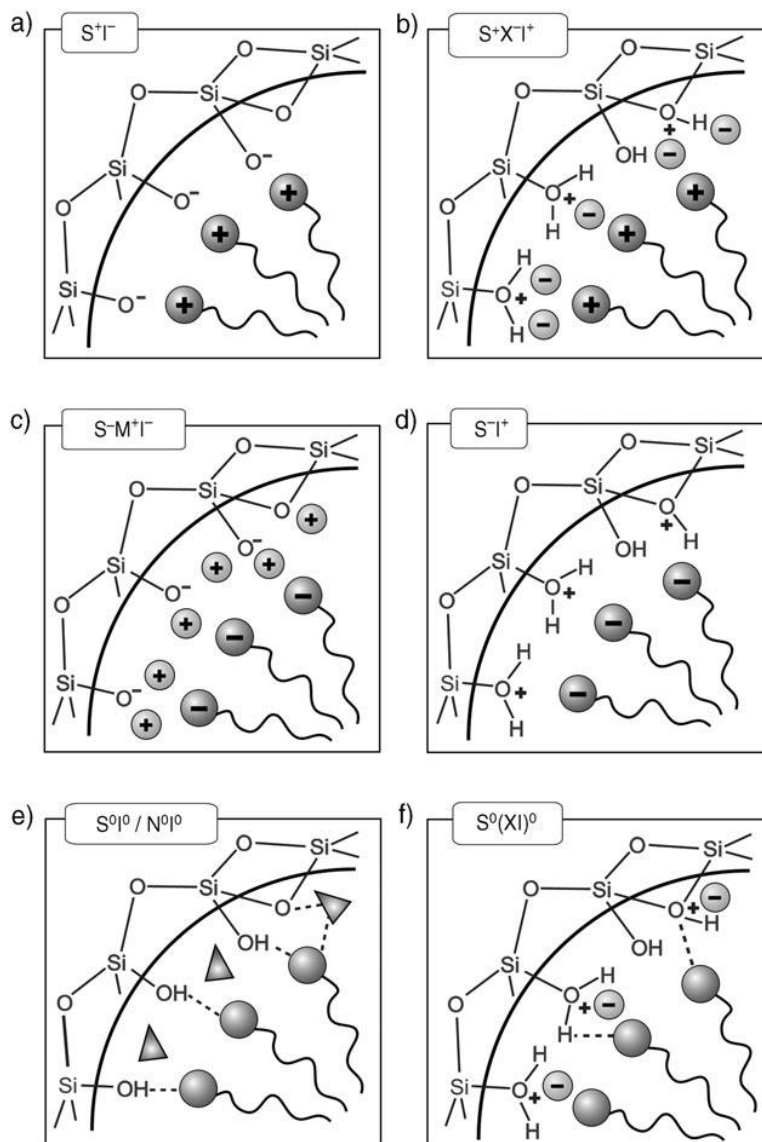
Figure 1.11: Interactions between the inorganic silica species and the head group of the surfactant with consideration of the possible synthetic pathway in acidic, basic or neutral media.[15] (a) and (d) show direct electrostatic interctions, (b) and (c) mediated electrostatic interations and (e) and (f) neutral/ non-ionic interactions.

1.5 Bioinspired silica – A 'greener' alternative silica material

In recent years, the investigation of more environmentally friendly or 'green' process routes for the production of nanostructured silica has been at the forefront of research efforts. This is largely due to increasingly stringent environmental regulations, environmental concerns and a drive for greater efficiency. The aforementioned traditional synthetic routes to silica production such as MCM-41 and SBA-15 use alkoxysilane precursors and harsh conditions in a sol-gel synthesis which is a time consuming, multistep method.[9, 21, 22] Through a process known as biomineralisation, biology produces inorganic materials such as silica at scales > 6.7×10^9 tonnes of silicon per year; orders of magnitude greater than the industrial capacity.[83] Nature has identified green routes to produce ornate structures of nanomaterials under mild conditions while achieving remarkable control over the biosilica produced.[84]

1.5.1 Biosilification

Biological silica formation, biosilification, has been defined accurately as ''the movement of silicic acid from environments in which its concentration does not exceed its solubility (< 2 mmol L^{-1}) to intracellular or systemic compartments in which it is accumulated for subsequent deposition as amorphous hydrated silica''.[85]

A number of marine and terrestrial organisms are able to uptake, accumulate and deposit silica from the environment moulding it with great sophistication to form a variety of complex and ornate, hierarchical patterned silica. Of these biological systems diatoms, sponges and plants are perhaps the most well-known biosilicifying organisms. Biosilica in organisms primarily serves as mechanical/ structural support (e.g. cell walls of diatoms and silica in rice leaves), provides protection from predators (e.g. silica spicules from sponges) and acts as sensors (e.g. biosilica as optical fibres).

1.5.2 Silica precursor – Silicic acid

A main characteristic of bioinspired synthesis is the ability to proceed at ambient temperatures and mild pHs (generally slightly acidic to neutral pH and < 40 ^{o}C).[86, 87]

Producing silica at ambient temperatures and near-neutral pHs has been problematic due to the lowest rate of hydrolysis occurring at pH = 7 and gelation taking longest at that specific pH.[33, 88] Synthetic procedures for silica and silicates generally involve a sol-gel process at low temperatures (<100 °C) with alkoxysilanes as silica precursors which are toxic.[10, 22, 88, 89]

Silicic acid ($SiOH_4$), however, is found in natural waters in extremely low concentrations (typically a few parts per million), is soluble and non-toxic in nature.[83, 84] Silica producing organisms use silicic acid as a precursor in a polymerisation mechanism to complete the biosilification process. In concentrations lower than 1 mM monosilicic acid $Si(OH)_4$ is stable between pH 2 – 9. However, at higher concentrations, monosilicic acid will spontaneously polymerise by condensation reactions to form dimers, trimers and higher molecular weight species of silicic acid. All of these species will polymerise further to maximise the number of siloxane bonds (Si-O-Si) and minimise the uncondensed silanol groups (Si-OH) remaining in the structure and hence, highly branched polysilicic acid particles predominate after the initial reaction phase.

When the monosilicic acid has depleted, a process known as the Ostwald ripening process is responsible for developing the polysilicic acid species into larger spherical particles. Thereafter, the growth of the larger particles is favoured over the smaller particles as a result of an increase in particle solubility with size. The size of the polysilicic particles produced from this process can range from 1 to 10 nm, depending on the pH and temperature conditions. Above pH 7, the particles of the polysilicic acid repel each other forming a stable solution where the precipitation of the silica does not occur.

Below pH 6, however, the polysilicic acid particles are uncharged and can undergo two processes to produce silica gel. The first is a method known as gelling, which involves the polysilicic acid particles forming branched particle chains, crosslinked by siloxane bonds. As the molecular mass increases, as does the viscosity of the sol, forming a transparent gel. However, this process is time consuming, ranging from hours to days to complete. Another method is flocculation, which occurs with the introduction of polycationic polymers to the polysilicic acid particles. This process takes mere minutes in comparison to the gelling process. It has been identified that naturally occurring silica forms by flocculation rather than gelling, due to the presence of polycationic polymer biomolecules. The successful identification and extraction of these biomolecules have been vital in the development of bioinspired silica and are discussed further in the following sections.

1.5.3 Bioinspired synthesis adapted from nature's processes

Nature's ability to form silica provides a source of inspiration for technical developments in the synthesis of silica-based nanomaterials. In comparison to synthetic silica formation, biological silica synthesis has numerous advantageous and outstanding features. The synthesis conditions are mild; neutral pH~7, ambient temperature in aqueous solution using the involvement of organic precursors.[90] In addition silica precipitation is rapid and the methods allow the production of elaborate and well controlled structures.[91]

It is of vital importance to fully understand how biology produces nanostructured silica *in vivo* in order to successfully mimic this knowledge for the formation of bioinspired silica *in vitro*. Such methods utilise analogues of biomolecules, called "additives" which possess the key functionalities required for silica formation under mild physiochemical conditions; thus, producing green, bioinspired nanomaterials. These additives can be natural biomolecules which have been isolated from biosilificating organisms such as proteins, polysaccharide and small amines[92-96] or their synthetic equivalents.

1.5.4 Bioextracted and synthetic additives

Biomolecule additives "bioextracts" have shown an ability to control silica formation in aqueous systems *in vitro* under conditions similar to those that they would be found for silica formation to occur *in vivo*.[97, 98] These biomolecules have been successfully extracted from silicifying organisms such as diatoms, or sponge, and their composition and structure investigated in order to reproduce this knowledge for developing bioinspired synthetic routes of silica formation.[99, 100]

For example, Kroger *et. al.*[94] have shown that some isolated proteins, silaffins, a set of cationic polypeptides, are capable of condensing aqueous silicic acid to silica particles *in vitro*. Similar results have been obtained by Stucky *et. al.*[101] using synthetic polypeptides to promote silica formation. In addition, it has been suggested that silicatein, a protein found in the silica spicules of the sponge and polyamines found in a range of diatoms are key to the biosilicification process in these organisms.[102] The polyamines extracted from the shells of diatoms were found to be a series with propylamine backbones of varying levels of methylation.[103] The application of these polyamines to silicic acid solutions was found to

successfully mimic the biological process; with silica spheres being rapidly precipitated measuring several hundreds of nanometers in diameter.[104, 105]

As a result of the complex nature of bioextracted additives, the ability to isolate the silica product with high purity and characterisation often proves difficult at times. Therefore, their analogues, synthetic additives, have been used to mimic their role in silica formation *in vitro*. It has been identified that silica formation in the presence of additives is governed by a number of key observations. These include the presence of cationically charged species and the importance of additive self-assembly prior and during silica polymerisation. The use of synthetic additives allows the ability to investigate not only the mechanisms involved in the complex process of silica formation but also how to control the properties (e.g. structure and assembly) of the silica produced. For example, synthetic additives such as polymers, block co-polymers and small amines have been investigated to determine their effects on silica polymerisation.[106-108] Silica has been precipitated by propylamines which are analogous to the amines found in diatoms and sponges, producing materials with low surface areas <10 m^2 g^{-1}. [91, 106] Belton *et. al.* reported the successful synthesis of a series of linear methylated propylamines with varying levels of methylation and amine lengths in order to study the influence of these amine synthetic additives on silica formation.[104, 109] A number of studies have shown that short alkylamines, such as poly(ethyleneamine), can promote the rapid condensation of silicic acid producing silica spheres, and their properties thought to be related to the number of amine units present.[106, 110, 111]

An understanding of the formation of biological silica has lead to significant improvements in the synthesis conditions under which the silica materials are traditionally produced; removing the need for strong pH as well as high temperature or pressure. The fundamentally new, biologically compatible synthetic approaches to design silica-based materials allow complex silica structures to be synthesised under environmentally benign conditions with high reproducibility.

1.6 Application of mesoporous silica materials for environmental remediation

Originally, the drive behind the synthesis of mesoporous silica was in the hope of yielding materials with larger pores, in comparison to microporous zeolites, for catalyst applications. However, as a result of their well-defined and controllable morphology and porosity, the application of these nanoparticles has expanded, and they are now being pursued in various different technology fields including drug delivery, biosensing, adsorption and separation. The area of interest of this thesis, and the research presented within, is the use of nanoparticulate materials for environmental remediation and the removal of pollutants from indoor air and water systems. Therefore, thesis will be dedicated, in part, to investigating the use of mesoporous silica-based materials as adsorbents. In addition, the performance of conventionally used sorbent materials, such as Tenax and powdered activated carbon (PAC), (discussed in detail in Section 4.1.3 and 6.1.3) is examined. The application of adsorption technology has been generally recognised as a preferred strategy for the treatment of both air and water environments due to the flexibility, low energy and cheap operational costs. Ordered mesoporous silica offers excellent features such as large pore volume, high surface area, controllable and narrowly distributed pore sizes, open pore structure and reliable desorption performance. These characteristics are greatly desirable, however, fail to be found as a collective in commercially available and industrially used sorbents, thus, highlighting the potential application of these materials in adsorption technologies.

1.7 Thesis outline - Overall aims and objectives

The basis of this thesis involves the synthesis of a variety of silica platforms and examines their use as adsorbents in environmental remediation alongside traditional sorbent materials. Furthermore, this research additionally investigates photocatalytic oxidation (PCO) as an alternative remediation technique. There are two target areas of the environment examined for the removal of pollutants during the scope of this work: air and water systems. These areas will form the structure of Part A and Part B of this thesis, respectively.

This thesis consists of 9 chapters. Chapter 1 provided an overall review into the synthesis, modification, formation mechanisms and applications of mesoporous silica materials in addition to examining nature's method of producing silica through biosilification and the potential of a bioinspired synthesis method for silica nanomaterials. Chapter 2 provides an overview of the instrumental and experimental theory behind the techniques used throughout this work. Chapter 3 will be dedicated to detailing the experimental procedures involved in the synthesis of each silica material used in this research. These include MCM-41, SBA-15, bioinspired silica and iron incorporated bioinspired silica materials. In addition, it will examine the physical properties of each sorbent material (silica materials and powdered activated carbon) using nitrogen adsorption-desorption analysis through the use of the Brunnauer, Emmett and Teller (BET) technique. The thesis subsequently splits into two investigations; Part A (Chapters 4 and 5) will examine at the remediation of selected pollutants in air and Part B (Chapters 6 and 7) the removal of target analytes in water.

Part A

The work presented in Part A of this thesis aims to examine and develop existing methods used to reduce concentrations of volatile organic compounds (VOCs) from indoor air in order to enhance air quality. Herein, monoaromatic hydrocarbons (MAHs), including toluene, ethylbenzene, cumene and dichlorobenzene were selected as targets due to their potential impact on human health. The two application areas in this work were to remove the selected VOCs by adsorption or photocatalytic oxidation (PCO).

Chapter 4 details a few of the key objectives of this work required to ensure that the sampling method can be trusted and thus transferred for use in the subsequent PCO experiments. This involves the generation of a steady stream of air polluted with known concentrations of VOCs for the subsequent dynamic sampling from an atmospheric chamber. It is of importance that this set up is robust and stable in order for both investigations (adsorption and PCO) to be applicable to true indoor air environments. Another crucial aspect to these investigations, reported in this Chapter, is the development of an accurate and precise method to analyse the VOCs trapped onto sorbent materials that can provide confidence in the sample analysis for use in the subsequent PCO study. This was completed using thermal desorption-gas chromatography-mass spectrometry (TDU-GC-MS), thus, producing calibration lines for quantitative analysis. The use of traditional adsorption techniques using conventional mesoporous materials such as MCM-41 and SBA-15 in comparison to commercial sorbent

Tenax TA were examined to determine the sampling efficiency; volume of air and mass of analyte trapped at breakthrough, and also the dynamic adsorption capacity of each sorbent. The best performing sorbent is chosen for use during the PCO investigation. The work presented in chapter 4 not only allows the performance of the aforementioned sorbent materials to be examined but also acts as a platform, providing the results needed for the next stage of the investigation to proceed.

Chapter 5 reports the evaluation of the process of photocatalytic oxidation (PCO) as an alternative for indoor air abatement. Titanium dioxide (TiO_2) thin film was used a photocatalyst. Traditional adsorption techniques merely trap pollutants on the sorbent material however PCO has the potential to completely destroy them. The study involves the preparation of TiO_2 film coated glass beads and quartz tubes used throughout the investigation, the determination of the number of TiO_2 film coatings required for optimum photocatalytic activity and the assessment of the long-term performance of the TiO_2 photocatalyst.

Part B

Part B of this research turns attention from removal of pollutants from the air to evaluating remediation techniques for use in aqueous environments. The adsorptive removal of two groups of water contaminants is investigated in this work: Pharmaceutically active compounds and nitrobenzene.

Chapter 6 examines the adsorption of these compounds from aqueous solution onto a variety of sorbent materials. This involves the evaluation of mesoporous silicas (As-syn MCM-41 and Calc MCM-41), bioinspired silica materials (As-syn Bio-Si and Calc Bio-Si) and iron incorporated bioinspired silica materials (As-syn Fe Bio-Si and Calc Fe Bio-Si). The performance of these sorbents for the removal of the target analytes is compared to the commercially available, industry standard sorbent, activated carbon. A full assessment of each sorbents performance was undertaken to provide a comprehensive understanding of the processes involved in adsorption from aqueous solution. This involved investigating the effect that solution conditions such as pH will have on the sorbent performance. For the adsorption of pharmaceutical target compounds by PAC and As-syn MCM-41 the parameters that influence the sorption process such as contact time, concentration of analytes in solution, the presence of other analytes and solution pH are investigated. The linearised Langmuir and Freundlich equations are used to fit the equilibrium isotherms to evaluate the sorbent

adsorption capacity. Kinetic data is analysed by pseudo-first-order, pseudo-second-order and intra-particle diffusion models to obtain the kinetic constants, establish the rate-limiting step of analyte removal and postulate the mechanism of analyte adsorption by each porous material.

Chapter 7 is dedicated to the investigation of advanced oxidation techniques; through the application of the photo-Fenton process and visible-light initiated PCO, for the removal of the selected target pharmaceuticals and nitrobenzene from water systems. Firstly, in a novel set of experiments iron incorporated bioinspired silica material (As-syn Fe Bio-Si and Calc Fe Bio-Si) is studied as a heterogeneous Fenton-like catalyst for the degradation of the target analytes in aqueous solution. The effects of different operational parameters such as H_2O_2 concentration and initial solution pH on the catalytic activity are also evaluated. Secondly, as examined in Part A for the degradation of pollutants in indoor air, the use of a TiO_2 thin film as a photocatalyst is further evaluated to assess its performance in aqueous solutions. As this reaction requires UV irradiation to proceed, the synthesis of an iron-incorporated TiO_2 thin film is detailed and the performance of the material assessed for the photodegradation of nitrobenzene in visible light.

Finally, all thesis conclusions and future work are presented within each corresponding Chapter with overall concluding remarks made in Chapter 8.

2. Theory of instrumental techniques

2.1 Determination of textural and surface properties – Nitrogen adsorption

2.1.1 Principles of adsorption

The term adsorption is universally understood to mean the enrichment of one or more of the components in the region between two bulk spaces (i.e. the interfacial layer or the adsorption space). When a porous solid material is exposed to a fluid (gas or liquid), adsorption occurs with the accumulation of the fluid on the interface between fluid and solid. The adsorbed fluid on the solid surface is term adsorbate and the solid is called the adsorbent. There are two types of adsorption: physisorption (physical adsorption) and chemisorption (chemical adsorption). The former is a surface phenomenon and resembles the condensation of gases to liquids, in which an adsorbate is held onto the surface of the adsorbent by Van der Waal's forces.[112, 113] These forces are physical in nature, which means that the process is reversible (using heat, pressure, etc.). Chemical adsorption involves a reaction between adsorbate and adsorbent resulting in chemical bond formation and, thus, it may be irreversible.[114]

2.1.2 Nitrogen sorption isotherms

The physical adsorption – desorption of nitrogen is an effective and widely used technique for the characterisation of porous materials. Whenever a gas is in contact with a solid, there will be an equilibrium established between the gaseous molecules and the adsorbed species bound to the surface of the solid. Adsorption of a gas by a porous solid is described quantitatively by an adsorption isotherm, representing the amount of gas adsorbed at a fixed temperature as a function of pressure.

The International Union of Pure and Applied Chemistry (IUPAC) conventions have been proposed for classifying gas adsorption isotherms.[115, 116] There are six types of isotherms (Figure 2.1) characteristic to different pore sizes with the shape of the isotherm giving direct information about the adsorbent – adsorbate interactions.

Type I isotherms

Type I isotherms are characteristic of microporous materials. The narrow nature of micropores means that during adsorption they are directly filled in a one-step process and resulting in an increased adsorbent-adsorbate interaction. The nearly horizontal plateau is reached at low relative pressures, indicating the relatively small external surface area of microporous materials.

Type II isotherms

These sigmoid shaped isotherms are commonly encountered for non-porous and macroporous materials, representing monolayer-multilayer adsorption on an open and stable surface. The knee-point at B indicates the stage at which monolayer coverage is complete and multilayer adsorption begins.

Type III isotherms

The Type III isotherm is convex over the entire relative pressure range and therefore does not exhibit a point B. These isotherms are very uncommon and are characteristic for materials with very weak adsorbate-adsorbent interactions.

Type IV isotherms

This type of isotherm is typical of mesoporous materials. The initial stage of the isotherm at low relative pressures is similar to that of type II, attributed to the adsorption of the monolayer with the presence of point B again indicating the multilayer adsorption. This is followed, at higher relative pressures, by a marked increase in adsorption which corresponds to the occurrence of capillary condensation in the pores. A hysteresis loop, associated with this pore condensation, is frequently observed in this type of isotherm; the different types of which are shown in Figure 2.2.

Type V isotherms

The type V isotherms are characteristic for porous materials with weak adsorbate-adsorbent interactions. Initially they are similar to the type III isotherms but with pore condensation taking place at higher relative pressures, usually indicated by the presence of a hysteresis loop. This is a result of cooperative effects; interaction between a molecule and a neighbouring adsorbed molecule aid coverage of the material surface. As a consequence of this lateral interaction, two-dimensional condensation occurs.

Type VI isotherms

These isotherms are characteristic of sharp steps representing multilayer adsorption on a highly uniform, non-porous surface. The step height corresponds to the monolayer capacity for each adsorbed layer.
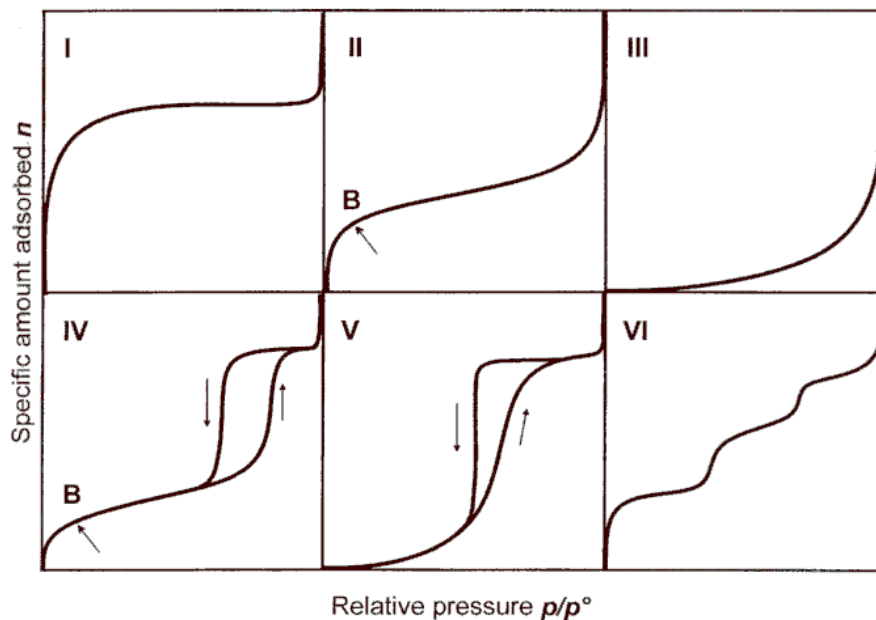
Figure 2.1: Types of sorption isotherms.[117]

As previously described, hysteresis loops are associated to capillary condensation phenomena in mesoporous or macroporous materials. A hysteresis loop is generated when the adsorption and desorption curves do not correspond. This is as a result of desorption from the pores via evaporation occurring at a relative pressure lower than that at which condensation during adsorption takes place. The four types of hysteresis loops, illustrated in Figure 2.2 can be associated to a well-defined pore structure, thus indicating how the pores are shaped.
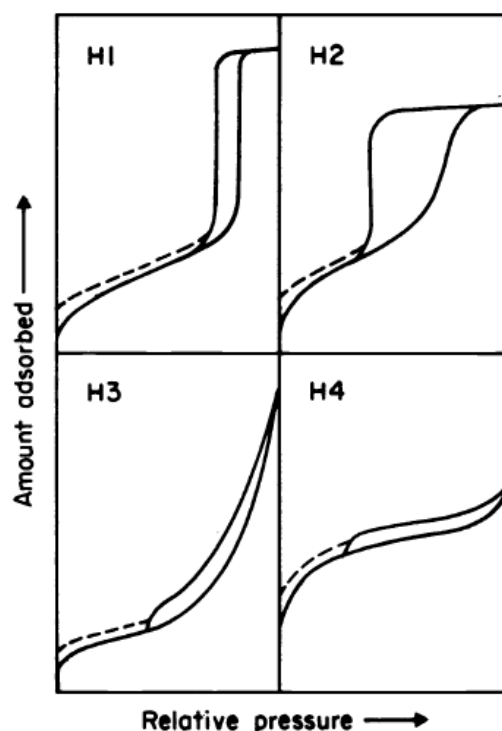
Figure 2.2: Types of hysteresis loops.[117]

H1

This type of hysteresis loop has steep parallel adsorption and desorption branches in a narrow range. It is typical for mesoporous materials with well-defined cylindrical pores.

H2

The H2 hysteresis loop has a smooth adsorption branch coupled with a steeper desorption branch. It is typical of disordered materials with a non-uniform distribution of pore shapes and sizes, e.g. silica gel or other metal oxides.

H3

This type of hysteresis loop is associated with slit-shaped pores. These often rise from aggregates of plate-like particles, as indicated by the absence of an upper adsorption limit.

H4

The H4 hysteresis loop is similar to H3, often associated with narrow slit-like pores. However, it has a more horizontal plateau, extended over a wide range of relative pressure which in the case of Type I isotherm is indicative of microporosity in the material.

Nitrogen is most commonly used as an adsorbate, due to its inertness, at a temperature of 77 K. At this cryogenic temperature, nitrogen gas is below the critical temperature and, therefore, condensable meaning adsorption on the surface of the material and capillary condensation in the pores would take place.

The shape of the isotherm reveals information about the textural properties of porous materials. A number of different theories or models can be applied, such as Bruanuer-Emmett-Teller (BET) and Barret-Joyner-Halenda (BJH), from which the surface area and pore size distribution can be calculated.

The adsorption isotherms can have different shapes depending on the type of adsorbent, adsorbate and molecular interactions between the adsorbate and adsorbent surface.

2.1.3 BET surface area

Originally, the concept of adsorption relating to an exposed surface was developed by Langmuir. He suggested that adsorption corresponds to a dynamic equilibrium between a gas and a solid surface resulting in a surface layer that is only one molecule thick. Brunnauer, Emmett and Teller[118] (BET) extended this theory and introduced the concept of multilayer adsorption. The BET gas adsorption method has become the most widely used standard procedure for the determination of the surface area of porous materials.

The BET equation in the linear form ($y = mx+c$), Equation 2.1, is expressed as:

$$\frac{(\frac{P}{P_0})}{[V\left(1-\left(\frac{P}{P_0}\right)\right)]} = \frac{1}{CV_m} + \frac{(C-1)(\frac{P}{P_0})}{CV_m} \qquad \textbf{Equation 2.1}$$

where P is the equilibrium pressure of nitrogen and P_0 is saturation pressure of nitrogen at the adsorption temperature; thus, (P/P_0) is the relative pressure. V is the moles of nitrogen adsorbed per gram of adsorbent, V_m is the monolayer capacity and C is the BET constant.

By plotting (P/P_0)/[V(1-(P/P_0))] versus (P/P_0), a straight line BET plot should be provided. However, the linear relationship of this function is restricted to a limited section of the isotherm, usually the relative pressure (P/P_0) range from 0.05 to 0.25, in which the monolayer adsorption is complete.

From the slope of the plot and the intercept with the x axis, values for V_m and C can be estimated. The second stage is the calculation of the surface area, S_{BET} (see Equation 2.2), of the adsorbent from the monolayer capacity, V_m.

$$S_{BET} = V_m N_A a_m$$

Equation 2.2

where N_A is the Avogadro constant and a_m is the molecular cross-sectional area occupied by the adsorbate molecule in the complete monolayer which for nitrogen at 77 K is 0.162 nm^2. Furthermore, the specific surface area can then be determined by surface area divided by the weight of the sample.

2.1.4 Micropore volume and external surface area: The t-plot method

The t-plot method, first proposed by Lippens and de Boer,[119, 120] is used to determine the micro and/or mesopore volume and specific surface area of a material. The method is based on standard isotherms and thickness curves which describe the statistical thickness of the film of adsorbate on a non-porous reference surface. It is with these standard Type II isotherms that the experimental isotherm is compared.

In general, the composite reference t-curve is obtained from data on a number of nonporous adsorbents with BET C constants similar to that of the microporous sample being tested. The experimental test isotherm is then redrawn as a t-curve. This involves plotting the volume of gas adsorbed, V, as a function of t, i.e. the standard multilayer thickness on the reference non-porous material at the corresponding P/P_0. These t-values are, in practice, calculated with the help of a thickness equation, which describes the particular reference curve. In this work, the Harkins-Jura[121] thickness equation was used and is based on the adsorption data obtained on nonporous Al_2O_3.

Differences in the shape of the experimental isotherm and the standard isotherm result in non-linear regions of the t-plot. Extrapolation of the t-plot to t = 0 can give rise to positive and negative intercepts. It is these deviations from the standard isotherm that can be used to obtain information regarding micropore volume and external surface area of the sample material.

Absence of micropores in the sample material would result in a t-plot resembling a straight line passing through the origin. When a relatively small fraction of micropores are present,

the adsorption isotherm will show an increased uptake of gas at low relative pressures. When the linear t-plot is extrapolated to the adsorption axis, the intercept will be equivalent to the micropore volume. From the slope of the t-plot the external surface area can be derived, i.e. the area of those pores that are not micropores. Mesopores, macropores and the outside surface are able to form a multilayer, whereas micropores which have already been filled cannot contribute further to the adsorption process. The micropore surface S_μ is the difference between the BET surface, S_{BET} and the external surface, S_{ext} and can be calculated from Equation 2.3.

$$S_\mu = S_{BET} - S_{ext}$$ **Equation 2.3**

2.1.5 Determination of pore size

The pore systems of solids may vary substantially in both size and shape. It can, therefore, be difficult to determine the pore width, or more precisely, the pore size distribution of a solid. To overcome this, the shape of the pores are usually assumed to be either cylindrical or slit shaped. The most commonly used methods of calculating pore size distribution are based on the Barrett-Joyner Halenda[122] (BJH) method. The BJH approach provides an algorithm to calculate the pore size distribution by assuming cylindrical pore geometry from nitrogen desorption data obtained at 77 K, taking into account the thickness of a multilayer of adsorbed nitrogen on the pore walls. The main principles for calculating pore sizes using the BJH method are based on the concept of capillary condensation and the Kelvin equation. For capillary condensation in cylindrical pores, the Kelvin radius as a function of relative pressure can be written as:

$$\ln \left(\frac{P}{P_0}\right) = \frac{2\gamma \bar{V}}{rRT}$$ **Equation 2.4**

where γ is the surface tension of the liquid and V is the molar volume of the condensed liquid contained in a narrow pore radius r, R is the gas constant and T is the temperature.
The pore size, r_p, is then obtained by adding the adsorbed layer thickness, t, to r.

$$r_p = 2(r + t)$$ **Equation 2.5**

2.2 Chromatography[123-127]

Chromatography is one of the most powerful techniques available to an analytical chemist in the analysis of complex samples. The dominance of this method lies in its ability to separate mixtures into individual components; making it easier determine the respective identity (chemical structure) and measure the concentration of the various compounds or 'analytes' within the sample. All chromatographic techniques depend upon the same basic principle; the variation in the rate at which an analyte molecule migrates through a column based on its distribution between a stationary phase (SP) and a mobile phase (MP). There are numerous chromatographic techniques such as gas chromatography (GC) and high performance liquid chromatography (HPLC); the selection of which separation technique to use depends on the compounds or molecules in the sample and the sample matrix itself.

2.2.1 Gas Chromatography (GC)[128, 129]

In gas chromatography, the sample mixture is introduced into a gaseous mobile phase, carrier gas, by means of sample vaporisation. It is then pumped through a stationary phase held within a column, where sample components are separated, and, finally, transferred to a detector. The column is held in a temperature-controlled oven and analytes travel through the column at a rate that is determined by their physical properties, the column temperature, and the composition of the stationary phase. In general, separation in GC occurs through differences in analyte boiling points and their relative affinities for the stationary phase, where elution is in order of increasing boiling point. To be suitable for GC analysis, a compound must be sufficiently volatile, thermally stable (up to few hundred °C) and have low molecular weight (up to ~ 400 – 500 a.u.); making GC the most widely used technique for separation and analysis of volatile compounds. A schematic of a typical GC instrument coupled to mass spectrometer (MS) detector with quadrupole mass analyser (discussed in detail in Section 2.3) is presented in Figure 2.3.
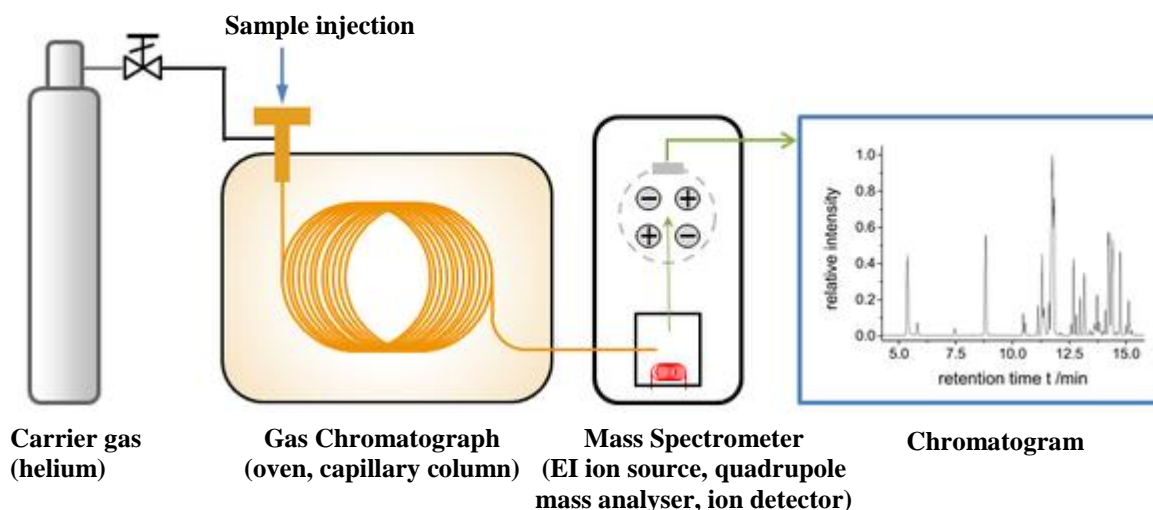
Figure 2.3: Schematic of GC-MS instrumentation.

Liquid or gaseous samples are introduced into an injection port using a syringe (in manual or automatic injection mode), as shown in Figure 2.3. However, in the case of air samples collected onto sorbent tubes and, thereby, for all sample analysis carried out in Part A of this thesis, they are introduced into the GC system by means of thermal desorption.

Thermal desorption

Thermal desorption is a commonly used sample introduction technique for GC which makes use of the decreased ability of a sorbent to retain compounds at elevated temperatures. It is a technique used to extract volatiles from a sorbent by heating the sorbent/sample in a stream of inert carrier gas. The extracted volatiles are refocused onto a cold trap from which they are transferred in a narrow band to a GC column for analysis.[130] The process involves initially sealing the sorbent tube into the thermal desorption unit. A leak test is automatically performed to ensure that the tube has been sealed correctly and to ensure that the rest of the system is leak tight. The tube is then purged with carrier gas at ambient temperature to remove oxygen and moisture. The subsequent injection of the sample is a two-stage process as illustrated in Figure 2.4. First the sample is heated with a flow of inert carrier gas to extract the volatiles. To ensure complete recovery of sampled components from sorbents such as Tenax, high desorption temperatures are required, 250 – 300 °C. The desorbed volatiles are carried by the gas into a low thermal mass, electrically cooled cold trap (-30 °C) for pre-concentration. In stage 2, the cold trap is flash heated and the vapourised compounds are

injected into the GC column through a heated transfer line. The rapid heating of the cold trap rapidly ensures efficient transfer of a narrow band of analytes to the GC system.

Stage one

Sample Tube
VOCs extracted by heating

Cold Trap
Sample band condensed

Carrier Gas

Heating

Cooling

Stage two

Cold Trap
Rapid Heating

GC Column
Separation of analytes

Samples introduced
to GC column

Heating
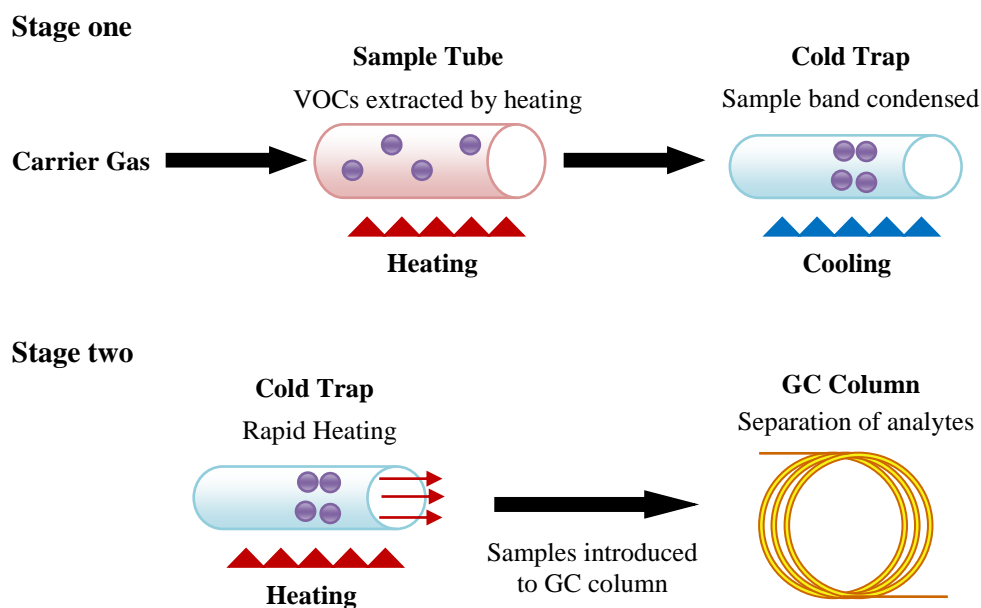
Figure 2.4: Two stage thermal desorption process.

Mobile phase in GC

The carrier gas must be chemically inert and of good quality, ensuring it is free from O_2 and moisture, protecting the column from degradation. Helium is the most commonly used carrier gas with typical flow rates between 0.5 to 50 cm^3 min^{-1}. However, hydrogen and nitrogen can also be used; the choice being dictated by the type of detector coupled to the instrument.

Column type

There are two types of column that can be used with a GC system, packed or capillary. Packed columns, usually made of glass or stainless steel, contain small uniform particles of the solid stationary phase, usually tightly packed silica particles, or solid support particles, coated in a stationary phase. Columns are typically 2 – 5 mm in diameter and 1 – 5 m long. The performance of packed columns is influenced by the particle size and distribution meaning that they have significantly lower resolving power than capillary columns. Therefore, the latter are more widely used for industrial and research applications. Capillary columns used with GC systems can be divided into two types; wall coated open tubular (WCOT) columns and support coated open tubular (SCOT) columns. WCOT columns have the liquid stationary phase coated as a thin film onto the high purity fused silica column.

47

SCOT columns have small inert solid support particles coated with liquid stationary phase fused to the inner wall of the column and are much less common than WCOT columns. Capillary columns in general offer greater resolution than packed columns and this is, in part, due to their dimensions, 0.2 – 0.5 mm in diameter and up to 10 – 60 m long. Due to the difference in column dimensions, packed columns are able to cope with sample sizes up to 20 µL whereas capillary columns require much less sample, 10^{-3} µL. Capillary columns require the use of a split/splitless injector to ensure that the column is not overloaded.

In split mode, the sample is injected into the injector port and diluted by flooding the port with carrier gas flowing at 50 – 100 times the normal flow rate. Only 1 – 2 % of the original sample is carried onto the top of the column and the rest is vented to waste. Samples with low analyte concentration are injected in splitless mode. The sample is vaporised upon injection and carried onto a cold-column, causing the sample and carrier gas to condense. A temperature programme then heats the column, initially causing the solvent to vaporise before the analytes are also vaporised as they are carried down the column as a sharp band.

Column temperature control

In GC the temperature of the column can be controlled by altering the temperature of the oven in which it is held. The separation of compounds using GC depends on the analyte boiling point as well as interaction of the analyte with the stationary phase. Thus, the injection is often made at a lower oven temperature and the temperature is programmed to some elevated temperature where elution of analytes is in the order of increasing boiling point. While sample analysis may be performed isothermally, compound elution time and resolution are extremely dependent on temperature. At higher temperatures, more analytes will be vapourised and present in the mobile phase thus causing them to elute faster therefore efficient analysis is at a cost of resolution. Equally if column temperature is too low analytes may take too long to elute from the column. A compromise is required and therefore the method of temperature-programming is commonly used for samples containing a large number of analytes. Low temperatures are used initially to resolve analytes with low affinities for the stationary phase and the temperature is elevated thereafter to increase the migration rate of analytes which interact more strongly with the stationary phase. By systematically altering the oven temperature and the rate of temperature change (ramp rate) throughout the chromatographic run, the GC method can be optimised to gain the greatest efficiency and resolution.

2.2.2 High Performance Liquid Chromatography (HPLC)[131-133]

In HPLC, the separation of mixtures is achieved by introducing the sample into a liquid mobile phase (eluent), which is pumped through a column. Figure 2.5 shows the main components of a HPLC system. These components and the factors that affect the quality of the chromatographic separation (in both GC and HPLC) will be discussed in this Section and Section 2.2.3, respectively.
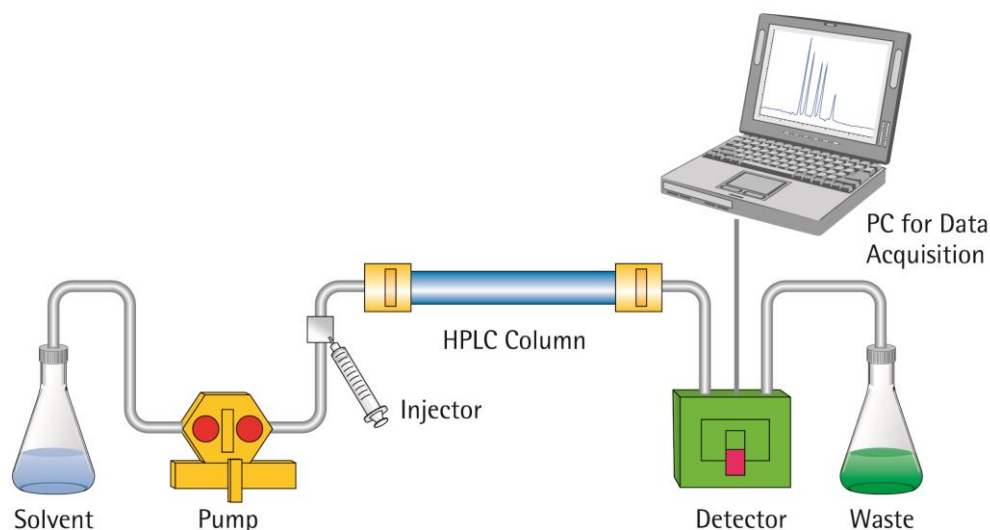
Figure 2.5: Typical set-up of HPLC system.[134]

Column

The column used in HPLC is packed with stationary phase particles, usually tightly packed silica particles of uniform size. This is known as a packed column; capillary columns can also be used in HPLC but are mostly employed in GC. Capillary columns are long thin tubes, ranging from 5 to 200 m in length and 50 to 500 µm in diameter,[135] where the stationary phase is coated as a thin film on the internal surface of the tube. The two most common separation methods used in HPLC are normal phase and reverse phase.

In normal phase HPLC, also known as adsorption, the stationary phase is more polar than the mobile phase. Typical stationary phases that this method can be conducted on are specially prepared silica (either unmodified or derivatised silica gel) and alumina.[136] Both of these materials are highly polar and adsorb molecules strongly. In silica gel, the adsorption sites are the oxygen atoms and silanol groups (-Si-OH) which readily form hydrogen bonds with polar molecules. The mobile phase used is a non-polar solvent such as hexane.[135] Separation of

solute molecules occurs with the more polar molecules having a greater affinity for the polar stationary phase. These molecules are retained in the column for a longer period of time and consequently elute later than the less polar molecules. Elution is in the order of increasing polarity. As well as the functional groups within an analyte, steric factors also have a significant effect on the interaction strength of analyte and stationary phase, allowing this technique to resolve structural isomers.

A drawback with this method is that very polar solvents, such as water, have a tendency of deactivating the stationary phase by blocking adsorption sites, forming a water layer on the stationary phase surface.[135] The change of hydration state of the stationary phase by water or protic organic solvents causes a lack of reproducibility of retention times. This along with the environmental implication of large volumes of organic solvents being generated as waste consequently makes normal phase HPLC an unfavourable method.

By far, the most extensively used HPLC method is reverse phase HPLC (RP-HPLC). This is the consequence of its capacity to separate a wide range of organic compounds, often including compounds of similar structures. In RP- HPLC, the stationary phase is non polar, created by the derivatization of silica particles. Derivatisation is most commonly accomplished by reaction of the hydroxyl groups with organosilanes:

$$-Si\text{-}OH \;+\; X_nSiR(CH_3)_{3\text{-}n} \;\rightarrow\; -Si\text{-}O\text{-}SiX_{n\text{-}1}R(CH_3)_{3\text{-}n} + HX$$
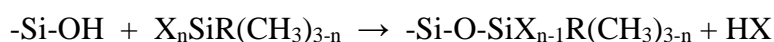
where X is a reactive group (usually a chloro species) and R is the functional group attached to the silica surface. For reverse phase separations the most commonly used non-polar functional groups R, are alkyl-bonded phases with R= C_8H_{17} and $C_{18}H_{37}$.[136] The separation of solute molecules occurs with the less polar molecules having a greater affinity for the non-polar stationary phase. These molecules are retained in the column for a longer period of time and consequently elute later than more polar molecules. Elution is in the order of decreasing polarity. Mixtures of water or aqueous buffers and organic solvents are used as mobile phases to elute analytes from a reversed phase column. The solvents have to be miscible with water and the most common organic solvents used are acetonitrile, methanol or tetrahydrofuran (THF).[137]

Elution Gradients

A major problem associated with HPLC is caused by molecules that have either limited interaction with the stationary phase and are eluted at the beginning of the chromatogram or form irreversible interactions with the stationary phase and will not elute from the column. The latter of these also results in decreased column activity and efficiency as potential sites of interaction are irreversibly occupied. The life-time of the column will, therefore, be reduced. Another problem with HPLC occurs when an isocratic flow is used to analyse a complex mixture containing both hydrophobic and hydrophilic components. Components with a wide range of polarities are unlikely to separate quickly and effectively, resulting in prolonged run-times and poor resolution. An isocratic mobile phase has a constant ratio of organic to aqueous composing the mobile phase throughout the chromatographic run and is preferably used to separate a single compound.[137]

This problem is overcome through the use of solvent gradients, a technique in which the composition of the mobile phase is changed by altering the ratio of organic to aqueous during the chromatographic run. Starting with a mobile phase containing a high percentage of water, making non-polar compounds adhere tightly to the top of the column, the amount of a more non-polar solvent such as acetonitrile is then gradually increased to wash them off. By changing either the initial or final amount of acetonitrile or the rate of change of acetonitrile addition, the separation achieved can be modified.[137]

Gradients allow the elution of both polar and non-polar molecules to occur within a fast analysis time. They also improve the chromatographic peak shape obtained as it forces the chromatographic band through the column, resulting in better resolving power and more accurate quantification of the compounds.

2.2.3 Chromatographic separation and selectivity factors

As the sample is injected into the mobile phase, the analytes migrate through the column where equilibration between the two phases occurs. The distribution coefficient, D_A, is a measure of the extent of the analyte equilibrium between the mobile phase and the stationary phase represented in Equation 2.6:

$$D_A = \frac{[A]_{SP}}{[A]_{MP}}$$
Equation 2.6

where D_A is the distribution of analyte, A, and $[A]_{SP}$ and $[A]_{MP}$ represent the concentrations of analyte, A, in the stationary phase and mobile phase respectively.

The distribution coefficient reflects the affinity of the analyte for the stationary phase and thereby, determines the rate at which it migrates through the column, giving rise to a characteristic retention time (t_R) under specific conditions. Those analytes with a large affinity for the stationary phase (larger D_A value) will be retained in the column for a longer period of time and thereby eluted later than those that are attracted more to the mobile phase. Once eluted from the column, analytes reach the detector and a chromatogram is produced, where each detected analyte is represented by a peak. Ideal chromatographic peaks should follow a Gaussian distribution resulting in a symmetrical peak shape.

Chromatography is described in terms of the following parameters:

t_o – the time of sample injection.

t_M – the void time, the time at which non-interacting solutes are eluted from the column. This is related to the void volume V_M (the volume of unretained solutes which are eluted).

t_R – the retention time of analyte, this is related to retention volume (V_R).

The aim is to produce well-resolved and narrow peaks with each analyte separated from the others. There are two factors that contribute to the quality of chromatographic separation; the difference in retention times between peaks (the further apart, the better their separation) and how broad the peaks are (the wider the peaks, the poorer their separation). The following parameters are used to measure the efficiency of a separation.

The retention factor, k', measures the migration rate of an analyte on a column. The retention factor for analyte A is defined in Equation 2.7:

$$k'_A = (t_R - t_M) / t_M \qquad \qquad \textbf{Equation 2.7}$$

where t_R is the retention time of analyte A and t_M is the column void time. If k' < 1 for an analyte, elution is so fast that accurate determination of the retention time is very difficult. Ideally k' = 1 - 5, if k' > 20 then the analysis time is considered to be inefficient.

The selectivity factor, α, measures the separation of two particular analytes (A and B) by a column, Equation 2.8:

$$\alpha_{A,B} = k'_B / k'_A \qquad \textbf{Equation 2.8}$$

where k'_B and k'_A are the retention factors of analytes B and A, respectively. Selectivity factors should always be greater than 1, with the later eluting peak placed on the numerator of the equation. If α = 1, there is no difference in interaction between the two analytes and the stationary phase and, therefore, peak separation will not be observed. Ideally, the selectivity factor should lie in the range of α = 1.05 – 2 and separation is considered to be inefficient if the value of α is >> 2.

Resolution is measured in terms of the resolution factor, R_S and can be estimated using Equation 2.9. The R_S value indicates the relationship between peak retention times and widths and is used to measure the extent of analyte separation when two adjacent peaks are equal in size:

$$R_S = \frac{t_{R_B} - t_{R_A}}{\frac{1}{2}[(Wb)_A + (Wb)_B]} \qquad \textbf{Equation 2.9}$$

where $(Wb)_A$ and $(Wb)_B$ correspond to the widths at the base of analyte peaks A and B, respectively. The calculated Rs value can be broadly interpreted as given below:

$R_S < 1$ peaks insufficiently resolved

$R_S = 1$ there is approximately 2.3 % overlap between analyte peaks

$R_S = 1.5$ optimum resolution with only 0.1 % overlap

$R_S > 1.8$ analyte peaks are too far apart indicating inefficient analysis time

The efficiency of the chromatographic system is measured in terms of the number of theoretical plates, N (Equation 2.10):

$$N = x \, (t_R/\sigma)^2 \qquad \textbf{Equation 2.10}$$

where σ is the peak width and x is a constant. The values of σ and x are dependent on whether the peak widths are measured at the base or at 50 % of the peak height. Symmetrical

peaks should be measured at the base where x = 16. Non-symmetrical peaks should be measured at 50 % of the peak height where x = 5.54. N decreases as a chromatographic column degrades over time resulting in difficult solute resolution.

2.2.2.3 Band Broadening in Columns – The Van Deemter Equation

When a sample is injected into a column, the solute molecules distribute themselves between the mobile phase and the stationary phase. Those solutes with a greater affinity for the stationary phase will be retained longest and elute last from the column. Different solutes can be separated if they have a different affinity for the stationary phase. The longer the sample remains in the chromatographic system, the broader the analyte zone becomes. This causes peaks to widen, known as band broadening, and thus decreases the efficiency of the chromatography (N $\propto$ 1/w), where w = peak width. The efficiency of a chromatography column can be calculated in terms of height equivalent theoretical plates (HEPT), represented by Equation 2.11:

$$HETP = H = L/N \hspace{3cm} \textbf{Equation 2.11}$$

where H= plate height, L = length of column (mm) and N = number of theoretical plates.

The most influential study using the kinetic approach to band broadening was published by Van Deemter and co-workers in 1956.[138] From this investigation three diffusion effects were identified as being main contributors to band broadening in packed columns: Eddy diffusion (the A term), longitudinal molecular diffusion (the B term), and mass transfer in the stationary liquid phase (the C term). Van Deemter described the band broadening in terms of the plate height (H = L/N), as a function of the average linear velocity of the mobile phase, u.

In its simplest terms, the Van Deemter equation is described by Equation 2.12:

$$H = A + B/u + C\,u \hspace{3cm} \textbf{Equation 2.12}$$

Since plate height is inversely proportional to plate number, a small value for H depicts a narrow peak – the desirable condition. Therefore, each of the three contributions, A, *B / u* and *C u* should be minimized to maximise column efficiency.

Eddy Diffusion

As originally proposed by Van Deemter, the A term deals with Eddy diffusion in packed columns.[138] This model describes the number of different routes that a particle can take when passing through a column. Some routes will be shorter than others (Figure 2.6). As the flow rate of the mobile phase is constant, the particles elute from the column at different times with the particles that travel the shorter routes through the column eluting before those that pass through a longer route. The molecules are separated from each other, thus, the analyte band becomes broader and more disperse.
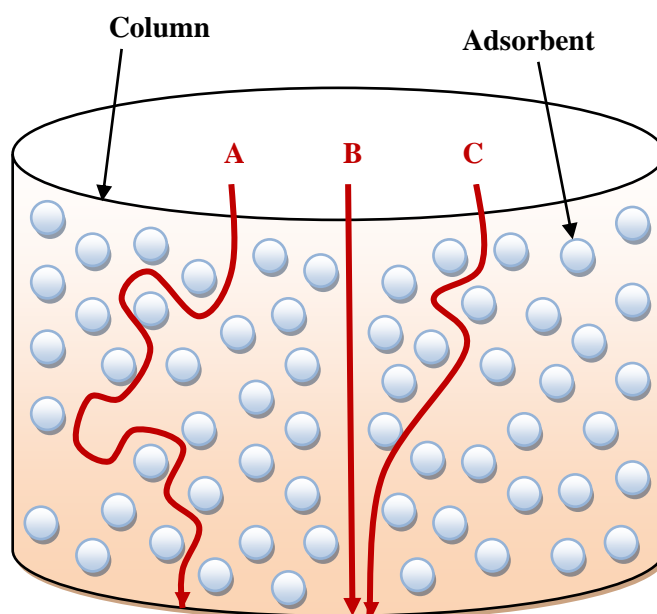
Figure 2.6: Schematic of the different pathways molecules can take in a packed column.

The diffusion paths of three molecules (A, B and C) are drawn schematically in Figure 2.6. Molecule B travels the shortest path through the column and will be eluted first, molecule C follows with molecule A passing through the longest path and consequently eluting last.

The A term in the Van Deemter equation is defined by Equation 2.13:

$$A = 2\lambda d_p$$ **Equation 2.13**

where d_p = the diameter of the particles packed in the column and λ = the packing factor. The A term can be decreased by using smaller more uniform particles that are packed into the column efficiently. Since A is a factor in packed columns it is effectively eliminated in GC where capillary columns are most commonly used; in this case the A term = 0.

Molecular diffusion

The B term deals with the forward and backward diffusion of the analyte in the mobile phase as the band moves down the column as shown in Figure 2.7.
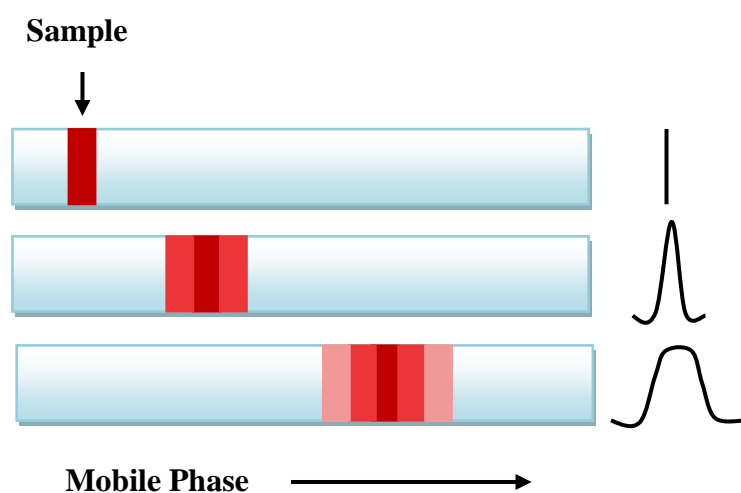
Figure 2.7: Molecular diffusion of analyte in column.

The second diffusion process is a function of both the analyte and the mobile phase flow rate, where broadening depends on the diffusion coefficient of the analyte in the mobile phase. Thus, the contribution of the second term to the Van Deemter equation can be altered by varying the type, pressure and flow rate of the carrier gas. The B term can be minimised by increasing the average linear velocity of the carrier gas, allowing the solute band to pass through the system quickly before it gets time to diffuse and broaden. It can also be minimised by decreasing the diffusion coefficient of the analyte in the mobile phase.[139]

Mass transfer

The C term in the Van Deemter equation concerns the finite time taken for the solute equilibrium to be established between the stationary and mobile phases. The solute molecules transfer into the stationary phase from the mobile phase at the leading edge of the zone, and from the stationary phase to the mobile phase at the trailing edge of the zone. Molecules in

the mobile phase tend to move faster than those in the stationary phase. The quicker the transfer can take place, the less the zone will broaden. This diffusion processes is therefore influenced by the partition coefficient. The third term can be minimised by increasing temperature, decreasing the stationary phase film thickness, increasing solubility of solute molecules in the stationary phase and reducing the flow rate of the mobile phase.[137]

All three terms can be combined in form of Van-Deemter plot to produce a non-symmetric hyberbola, see Figure 2.8.
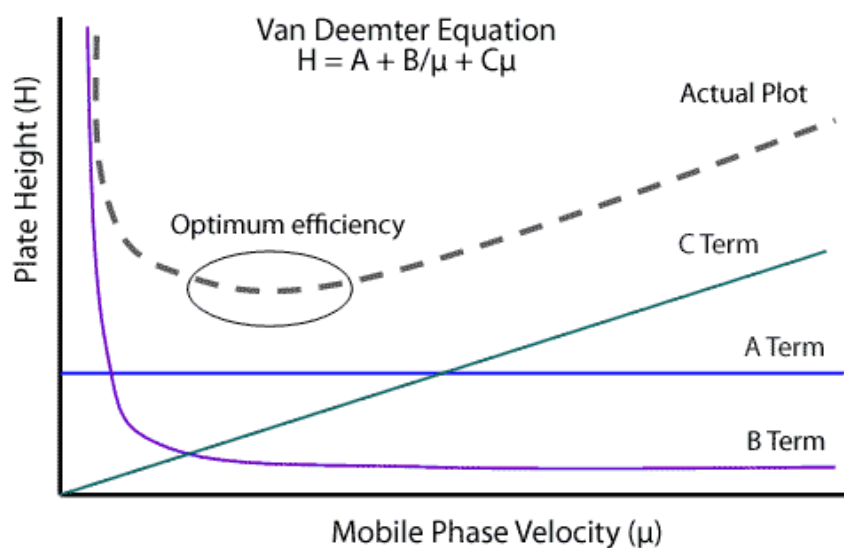
Figure 2.8: A typical Van Deemter plot.[140]

The A-term is independent of the mobile phase velocity and so is a constant over the range of flow rates. If the A-term is high the full hyperbola is shifted upwards (lowering efficiencies) and if the A-term is low the hyperbola is shifted downwards (increasing efficiencies). Since the A-term is zero in GC using a capillary column the efficiency is increased in comparison to the use of a packed column. The B-term is only important at low mobile phase velocities (this can be seen at the LHS of the graph). This term will decrease at higher flow rates. The C-term is directly proportional to flow rate, increasing as flow rate increases. This term is important at all flow rates. Attention is thus usually directed at this term, which is considered to be the most important contribution to band broadening in chromatography.[137]

2.3 Mass Spectrometry[123-125, 129, 141]

2.3.1 Principles of the mass spectrometer

A mass spectrometer (MS) is an analytical instrument that separates and detects molecular ions on the basis of their mass to charge ratio (m/z). All MS instruments consist of three main components: an ion source that generates the ions, a mass analyser which separates ions according to their m/z ratio, and an ion detector. The system is maintained under high vacuum (10^{-6} Torr) to prevent ions being deflected off their intended path due to collisions with gaseous molecules in the air.
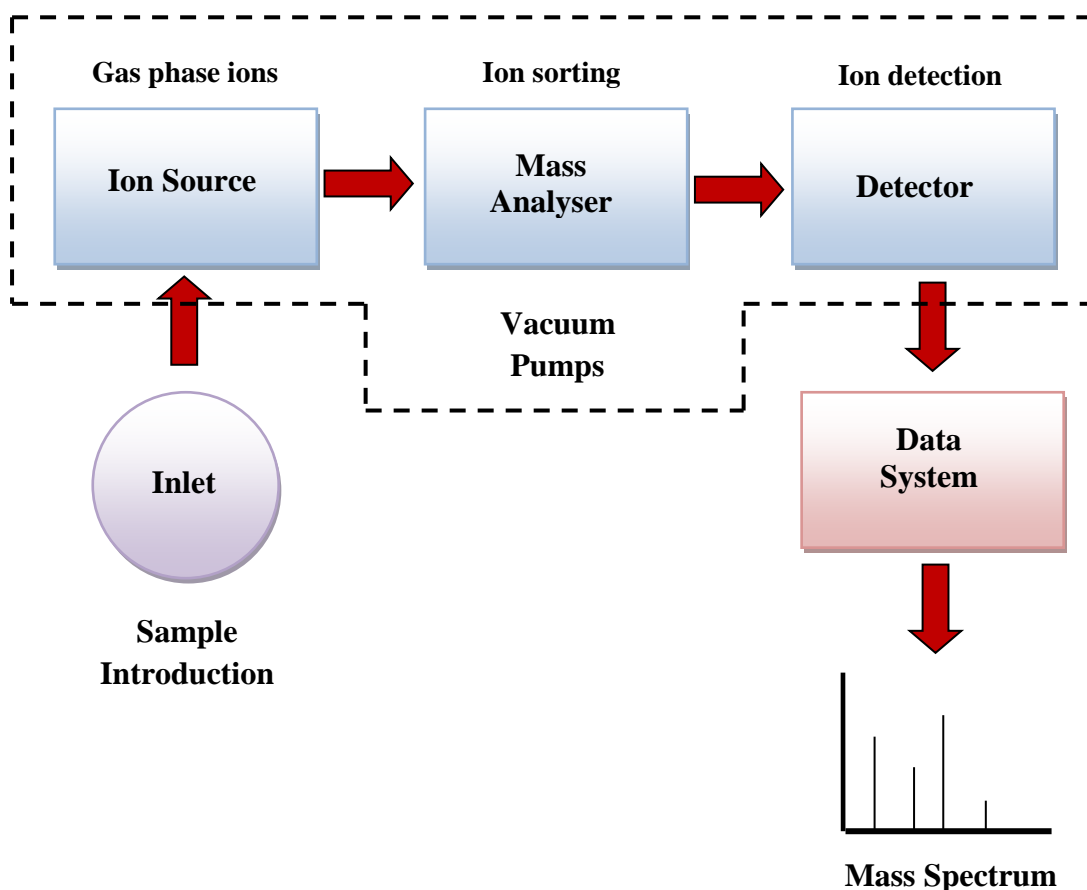
Figure 2.9: Basis of a mass spectrometer.

2.3.2 Ionisation techniques

Electron ionisation[142] (EI)

In GC, the most widely used ionisation technique is electron ionisation. This method involves molecules being introduced to the ion source where they are bombarded by high-energy electrons (70 eV), creating high energy, singly charged molecular ions. This is followed by the loss of excess energy via fragmentation, producing a collection of fragment ions characteristic of the compound. EI is employed for generating spectra with controlled and reproducible fragmentation patterns. Virtually identical spectra can be obtained employing different types of EI mass spectrometer as long as the electron energy is the same, which has led to the compilation of extensive libraries of 70 eV EI spectra e.g. the National Institute of Standard and Technology (NIST) library. EI is, therefore, preferred for identification of unknowns, determination of molecular structure and confirmation of target component identity through consistent ion abundance ratios.

Chemical ionisation[142] (CI)

A drawback of EI fragmentation is that in some cases the ionisation process is too extensive, leaving little or no trace of a molecular ion, which makes the determination of the molecular weight and consequently the identification of particular compounds somewhat difficult. This problem can be overcome by applying a low energy or 'soft' approach such as positive chemical ionisation (PCI). In PCI, the ion source is charged with a reagent gas (e.g. methane and ammonia), at a relatively high pressure (0.1 – 100 Pa), which undergoes EI ionisation, producing an excess of reagent ions. Sample molecules are subsequently ionised by the reagent gas ions predominately via proton transfer, producing pseudo molecular ions, $[M+H]^+$, and, depending on the choice of a reagent gas, adduct ions may be formed. The pseudo molecular ions generated have less residual energy, as a result of PCI being a low energy process and are consequently less prone to fragmentation than the molecular ions generated under EI conditions. The combination of less fragment ions and detection of a higher abundance of pseudo molecular ions yields much simpler mass spectra, providing unambiguous molecular–weight information. Furthermore, PCI can offer both increased sensitivity and improved detectability as a result of reduced chemical ionisation from background or coeluting analytes, leading to an increased signal to noise (S/N) ratio.

The production of a large population of low-energy electrons during CI operation provides an opportunity for another ionisation technique: *negative chemical ionisation* (NCI), alternatively called *electron capture negative ionisation* (ECNI). The basic mechanism of this technique involves the capture of a low-energy electron by an electronegative sample molecule, forming the molecular anion, which may undergo fragmentation, depending on its structure. ENCI has two important advantages over EI and CI:

1. It allows a 100-fold or greater improvement in sensitivity and
2. It is highly selective, since only a limited number of analytes are prone to efficient electron capture (*e.g.* analytes containing a halogen atom, a nitro group, or an extended aromatic ring system).

2.3.3 Mass analysers

Although there are many different types of MS analysers, the basic principles are the same in all cases: ions produced from the ion source are transferred to the mass analyser where they are separated according to their mass-to-charge ratio (m/z) and accelerated towards a detector where the abundance of each is recorded. There are many types of detectors but most work on the principle of producing an electronic signal when struck by an ion. Timing mechanisms which integrate those signals with the scanning voltages allow the instrument to report which m/z strikes the detector. The data system compiles a spectrum showing the mass distribution of the ions produced from the sample – a snapshot of ion intensities plotted against their m/z. The most common mass analyser used for routine practise and throughout the course of this investigation is the quadrupole mass analyser.

Quadrupole instruments consist of four parallel metal rods of circular cross-section which are electrically conducting and connected in opposite pairs as shown in Figure 2.10. Quadrupoles achieve ion separation under the combined influence of direct current (DC) and radio frequency (RF) voltages which are applied to the rods. A positive DC voltage is applied across one pair of rods and a negative voltage across the other. In addition, an oscillating RF voltage is applied. These applied voltages affect the trajectory of the ions moving down the cavity between the four rods, resulting in a motion that is perpendicular to their direction of travel. This causes the ions to follow an irregular, oscillating path through the cavity and is

the basis for mass separation within the quadrupole. The majority of ions (non-resonant) have unstable trajectories and a magnitude of off-axis motion, which becomes so great that the ions either hit the rods and are neutralised (and are pumped away by the vacuum) or escape from the cavity and cannot be detected. Only the ions with the correct mass to charge ratio, as determined by the applied electromagnetic fields to correspond with the fragment of interest, are said to be in resonance with the cavity and follow a stable trajectory through the quadrupole for further analysis or detection. By varying these voltages (scanning), at a fixed frequency, a mass spectrum is produced from low energy ions. A quadrupole can be operated in two modes: (i) full scan of a selected mass range, usually m/z 50-500 and (ii) selected ion monitoring (SIM). In SIM mode, sensitivity is enhanced by monitoring only a few selected m/z ions, thus proportionally increasing the acquisition time of the ions of interest; however, this is at the sacrifice of spectral information.
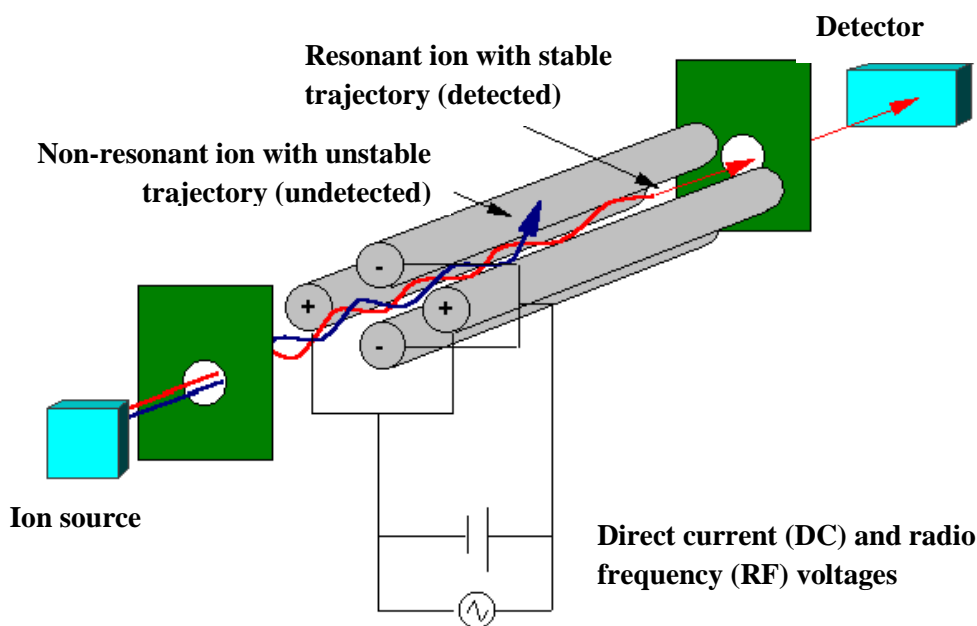
Figure 2.10: Schematic of a quadrupole mass analyser.[143]

2.3.4 Detectors

After passing through the mass analyser the ions are then detected and transformed into a usable signal by a detector. From the incident ions detectors are able to generate an electric current that is proportional to their abundance. Several types of ion detectors are commonly

used in mass spectrometry; however, they can generally be divided into two categories. The first of which are detectors based on the measurement of the direct charge current that is produced when an ion hits a surface and is neutralised such as Faraday cup detectors. The second category of detectors are based on the kinetic energy transfer of incident ions by collision with a surface that in turn generates secondary electrons, which are further amplified to give an electric current, thereby multiplying the signal by a cascade effect. Examples of such detectors are electron multipliers, photomultipliers or array detectors.

The photomultiplier detector consists of two conversion dynodes, a photomultiplier and a phosphorescent detector.[142] In this detector, ions from the analyser are accelerated to a high velocity in order to enhance detection efficiency. This is achieved by holding an electrode called a conversion dynode at a high potential from ± 3 to ± 30 kV, opposite to the charge on the ions being detected. This device enables the detection of both positive and negative ions by striking the high voltage negative and positive conversion dynodes, respectively. Secondary electrons are generated from this process and are subsequently accelerated towards the phosphorescent screen, which is coated in a thin layer of aluminium conductor to avoid accumulation of a charge. At the phosphorescent screen the electrons are converted to photons. These photons are amplified by a cascade effect in the photomultiplier to produce a current which is then detected. The main advantage of using photomultipliers, as opposed to electron multipliers, is that it can be kept sealed in a vacuum thereby preventing contamination and greatly extending the lifetime of the detector. As a consequence, photomultipliers are the most common detectors in modern mass spectrometers.

2.4 Ultra violet (UV) absorption spectroscopy[144-147]

2.4.1 UV absorption

UV absorption spectroscopy is used to measure the transitions of electrons between the electronic energy levels of organic molecules. UV absorptions take place between 100 – 400 nm, with absorptions in the visible light region between 400 – 700 nm. In most organic compounds the bonding and non-bonding orbitals are filled and the anti-bonding orbitals are

vacant. The transitions generally occur between the occupied molecular orbitals of a bonding or lone pair of electrons and an unfilled anti-bonding molecular orbital. The wavelength at which the absorption takes place is relative to the separation of the energy levels involved. The energy associated with each wavelength in the UV-visible region can be determined using Planck's theory (Equation 2.14):

$$E = h\nu$$

$$\nu = c/\lambda$$

Therefore:

$$E = hc / \lambda \hspace{3cm} \textbf{Equation 2.14}$$

where E = energy, h = Planck's constant (6.63×10^{-34} Js), ν = frequency, c = speed of light (3×10^8 m s^{-1}) and λ = wavelength.

UV absorption depends on the total quantity of absorbing compound and is governed by the Beer-Lambert Law (Equation 2.15):

$$\text{Absorbance} = \log (I_o/I) = \varepsilon\, b\, c \hspace{2cm} \textbf{Equation 2.15}$$

where I_o is the monochromatic incident light beam, I is the transmitted beam, ε is the molar absorption coefficient (L mol^{-1} cm^{-1}), b is the path length (cm) of the cell and c is the solute concentration (mol L^{-1}).

The Beer-Lambert law states that when monochromatic radiation passes through a homogeneous solution, the absorbance is directly proportional to the concentration of the absorbing species and the path length. Thus, for a constant path length, UV spectroscopy can be used to establish the concentration of the absorbing compound. An important assumption made when using the Beer-Lambert law is the independent behaviour of absorbing particles with regard to light such that they do not have an effect on each other. If absorbance is plotted against concentration, a straight line passing through the origin is obtained. However, the relationship between absorption and concentration becomes non-linear at high concentrations due to the diminishing distance between particles which allows the particles to influence each other's charge distribution, thereby, affecting the ability of a species to absorb

UV radiation. Practically, if high absorption values are measured, dilution is necessary to attain accurate results.

In order for a molecule to absorb light in the UV region, and be detected by UV detection methods, it must contain a chromophore. A chromophore is a structural feature or moiety of the molecule that can absorb a photon resulting in the promotion of an electron from the ground state into an excited state.[148] The electronic transitions are classified according to the orbitals involved, as shown in Figure 2.11.
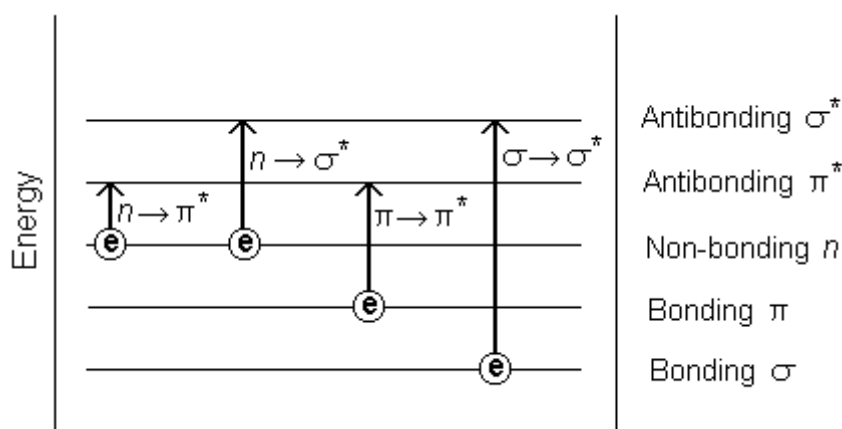
Figure 2.11: The possible electronic transitions involved in the absorption of a photon.[149]

As depicted in Figure 2.11, it can be seen that the lowest energy and, therefore, the highest wavelength transitions are from the non-bonding orbitals to anti-bonding orbitals, i.e. $n \rightarrow \pi^*$ transitions. Theses give rise to bands in the near UV and visible regions. Other allowed transitions in order of increasing energy (shorter wavelength) are $n \rightarrow \sigma^*$ and $\pi \rightarrow \pi^*$, which have comparable energies, and $\sigma \rightarrow \sigma^*$. The latter occur in the far uv or vacuum region below 200 nm and are of little use analytically. Intense bands (large ε) are produced by $\sigma \rightarrow \sigma^*$ and $\pi \rightarrow \pi^*$ transitions, whereas those arising from $n \rightarrow \sigma^*$ and $n \rightarrow \pi^*$ transitions are characteristically weak because of unfavourable selection rules.[135]

UV absorption is governed by selection rules which determine whether a particular transition between electronic energy levels is allowed or forbidden. There are two types of rules, spin selection rules and orbital symmetry selection rules.

Spin Selection Rule

The rules states that, for an allowed transition, electron spin must be conserved.

Most organic molecules in the ground state (unexcited) are in a single energy state. This can be seen on the left-hand side of Figures 2.12 and 2.13, where all the electrons in the molecule are paired and hence the total electron spin (represented by the spin quantum number, s) is zero. For an electronic transition to be spin allowed, the spin of the electron must be conserved (the value of s is unchanged). This can be observed in Figure 2.12 where the promoted electron remains anti-parallel.
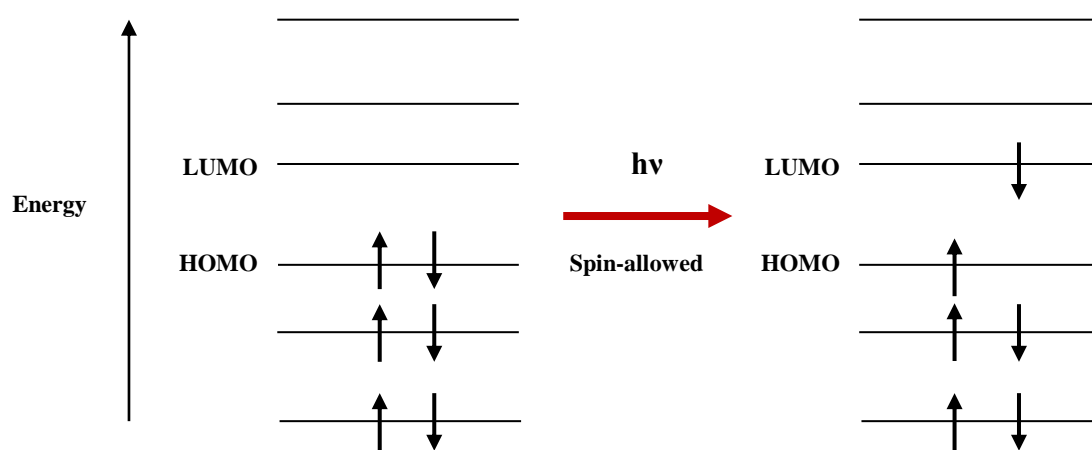
Figure 2.12: A spin-allowed transition

HOMO = Highest Occupied Molecular Orbital

LUMO = Lowest Unoccupied Molecular Orbital

If the spin of the excited electron were to be inverted upon transition, a triplet energy state would result (s=1) where the molecule would contain two unpaired electrons with parallel spins, as shown in Figure 2.13. This is on account of Hund's rule of maximum multiplicity, which states that electrons will fill orbitals individually with parallel spins before spin pairing occurs. The triplet state is, therefore, lower in energy than the singlet state. A spin-forbidden transition could result in a lower energy transition however, spin selection rules are strictly adhered to and promotion to a triplet electronic excited state is seen very rarely with UV-visible absorption.
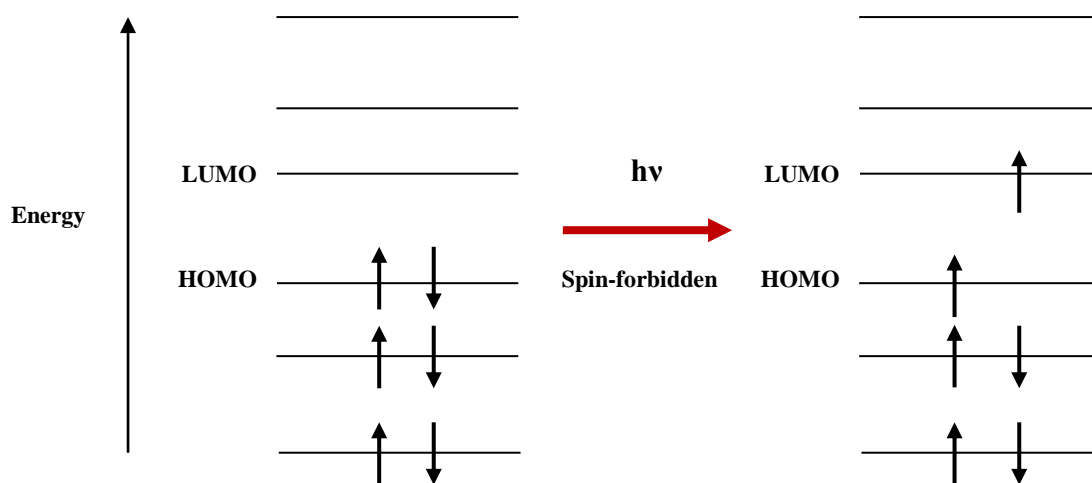
Figure 2.13: A spin-forbidden transition

Orbital Symmetry Selection Rule

These rules help to determine the probability of a transition occurring based on the symmetry/ overlap and multiplicity of the ground state and excited state molecular orbitals involved e.g. HOMO and LUMO. No simple rules can predict a symmetry–allowed or symmetry-forbidden transition however there are some general trends:

- n$\rightarrow \pi^*$ transitions of carbonyl compounds are symmetry-forbidden.
- $\pi \rightarrow \pi^*$ transitions of benzene derivatives are symmetry-forbidden.
- $\pi \rightarrow \pi^*$ transitions of isolated double bonds, dienes, trienes and polyenes are symmetry allowed.

The positions and intensities of the absorption bands are sensitive to substituents close to the chromophore, to conjugation with other chromophores and to solvent effects. Saturated groups containing heteroatoms, which modify the absorption by conjugating to a chromophore, are called auxochromes and include –OH, -Cl, -OR and –NR$_2$. Absorption bands due to conjugated chromophores experience a shift in absorption maximum to a longer wavelength and intensified relative to an isolated chromophore.[135] This is known as a red shift/ bathochromic effect. The electronic absorption of a chromophore is also affected by the solvent in which it is dissolved. The energy levels of all electronic states are lowered by attractive polarisation forces between the solvent and absorbing molecule. This causes a red shift in the absorption maximum. Alternatively, increasing solvent polarity increases salvation of lone pairs and causes the absorption maximum to shift to a shorter wavelength. This is a blue shift/ hypsochromic effect. When using UV absorption as a detection technique

in chromatography, the absorption of the target analyte could therefore be improved by altering the mobile phase composition.

2.4.2 UV detectors

There many different types of HPLC detectors available including mass spectrometry, electrochemical, UV fluorescence and/or absorbance, refractive index, conductivity and infrared spectroscopy. Throughout this project, UV absorbance was the principle method of detection when used in conjunction with HPLC. The most current UV absorbance detectors are either variable-wavelength systems, using a continuum source in conjunction with a scanning monochromator, which gives single wavelength detection or photodiode-array detectors (PDA), in which reversed optics are used and the spectrum is spread across an array of photodiodes.[150]

The operation of a variable-wavelength UV detector involves a high energy source lamp (typically deuterium) being focussed through a slit and onto a diffraction grating where the radiation is distributed out into its component wavelengths. A single wavelength of light is then focussed through another slit, detector cell and ultimately onto a photodetector. This is achieved by rotating the grating to select the desired wavelength. The use of a variable-wavelength detector allows programmed wavelength changes to occur during a separation.[150]

The PDA detector consists of a linear array of discrete photodiodes on an integrated circuit chip. The full spectrum that emerges from the sample cell is dispersed by a holographic dispersion grating into single wavelengths, which are focussed simultaneously onto the photodiodes. PDA detectors therefore allow a wide range of wavelengths to be detected concurrently (as opposed to single wavelength monitoring with the variable-wavelength detector) and are used for recording the full UV-visible absorption spectra of a sample. The PDA can contribute to peak identification and are hence the preferred detector of choice for analyte method development.[151] The diode array detector allows simultaneous detection over the entire UV-vis range to be achieved as well as providing information on the wavelength of maximum absorbance (λ_{max}) which, once known, can allow the rapid quantification of an analyte in a sample using a fixed wavelength detector.

3. Silica material preparation and sorbent characterisation

3.1 Materials and reagents

Cetyltrimethylammonium bromide (CTAB) was supplied by BDH Chemicals. Aqueous ammonia (NH_3 30%), tetraethoxysilane (TEOS, 98%), hydrogen peroxide solution (H_2O_2, 30 wt. %), hydrochloric acid (HCl, 37 %), absolute ethanol, methanol (99 %) and iron (III) nitrate were purchased from Sigma Aldrich. Nitric acid (HNO_3, 65 wt. %) and sodium metasilicate pentahydrate, ($Na_2SiO_3.5H_2O$) were provided by Fisher Scientific. Pluronic P123, $PEO_{20}PPO_{70}PEO_{20}$, block copolymer was supplied by the BASF Corporation. Pentaethylenehexamine (PEHA, $C_{10}H_{28}N_6$) was purchased from ACROS Organics.

All products were used as supplied and distilled water was used throughout this work.

3.2 Sorbents and silica material synthesis methods

Commercially available Norit CA1 powdered activated carbon (PAC) was supplied by Sigma Aldrich.

3.2.1 MCM-41

MCM-41 was synthesised according to the method previously reported by Idris *et al.*[152] TEOS was used as the silica source and CTAB acted as the structure directing agent for pore formation. 8.8 g of CTAB was dissolved under slight heating (35 °C) in a mixture of 208 cm^3 of distilled water and 96 cm^3 of aqueous NH_3. To this clear solution, 40 cm^3 of TEOS was added drop wise under stirring. After further stirring for 3 h, the gel was aged at room temperature for 24 h in a closed container. The product was obtained by filtration, washed with distilled water and dried in air at room temperature. This as-synthesised material will be referred to as 'As-syn MCM-41'.

For comparison purposes, the organic template was then removed from three batches of the prepared MCM-41 using one of the following methods: microwave digestion, calcination, or solvent extraction. The organic template was removed from the first batch of MCM-41 using a microwave digestion method.[152] As-syn MCM-41 samples, approximately 0.3 g, were placed in multiple Teflon vessels to which 5 cm^3 of HNO_3 and 2 cm^3 of H_2O_2 were added. A MARS 5 microwave digestion system (CEM Corporation, Buckingham, UK) was used at an

operating power of approximately 1600 W. The pressure and temperature inside the microwave were controlled to be lower than 1.3 MPa and 200 °C, respectively at a working frequency of 2450 MHz and 220 V for 15 min. The product was filtered, washed with copious amounts of distilled water and dried in an oven at 100 °C for 2 h. This material will be referred to as 'MWD MCM-41'. A second batch of MCM-41 was produced where template removal was performed using a conventional calcination rig by heating in air at 500 °C for 8 h. This material will be referred to as 'Calc MCM-41'. A third batch of MCM-41 was produced using a solvent extraction method of template removal. Approximately 1 g of as-synthesised MCM-41 was added to 200 cm^3 1M HCl in ethanol and the solution was stirred for 1 h at 70 °C. The product was filtered and the solvent extraction repeated a further 4 times to maximise efficiency of the removal process. The final product was filtered, washed with distilled water and dried in an oven at 100 °C for 2 h. This material will be referred to as 'Sol Ext MCM-41'.

3.2.2 SBA-15

SBA-15 was prepared previously according to the method described by Ewlad-Ahmed.[153] This method was based on the preparation technique reported by Zhao *et. Al*, [22] using non-ionic surfactants as structure-directing agents. In summary, 4 g of a surfactant tri-block copolymer, Pluronic P123, was dissolved in 60 cm^3 of distilled water and 120 cm^3 of 2 M HCl solution. This was carried out in a glass bottle, under stirring and at room temperature. This surfactant solution was then heated to 40 °C prior to the addition of 11.3 g of TEOS and the mixture was left under stirring for 24 h at 40 °C before being placed in an oven at 60 °C for 5 days. The solid produced was filtered, washed with distilled water and dried overnight at 60 °C before it was calcined at 550 °C for 24 h. The resulting solid had a ratio of SiO_2: 0.0032 P123: 4.4 HCl: 144 H_2O.

3.2.3. Bioinspired silica preparation

The synthesis of the bioinspired silica materials was achieved using the method described below. The preparation was repeated four times to determine the repeatability of the synthesis method by comparing properties such as pore size, surface area and isotherm data. This was necessary as the mass of bioinspired silica material prepared during synthesis is small (0.6 g

and 0.5 g for the as-synthesised and calcined, respectively); one batch would not be sufficient to produce enough material for all subsequent adsorption experiments. Therefore, multiple batches are required and the properties of the material produced should be consistent and precise.

Sodium metasilicate pentahydrate was used as the silica source at a concentration of 30 mM. PEHA was used as the bioinspired additive at a Si: N molar ratio of 1:1. The procedure for synthesising this material involved the preparation of two solutions (A and B), the combination of these solutions and the immediate pH adjustment of the final solution (C) using a pre-determined amount of acid. To produce solution A, 6.36 g of sodium metasilicate pentahydrate was added to a 1000 cm^3 polyethylene bottle and dissolved completely, with thorough shaking, in 500 cm^3 distilled water. 1.65 g of PEHA was dissolved in 400 cm^3 of distilled water in a 500 cm^3 polyethylene bottle to provide solution B. Solution B was subsequently added to solution A and to provide the resulting solution C. A stirrer bar was added and solution C was then placed on a Gallenkamp magnetic stirrer plate and stirred at moderate speed. A pH meter was inserted to monitor the solution pH. After the pH had stabilised, the initial starting pH of solution C was recorded (time = 0).

The pH of solution C was adjusted using 1M HCl. One of the more challenging aspects of the synthesis of bioinspired silica was the determination of the volume of HCl required for the preparation. Both reactants used (sodium metasilicate pentahydrate and PEHA) are strong bases; meaning that the addition of HCl was essential to neutralise the solution mixture and, in turn, form the precipitated silica. Many factors can affect the formation of silica (see Section 1.4), so in order to maximise repeatability of the synthesis method, the acid required for neutralisation was added in quick succession and all at once. Preliminary experiments, conducted using a trial and error method, were used to determine the amount of acid required for neutralisation, i.e. an end point of pH 7 ± 0.1, within a reaction time of 5 min. The pre-determined volume of 1M HCl required was found to be 71.1 cm^3. Accordingly, before the addition of any acid, an extra 28.3 cm^3 of distilled water was added to bring the final reaction solution volume to 1 L. The pre-determined, 71.1 cm^3 1M HCl was then added steadily within 10 s. Simultaneously following the addition of all the acid to the solution mixture, a timer was started and the pH recorded at 20 s intervals to produce a pH profile. After the last pH reading was recorded at 5 min at a value of pH 7 ± 0.1, the reaction was stopped by immediately filtering the resulting product. The reaction vessel was washed with 500 cm^3 distilled water and added to the filtrate, which was then subsequently washed with a further 1L distilled water. The resulting waste solution produced from this procedure could be

disposed of down the sink as the reagents used were environmentally friendly and the end solution a neutral pH. The product was then dried in an oven at 85 °C for 24 h. The material produced was referred to as 'as-synthesised bioinspired silica' (As-syn Bio-Si). A portion of the as-synthesised material was then calcined at 500 °C for 5 h using a conventional oven furnace, as described in Section 3.2.2, to remove the additive and was referred to as 'calcined bioinspired silica' (Calc Bio-Si). The above procedure was then repeated another three times, producing a total of four samples of both as-synthesised and calcined bioinspired silica material prepared under the same conditions. This allowed the repeatability of the synthesis method to be assessed through comparison of the material samples resultant physical properties. As previously discussed in Section 1.5.4, this synthesis method, using small amine molecule additives such as PEHA, is known to produce bioinspired silica material with a structure consisting of spherical silica particles.[90, 91, 96]

3.2.4. Iron incorporated bioinspired silica preparation

The iron incorporated bioinspired silica was prepared using the same synthesis method as the bioinspired material, see Section 3.2.3. Sodium metasilicate pentahydrate was further used as the silica source and PEHA as the amine additive, the weights of which remained constant as did the final solution volume (1L). The only difference to the procedure was the addition of iron nitrate, used as the iron source, to the reaction mixture. This involved the addition of 5.40 g of iron nitrate to the solution before the solution was acidified with HCl.

Preliminary experiments, conducted using a trial and error method, were used to determine the amount of acid required for neutralisation, i.e. an end point of pH 7 ± 0.1, within a reaction time of 5 min. The pre-determined volume of 1M HCl required was found to be 28.2 cm^3. Accordingly, an extra 71.8 mL of distilled water was added to bring the final reaction solution volume to 1 L. Again, the pH of the solution recorded at 20 s intervals. After 5 min and a final pH reading of 7 ± 0.1, the reaction mixture was immediately filtered, the precipitated iron-incorporated silica product was washed with distilled water and dried in an oven at 85 °C overnight. This material will be referred to as 'As-syn Fe Bio-Si'. Removal of the organic template was performed using a conventional calcination rig by heating in air at 550 °C for 8 h. This material will be referred to as 'Calc Fe Bio-Si'. As in the bioinspired silica synthesis, the procedure was repeated another three times and the physical properties of the samples were compared.

3.3 Measurement of Brunauer-Emmett-Teller (BET) isotherms

Characterisation of each sorbent's physical properties was conducted using a Micrometrics ASAP 2420 accelerated surface area and porosity analyser with nitrogen adsorption/ desorption isotherms collected at 77 K. Each sample, approximately 0.3 g in weight, was accurately weighed before being transferred to a gas adsorption sampling tube. The weight of the sampling tube was recorded before and after the addition of the sorbent. The sample tube was then attached to the degas port of the nitrogen sorption instrument and degassed prior to analysis for 6 h at 200 °C. The BET surface areas were calculated using experimental points at a relative pressure (P/P$_0$) of 0.05 – 0.25. The total pore volume was calculated from the nitrogen amount adsorbed at a P/P$_0$ of 0.99 for each sample and the average pore size distribution of the materials was calculated using the Barret-Joyner-Halenda[122] (BJH) model from a 28 point BET surface area plot. The desorption branch of the isotherms was used to calculate the pore diameters.

3.4 Characterisation of sorbent materials

MCM-41 material was prepared as described in Section 3.2.1 and the organic template was removed from the three batches of the as-synthesised MCM-41 using one of the following methods: microwave digestion (MWD MCM-41), calcination (Calc MCM-41) or solvent extraction (Sol Ext MCM-41). Four samples of both As-syn Bio-Si and Calc Bio-Si were synthesised using the procedure outlined in Section 3.2.3. Four samples of both As-syn Fe Bio-Si and Calc Fe Bio-Si were synthesised using the procedure outlined in Section 3.2.4. Each was analysed using a Micrometrics ASAP 2420 accelerated surface area and porosity analyser under the operating conditions outlined in Section 3.3. In addition, the pre-prepared SBA-15 and commercially purchased powdered activated carbon (PAC) were also analysed as received (no further sample preparation involved prior to characterisation).

3.4.1 Textural Properties and nitrogen sorption isotherms

Analysis of the porous materials using nitrogen sorption isotherms provided the characteristic data of surface area, average pore size and pore volume; all the data are summarised in Table 3.1 for MCM-41 and SBA-15 materials, Table 3.2 for Bio-Si and Fe Bio-Si materials and Table 3.3 for PAC.

3.4.1.1 Mesoporous silica materials: MCM-41 and SBA-15

The surface areas of As-syn MCM-41, Calc MCM-41 and SBA-15 were measured at 17, 1077 and 658 m^2 g^{-1}, respectively, which are in agreement with data commonly reported in literature (for example 1050 m^2 g^{-1} and 678 m^2 g^{-1} for Calc MCM-41[154] and SBA-15[155], respectively). The As-syn MCM-41 was shown to have the lowest surface area and a lack of porosity (no pore volume or pore size due to inclusion of the template), which increased significantly, as expected, after the removal of the template. Interestingly the results demonstrated that the total surface area of MCM-41 was reduced (from 1077 to 874 m^2 g^{-1}) when the template was removed by microwave digestion compared to calcination. Additionally, the average pore size diameter of the MWD MCM-41 was found to be higher, 3.4 nm, than that of the Calc MCM-41, 2.8 nm (see Figure 3.1(b) and Table 3.1). The larger surface area of Calc MCM-41 was shown to be as a result of the small, well-defined pores present in the material. The total surface area and pore volume of the Sol Ext MCM-41 was shown to be significantly less than that of both the Calc MCM-41 and MWD MCM-41. This implies that, either, the successive solvent extraction steps have damaged the mesostructure of MCM-41 or the procedure was unsuccessful in removing all of the template molecule. This is reflected in the pore wall thickness calculated for Sol Ext MCM-41 (0.9 nm) which could be a result of the remaining template in the material giving a thickness larger than expected (0.4 nm for Calc MCM-41) or the framework no longer being represented by a hexagonal unit cell (see Equation 3.1 and 3.2). The presence of the template could be examined using carbon, hydrogen, nitrogen (CHN) elemental analysis. SBA-15 exhibited a lower surface area, 658 m^2 g^{-1}, than the MCM-41 materials however it was found to have the largest pore size, 5.9 nm, and a pore volume comparable to that of Calc MCM-41.

Table 3.1: Physiochemical properties of the silica materials.

Sample Name	BET Surface Area ($m^2\,g^{-1}$)[a]	Average Pore Size (nm)[b]	Pore Volume ($cm^3\,g^{-1}$)[c]	Pore Wall Thickness (nm)[d]
As-syn MCM-41	17	-	-	-
MWD MCM-41	874	3.4	0.90	0.5
Calc MCM-41	1077	2.8	0.84	0.4
Sol Ext MCM-41	664	2.9	0.42	0.9
SBA-15	658	5.9	0.78	1.0

[a] **Calculated by the BJH model from sorption data in the relative pressure range 0.05 – 0.25.**

[b] **Calculated by the BJH model from the desorption branches of isotherms.**

[c] **Calculated from N_2 amount adsorbed at relative pressure P/P_0 of 0.99.**

[d] **Calculated from average pore size and pore volume.**

An example calculation of the pore wall thickness using the average pore size and pore volume measured for MWD MCM-41 is detailed below:

Assuming a hexagonal unit cell:

Volume of unit cell $= \sqrt{3}\,a^3/2$ **Equation 3.1**

where a represents the unit cell axes (assumed x = y = z)

Pore volume $= 0.9\ cm^3\ g^{-1}$

Density of silica $= 2.65\ g\ mL^{-1} = 0.38\ cm^3\ g^{-1}$

Total volume of silica = Pore volume + Silica volume $= 0.9 + 0.38 = 1.28\ cm^3\ g^{-1}$

and therefore, Relative pore volume $= 0.9/1.28 = 0.7$

Volume of pores in unit cell $= 0.7 \times (\sqrt{3}\,a^3/2)$

We know that the unit cell contains one pore in total.

Pore volume $= \pi r^2 a$ **Equation 3.2**

where r is the radius of the pore

Therefore,

$\pi r^2 a = 0.7 \times (\sqrt{3}\,a^3/2)$

$a^2 = 2\,\pi\,r^2 / (\sqrt{3} \times 0.7)$

$\quad = 2\,\pi\,(1.7)^2 / (\sqrt{3} \times 0.7)$

$a = 3.9\ nm$

Pore wall thickness $= 3.9 – 3.4 = 0.5\ nm$

Figure 3.1 (a) shows the nitrogen absorption-desorption isotherms for the MCM-41 materials; As-syn MCM-41, MWD MCM-41, Calc MCM-41, Sol Ext MCM-41, and SBA-15. The non-porous nature of the As-syn MCM-41 is further supported by the lack of nitrogen adsorption. All other materials exhibited a type IV isotherm, according to IUPAC classification, and had a H1 hysteresis loop; confirming the mesoporous nature of the materials. However, differences in the capillary condensation steps were observed with SBA-15 and MWD MCM-41 at higher relative pressures (0.59 - 0.78) and (0.45 - 0.72), respectively, compared to Calc MCM-41 (0.28 - 0.36). This confirms, the presence of larger pores in SBA-15 and as expected, that the microwave digested method induced larger pores in the MCM-41 material than calcination. The capillary condensation step for the Sol Ext MCM-41 was subtle, with the isotherm appearing relatively flat over the entire relative pressure range. This reinforces the possibility that template removal using the solvent extraction method was damaging to material mesostructure, perhaps as a result of recrystallisation taking place in the solvent and hence, the Sol Ext MCM-41 was not used in any further investigations in this thesis.

The hysteresis loop was broader for SBA-15 and MWD MCM-41 indicating that these materials contained pores of different shape and size compared to Calc MCM-41 or Sol Ext MCM-41. This phenomenon is normally observed for SBA-15 type material as it has both micro- and meso- pores on the surface but this characteristic is not commonly observed with MCM-41 materials. Since the sharpness of the capillary condensation step reflects the uniformity of the pores in the materials, the gradual incline of the step observed for the MWD MCM-41 suggests the possibility that the microwave digestion process was damaging to the usually highly uniform pores and ordered lattice of MCM-41. It was thought that the larger average pore size and pore size distribution found for MWD MCM-41 was due to pore wall teardown which occurred during intense temperature and pressures created during the microwave digestion procedure. However, the calculated pore wall thickness for MWD MCM-41 is larger than that of the calcined material (0.5 and 0.4 nm, respectively), therefore implying that thinning of the pore walls has not occurred during the harsh procedure. It is possible, however, that the process was damaging to the ordered lattice of the material which would mean it could no longer be assumed to be hexagonal (see Equation 3.1). Calc MCM-41 had an isotherm that did not contain a hysteresis loop, with only minor deviation of the adsorption and desorption branches and exhibited a steep capillary condensation step which is indicative of a narrow range of well-defined pores.
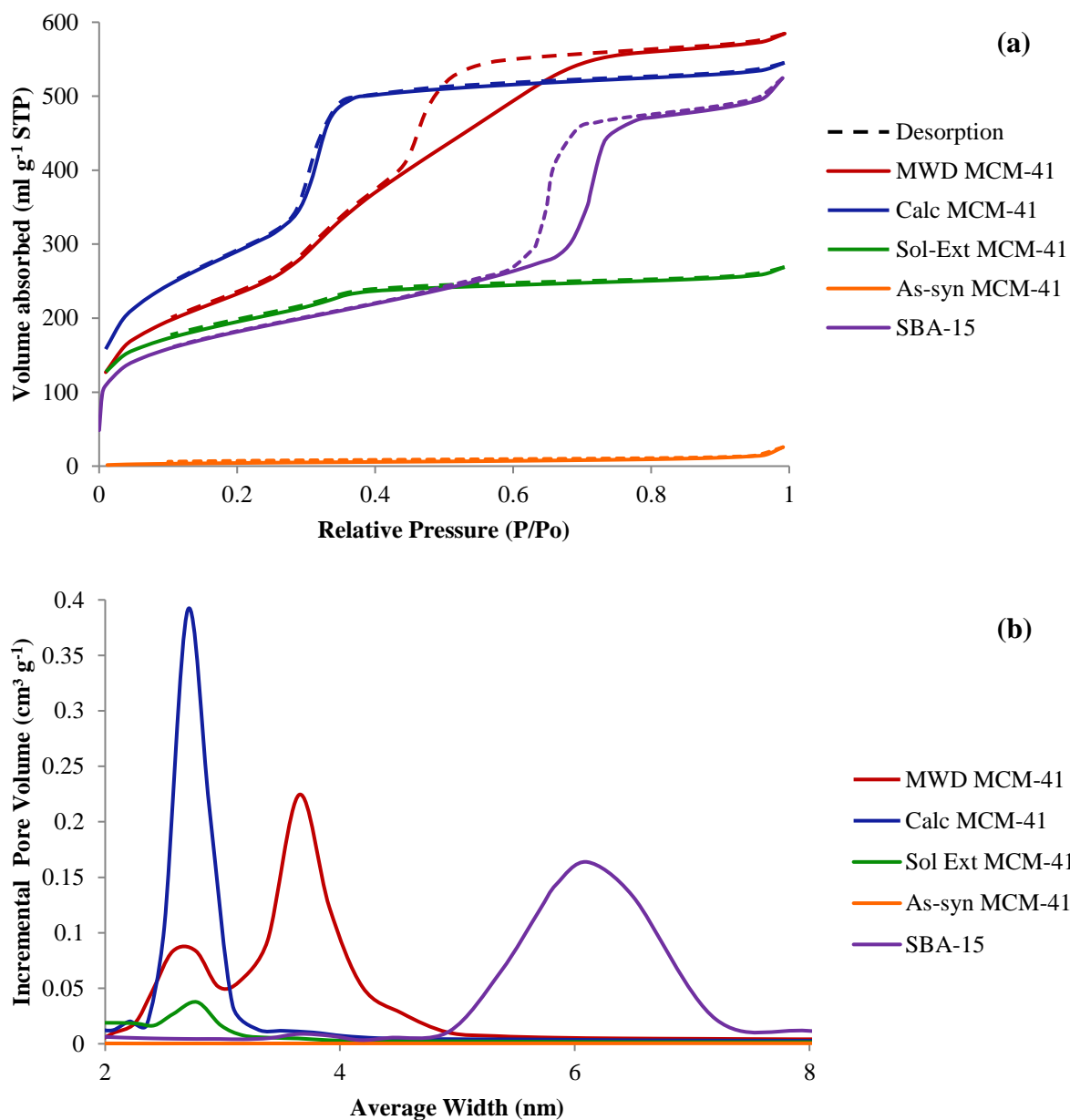
Figure 3.1: Nitrogen sorption isotherms (a) and relative pore size distributions (b) for silica materials.

The pore size distributions (PSDs) of the silica materials are shown in Figure 3.1 (b). These results provide further evidence for the material observations previously mentioned. The SBA-15 and MWD MCM-41 materials showed a larger pore size and broader pore size distribution than that of the Calc MCM-41 or Sol Ext MCM-41.

3.4.1.2 Bioinspired Silica materials: Bio-Si and Fe Bio-Si

pH profile

A pH profile was measured for each Bio-Si and Fe Bio-Si sample synthesised following the addition of the pre-determined amount of acid. As an example, the pH profiles of each Bio-Si synthesis are shown in Figure 3.2. The pH profiles collected during the trial and error process revealed that even a small deviation of 0.1 cm^3 from this predetermined volume had a large impact on the end pH at 5 min. In addition, the mass of Bio-Si and Fe Bio-Si material prepared during synthesis is insufficient for all subsequent adsorption experiments (~0.6 g) and multiple batches are required. Figure 3.2 indicates good repeatability and high precision between the samples synthesised. This is reflected in the adsorption isotherms and relative pore size distributions (Figure 3.3 and 3.4) produced for each sample and, thus, their resultant properties. The similarity between samples is important so they can be combined and, thus, provide enough material for all applications that follow. Although not shown, the pH profiles and resultant material properties obtained for the Fe Bio-Si material indicated high precision between samples. Thus, only the nitrogen sorption isotherm and corresponding pore size distribution of one sample is shown, see Figure 3.5 (a) and (b) respectively.

A reaction time of 5 min was found to be a sufficient amount of time for silica formation to successfully occur. However, it is important to note that the reaction does not stop at 5 min and, if left to proceed, the pH would continue to decrease albeit at a slower pace. Hence, each sample was immediately filtered.
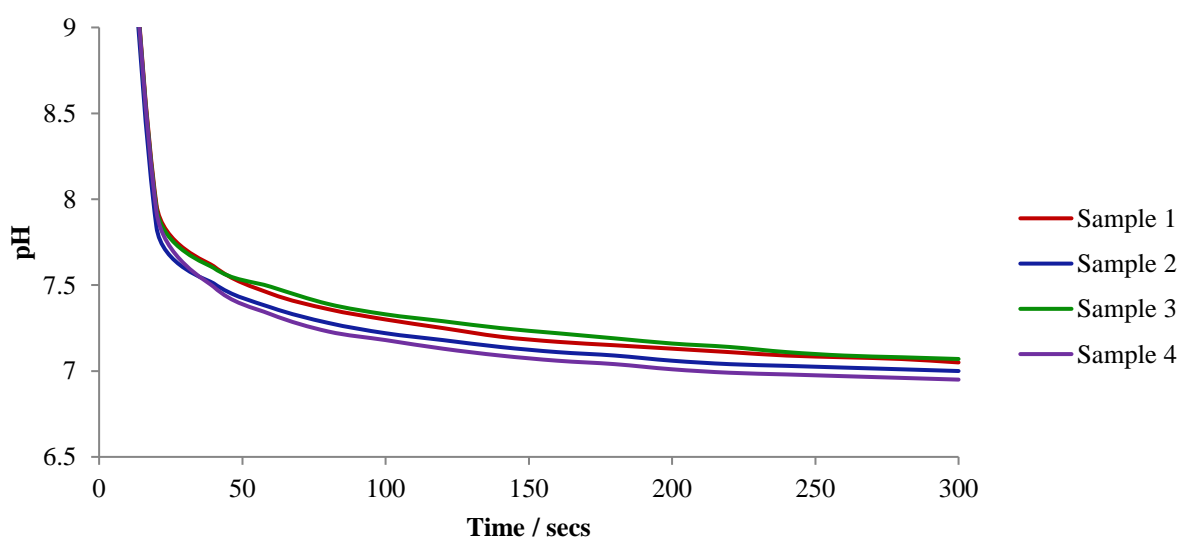
Figure 3.2: pH profiles of Bio-Si samples.

Nitrogen sorption isotherms

Nitrogen sorption isotherms were used to provide information on the physical properties, including surface area and pore diameter, of the Bio-Si and Fe Bio-Si samples. The collected data is summarised in Table 3.2 showing the average values for the four samples analysed of each material.

Table 3.2: Physiochemical properties of the Bio-Si and Fe Bio-Si materials (average of four samples).

Sample Name	BET Surface Area (m^2 g^{-1})[a]	Average Pore Size (nm)[b]	Pore Volume (cm^3 g^{-1})[c]	Micropore Area (m^2 g^{-1})[d]	Micropore Volume (cm^3 g^{-1})[d]
As-syn Bio-Si	19	N/A	0.04	4	-
Calc Bio-Si	338	N/A	0.07	294	0.13
As-syn Fe Bio-Si	266	8.8	0.54	8.8	-
Calc Fe Bio-Si	217	8.9	0.45	7.2	-

[a] Calculated by the BJH model from sorption data in the relative pressure range 0.05 – 0.25.

[b] Calculated by the BJH model from the desorption branches of isotherms.

[c] Calculated from N$_2$ amount adsorbed at relative pressure P/P$_0$ of 0.99.

[d] Determined by t-plot analysis using the Harkins and Jura equation.

N/A: no clear size seen, only broad line, see Figure 3.4 (b) and 3.5 (b).

The isotherms for all As-syn Bio-Si samples exhibited a type II isotherm, commonly encountered for non-porous materials. This, in addition to the low surface area and pore volume, is expected with the inclusion of the PEHA additive in the material. The isotherms for all Calc Bio-Si samples (illustrated in Figure 3.4(a)) were thought to reflect combined features of type I and type II isotherms. Very little or no hysteresis was observed for any of the Calc Bio-Si isotherms. The Calc Bio-Si samples showed significant adsorption of nitrogen at very low pressure, these sharp rises at low partial pressure and overall isotherm shapes are consistent with the presence of micropores. The micropore surface area and volume for the Calc Bio-Si were determined to be 294 m^2 g^{-1} and 0.13 cm^2 g^{-1}, respectively, which were not observed in the As-syn material. It can therefore be implied that the microporosity of the material is a direct result of the loss of the additive during the calcination procedure, which is consistent with the small molecular size of the PEHA additive used in the Bio-Si synthesis. The large volume adsorbed between 0.9 and 1 represented the

filling of the inter-particle spaces. The Bio-Si materials possessed low pore volumes and the data did not permit the calculation of an average pore size within the mesoporous range. (See Figure 3.3(b) and 3.4(b)).
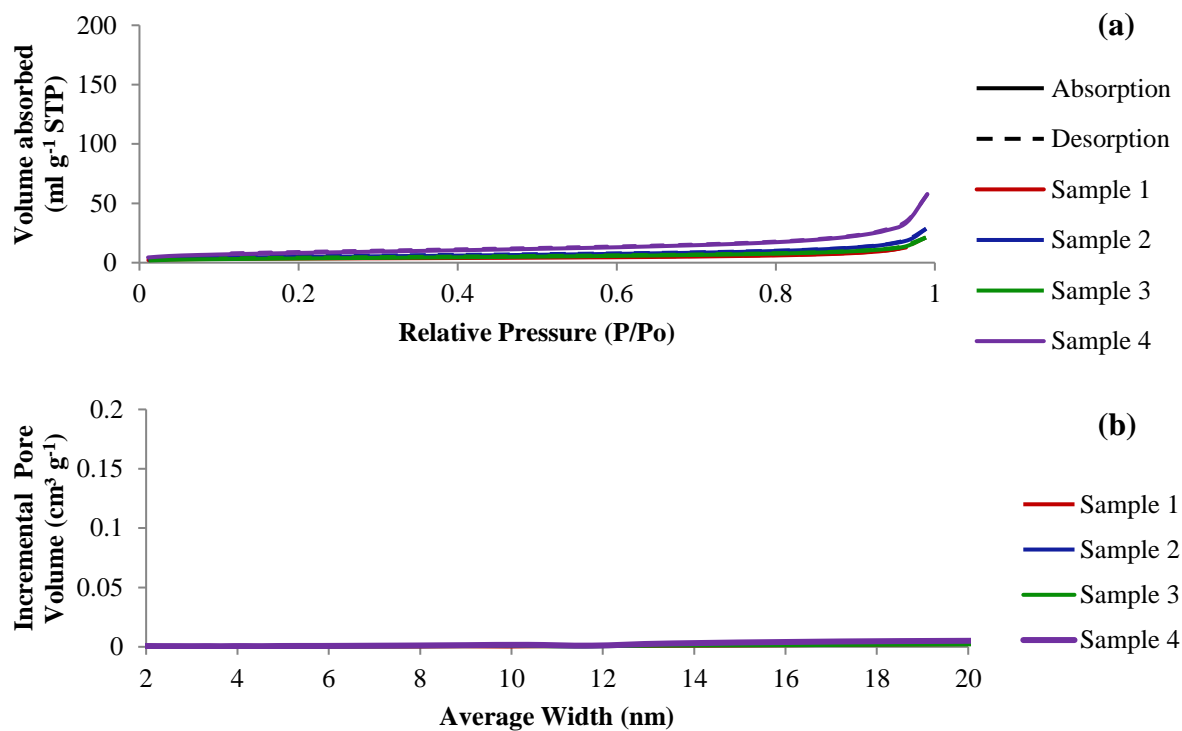
Figure 3.3: Nitrogen sorption isotherms (a) and relative pore size distributions (b) of the As-syn Bio-Si samples.
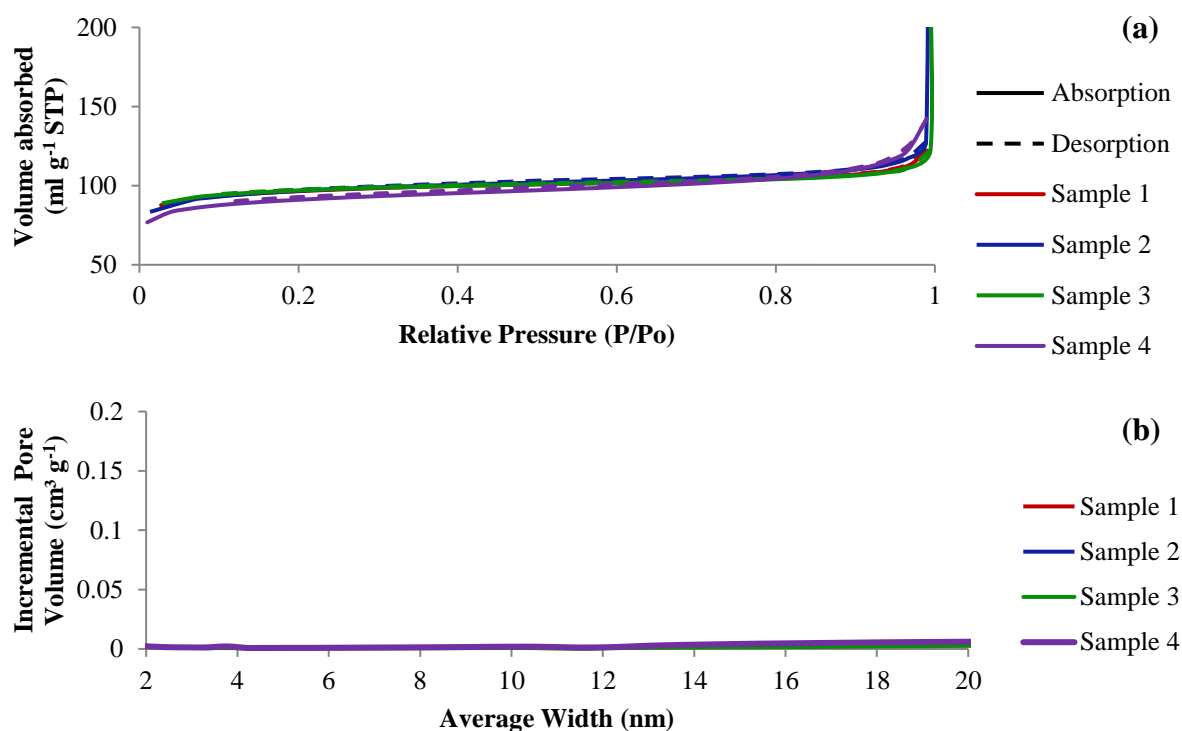
Figure 3.4: Nitrogen sorption isotherms (a) and relative pore size distributions (b) of the Calc Bio-Si samples.

Results demonstrated that the rapid, environmentally friendly synthesis route used in the preparation of Bio-Si produced a calcined material with an average surface area of 338 $m^2\ g^{-1}$ and micropore area of 294 $m^2\ g^{-1}$. This is significantly lower than that for Calc MCM-41 or SBA-15 at 1077 and 658 $m^2\ g^{-1}$, respectively. However, the mesosilica materials were prepared via a sol-gel method under harsh conditions and using longer, multistep synthesis procedures (see Section 3.2.1 and 3.2.2).

For As-syn Fe Bio and Calc Fe Bio, surface areas of 266 and 217 $m^2\ g^{-1}$ were measured respectively (see Table 3.2). These surface areas are significantly higher, for As-syn Fe Bio-Si, and lower, for Calc Fe Bio-Si, than their non-iron incorporated equivalents. Interestingly, and unlike the As-syn and Calc Bio-Si, both materials produced type IV N_2 sorption isotherms, as shown in Figure 3.5 (a), suggesting that they are mesoporous. Both As-syn and Calc Fe Bio-Si were shown to have average pore sizes of around 8.8 nm and larger pore volumes than the original bioinspired materials. These observations along with the type I/II isotherm obtained for the Calc Bio-Si indicates that the silica framework of the bioinspired material was greatly altered when iron was incorporated into the synthesis mixture. It is likely

81

that the use of a mild, room temperature, aqueous synthesis method in the presence of the iron led to a change in the material assembly during synthesis. With the amine additive template remaining intact within the As-syn Fe Bio-Si material, a low surface area and lack of porosity would be expected. However, surprisingly, the material has a surface area and pore volume similar to that of the Calc Fe Bio-Si. This characteristic of As-syn Fe Bio-Si could be attributed to the influence of the Fe^{3+} ions on silica condensation reactions, manifesting in a material with a different structure than would be expected if the iron was not present. It is possible that there are ionic interactions occurring during the material assembly; with both the amine and iron being cationic, they would compete with each other for the anionic silicate sites. The As-syn and Calc Fe-Bio were shown to have broad pore size distributions, supported by the presence of broad hysteresis loops (Figure 3.5 (b) and (a), respectively), indicating that these materials contain pores of different shape and size. Most interestingly, however, Figure 3.5 (b) also reveals steps or shoulder peaks on the curve at around 6, 8 and 10-12 nm that reached a maximum at 14 nm. These are common to both As-syn and Calc Fe Bio-Si, with the step at 10-12 nm decreasing in volume and when the amine additive is removed by calcination. These steps indicate groups of pores within the structure with distinct size that perhaps correspond to different, yet controlled, arrangements of the silica, iron and additive to produce a framework that possesses a remarkable multimodal pore system. The features of these iron incorporated bioinspired silica materials, to the authors best knowledge, have not been reported in literature and are perhaps one of the most thought-provoking, exciting discoveries made in this thesis. The exact mechanism by which they are formed and the role of iron on the framework assembly are of great interest and are owed further investigation. The final structure requires full characterisation to establish whether, as believed, a fascinating novel material has been produced.

The pore sizes observed for the Fe Bio-Si materials are larger than any other material used in this investigation which, along with their possible multimodal pore system, could prove to be a significant advantage as a sorbent, providing accessibility to bulky analytes.
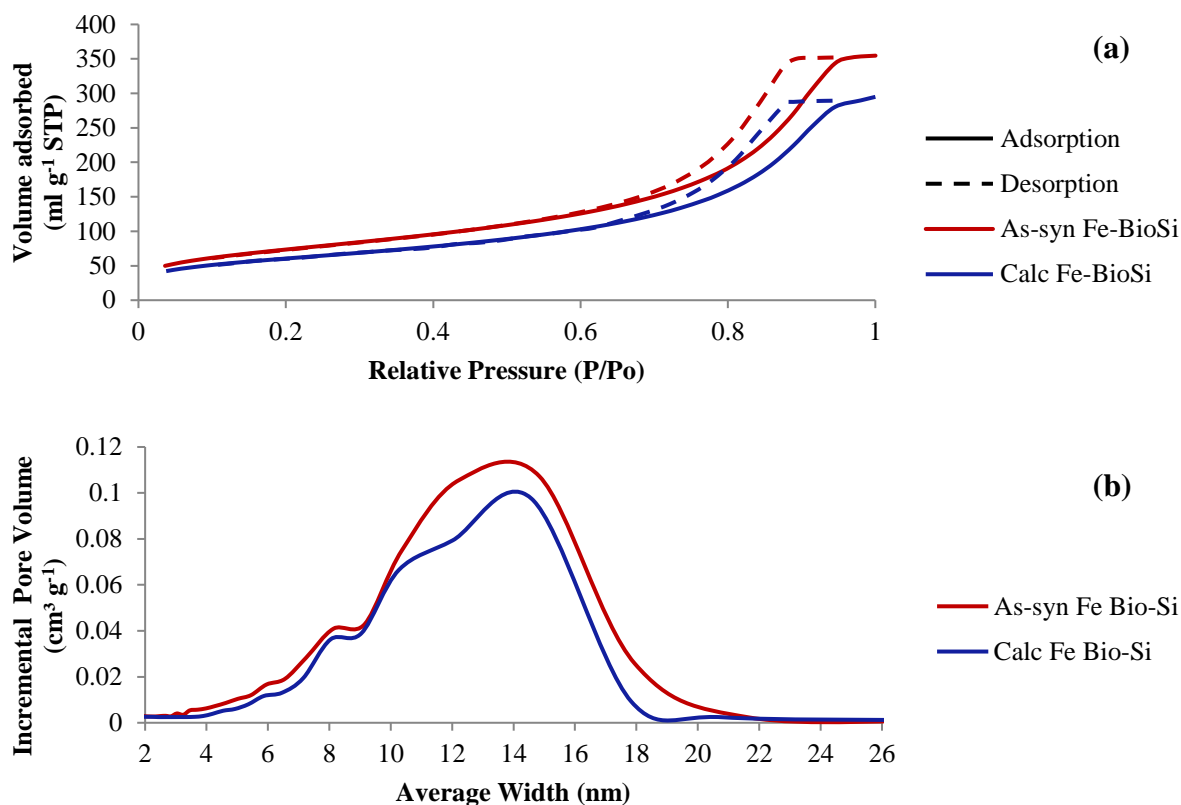
Figure 3.5: Nitrogen sorption isotherms (a) and relative pore size distributions (b) of the Fe Bio-Si samples.

3.4.1.3 Powdered activated carbon (PAC)

The nitrogen sorption isotherm of the commercially available powdered activated carbon (PAC) provided information on the textural properties of the sorbent material (Figure 3.6 and Table 3.3). A surface area of 1403 m^2 g^{-1} was measured for the commercially available PAC which is in agreement with the value reported by the supplier. The isotherm for PAC was of type I, it showed rapid adsorption of nitrogen at low relative pressure, indicative of microporosity in the material. The micropore area and volume deduced for PAC were 389 m^2 g^{-1} and 0.2 cm^3 g^{-1} respectively. A H4 hysteresis was observed which was attributed to the presence of mesopores in addition to the micropores and is associated with narrow slit-like pores in the material.
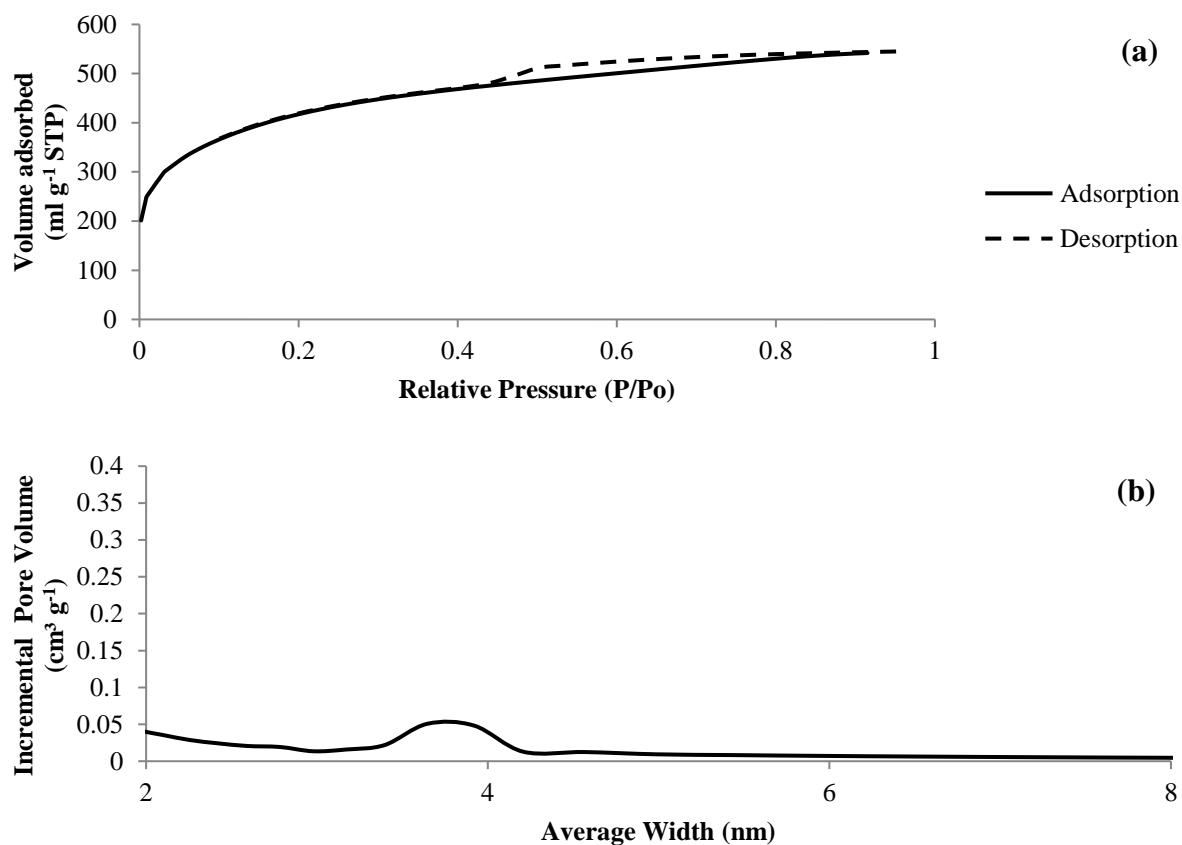
Figure 3.6: Nitrogen sorption isotherms (a) and relative pore size distributions (b) of the PAC sample.

Table 3.3: Physiochemical properties of PAC

Sample Name	BET Surface Area $(m^2\,g^{-1})$[a]	Average Pore Size (nm)[b]	Pore Volume $(cm^3\,g^{-1})$[c]	Micropore Area $(m^2\,g^{-1})$[d]	Micropore Volume $(cm^3\,g^{-1})$[d]
PAC	1403	2.8	0.84	389	0.2

[a] **Calculated by the BJH model from sorption data in the relative pressure range 0.05 – 0.25.**

[b] **Calculated by the BJH model from the desorption branches of isotherms.**

[c] **Calculated from N_2 amount adsorbed at relative pressure P/P_0 of 0.99.**

[d] **Determined by t-plot analysis using the Harkins and Jura equation.**

Part A – Air remediation

4. Adsorption of volatile organic compounds (VOCs) from indoor air

4.1 Introduction

Indoor air pollution has become a very important environmental issue in recent years. The lifestyles, work and leisure activities, of people living in developed, industrialised countries mean they typically spend more than 90 % of their time indoors.[156] Since the worldwide energy crisis in 1973, advances have been made to construct energy efficient buildings. This, unfortunately, has not been without a downside. Efforts to reduce thermal energy losses have resulted in increasingly insulated, airtight buildings; consequently reducing air exchange rates.[157] The restricted ventilation in these modern buildings lowers the turnover rate of indoor air, thereby, increasing concentrations of indoor pollutants.[158, 159]

Volatile organic compounds, as defined by the U.S. Environmental Protection Agency (EPA), vaporise at room temperature. This includes all organic compounds with up to seventeen carbons in their molecular structure that have a boiling point up to 250 °C. VOCs are an important class of indoor air pollutants; their continuous emission from various sources and diffusion properties make them prevalent in indoor environments which has become a concern due to their well-documented effect on human health.[160-162]

The most dominant route to VOC exposure is by inhaling the contaminated air. Other potential exposure routes may include ingestion through contact with VOC-enriched airborne particles. The health effects depend on the specific composition of the VOCs, the concentration and the frequency and length of exposure; high concentrations of some compounds are related to serious health effects. Exposure to VOCs can cause both acute and chronic health effects. The chronic effects of VOC exposure can cause liver, kidney and central nervous system damage. Asthma and 'sick building syndrome' (SBS) symptoms are the most common health symptoms due to VOC exposure.[163, 164] Exposure to aldehydes in particular are known to cause acute symptoms such as eye, nose and throat irritation as well as lower airway and pulmonary effects. Some VOCs such as benzene, 1,3-butadiene, formaldehyde, naphthalene, p-dichlorobenzene, perchloroethylene, styrene and trichloroethylene are suspected of causing or known to cause cancer in humans.[165]

4.1.1 Sources of VOCs in indoor air

VOCs that are present in indoor atmospheres arise from a number of sources. Many volatile organic compounds are emitted from construction materials,[166, 167] furnishings and consumer products in the building, cigarette smoke[168] and from cars in attached garages.[169-171] Construction materials and building contents including wood composites made from chips or sawdust, insulation foams, floor tiles, carpet and the adhesives used for installation, all contribute to the VOC burden in an indoor atmosphere. Emissions from freshly manufactured and installed material are particularly high in a new building;[166, 167] they decline rapidly over the first few months and then more slowly over extended periods of time. There are various VOCs that contribute to concentrations emitted from building materials, with chloroform, acetone, chlorinated compounds and formaldehyde being predominant. Consumer products used in homes also contribute other VOCs to the atmosphere. For example, latex paint contains toluene, ethylbenzene, 2-propanol and butanone. Cleaning agents, household solvents, detergents and waxes all contain various small molar mass volatile organic species. Indoor levels of VOCs are found to be generally 2 to 5 times higher than outdoor environments but may even reach 1000 times that of the outside air as a result of certain activities such as cooking or smoking and low air exchange. Many studies on indoor VOCs have reported that aromatic hydrocarbons such as benzene, toluene, styrene, *m,p*-xylene, *o*-xylene, ethylbenzene and trimethylbenzene account for a great proportion of the indoor VOCs with emission of these compounds found to be significantly higher.[172-174] For this reason benzene, toluene, ethylbenzene and xylenes (BTEX) are the compounds most routinely monitored to assess the concentrations of VOCs in indoor air.[158, 175]

4.1.2 Sampling of indoor VOCs

To assess the degree of exposure of VOCs in indoor air, monitoring concentrations of these pollutants is of the utmost importance. The technique used for sampling VOCs from air must allow representative samples to be taken whilst avoiding variation in sample composition. It should also be as simple as possible to allow the use in field sampling. Moreover, the typical concentrations of commonly encountered VOCs in indoor environments are very low, usually at ppb to sub ppm levels. [96, 97] Therefore, the sampling of VOCs in atmospheres where they

are present at trace levels normally requires a pre-concentration step to obtain sufficient concentrations that achieve the detection limits of commonly applied analytical techniques and also allow quantitation of target compounds with the required precision. A widely used sampling technique, which combines pre-concentration with the sampling stage, is adsorptive enrichment on solid sorbents. Depending on the course of enrichment, there are two principle strategies for collecting VOC samples: active[176] and passive[177, 178] sampling.

Active Sampling

The active sampling process involves drawing a defined volume of air through a sorbent-filled tube or trap, where the VOCs are retained. The active flow of the stream of air through the sorbent bed forces the diffusion of analytes and is achieved using apparatus such as a calibrated pump. The active sampling process is a more efficient way to sample air and is the preferred method in cases where a high sensitivity and therefore a large sample volume is required. During the active sampling process the accuracy of the sample is determined by the sample volume, therefore, measuring the correct volume of air is one of the most important quality issues. Calibrated pumps and mass flow controllers are often used to control the sample volume. If the sample volume is small and the sampling time short, active sampling allows the measuring of dynamic processes with a high sensitivity and is, therefore, a preferred method for the study of kinetic experiments in emission test chambers.

Passive Sampling

VOC enrichment in passive samplers results from the gradient-driven diffusion of analytes from the immediate surroundings to a well-defined sorbent bed inside the sampler. Passive sampler designs are most commonly in the form of a tube or badge, in which the sorbent is contained at one end, with the other being exposed to the atmosphere. The adsorbent is separated from the atmosphere by a diffusion zone which is either an air gap or inert porous polymer. A concentration gradient is established which favours the diffusion of VOCs from the air to the sorbent.[179]

The use of a passive sampler is characterised by long sampling times which are needed, due to very low uptake rates, to allow the airborne compounds to diffuse into the sampler and become trapped on the sorbent surface. Sampling times often exceed several days. Compared with active sampling, passive samplers offer several advantages such as lower cost, ease of use and the elimination of noisy, expensive pumps. Passive samplers are small and simple; they do not require a power source and can be left unattended. This technique is unsuitable

for monitoring short-term variations in analyte concentration but offers a convenient way to assess long-term exposure of VOCs in an indoor environment. Limitations of passive sampling include the sensitivity of the technique to temperature fluctuations and air movement, and the enrichment process is considered less effective than the active sampling technique.

Once the VOCs are trapped on the sorbents they must then be released for analysis. The most common extraction techniques are either by solvent extraction or thermal desorption.[180, 181] Solvent extraction involves the use of a low boiling point solvent (e.g. dichloromethane or carbon disulfide) to release the analytes from the sorbent.[181] Solvent extraction allows the use of longer sorbent beds, higher flow rates and larger total sample volumes than thermal desorption. It is often used for processing passive samplers and is the best technique for thermally labile compounds. Furthermore, samples can be analysed repeatedly and no expensive equipment is required. However, the sample is diluted and only a small fraction of the extract may be injected into the analytical system, resulting in samples that may fail to achieve the instrumentation detection limit. Due to the low concentrations of VOCs present in indoor air environments, samples collected cannot normally be analysed using a solvent extraction method without an additional sample concentration step.

Thermal desorption, on the other hand, is a solvent free method that works extremely well when coupled with gas chromatography as a separation technique. It has the advantage of recovering the entire sample from the sorbent tubes, ensuring complete transfer to the chromatographic column and avoids the presence of a solvent peak which can mask analyte peaks. Thermal desorption therefore offers the advantage of lower detection limits. However, a limitation associated with this technique is that the sample can be analysed only once, meaning repeat analysis of the sample cannot be performed without re-collecting the sample. Finally, the sample is introduced into an analytical instrument for separation, identification and quantification, usually by means of gas chromatography coupled to mass spectrometry.

4.1.3 Sorbents used for VOC sampling

In general, both passive and active sampling can employ the same adsorbent material for enrichment of VOCs present in indoor air. There are a number of different sorbents

commercially available and the following criteria should be taken into account in the selection of a suitable trapping medium to guarantee an accurate determination of VOCs: the strength of interactions between sorbent and analyte needs to be considered as it affects both the sorption and desorption processes. An ideal sorbent for enrichment of VOCs should also have a high adsorptive capacity for the compounds of interest; complete and efficient desorption of the analytes; and a homogenous and inert surface to avoid the generation of artifacts, irreversible adsorption and catalytic effects.

Two main types of solid sorbent are mainly used for trapping VOCs in air:[181-185] carbon-based porous materials, which can be sub-divided into activated carbon, carbon molecular sieves and graphitised carbon; and porous organic polymers, the most commonly used being Tenax.

An overview of the available sorbents for VOC sampling is given in Table 4.1.

Activated carbon

Activated carbon is the most widely used of the carbon adsorbent materials. It is a microporous carbon material, characterised by a broad pore size distribution, high specific surface area ($800 - 1500 \ m^2 \ g^{-1}$) and high temperature stability.[186] The usefulness of activated carbon for the removal of very low concentrations (sub ppm) of VOCs from indoor air environments derives from its large adsorption capacity which originates from its developed microporosity and the resulting high surface area.[187] Activated carbon is created from carbon-containing biological materials such as wood, coconut husks and lignite. The production usually comprises of two stages: carbonisation of the starting material and activation; which could be done successively or at once. The carbonisation stage involves pyrolysis of the starting material at temperatures of $500 - 1200 \ °C$ leading to the formation of the pore structure. This process is commonly followed by physical activation which involves the treatment of the carbonised material with water vapour and/ or carbon dioxide at $700 - 1000$ °C.[188, 189] Activation can also be performed chemically where the carbonisation procedure of the starting material is carried out in the presence of dehydration agents, phosphoric acid or zinc chlorides, which are later washed out.[188] The porous material formed consists of an irregular arrangement of micro, graphite crystallites and amorphous carbon. The pore widths of activated carbon can range from <1 nm to 50 nm with surface compositions varying from clean graphitic to oxygenated surfaces exhibiting significant polarity. It is interactions with these surface oxides which result in several of the drawbacks associated with activated carbon including the strong retention of water and the irreversible adsorption of polar

analytes such as alcohols.[190] The application of activated carbon is limited further by the sensitivity to high temperature, added fire risk, difficult regeneration and shortcomings of pore blocking and hygroscopicity.

Tenax

Tenax is one of the most extensively used sorbents or perhaps more accurately described, swelling agent, especially for environmental sampling such as the trapping of low concentration VOCs in indoor air. Tenax is a porous polymer based on 2,6-diphenyl-p-phenylene oxide (Figure 4.1), it is a hydrophobic material, characterised by high thermal stability. The ability to withstand temperatures of up to 350 °C permits the use of Tenax for thermal desorption. Tenax has many favourable properties besides temperature stability which make it useful for air sampling such as a high adsorption capacity for C_7 to C_{26} VOCs and low water retention.[191] Tenax sorbents also have several limitations including its low capacity for highly volatile organic compounds due to the materials low specific surface area (30 m^2 g^{-1}) and its tendency to form artifacts.
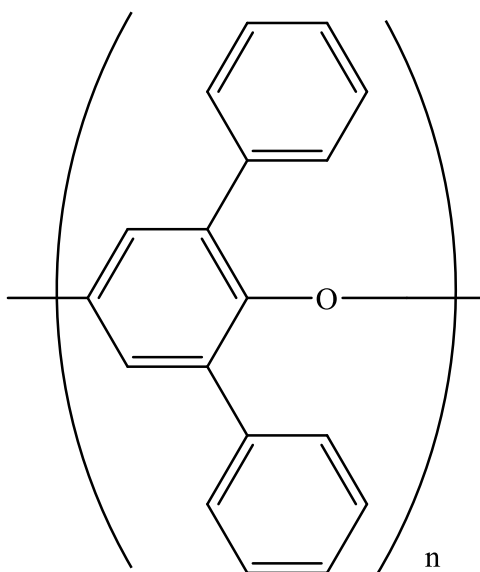
Figure 4.1: Chemical structure of Tenax.

Table 4.1: Characteristics of sorbents used for the enrichment of VOCs from indoor air.[181, 182]

Sorbent Type	Structure	Surface Area/ $m^2 g^{-1}$	Commercial Products	Desorption Technique	Compounds trapped	Thermal Stability / °C
Carbon based	Activated Carbon	800 - 1200		Solvent	Aliphatic and aromatic hydrocarbons e.g $C_2 - C_4$	400
	Carbon molecular sieves	400 - 1200	Carbosieve, Ambersorb, Spherocarb Carboxen	Solvent / Thermal	Very volatile organic compounds	> 400
	Graphised carbon	12 - 100	Carbotrap, Carbopack, Carbograph	Thermal	Hydrocarbons $< C_{20}$, oxygenated VOCs	> 400
Porous polymers	Styrene, Divinylbenzene or Polyvinylpyrrolidone polymers	300 - 800	Porapak Q/N Chromosorb 106/107	Thermal / solvent	$C_5 - C_{12}$ hydrocarbons, oxygenated VOCs	< 250
	Phenylphenylene oxide polymers	20 - 35	Tenax	Thermal	Aromatic and non-polar VOCs (b. pt. > 100 °C)	< 350

4.1.4 Mesoporous silicates as sorbents for the removal of VOCs from indoor air

The prevalence of VOC emission in indoor environments has triggered an increasing awareness due to their potential adverse health effects; with efforts focused on the development of abatement technologies to remove these compounds from the indoor atmosphere. Among the different alternatives available to remove VOCs from indoor air, adsorption technology has been generally recognised as a preferred strategy due to the flexibility, low energy and cheap operational costs of the method.[192-194] Adsorption is

especially favoured in cases where the organic pollutants to be captured have alternative uses.[195] As a result of the various limitations associated with traditional sorbents, discussed in Section 4.1.3, the development of alternative sorbents for the abatement of VOCs has attracted considerable attention. Recently, ordered mesoporous materials such as MCM-41[196, 197] and SBA-15[198-200] have been introduced as novel sorbents for the removal of VOCs. Ordered mesoporous silica offers excellent features such as large pore volume, high surface area, controllable and narrowly distributed pore sizes, open pore structure and reliable desorption performance; characteristics that are greatly desirable as a sorbent and highlight the materials' potential application in adsorption technologies.[201-204]

Wu et al.[197] synthesised and assessed mesoporous silica, MCM-41, for its applicability to trap VOCs and compared the results with several commercially available microporous carbon molecular sieves. MCM-41 was shown to effectively adsorb C_8 - C_{12} compounds, however unlike the carbon sorbents which had the ability to trap VOCs across a wide range ($C_3 - C_{12}$), it showed little adsorption for the smaller molecules. With regards to desorption temperatures, it was shown that for MCM-41 the adsorbed VOCs could be sufficiently recovered at moderate temperatures of about 150 °C, much lower than those required in the case of the carbon sorbents which needed temperatures in the excess of 300 °C due to the stronger interaction of VOC molecules in the microporous structure.

Studies have indicated that SBA-15-type mesoporous silicas with bimodal pore distribution have a high affinity for various VOCs due to their complementary micropores, which are favourable to the diffusion process.[198, 200, 203] In particular, they have been shown to have a high selectivity for benzene[199] and a high affinity for light hydrocarbons[198] and toluene.[194, 200] The application of mesoporous silicas is expanded by the presence of silanols on the amorphous wall surfaces which, by making the material less hydrophobic, enhance the adsorption of more polar VOC molecules through hydrogen bonding and also enable the chemical derivatisation of mesoporous silicas. Furthermore, surface siloxanes of the silica materials have the potential to hydrolyse to silanols by water adsorption.[205, 206] The material surface chemistry can be tailored to improve selectivity of VOCs adsorbed by functionalising the mesoporous silica through the introduction organic functional groups, such as alkyl chains or phenyl groups to the surface or silica framework of the material[61]. Studies performed by Dou et al.[201] and Huo et al.[193] found that phenyl-grafted mesoporous materials not only significantly enhanced the surface hydrophobicity of the silica, but also enhanced the materials selectivity for aromatic compounds. The affinity between the surface phenyl groups and aromatic compounds, as a result of π-electron effect, led to a larger dynamic adsorption

capacity for benzene compared to that of cyclohexane. Dou also compared the adsorption abilities of phenyl functionalised, MCM-41 and SBA-15, and concluded that MCM-41 exhibited a lower adsorption efficiency for benzene due to the one-dimensional mesoporous channels.

Limited literature has been published on the dynamic adsorption performance of these materials with the majority of studies focussed on investigation of the equilibrium adsorption by means of adsorption isotherms or temperature programme desorption studies.[194, 196, 204, 207, 208] Although it has been shown that the VOC adsorption capacity for mesoporous silica is high using equilibrium data, the adsorption capacity for MCM-41 is considerably lower in the low-pressure range, as would be encountered during the dynamic sampling of indoor air.

4.1.5 Aims and objectives

The aim of this chapter was to assess the use of mesoporous silicates, MWD MCM-41 and SBA-15, (synthesised as outlined in Section 3.2) as sorbents to extract VOCs from indoor air in order to compare their efficiency with commercial sorbent, Tenax TA.

There were a number of objectives associated with this research that required performing to fully investigate this aim.

1. Generation of known concentrations of VOCs (toluene, ethylbenzene, cumene and dichlorobenzene) using a dynamic atmospheric chamber.

2. Preparation of different sorbent tubes: Commercially available Tenax TA and mesoporous silicates (MWD MCM-41 and SBA-15).

3. The use of TDU-GC-MS to analyse the VOCs trapped onto the sorbent, using calibration lines for quantitative analysis.

4. Comparison of the adsorption capacity (5 % breakthrough) of different sorbents.

4.2 Experimental

4.2.1 Materials and reagents

Ethylbenzene (99 %) and dichlorobenzene (99 %) were purchased from Sigma Aldrich. Toluene (99.5 %) was provided by Fisher Scientific. Cumene (99 %) was purchased from ACROS Organics. Tenax TA was supplied by Markes International Limited.
As-syn MCM-41 and Calc MCM-41 were synthesised as detailed in Section 3.2.1. SBA-15 was synthesised as detailed in Section 3.2.2.

4.2.2 Dynamic atmospheric chamber

A dynamic atmospheric chamber was used to produce a constant and controlled polluted air stream containing known concentrations of VOCs. The atmospheric chamber system consisted of a VOC source, two flow streams and a 20 dm^3 sampling chamber as shown in Figure 4.2
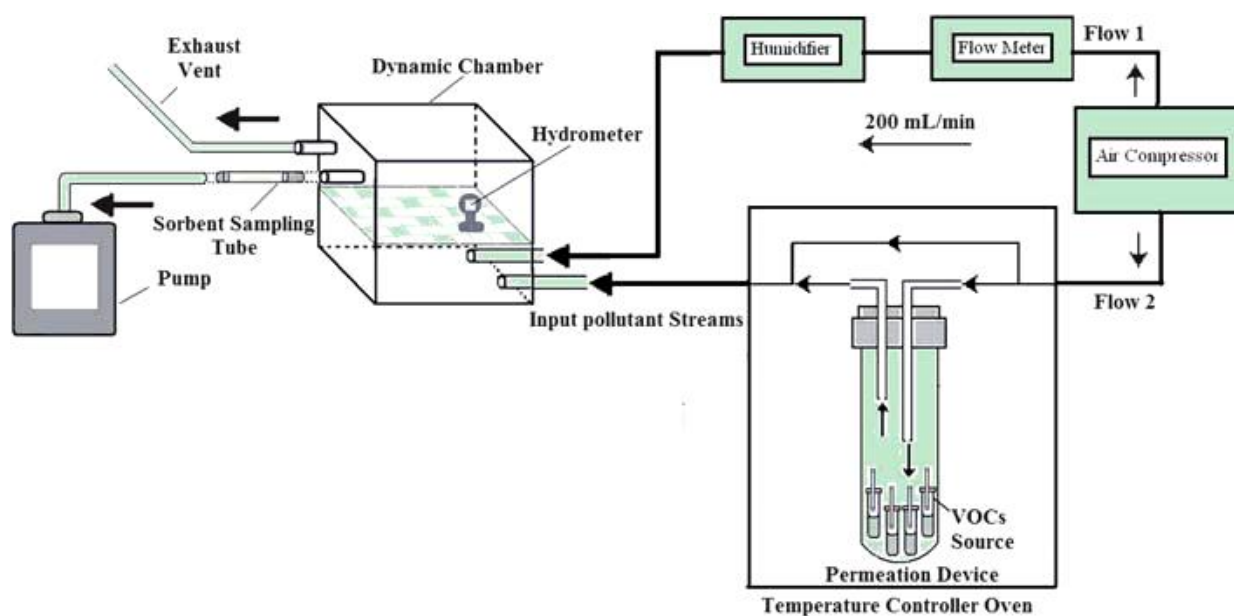
Figure 4.2: Atmospheric chamber set-up.

The initial air stream, produced using an air compressor (ABSOLUTE L-S20-4), was split into two main flows. One flow was passed through a humidification system, which consisted of a dreshel bottle containing distilled water, providing the chamber with a diluent air flow that contained additional moisture. The air in the sampling chamber was maintained at approximately 60 % relative humidity (RH) by controlling the air flow rate passing through the dreshel bottle using a mass flow controller at 200 cm^3 min^{-1} (Flow 1). An approximate RH value was measured inside the permeation chamber using a room dial hydrometer which indicates the level of humidity in 5 % divisions over the range of 0 to 100 % RH (ETI Ltd). The second flow stream entered a temperature-controlled oven (Kin-Tek Laboratories Inc. Model 491 M-B) which was set at 25 °C and passed over a VOC source at a measured flow rate of 200 cm^3 min^{-1}. The mass flow controller used was housed inside the Kin Tek system and ensured a constant accurate flow rate of air passing over the heated VOC source. The VOC source stored four GC auto-sampler vials containing 1 cm^3 of either toluene, ethylbenzene (EB) cumene and dichlorobenzene (DCB) and each sealed with silicon-seal tops. To allow controlled permeation, each vial was pierced with an 18 gauge GC syringe needle and the vials, complete with needle, were placed inside the oven in a glass housing unit which was o-ring sealed. The emission rates of the VOCs were controlled by the oven temperature and flow rate of air passing through the glass housing unit. At 25 °C and 200 cm^3 min^{-1}, average (n=4) emission rates of 4293, 2530, 2450 and 1173 ng min^{-1} were calculated for toluene, ethylbenzene, cumene and dichlorobenzene, respectively. (See Section 4.3.1) Both the humidified air flow and polluted air flow were recombined in the sampling chamber. The chamber was set up and left for at least 48 h prior to sampling to ensure equilibration of VOC concentrations and RH conditions.

4.2.3 Dynamic sampling of VOCs from atmospheric chamber

In this set of experiments, the adsorption performance of a widely used, commercially available sorbent, Tenax TA, was compared to mesoporous silica trapping media MWD MCM-41 or SBA-15 for trapping 4 target monoaromatic hydrocarbons; toluene, ethylbenzene, cumene and dichlorobenzene.

4.2.3.1 Preparation of sorbent packed sampling tubes

Stainless steel sampling tubes pre-packed with 100 mg of Tenax TA were used. (Markes International) Sorbent tubes were also prepared containing mesoporous silica materials MWD MCM-41 or SBA-15. Before the sorbents were loaded into the stainless steel tubes they were pressed into a disc, crushed and sieved between 40 – 60 mesh. Each sampling tube was then packed with 100 mg of sorbent inter-dispersed with 1.5 g of glass beads (750 – 1000 μm), contained within two plugs of glass wool as shown in Figure 4.3. The glass beads were incorporated within the sampling tubes to reduce the backpressure and enable the air flow rate required through the powdered adsorbents. Newly prepared mesoporous silica sampling tubes were conditioned by heating under a flow of air using a thermal desorption unit (TDU) at 300 °C for 2 h. All sampling tubes were subsequently conditioned for 30 min before any sampling of VOCs was performed.
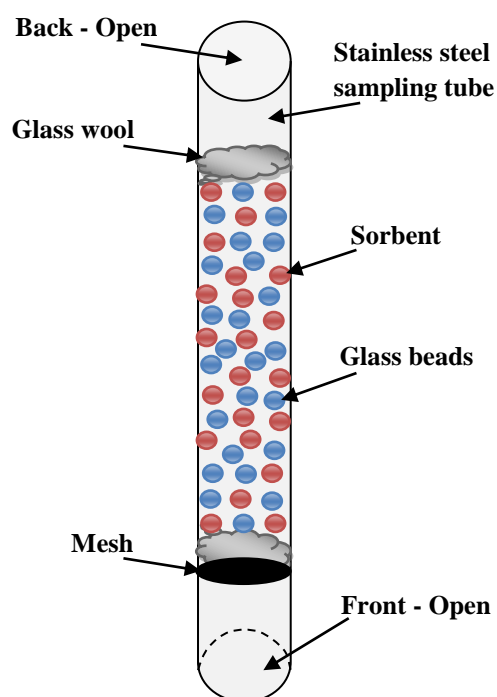
Figure 4.3: Inter-dispersed sorbent and glass beads packed into sampling tubes.

4.2.3.2 Trapping efficiency

The dynamic sampling chamber was used, under the conditions described in Section 4.2.2, to generate a known concentration of VOCs. The atmosphere containing 10.7, 6.3, 6.1 and 2.9 mg m^{-3} of toluene, ethylbenzene, cumene and dichlorobenzene, respectively, was then

actively sampled using a specific flow rate of 100 cm^3 min^{-1}. The front end of the sampling tube was connected to an outlet sampling port in the chamber and the back end was connected to an air sampling pump (SKC sidekick pump). The flow rate passing through the individual sampling tubes was calibrated to 100 cm^3 min^{-1} using a bubble meter.

The trapping efficiency of three different sorbents; Tenax TA, MWD MCM-41 and SBA-15 were determined by using tubes containing each sorbent to sample a 100 cm^3 aliquot of contaminated air from the experimental chamber. This was performed using identical conditions; a sampling flow rate of 100 cm^3 min^{-1} for 1 min. The VOCs were thermally desorbed from the sampling tubes using a TDU and then diverted into the GC-MS for analysis. Calibration lines, prepared for each analyte, were used to determine the VOC masses trapped by each sorbent. The trapping efficiency of each sorbent for the VOCs under investigation was calculated using Equation 4.1.

Trapping Efficiency (%) = $\dfrac{\textit{Weight of analyte trapped on sorbent}}{\textit{Theoretical Weight of analyte applied onto sorbent}}$ *× 100*

Equation 4.1

4.2.3.3 Dynamic capacity (breakthrough) experiments

It is known that sorbents have a limited capacity for absorption of a given analyte, either by saturation or chemical displacement. Once this capacity has been reached the analyte will pass through the sorbent un-absorbed. This is commonly referred to as 'breakthrough'. Breakthrough experiments were carried out using 2 sampling tubes connected in series, the set up of which is shown in Figure 4.4. The principle of this experiment was to determine when breakthrough occurred for each sorbent using one set of VOC concentration, where breakthrough is defined as the point at which 5 % of the analyte is trapped by the second sampling tube.

Using the results from the trapping efficiency experiment outlined in Section 4.2.3.2, where the chamber atmosphere was sampled for 1 min at 100 cm^3 min^{-1}, the masses (M_1) of each VOC trapped by the three different sorbents Tenax TA, MWD MCM-41 and SBA-15 were then measured for the 100 cm^3 aliquot of air.

To introduce higher masses of analyte to each sorbent, the sampling times were increased to

2, 5, 10, 15 and 20 min. For these experiments it was not possible to directly measure the VOCs trapped by one tube because the detector would have become saturated, particularly for the latter experiments, instead the masses of the VOCs expected to be trapped by each sorbent were estimated by multiplying the masses trapped in the previous experiment by the sampling time ($M_1 \times$ time). These will be referred to as mass expected (M_E).

To determine breakthrough, the VOCs trapped by the second tube were measured (M_2) and the percentages of VOCs trapped were calculated using Equation 4.2:

$$\textit{VOCs trapped on second tube (\%) = } M_2 / M_E \times 100 \qquad \textbf{Equation 4.2}$$

Breakthrough was reported when the percentage of VOC measured on the second tube exceeded 5 % of the mass expected.
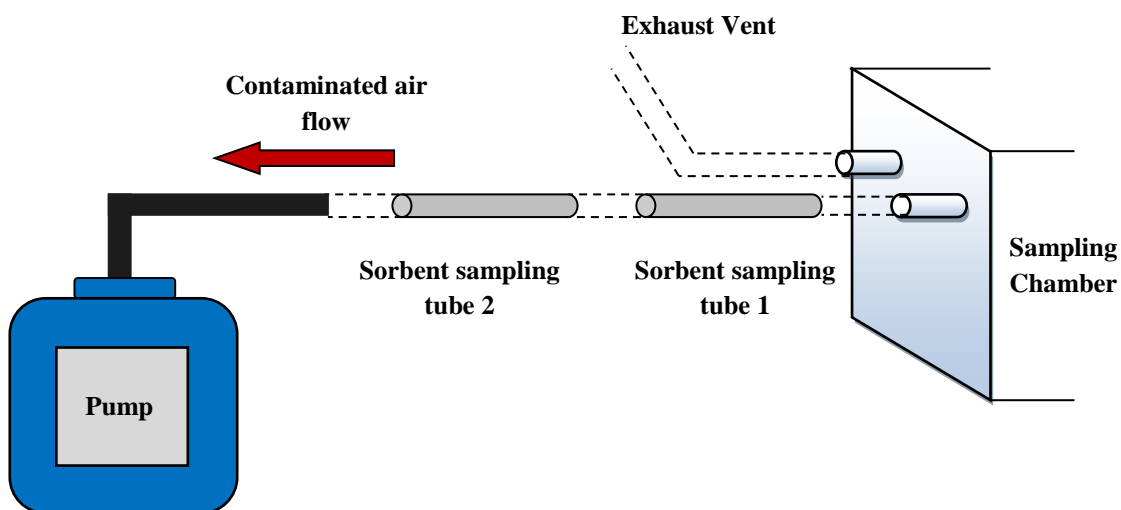
Figure 4.4: Schematic of breakthrough experiment set-up.

4.2.4 Analysis of sampling tubes

4.2.4.1 TDU-GC-MS analysis method

The analytical instrument used for desorption, identification and quantification of the VOCs trapped in the sampling and sorbent tubes was a thermal desorption unit coupled to a gas chromatograph and mass spectrometer (TDU-GC-MS). For the sorbent trapping efficiency and breakthrough experiments the thermal desorption unit used was a Perkin Elmer Turbo Matrix TD, the operating conditions for which are outlined in Table 4.2. The TDU was coupled to a Perkin Elmer GC and Turbo Mass Gold Mass Spectrometer, the operating conditions for both are outlined in Tables 4.3 and 4.4 respectively.

Table 4.2: Operating conditions of the TDU for the desorption of VOCs.

Desorb Flow	19 cm^3 min^{-1}
Desorb Temperature	300 °C
Cold Trap Sorbent	Tenax TA
Cold Trap Temperature	Held at -30 °C, ramped at 99 °C s^{-1} to 300 °C, held at 300 °C for 5 min
Split Ratio	1 %

Table 4.3: Operating conditions of the GC for the separation of VOCs.

Inlet Line Temperature	180 °C
Oven Temperature Program	60 °C for 4 min. Ramped to 65 °C at 10 °C min^{-1} and held for 5.5 min. Ramped to 90 °C at 8 °C min^{-1} for 1.87 min
Column	Perkin Elmer, SMS Elite, (dimethylpolysiloxane 5 % diphenyl), 30 m × 0.25 mm i.d and 0.25 μm thickness
Carrier Gas	Helium
Carrier Gas Flow	1 cm^3 min^{-1}

Table 4.4: Operating conditions of the MS for the detection of VOCs.

Electron Energy (eV)	Trap Emission (eV)	Multiplier (V)	Scan Run Time (min)	Scan Time (s)	Inter Scan Delay (s)	m/z Range (amu)	Solvent Delay (min)
70	100	315	15	0.2	0.1	50 - 300	3

As a result of instrument maintenance the above method was transferred to an alternative TDU-GC-MS for subsequent photocatalytic oxidation (PCO) experiments. A Series 2 UNITY thermal desorption unit (Markes International) was used for the thermal desorption process. An Agilent 7890A GC system coupled to an Agilent 5975C inert XL MSD with triple axis detector. The column used was a HP-5MS (methylpolysiloxane, 5 % phenyl groups), 30 m × 0.25 mm i.d and 0.25 μm thickness. The oven temperature program was adjusted as follows: an initial temperature 40 °C for 3 min, ramped to 65 °C at 20 °C min^{-1} and held for 6 min, then ramped to 90 °C at 10 °C min^{-1} and held for 2.2 min; giving an overall GC run time of 15 min.

4.2.4.2 Preparation of VOC calibration solution

The TDU-GC-MS was calibrated for the quantification of detected analytes using a standard solution of the 4 target VOCs. A methanolic solution containing toluene, ethylbenzene, cumene and dichlorobenzene was prepared in a 100 cm^3 volumetric flask where the final analyte concentrations were 60 ng μL^{-1}. Table 4.5 contains information on the physical properties of the VOCs studied.

Table 4.5: Physical properties of the 4 target VOCs studied.

VOC	Liquid Density at 25 °C / g cm^{-3}	Boiling Point / °C	Vapour Pressure at 20 °C / mmHg	Molecular Weight / g
Toluene	0.87	111	22	92.14
Ethylbenzene	0.87	136	10	106.17
Cumene	0.86	154	8	120.2
Dichlorobenzene	1.3	180	1.2	147

An example calculation to obtain the volume of toluene required to prepare a 60 ng µL^{-1} stock solution is given below.

Concentration of each VOC required is 60 ng µL^{-1} $\equiv$ 60 µg cm^{-3}

Required mass in 100 cm^3 volumetric flask = 100 cm^3 × 60 µg cm^{-3}

$$= 6000 \text{ µg} \equiv 6 \text{ mg}$$

Liquid density of toluene = 0.87 g cm^{-3} $\equiv$ 870 mg cm^{-3}

Volume of toluene required = 6 mg/ 870 mg cm^{-3} = 6.9 x10^{-3} cm^3 = 6.9 µL

Similar calculations were performed to obtain the volumes required for the preparation of 60 ng µL^{-1} of ethylbenzene, cumene and dichlorobenzene; giving volumes of 6.9, 7 and 4.6 µL, respectively. Thus, the calculated volumes for each VOC were transferred into a 100 cm^3 volumetric flask and methanol was added to the 100 cm^3 mark.

4.2.4.3 Injection of calibration solutions into sampling tube

To calibrate the TDU-GC-MS, the 60 ng µL^{-1} standard solution was introduced onto conditioned Tenax TA sampling tubes. A set of calibrant tubes containing 60, 120, 180, 240, 300 and 360 ng of VOCs were prepared by injecting 1, 2, 3, 4, 5 and 6 µL, respectively, of the 60 ng µL^{-1} stock solution into the tubes using the direct injection method discussed below. A Perkin Elmer GC 8000 injection port was modified to allow efficient liquid sample introduction into the Tenax TA tubes. An adaption unit was used to connect the sampling tube to the injection port of the GC. The calibration solution was injected into the port using a GC syringe and air was used as a carrier gas, transporting the injected analytes onto the Tenax TA tube. After injection of the standard solution, the GC syringe needle was kept within the injection port for a short interval of 20 seconds to achieve complete evaporation of target analytes. Air continued to be passed over the Tenax TA tube for 2 min at a flow rate of 100 cm^3 min^{-1}, aiding retention of the VOCs onto the sorbent bed while removing methanol solvent from the tube. The Tenax TA tube was removed, capped and analysed immediately after injection. The peak areas were obtained and used to prepare calibrations for each analyte under investigation.

4.3 Results and discussion

4.3.1 Generation of VOCs inside exposure chamber

4.3.1.1 Determination of VOC emission rates from permeation vials

The four permeation vials each containing a 1 cm^3 aliquot of a target VOC; toluene, ethylbenzene, cumene or dichlorobenzene were accurately weighed before being placed inside the glass housing unit which was subsequently place inside a temperature-controlled oven. The temperature of the oven was set at 25 °C and the air passing through the glass housing unit was set to 200 cm^3 min^{-1}. To determine the emission rate of each VOC under the chosen conditions, the vials were removed after set periods of time, weighed and placed back in the oven. The emission rates (ng min^{-1}) were measured by dividing the masses (ng) of VOC lost from the permeation device by time (min). The weights were measured weekly on 4 occasions and the resulting average weight losses (ng min^{-1}), standard deviations and % RSD values are given in Table 4.6.

Table 4.6: Permeation vial emission rates of VOCs determined through weight loss.

VOC	Weight Loss (g week^{-1})				Average Weight Loss (g week^{-1})	Average Weight Loss (ng min^{-1})	% RSD
	Week 1	Week 2	Week 3	Week 4			
Toluene	0.0451	0.0413	0.0421	0.0446	0.0433	4293	4.3
Ethylbenzene	0.0272	0.0239	0.0245	0.0264	0.0255	2530	6.1
Cumene	0.0267	0.0226	0.0236	0.0259	0.0247	2450	7.8
Dichlorobenzene	0.0131	0.0106	0.0114	0.0122	0.0118	1173	9.1

All % relative standard deviation (RSD) values were below 10 % with toluene weight loss below 5 %, indicating a constant weight loss of VOCs from the permeation vials. This confirmed the stability of the in-house prepared permeation devices and the ability to produce stable streams of contaminated air using the exposure chamber system. It was observed that, as expected, the emission rates of VOCs in this study were indirectly proportional to the boiling points of the analytes with toluene at 110.6 °C, ethylbenzene at 136 °C, cumene at

152 °C and dichlorobenzene at 180.5 °C. It was also be noted that the % RSD values increased proportionally with VOC boiling point, suggesting that there is less variation in the emission rates for more volatile compounds.

4.3.1.2 Calculation of theoretical concentration of VOCs generated by system

Using the average emission rate of each analyte (ng min^{-1}), given in Table 4.6, the theoretical atmospheric concentration (ug g^{-1} or ppm) of each VOC generated in the polluted air stream was calculated using Equation 4.3 below.

$$C = \frac{K_0 E}{F}$$ **Equation 4.3**

where C is the VOC concentration (ppm), E is the emission rate (ng min^{-1}) and F is the flow rate of the air stream passing through the VOC source (cm^3 min^{-1}). K_0 is used to convert the gas units to a convenient term quoted in ppm. The value of K_0 (L g^{-1}), which is the inverse density of the gas, depends on temperature. Often a nominal temperature of 25 °C is used to convert gas units and this temperature is used in this research. At 25 °C K_0 is then the molar volume of the gas at 25 °C divided by its molecular weight as shown in Equation 4.4.

$$K_0 = \frac{24.46 \ (L)}{MW \ (g)}$$ **Equation 4.4**

Thus, K_0 for toluene, ethylbenzene, cumene and dichlorobenzene were 0.265, 0.230, 0.204 and 0.166 L g^{-1}, respectively.

Since the polluted air stream was combined with the humidified air stream, the final VOC concentrations in the atmospheric chamber were divided by 2 (see Table 4.7).

Table 4.7: Theoretical concentrations of VOCs generated in the air stream.

VOC	Calculated Emission Rate (ng min^{-1})	K_0 (L g^{-1})	Flow (cm^3 min^{-1})	Concentration of VOCs in air stream (ppm)	Concentration of VOCs in chamber (ppm)
Toluene	4293	0.265	200	5.688	2.844
Ethylbenzene	2530	0.230	200	2.909	1.455
Cumene	2450	0.204	200	2.499	1.250
Dichlorobenzene	1173	0.166	200	0.974	0.487

In literature, gases are often quoted in terms of a mass per volume unit (mg m^{-3}) in addition to ppm (ug g^{-1}). To convert ppm to mg m^{-3} the density of the gas, D, must be considered and the ideal gas equation, Equation 4.5 (a), used:

$$PV = nRT \qquad \textbf{Equation 4.5 (a)}$$

And since,

$$D = \frac{m}{V} \;\textbf{(b)} \quad and \quad n = \frac{m}{MW} \;\textbf{(c)}$$

Rearrangement of the Equations 4.5 (a) and (c) and substitution into (b) gives Equation 4.6:

$$D = \frac{PMW}{RT} \qquad \textbf{Equation 4.6}$$

where D is the gaseous density (g L^{-1}), R is the gas constant (0.0821 L atm mol^{-1} K^{-1}), T is the temperature (298 K) and P is the pressure (1 atm).

Thus, to convert from ppm to mg m^{-3}, gaseous VOC concentrations are multiplied by their respective gas densities (see Table 4.8).

Table 4.8: Theoretical concentration of VOCs generated in the chamber and expected mass of analyte in a 100 cm^3 aliquot of air.

VOC	Concentration of VOCs in chamber (ppm)	Gaseous Density at 25 °C (g L^{-1})	Concentration of pollutants in chamber (mg m^{-3})	Mass of VOC trapped in 100 cm^3 aliquot of air (ng)
Toluene	2.844	3.767	10.714	1071
Ethylbenzene	1.455	4.340	6.313	631
Cumene	1.250	4.914	6.141	614
Dichlorobenzene	0.487	6.010	2.926	293

The investigation into the use of three different sorbents types for the trapping of VOCs from indoor air involved the determination of VOCs present in a 100 cm^3 aliquot of the contaminated chamber air. Based on theoretical calculations, the masses (ng) of each analyte expected to be trapped in this 100 cm^3 aliquot of air are 1071, 631, 614 and 293 ng of toluene, ethylbenzene, cumene and dichlorobenzene, respectively.

4.3.2 Assessment of VOC sampling method: Validation

Two TDU-GC-MS instruments were used for VOC analysis throughout the duration of this work, both of which are described fully in Section 4.2.4.1. A Perkin Elmer system was used for the investigation of mesoporous silicates as sorbents for trapping VOCs from indoor air. An Agilent system was then used during the study into VOC degradation using photocatalytic oxidation. Prior to the analysis of any VOC samples collected using the dynamic atmospheric chamber, the sampling method required validating to ensure robustness of the method. This was achieved through the calibration of the TD-GC-MS instruments for the quantification of the four target VOCs; toluene, ethylbenzene, cumene and dichlorobenzene. Analysis of calibrant Tenax TA tubes was performed in order to establish the limit of quantification, accuracy, precision and reproducibility of the sampling method on each TD-GC-MS instrument.

4.3.2.1 Calibration of TD-GC-MS instruments

Calibration of both TD-GC-MS instruments involved the analysis of Tenax TA tubes loaded with increasing volumes of a 60 ng μL^{-1} VOC calibration solution, as described in Section 4.2.4.3., using the TD-GC-MS conditions outlined in Section 4.2.4.1. The peak areas obtained for each analyte were plotted against the mass of each VOC injected onto the sampling tubes. An example set of results for each VOC, obtained using the Agilent system, is outlined in Tables 4.9 – 4.12 with the corresponding regression lines shown in Figures 4.5 – 4.8.

Table 4.9: TD-GC-MS results from analysis of toluene standards.

Nominal Mass / ng	RT / min	Peak Area / counts	Calculated Mass / ng	Accuracy / %
60	4.358	337145948	62	104.0
120	4.353	583278890	119	99.4
180	4.358	832335159	177	98.2
240	4.358	1107474004	240	100.1
300	4.358	1367380860	300	100.1
360	4.311	1630336720	361	100.3
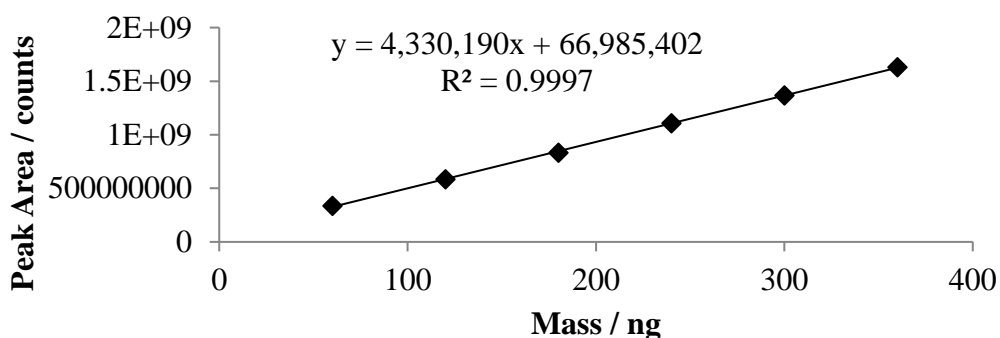
Figure 4.5: Toluene calibration line.

Table 4.10: TD-GC-MS results from analysis of ethylbenzene standards.

Nominal Mass / ng	RT / min	Peak Area / counts	Calculated Mass / ng	Accuracy / %
60	6.115	366815448	59	98.1
120	6.12	680607142	120	100.1
180	6.13	1003515359	183	101.7
240	6.134	1286175424	238	99.3
300	6.144	1599114894	299	99.8
360	6.139	1911938839	360	100.1

$y = 5{,}125{,}619.x + 64{,}981{,}157$
$R^2 = 0.9998$
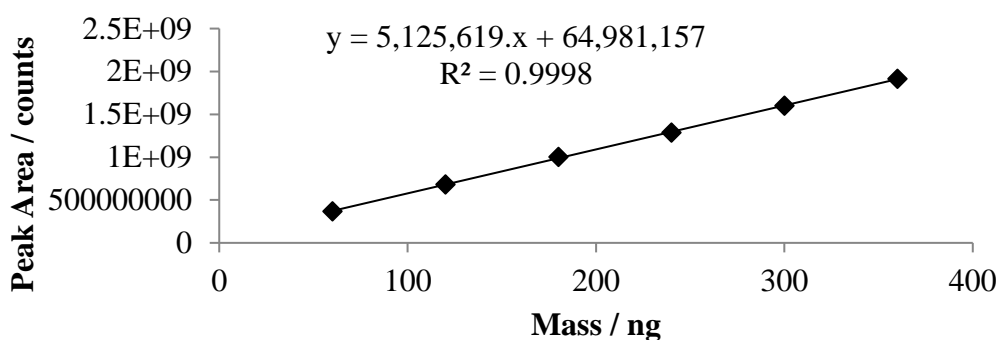
Figure 4.6: Ethylbenzene calibration line.

Table 4.11: TD-GC-MS results from analysis of cumene standards.

Nominal Mass / ng	RT / min	Peak Area / counts	Calculated Mass / ng	Accuracy / %
60	7.944	400381512	59	97.6
120	7.953	726744793	119	99.2
180	7.968	1079639769	184	102.4
240	7.982	1379333189	240	99.9
300	7.997	1694205934	298	99.4

$y = 5{,}400{,}395x + 83{,}989{,}867$
$R^2 = 0.9993$
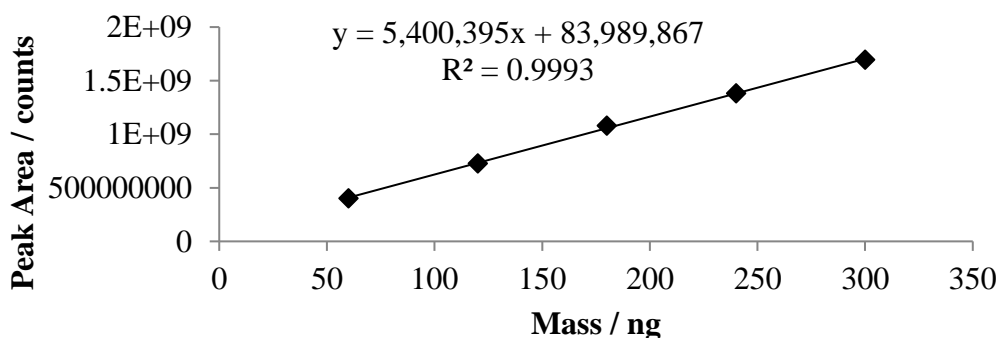
Figure 4.7: Cumene calibration line.

Table 4.12: TD-GC-MS results from analysis of dichlorobenzene standards.

Nominal Mass / ng	RT / min	Peak Area / counts	Calculated Mass / ng	Accuracy / %
60	11.377	344377965	62	103.0
120	11.392	604974445	118	98.4
180	11.406	884754070	179	99.2
240	11.42	1175608859	241	100.6
300	11.439	1446899916	300	100.0
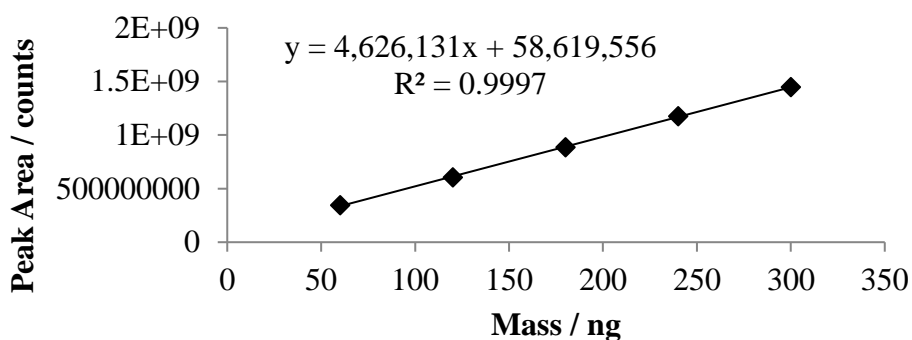
Figure 4.8: Dichlorobenzene calibration line.

By examination of the regression lines and the correlation coefficients, the method was shown to be linear for the analysis of toluene and ethylbenzene from 60 – 360 ng and for cumene and dichlorobenzene from 60 – 300 ng. The signal response for each VOC was linear over the specified ranges with R^2 values more than or equal to 0.9993. All standards within these ranges were within +/- 5 % of the nominal VOC masses, thereby demonstrating a high degree of accuracy. From Tables 4.5 – 4.8 it can also be shown that the retention time of each VOC was constant through the analysis runs. Standards containing masses containing 360 ng for cumene and dichlorobenzene were rejected to bring the lower end of the calibration line within +/- 5 % accuracy. At these higher concentrations of cumene and dichlorobenzene, the detector experienced saturation and the calibration line deviated from linearity. Over the duration of this work, calibration standards were run on both instruments and a new calibration line was acquired for each set of samples analysed with the corresponding regression equations being used to quantify the peaks obtained. All calibrations showed good reproducibility, were of the same accuracy as the example shown and exhibited R^2 values above 0.999.

4.3.2.2 Precision of the calibration method

To establish the repeatability and precision of the method, calibrant Tenax TA tubes, loaded with 3 μL standard solution corresponding to a VOC mass of 180 ng, were analysed in replicates of 5. The results of this analysis are shown in Tables 4.13 – 4.16 with the variation between replicates shown in Table 4.17.

Table 4.13: Analysis of standards containing 180 ng toluene.

Std 180 ng Repeat	RT / min	Peak Area / counts	Calculated Mass / ng	Accuracy / %
1	4.355	833195686	177	98.3
2	4.355	865314711	184	102.4
3	4.355	820040746	174	96.6
4	4.355	870729868	186	103.1
5	4.355	873768540	186	103.5

Table 4.14: Analysis of standards containing 180 ng ethylbenzene.

Std 180 ng Repeat	RT / min	Peak Area / counts	Calculated Mass / ng	Accuracy / %
1	6.129	1002930852	183	101.7
2	6.129	993382183	181	100.6
3	6.128	974863858	178	98.6
4	6.13	1022913803	187	103.8
5	6.13	1013898050	185	102.9

Table 4.15: Analysis of standards containing 180 ng cumene.

Std 180 ng Repeat	RT / min	Peak Area / counts	Calculated Mass / ng	Accuracy / %
1	7.973	1107143566	189	105.3
2	7.973	1072434240	183	101.7
3	7.972	1069474253	182	101.4
4	7.974	1114997807	191	106.1
5	7.971	1096813550	188	104.2

Table 4.16: Analysis of standards containing 180 ng dichlorobenzene.

Std 180 ng Repeat	RT / min	Peak Area / counts	Calculated Mass / ng	Accuracy / %
1	11.412	921562671	187	103.6
2	11.412	888261104	179	99.6
3	11.41	867049956	175	97.1
4	11.413	904239539	183	101.6
5	11.41	922030040	187	103.7

Table 4.17: Variation between replicates for each VOC.

VOC	Average Accuracy / %	Std Dev	%RSD
Toluene	100.79	3.13	3.10
Ethylbenzene	101.52	2.02	1.99
Cumene	103.71	2.10	2.03
Dichlorobenzene	101.12	2.81	2.78

The % relative standard deviation (RSD) values obtained across the peak areas for each VOC were all under 4 % which demonstrated that the peak area obtained for each analyte did not vary significantly with each Tenax TA calibrant tube analysed. This illustrates good repeatability and precision of both the sampling method using Tenax tubes and the TDU-GC-MS method for analysis, thereby giving confidence in the results obtained from further studies.

4.3.3 Dynamic sampling from atmospheric chamber

4.3.3.1 Comparison of VOC masses trapped on different sorbents

The permeation chamber was set to generate an atmosphere containing approximately 2.8, 1.5, 1.3 and 0.5 ppm of toluene, ethylbenzene, cumene and dichlorobenzene respectively. The polluted chamber environment was then sampled at 100 cm^3 min^{-1} for 1 min and the theoretical masses of each analyte expected to be trapped in the sample of air were 1071, 631, 610 and 288 ng, respectively. Experiments were conducted where the VOCs were trapped on

3 sampling tubes of each sorbent (Tenax TA, MWD MCM-41 and SBA-15) and the masses trapped were determined by TDU-GC-MS.

Sampling 100 cm^3 of air from the atmospheric chamber failed to trap a quantifiable amount of dichlorobenzene regardless of the sorbent used. Therefore, the results only record the masses of toluene, ethylbenzene and cumene trapped by each sorbent which are shown in Tables 4.18 – 4.20.

Table 4.18: VOC masses trapped on Tenax TA (3 replicates).

		VOC		
		Toluene	Ethylbenzene	Cumene
Mass of VOC Trapped / ng	**Sample 1**	1162	251	144
	Sample 2	1189	266	156
	Sample 3	1134	263	150
Average Mass Trapped / ng		1162	260	150
Standard Deviation		27.5	7.9	6.0
% RSD		2.4	3.1	4.0

Table 4.19: VOC masses trapped on MWD MCM-41 (3 replicates).

		VOC		
		Toluene	Ethylbenzene	Cumene
Mass of VOC Trapped / ng	**Sample 1**	744	163	92
	Sample 2	773	168	91
	Sample 3	673	144	81
Average Mass Trapped / ng		730	158	88
Standard Deviation		51.4	12.7	6.1
% RSD		7.0	8.0	6.9

Table 4.20: VOC masses trapped on SBA-15 (3 replicates).

		VOC		
		Toluene	Ethylbenzene	Cumene
Mass of VOC Trapped / ng	**Sample 1**	1257	309	153
	Sample 2	1245	293	157
	Sample 3	1210	282	137
Average Mass Trapped / ng		1237	295	149
Standard Deviation		24.4	13.6	10.6
% RSD		2.0	4.6	7.1

From Tables 4.18 – 4.20, it can be seen that the % RSD values for each VOC trapped on the three sorbents were all below 9 %, indicating that repeatable results were achieved independent of the sorbent used. Tenax TA exhibited the highest precision for VOC trapping with the % RSD values for all VOCs below 5 %.

It was noted that the masses of VOCs trapped on MWD MCM-41 were significantly lower than the masses trapped by Tenax TA and SBA-15. The higher masses trapped by SBA-15 compared to MWD MCM-41 was perhaps due to the bimodal pore system in this material.[203] The high performance of SBA-15 is likely derived from the intrinsic pore connection between long one dimensional mesopore channels and complementary micropores. A pore network of this nature leads to the strong adsorption of VOCs by the micropores and, moreover, results in additional diffusivity of the adsorbed VOCs through the mesopores. Micropores are responsible for the adsorption of gas molecules at low concentrations due to the overlap of attractive forces from opposing pore walls.

In all experiments the masses of VOCs trapped, with the mass of toluene trapped on Tenax TA and SBA-15 being the exception, were lower than the theoretically expected values. This was thought to be a result of leaks in the system or loss of VOCs into the plastic walls or tubing, through swelling of the polymers, causing the differences observed between theoretically determined and experimentally measured values. Therefore, the concentrations generated in the chamber could not be determined theoretically but were determined experimentally.

A possible explanation for the failure of the sorbents to trap dichlorobenzene, apart from its significantly lower initial concentration in the chamber, may lie in the molecular differences

between the aromatic VOC structures. The vapour adsorption of the aromatic VOCs by silica occurs through the weak π – electron system hydrogen bonding with silanols on the silica surface.[209] The presence of substituents on the aromatic ring can effect this interaction. Chlorine as a result of being substantially more electronegative than carbon, deactivates the aromatic ring by withdrawing electron density away from the π - system. The presence of two Cl atoms on dichlorobenzene would, thereby, significantly weaken the compounds interaction with the sorbent causing it to pass through un-adsorbed. Toluene, on the other hand is an example of an activated aromatic ring whereby electrons have been donated into the ring system by the attached alkyl group, it could then be postulated that toluene would adsorb onto the silica surface more strongly than dichlorobenzene.

4.3.3.2 Dynamic adsorption capacity of sorbents - Breakthrough

Breakthrough is used to assess the dynamic performance of a sorbent for, in this study, VOC adsorption. It is known that sorbents have a limited capacity for adsorption of a given analyte and that once this capacity is reached the analyte will pass through the sorbent un-adsorbed. This is commonly referred to as breakthrough and can be identified when the concentration of analyte in the outlet stream is at least 5 % of that in the inlet stream. The dynamic adsorption capacity of each sorbent was examined as outlined in Section 4.2.3.3. Two sampling tubes were connected in series with the first tube attached to a sampling port on the atmospheric chamber and the second was attached to a sampling pump. Contaminated air was drawn through the tubes at a constant flow rate of 100 cm^3 min^{-1} for extended periods of time and only the VOCs trapped on tube 2 were analysed. Tube 1 was not analysed as the high VOC concentrations present would have saturated the GC-MS. Instead, sampling using each sorbent was performed for 1 min (n = 3) to obtain an M_1 value from which the expected VOC mass, M_E, for extended sampling times could be calculated. Tables 4.21 – 4.23 outline the results of the toluene breakthrough experiments for the three sorbents (Tenax TA, MWD MCM-41 or SBA-15). The corresponding % toluene breakthrough plots for each sorbent are shown in Figure 4.9 where 5 % breakthrough is indicated with a red line.

Table 4.21: Breakthrough of toluene on Tenax TA.

Sampling Time / min	Volume of Air / dm^3	Mass Expected, M_E / ng	Calculated Mass of Toluene / ng	% VOCs on Tube 2
1	0.1	1162	0	0.00
2	0.2	2323	0	0.00
5	0.5	5808	0	0.00
7	0.7	8131	0	0.00
10	1	11616	35	0.30
15	1.5	17424	163	0.93
17	1.7	19748	805	4.08
20	2	23233	1437	6.18

Table 4.22: Breakthrough of toluene on MWD MCM-41.

Sampling Time / min	Volume of Air / dm^3	Mass Expected, M_E / ng	Calculated Mass of Toluene / ng	% VOCs on Tube 2
1	0.1	730	0	0.00
2	0.2	1460	0	0.00
5	0.5	3649	0	0.00
7	0.7	5109	14	0.27
10	1	7298	78	1.07
12	1.2	8758	190	2.17
15	1.5	10947	861	7.86

Table 4.23: Breakthrough of toluene on SBA-15.

Sampling Time / min	Volume of Air / dm^3	Mass Expected, M_E / ng	Calculated Mass of Toluene / ng	% VOCs on Tube 2
1	0.1	1237	0	0.00
2	0.2	2475	0	0.00
5	0.5	6187	0	0.00
7	0.7	8661	0	0.00
10	1	12373	0	0.00
15	1.5	18560	93	0.50
17	1.7	21375	1406	6.58
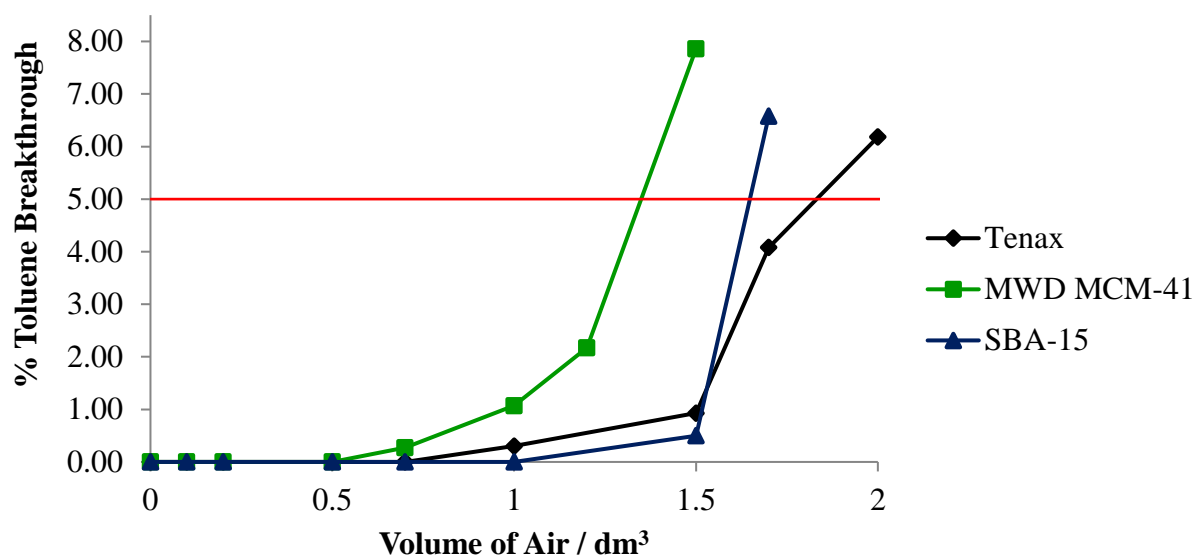
Figure 4.9: Breakthrough of toluene on different sorbent types.

From Figure 4.9, Tenax TA was shown to have the greatest breakthrough volume for toluene, followed by SBA-15 and then MWD MCM-41. The results indicated that at a fixed sampling flow rate of 100 cm^3 min^{-1} and with a set concentration of VOCs, Tenax TA had the ability to sample the largest volume of contaminated air.

4.3.3.3 Calculation of sorbent capacities

To fully assess the dynamic performance of sorbents for the adsorption of VOCs, in addition to examining of breakthrough volumes, it was important to examine the masses of VOCs retained by each sorbent when breakthrough occurred and hence consider the concentration (mass trapped / air volume) of VOCs sampled. (See Table 4.24).

Table 4.24: Comparison of sorbent performance for VOC dynamic adsorption.

Adsorbent	Air Volume at breakthrough / dm^3	Mass trapped at breakthrough / ng	Mass trapped / Air Volume / ng cm^{-3}
Tenax	1.83	21258	11.6
MWD MCM-41	1.35	9852	7.3
SBA-15	1.65	20747	12.5

It was noted that Tenax TA trapped the highest mass of toluene (21258 ng) before breakthrough occurred, implying that Tenax TA had the highest capacity for toluene compared to SBA-15 and MWD MCM-41. A similar performance was observed for SBA-15 which trapped a toluene mass only slightly lower (20747 ng) than that of Tenax TA. When the concentration of VOC sampled at breakthrough was taken into account, SBA-15 showed the best dynamic adsorption capacity. It would, therefore, appear that the silicate sorbent SBA-15 performed better than the commercially available material for the VOCs examined in this study. The enhanced performance of SBA-15 in comparison to the other silica material, MWD MCM-41, is perhaps due to the bimodal pore system found in SBA-15; the presence of micropores in the pore network providing additional diffusivity of the adsorbed VOCs through the mesopores. Another possibility is a direct result of SBA-15 possessing a larger average pore size (5.9 nm) than MWD MCM-41 (3.4 nm), thereby, facilitating access of the bulky VOC molecules into the pores.

4.4 Conclusion

The results obtained during this research are of significant importance to the investigation that follows, without which the study into the process of photocatalytic oxidation as an alternative VOC abatement technique (see Chapter 5) could not proceed.

This work demonstrated the successful generation of a steady stream of contaminated air for the subsequent dynamic sampling from an atmospheric chamber. This confirmed the stability of the in-house prepared permeation devices and the ability to produce stable streams of contaminated air using the exposure chamber system; both highly important and necessary outcomes that ensure the sampling system is robust enough for subsequent PCO studies. The VOC concentrations produced inside the chamber were 2.8, 1.4, 1.2 and 0.4 ppm for toluene, ethylbenzene, cumene and dichlorobenzene respectively. These sub ppm VOC concentrations make both the sorbent and subsequent photocatalytic oxidation investigations applicable to true indoor air environments as they are at the low level commonly found.

Direct injection of VOCs onto Tenax TA tubes was shown to be a suitable method for producing calibrant tubes as indicated by the linearity of the standard regression lines. The

calibration method was proved to be accurate, precise and reproducible. This gives confidence in the results obtained from the sample analysis and for the continued use of the sampling and TDU-GC-MS method in PCO experiments.

Breakthrough experiments were conducted to assess the efficiency of mesoporous materials as sorbents in comparison to commercially available Tenax TA. Tenax TA was shown to sample the highest volume of air and trap the highest mass of toluene at breakthrough (21258 ng). However, it was mesoporous silicate, SBA-15, which proved to be the best performing sorbent with regards to dynamic adsorption capacity; trapping the highest mass of toluene per unit volume of air (12.5 ng cm^{-3}). This is possibly as a result of the bimodal nature of its pores. Tenax TA was shown to have a slightly lower performance (11.6 ng cm^{-3}) and MCM-41 considerably lower (7.3 ng cm^{-3}). MWD MCM-41 proved to be the weakest performing sorbent for the adsorption of VOCs. Additional work could be carried out to make use of the increased silanol groups in this MCM-41 material by introducing functional groups that may increase the interaction of the material with the aromatic VOCs. One way would be to introduce phenyl groups into the pores, thereby increasing interaction via overlapping of the delocalised π systems. The results obtained in this section of the investigation allow the best performing sorbents to be matched to specific sampling situations. In the case of a sorbent favourable for use as a scavenger to reduce the concentration of indoor air VOCs, then SBA-15 should be employed. SBA-15 was shown to have the highest dynamic adsorption capacity of the three sorbents investigated. Although SBA-15 has not been used to calibrate VOC concentrations, it would be useful for removal of VOCs from air where the results do not require quantification. A further study could be to investigate the calibration of the silica sorbent tubes for VOC quantification. However, this is believed to be difficult as spiking of methanolic calibrant standard solutions onto the silica material has the potential to result in adsorption competition between the analyte molecules and methanol with the silica surface. If quantitative air sampling is required and accurate results are to be achieved then Tenax TA should be used as the sorbent of choice in the sampling tubes. It was shown with this material that a simple, accurate and reproducible calibration method, involving spiking Tenax TA sampling tubes with methanolic solutions of VOC standards, can be achieved for the quantification of VOCs. In addition, Tenax TA was shown to have a high adsorption performance. These results indicate that Tenax TA is the most suitable sorbent for subsequent use in the PCO investigations.

5. Photocatalytic oxidation as an alternative method for VOC abatement

In the previous chapter it was shown that mesoporous silicate, SBA-15, has the highest dynamic adsorption capacity. However, SBA-15 would only be useful as a scavenger sorbent, for removal of VOCs from air where the results do not require quantification since the sorbent was not used to calibrate VOC concentrations. If quantitative air sampling is required and accurate results are to be achieved then Tenax TA, which also shown to have a high adsorption performance, should be used as the sorbent of choice. For this reason, Tenax TA has been chosen as the sorbent of choice for trapping residual VOCs and for their quantification in the following photocatalytic oxidation investigation. These traditional VOC adsorption techniques are restricted in application because of several inherent drawbacks: they fail to destroy the pollutants but merely transfer them from air to a sorbent which, after a certain concentration is reached, requires regeneration and a further treatment of the pollutants.[210] Therefore alternative abatement methods that overcome this disadvantage are of interest. In this chapter the use of photocatalytic oxidation is assessed for the removal of the same key targets as examined in Chapter 4: toluene, ethylbenzene, cumene and dichlorobenzene.

5.1 Introduction to photocatalytic oxidation

Photocatalytic oxidation (PCO) is a cost effective, more efficient and environmentally friendly technology for treating low concentration VOCs. This technique was pioneered in 1972 by Fujishima and Honda,[211] who discovered the photocatalytic decomposition of water on TiO_2 electrodes by UV light irradiation. In the subsequent three decades, PCO has received considerable attention as an alternative method for the purification of both air and water streams.[212, 213] The process involves the use of semiconductors together with UV light irradiation to degrade organic pollutants. It has been demonstrated that organics can be oxidised into products with less harmful human effects, carbon dioxide and water, under mild conditions; making PCO particularly attractive for treating indoor air VOCs.[213-215] PCO offers several additional advantages: the main oxidant required is oxygen present in the air; chemical activation is provided by UV photons allowing the reaction to proceed at low temperature and ambient pressure; potential catalysts are chemically stable, non-toxic, relatively inexpensive and active in several physical forms; and in principle, as a result of the non-selective nature of the catalyst, this technology can destroy a large variety of VOCs.

5.1.1 Band Theory[216, 217]

In any given material, there are two distinct energy bands in which electrons can exist; the valence band and the conduction band. The energy gap between valance band and conduction band is known as the band gap. The conduction properties of any material depend upon the energy band structure as shown in Figure 5.1. Electrical insulators have a large band gap between valence and conduction bands whereas in the case of conductors these bands overlap, meaning there are a large number of free electrons available for conduction even at room temperature. Semiconductors have conduction properties somewhere in between insulators and conductors and require a certain amount of energy (more than the band gap energy) to excite electrons from the valence band to conduction band.
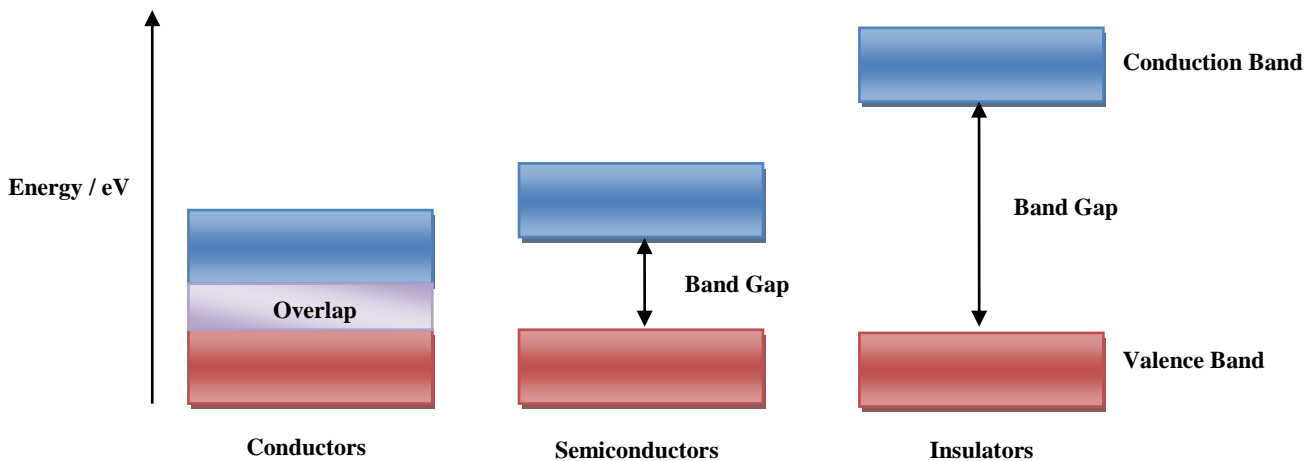
Figure 5.1: Schematic band diagrams for conductors, semiconductors and insulators.

When an electron is excited to the conduction band, the vacancy left in the valence band is known as a hole. For every electron leaving the valence band, a hole is generated and, hence, under thermal equilibrium, the number of electrons is equal to the number of holes, thus forming an electron-hole pair. Under an electric field, the equilibrium condition is disturbed and electrons move in opposite direction to that of holes, as holes can be thought of as positively charged particles. This movement of electrons in the conduction band and holes in the valence band constitutes current in a semiconductor. The electrons and holes are both known as charge carriers whereas in metals, conduction is due to electrons only. It is possible that some of the free electrons in the conduction band may combine with holes in the valence band, a process known as recombination. Recombination is undesirable as it a non-radiative process that involves an electron losing energy.

5.1.2 TiO$_2$ – The photocatalyst of choice

The use of a highly effective photocatalyst for the photocatalytic oxidation of indoor air pollutants is imperative as the VOCs of interest may be difficult to degrade, yielding undesirable intermediates which can result in catalyst deactivation.[214] An ideal photocatalyst depends strongly on the efficiency of electron-hole pair separation and the adsorption ability of organic substrates on the surface of the catalyst.[218, 219] Various semiconductors[220] such as TiO$_2$, ZnO, ZrS, CdS, MoS$_2$, Fe$_2$O$_3$ and SnO$_2$, have been found to have sufficient band gap energies for promoting photocatalytic activities and subsequently examined as photocatalysts for the degradation of organic contaminants.[221] However, TiO$_2$ has been proven to be the most efficient catalyst used in widespread environmental applications for the UV induced degradation of many organic compounds due to its favourable characteristics. It is inexpensive, non-toxic, photo-stable, chemically and biologically inert and has the ability to be supported on suitable reactor substrates. TiO$_2$ shows high photocatalytic efficiency and its strong oxidising power allows ambient temperature oxidation with the complete degradation of a broad range of pollutants.[222-224]

The photocatalytic oxidation efficiency of TiO$_2$ is affected by its crystal structure. There are two photoactive polymorphs of TiO$_2$; anatase and rutile with energy band gaps of 3.2 and 3.02 eV, respectively. The anatase form of titania is reported to be superior for the PCO application, giving the best combination of photoactivity and photostability. This is a result of the band gap and the closer energy levels of rutile being more susceptible to non-radiative processes such as recombination whereas with anatase this undesired process is less efficient.[213] For photocatalytic reactions, it is necessary to have a light source of sufficient energy, exceeding that of the TiO$_2$ band gap energy, which in the case of anatase is 3.2 eV. The minimum energy of the photon required to cause photogeneration of charge carriers corresponds to a wavelength of 388 nm. Hence, irradiation of TiO$_2$ with UV light $\leq$ 388 nm, generally in the UVA region, is required for photoactivation. In spite of research efforts over the last three decades in search of an ideal photocatalyst, titania in the anatase form continues to act as a benchmark, against which, any emerging material candidate is measured.[225]

5.1.2.1 Mechanism of titania-assisted photocatalytic degradation

The mechanism of photocatalytic oxidation of organic compounds on the TiO_2 surface involves multiple processes.[226] The initial and largely important stage in the photoreaction is the generation of electron-hole pairs in the TiO_2 particles which occurs when the catalyst surface is irradiated with light of energy greater than or equal to the band gap. An electron is promoted from the valence band to the conduction band of TiO_2, thus creating a 'hole' at the valence band edge. A hole is essentially a lack of the electron density that was localised on that orbital and is usually assigned a positive charge (h^+). The valence band hole is powerfully oxidising, whereas the conduction band electron is strongly reducing. The hole has the potential to migrate to the surface of the material and oxidise water that may be present resulting in the formation of hydroxyl radicals. Hydroxyl radicals are also very powerful oxidisers and can easily oxidise any organic species adsorbed on the TiO_2 surface, ultimately to carbon dioxide and water. In the conduction band, oxygen is rapidly reduced to form the superoxide anion which subsequently reacts with water to form another hydroxyl radical.[215] A schematic of the UV activated PCO process of VOCs using TiO_2 as a catalyst is shown in Figure 5.2.
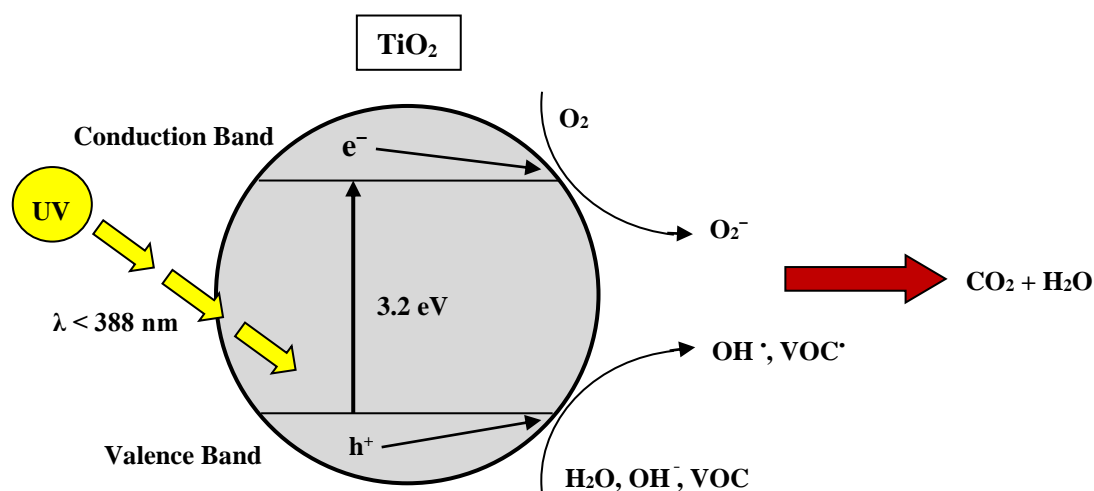
Figure 5.2: Schematic of TiO_2 UV photocatalytic oxidation process of VOCs.

The activation of TiO_2 by UV light[227] can be written as shown in Equation 5.1:

$$TiO_2 + h\nu \rightarrow h^+ + e^-$$ **Equation 5.1**

In this reaction h^+ and e^- are powerful oxidising and reductive agents respectively. The oxidative and reduction reactions are expressed in Equations 5.2 and 5.3, respectively:[226, 228]

$$\text{Oxidation reaction: } OH^- + h^+ \rightarrow OH^{\bullet} \qquad \textbf{Equation 5.2}$$

$$\text{Reduction reaction: } O_2 + e^- \rightarrow O_2^- \qquad \textbf{Equation 5.3}$$
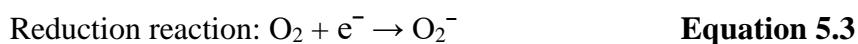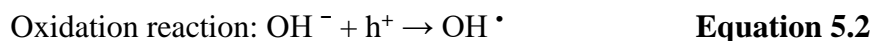
In the degradation of organic compounds, the hydroxyl radical, $OH^{\bullet}$, derived from the oxidation of adsorbed water or adsorbed OH^-, is the primary oxidant; and the presence of oxygen can prevent the re-combination of hole-electron pairs. For a complete PCO reaction, the final products are CO_2 and H_2O as shown in Equation 5.4.

$$OH^{\bullet} + \text{pollutant} + O_2 \rightarrow \text{products } (CO_2, H_2O \text{ etc.}) \qquad \textbf{Equation 5.4}$$

The requirements for efficient photocatalysis can be deduced from the electronic reactions; there should be surface bound water to allow for efficient oxidation and the water should be aerated to provide oxygen to the system. Additionally, the degradation of the pollutant by the catalyst requires for the pollutant to be adsorbed or be very close to the surface of the material, allowing reaction with the active species and, hence, the greater the surface area of the material, the more pollutant that can be adsorbed.

5.1.2.2 Surfactant templating method for synthesis of TiO₂ thin films

As previously discussed in Sections 1.3 and 1.4, the discovery of the M41S family of ordered mesoporous silica by Mobil[9] in 1992 gave rise to a new era in the synthesis of porous materials. There has since been a great deal of interest in applying this preparative route for the synthesis of mesoporous transition metal oxides such as TiO_2. It is known that for optimum photocatalytic activity of TiO_2 the material should possess high crystallinity and a large surface area would ensure maximum adsorption of pollutant organic molecules. Thus, a high surface area porous titania with controlled crystalline framework is greatly desired for photocatalytic applications. This material can be obtained via a surfactant-templated synthesis incorporating a sol-gel approach as described for the preparation of mesoporous silica.

In sol-gel processing of early transition metal alkoxides, hydrolysis and condensation reactions occur very rapidly, thereby making uniform and ultrafine products difficult to obtain. With the use of bulky, branched alkoxy groups such as isopropoxides, the hydrolysis and condensation rates can be reduced to favour the formation of small colloidal clusters, yielding a more uniform particle size. Hence titanium (IV) isopropoxide[229] is most commonly

used as a titanium precursor. The sol-gel reaction is generally performed under acidic conditions using HCl[230] which serves not only as a catalyst for the reaction but also as an electrolyte, inhibiting agglomeration of particles through electrostatic repulsion. Since the isoelectric point of TiO_2 lies at a pH of 5-7,[231] surface charges on the particles in an acidic medium help to keep discreet particles in the dispersed state. The presence of an acid catalyst promotes the hydrolysis reaction versus the condensation reaction, delaying the gelation process so that a gel is formed instead of the white precipitates that are formed in an acid-free synthesis.[232]

In the synthesis of TiO_2 thin films, block copolymer surfactants such as P123 are routinely used as templating agents[233, 234] to introduce larger pores in the resultant film.[235] It is known that the addition of a co-solvent such as ethanol into the synthesis solution favours particles with spherical and cubic phase structures, where otherwise hexagonal structures would be formed.[236, 237] Finally, and as carried out in this work, the gel produced can be coated onto support materials such as glass beads. Calcination is then commonly used at temperatures of 400 °C or greater, to remove the surfactant while transforming the TiO_2 gel into its crystalline form, thereby generating a porous TiO_2 thin film.

There has been various reported syntheses using alkoxide/alcohol/water/template mixtures under acidic conditions,[233, 238-242] each effectively yielding mesoporous titania thin films with high surface area, high crystallinity and hence good photocatalytic activity.

5.1.3 Aims and objectives

The aim of this chapter was to investigate the process of photocatalytic oxidation, using TiO_2 as a photocatalyst, as an alternative for indoor air VOC abatement.

The research investigated in Chapter 4 was necessary as a platform to ensure that there was a robust method to generate and measure dynamic flow of VOCs from the atmospheric chamber set up. It also proved that the developed TDU-GC-MS method for the quantitative analysis of VOCs was accurate and precise.

This chapter involved:

1. The preparation of TiO_2 film coated glass beads and quartz tubes.
2. Determination of the optimum TiO_2 film coating number.
3. Assessing the long-term performance of the TiO_2 photocatalyst.

5.2 Experimental

5.2.1 Materials and reagents

Titanium (IV) isopropoxide (97 %), hydrochloric acid (HCl, 37 %), absolute ethanol, ethylbenzene (99 %) and dichlorobenzene (99 %) were purchased from Sigma Aldrich. Toluene (99.5 %) was provided by Fisher Scientific. Cumene (99 %) was purchased from ACROS Organics. Pluronic P123 block copolymer was supplied by the BASF Corporation. Glass beads (600 – 800 μm) were purchased from Sigma Aldrich. Quartz tubes were prepared within Strathclyde University. Tenax TA was supplied by Markes International Limited.

5.2.2 Preparation of TiO$_2$ thin film photocatalysis tubes

Mesoporous titanium dioxide was prepared via a surfactant templated synthesis using the sol-gel approach. For the synthesis a triblock copolymer, P123, was employed as a structure directing agent and titanium (IV) isopropoxide as a Ti source. Removal of the organic template from the catalyst was carried out by calcination. In a typical synthesis, 4.2 g of titanium (IV) isoproxide was dissolved in 3 cm^3 of concentrated HCl and stirred at room temperature for 10 min. A separate solution was then prepared where 1.3 g of P123 co-polymer was dissolved, under slight heating, in 12 g of ethanol. Both solutions were then mixed and stirred for a further 15 min. Glass beads (600 – 800 μm) and quartz tubes were coated with the resulting TiO$_2$ gel and left overnight in the fridge. Both beads and tubes were then calcined at 400 °C for 10 min (heated at 25 °C min^{-1} to 400 °C and held at for 10 min). This technique generated a TiO$_2$ thin film on the surface of the support materials. The procedure was repeated daily until quartz tubes and glass beads with 1 to 5 coatings of TiO$_2$ thin film were prepared. TiO$_2$ photocatalyst tubes were subsequently produced by packing 2 g of coated glass beads into coated quartz tubes, contained within two plugs of glass wool. Catalyst-free, 'blank' tubes, with the beads and tube containing no TiO$_2$ were also prepared. Figure 5.3 shows an example of the blank tube and TiO$_2$ photocatalyst tubes, with 1 to 5 coatings of TiO$_2$ in order.
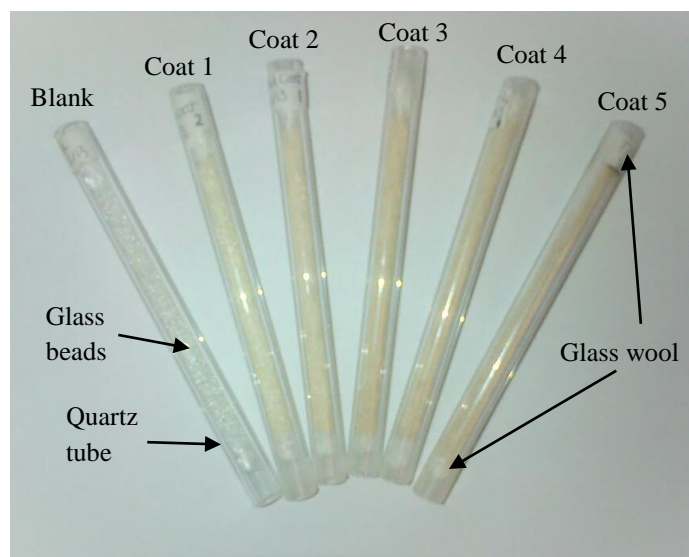
Figure 5.3: Photocatalyst tubes - blank and 1 to 5 coating of TiO$_2$.

5.2.3 Photoreactor set-up

The experimental set-up for the photocatalytic reactions, shown in Figure 5.3, consisted of a black box, inside which a TiO$_2$ photocatalyst tube was held; this was connected at one end to the atmospheric sampling chamber, where the reactant VOCs entered and at the other end was an attached Tenax TA tube which collected any unreacted VOCs and reaction intermediates. Illumination of the TiO$_2$ tubes was provided by two UV light sources: a 2 x 4 W blacklight blue, BLB, lamp (UVITEC, Cambridge, UK) and a 4 W BLB lamp (UVP Ltd, Cambridge, UK), both of which had a maximum light intensity output at 365 nm. The lamps were positioned at either side of the tube approximately 40 mm away. With the band gap of TiO$_2$ being 3.2 eV, photons with wavelengths shorter than 388 nm are required to excite the catalyst. Both BLB lamps emit photons with wavelengths in the region of 300 – 425 nm, with a primary peak at 365 nm, thereby providing sufficient energy to promote electrons from the valence to the conduction band of the TiO$_2$ particles and sustain the PCO reaction. The photocatalyst tubes and UV lamps were placed inside a black box to ensure that when closed, only the light emitted from the UV lamps was affecting the PCO reaction and also to avoid subjecting the operator to UV irradiation.

Figure 5.4: Photoreactor set-up.

5.2.4 Photocatalytic oxidation (PCO) experiments

The dynamic sampling chamber was used, under the conditions previously described in Section 4.2.1, to generate an atmosphere containing 10.7, 6.3, 6.1 and 2.9 mg m^{-3} of toluene, ethylbenzene, cumene and dichlorobenzene, respectively. The polluted atmosphere was drawn through the TiO$_2$ photocatalyst tube, which was subjected to UV irradiation. One end of the photocatalyst tube was connected to an outlet sampling port in the chamber and the other to a Tenax TA tube, which was subsequently, attached to an air SKC sampling pump. The flow rate passing through the photocatalyst tubes was calibrated to 50 cm^3 min^{-1} using a bubble meter. Prior to the PCO experiments being performed the contaminated air was allowed to achieve adsorption equilibrium with the coated catalysts for 15 min in the absence of UV illumination and also the UV lamps were switched on for 30 min to allow time for the lamps to heat up. In order to determine the initial mass of each VOC passing through the photocatalyst tubes without any reaction taking place, (M$_0$), control samples were run by drawing the contaminated air through a catalyst-free tube containing blank beads and measuring the VOCs subsequently trapped on the Tenax TA tube. Since there is the possibility of direct photolysis of some VOCs under UV irradiation, analysis of the blank

tubes was carried out with the UV lamps initially off and then on and the VOC concentrations trapped under each condition were compared.

Determination of optimum number of TiO₂ coatings

To obtain M_0 values, the chamber atmosphere was drawn through blank tubes for a sampling time of 4 min at a flow rate of 50 $cm^3\,min^{-1}$ and trapped onto a Tenax TA tube. Analysis of a blank tube was performed at the start and the end of the PCO experiments to ensure the VOC concentrations being drawn from the chamber remained steady. The blank tube was replaced with photocatalyst tubes that had been coated 1-5 times with TiO₂. Under UV irradiation contaminated air was drawn through each tube for 4 min at 50 $cm^3\,min^{-1}$ and the connected Tenax TA tube analysed to obtain the mass of each unreacted VOC, M_1. The photocatalytic efficiency of each coated TiO₂ tube was calculated, in terms of degradation percentage, for the VOCs under investigation using Equation 5.5 below.

$$Degradation\ (\%) = M_1/M_0 \times 100$$ **Equation 5.5**

The optimum number of TiO₂ coatings was chosen from the photocatalyst tube which gave the highest degradation percentage.

Photocatalyst long-term performance

To estimate the efficiency of the photocatalyst when used for extended periods of time, the chamber atmosphere was again drawn through the system at a flow rate of 50 $cm^3\,min^{-1}$. However, the sampling time was increased to 10, 30, 60 and 120 min; giving a total time of 220 min. The Tenax TA tubes were analysed for unreacted VOCs and any intermediates which may have been generated as a result of the extended use of the photocatalyst. Blank tubes were sampled for 4 min, as previously mentioned. Knowing the masses of each VOC trapped during 4 min of sampling allows the calculation of the masses expected for the extended sampling times. The procedure was repeated a few days later, allowing time for the system to cool down and re-equilibrate, with the sampling times extended further to include 4 and 6 h; giving a total time of 13 h 44 min. All Tenax TA tubes used throughout the photocatalysis experiments were analysed by TDU-GC-MS using the validated method outlined in Section 4.2.4.1.

5.3 Results and Discussion

Photocatalytic oxidation is an alternative technique used for VOC abatement which involves the use of semiconductors together with UV light irradiation to degrade organic pollutants into harmless constituents, CO_2 and water. The semiconductor used as a photocatalyst, in this investigation was TiO_2.

5.3.1 Determination of optimum number of TiO_2 coatings

Photocatalyst tubes were prepared, as described in Section 5.2.2, by coating glass beads and quartz tubes with a TiO_2 gel before being calcined, to generate a TiO_2 thin film on the surface of the support materials. This process was repeated to produce photocatalyst tubes with 1 to 5 coatings of TiO_2 film. Contaminated air was then drawn through each tube under UV light irradiation at a flow rate of 50 cm^3 min^{-1} for a sampling time of 4 min. To determine the initial mass of each VOC entering the tubes without photocatalytic reaction taking place, blank tubes, containing no TiO_2, were analysed using the same conditions. Table 5.1 records the masses of toluene passing through the blank photocatalyst tube. Table 5.2 and Figure 5.5 show the percent degradation of this toluene mass obtained using the TiO_2 film tubes, coated 1 to 5 times.

Table 5.1: Masses of toluene entering the photocatalyst tube.

Blank	Calculated Mass of Toluene / ng
1	775
2	796
Average	786

Table 5.2: % degradation of toluene using 1 – 5 coats of TiO_2 film.

Coat Number	Average Calculated Mass of Toluene / ng	% Degradation
1	450	42.7
2	296	62.3
3	177	77.5
4	91	88.4
5	46	94.1
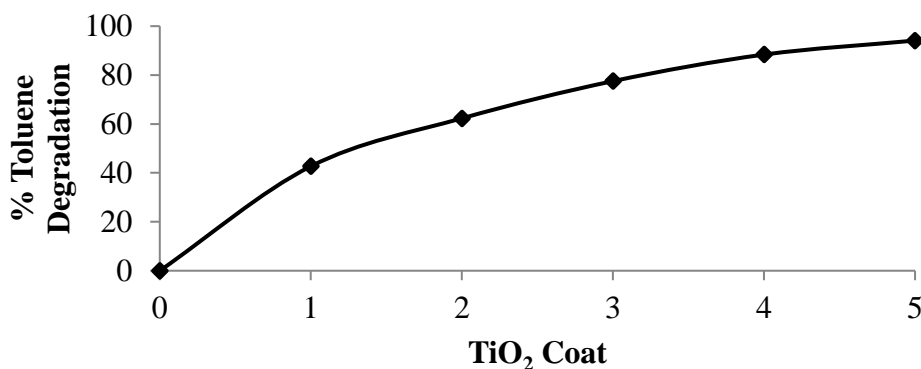
Figure 5.5: Toluene photodegradation with increasing TiO₂ film coatings.

Since there was the possibility of direct photolysis of some VOCs when they were exposed to UV irradiation, analysis was carried out using the blank tube with and without UV irradiation in order to assess the degradation of VOC due to photolysis. There was no observed change in VOC mass under UV irradiation when compared to without UV irradiation, indicating that the VOCs used in this study could not be directly decomposed by UV light. This was expected for the VOCs investigated as the maximum wavelength required for breaking a C=C bond, C-H bond and C-Cl bond are 196.1, 353.0 and 289.7 nm respectively, hence light of 365 nm is not capable of breaking the bonds in the chosen VOCs.

From Table 5.2 and Figure 5.5 it can be clearly seen that the % degradation of toluene steadily increases with each TiO₂ film coating, suggesting that photocatalytic activity was enhanced by an increase in film thickness. This result was expected and could be simply explained by an increase in film thickness meaning there was more titanium dioxide available to participate in the photocatalytic reaction.

The increase in photocatalytic activity reduced as the number of coating cycles approached 5, with the curve appearing to plateau after the 5th TiO₂ coating. This observation was thought to be a result of several factors. Photocatalytic chemical reactions mainly occur on the surface active sites of TiO₂ thin films as a consequence of TiO₂ in the interior region of the films being less accessible to reactant VOCs. Also, an increase in opacity and light scattering is observed with TiO₂ film above a certain thickness which leads to a decrease in the passage of UV irradiation through the film. Therefore, once an optimum thickness is reached the photocatalytic activity will remain constant despite additional TiO₂ film coatings. The results obtained here indicated that 5 film coatings were required for best photocatalytic activity with an average toluene degradation of 94.1 % being successfully achieved. % RSD values were

131

all under 5 % for coatings 1-4 and under 2 % for the 5th TiO$_2$ coating indicating good repeatability and precision of the degradation efficiency of the photocatalyst tubes.

As experienced with the sorbent experiments, sampling from the atmospheric chamber failed to trap a quantifiable amount of dichlorobenzene using the blank beads for 4 min at a flow rate of 50 cm^3 min^{-1}. Therefore, results are only shown for the degradation of toluene, ethylbenzene and cumene. The chromatogram shown in Figure 5.6 illustrates the decrease in toluene (T) peak area obtained with each TiO$_2$ coat applied. The peaks for ethylbenzene (EB) and cumene (C) can also be observed in this chromatogram, both of which can be seen to be 100 % degraded using photocatalysts where the TiO$_2$ film had been coated 3 times or more.
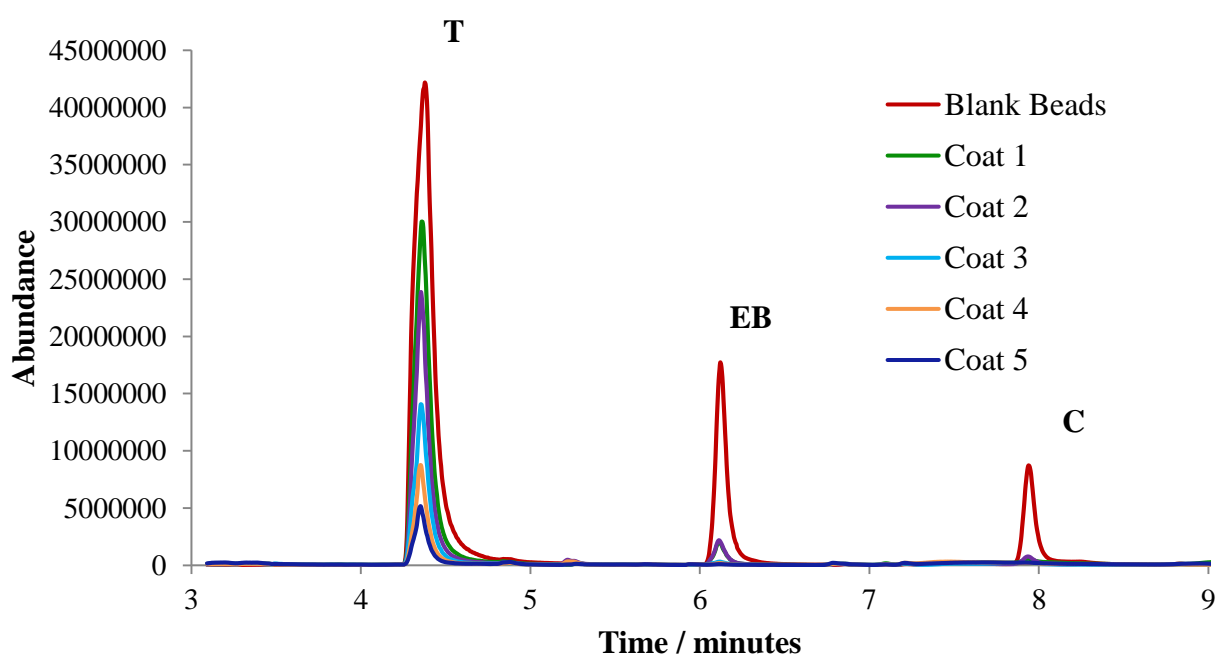
Figure 5.6: Chromatograms for VOC photodegradation using increasing coatings of TiO$_2$ film.

5.3.2 Photocatalyst long-term performance

The ability of the 5 times coated TiO$_2$ tube to maintain sufficient long-term photocatalytic activity was investigated, as described in Section 5.2.4. This involved sampling the contaminated chamber atmosphere at a flow rate of 50 cm^3 min^{-1} for extended periods of time; 10, 30, 60 or 120 min. The masses of each VOC expected to pass through the photocatalyst were calculated from the analysis of blank tubes that had been sampled for 4

min. The unreacted VOCs from the photocatalytic reactions were then compared to the expected masses and expressed as percent degradation values, the results of which are presented in Tables 5.3 – 5.5 for toluene, ethylbenzene or cumene, respectively.

Table 5.3: % degradation of toluene for increasing sampling times.

Average Mass of Toluene in Blank / ng			970
Sampling Time / min	Mass Expected / ng	Average Calculated Mass of Toluene / ng	% Degradation
10	2426	239	90.1
30	7278	214	97.1
60	14556	207	98.6
120	29112	0	100.0

Table 5.4: % degradation of ethylbenzene for increasing sampling times.

Average Mass of Ethylbenzene in Blank / ng			327
Sampling Time / min	Mass Expected / ng	Average Calculated Mass of Ethylbenzene / ng	% Degradation
10	817	47	94.2
30	2450	58	97.6
60	4900	135	97.2
120	9800	0	100.0

Table 5.5: % degradation of cumene for increasing sampling times.

Average Mass of Cumene in Blank / ng			182
Sampling Time / min	Mass Expected / ng	Average Calculated Mass of Cumene / ng	% Degradation
10	454	13	97.1
30	1363	23	98.3
60	2726	78	97.1
120	5453	0	100.0

From Tables 5.3 – 5.5 it can be seen that the photocatalytic activity of the TiO_2 tube remained high for the degradation of toluene, ethylbenzene or cumene when sampling time periods

increased. With % RSD values below 1 %, the % degradation values achieved for all VOCs at each sampling time were between 90 and 100 %, indicating the continued efficiency of the photocatalyst when continually operated for a total time of 220 min.

The chromatogram shown in Figure 5.7 illustrates the decrease in toluene (T), ethylbenzene (E) and cumene (C) peak areas for each sampling time with respect to the peak areas obtained from the 4 min sampling using blank beads. The 2 h sampling time point proved to be most efficient; 100 % degradation was obtained for the three VOCs with any small peaks present being unquantifiable. This may be a result of the photocatalyst tube requiring the previous 100 min continuous operation to fully equilibrate and activate to reach its complete photocatalytic activity potential. An additional blank was analysed after the 2 h sample to assess whether the absence of VOC peaks was merely a result of the emptying of the atmospheric chamber from which the VOC were being sampled. This was proved not to be the case; as can be seen from Figure 5.7 both blanks, before and after the 220 min of continual sampling, were of comparable peak areas therefore indicating that the result was due to the high photocatalyst performance.

It has been reported that the catalytic activity of TiO_2 is significantly affected by water vapour present in the system. If long-term catalytic activity is to be maintained then the catalyst surface requires constant rehydration with a dramatic decrease in catalytic activity observed after only a few minutes of irradiation in the absence of water vapour.[243] This is a result of UV illumination of hydroxylated TiO_2 in the presence of gaseous O_2 producing adsorbed O_2^- and surface hydroxyl radicals. The hole trapping by the hydroxyl species prevents electron-hole recombination, thus allowing the PCO reaction to take place. In this work the synthetic air containing 60 % relative humidity, appears to have been sufficient to maintain long-term photocatalytic activity.

5.3.3 Observation of degradation by-products

One additional observation to be noted is the appearance of a phenol peak (Ph) in the chromatogram of the 2 h sample which can be presumed to be an intermediate of the PCO reaction of one or more of the target VOCs. The presence of intermediates is discussed in greater detail later in the section.
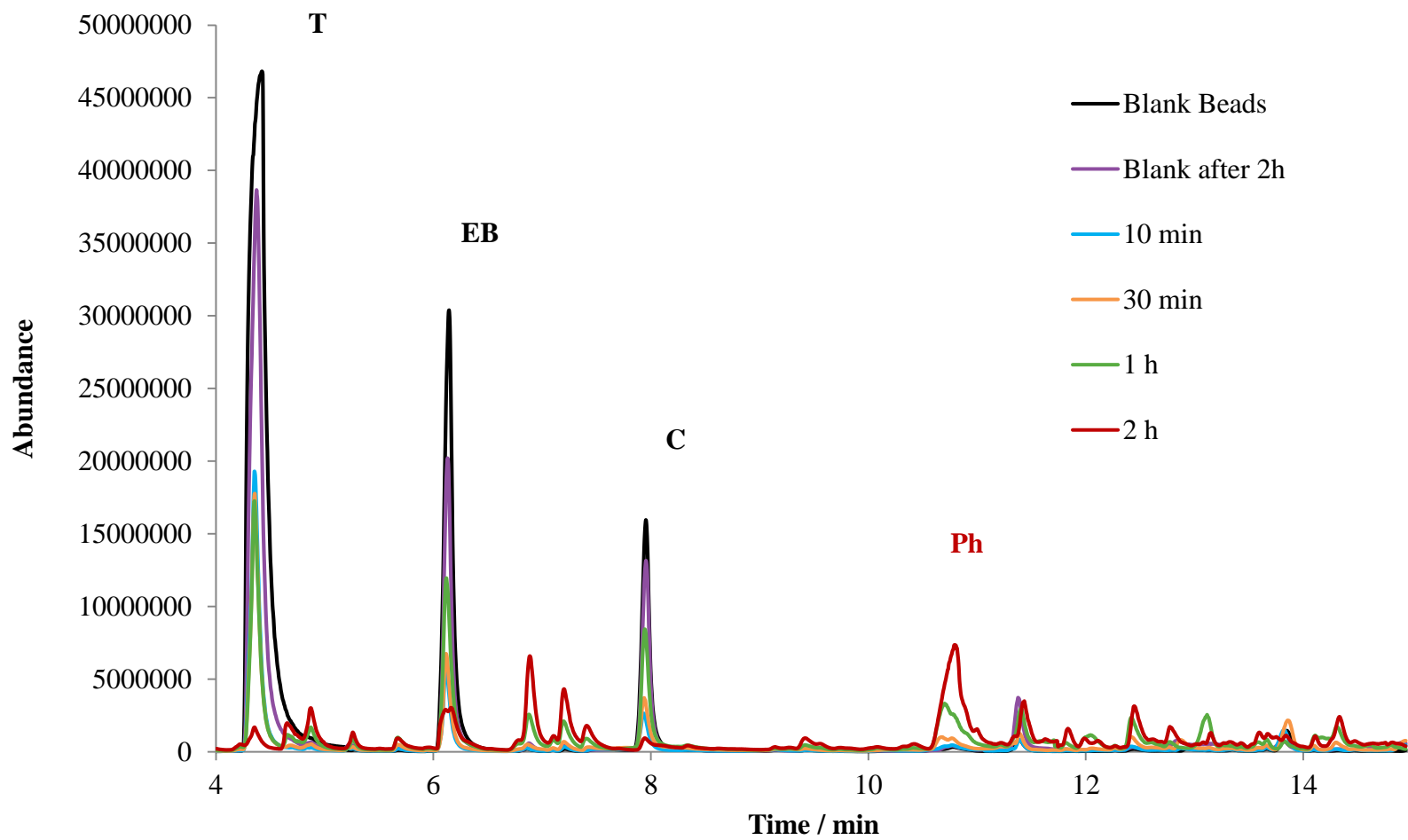
Figure 5.7: Chromatograms for VOC photodegradation.

The system was then left un-operational for a few days; allowing the photoreactor to cool down and the chamber to re-equilibrate. To reassess the photocatalyst performance, using the same photocatalyst tube, the experiment of sampling for 4, 10, 30, 60 and 120 min was repeated and the operational time extended further to include 4 h and 6 h sampling time periods. The results obtained for the long-term degradation of toluene are recorded in Table 5.6 and Figure 5.8.

Table 5.6: % degradation of toluene for increasing sampling times.

Sampling Time / min	Mass Expected / ng	Average Calculated Mass of Toluene / ng	% Degradation
4	676	103	84.7
10	1690	20	98.8
30	4349	83	98.1
60	10138	128	98.7
120	20276	44	99.8
240	40551	1596	96.1
360	60827	1732	97.2
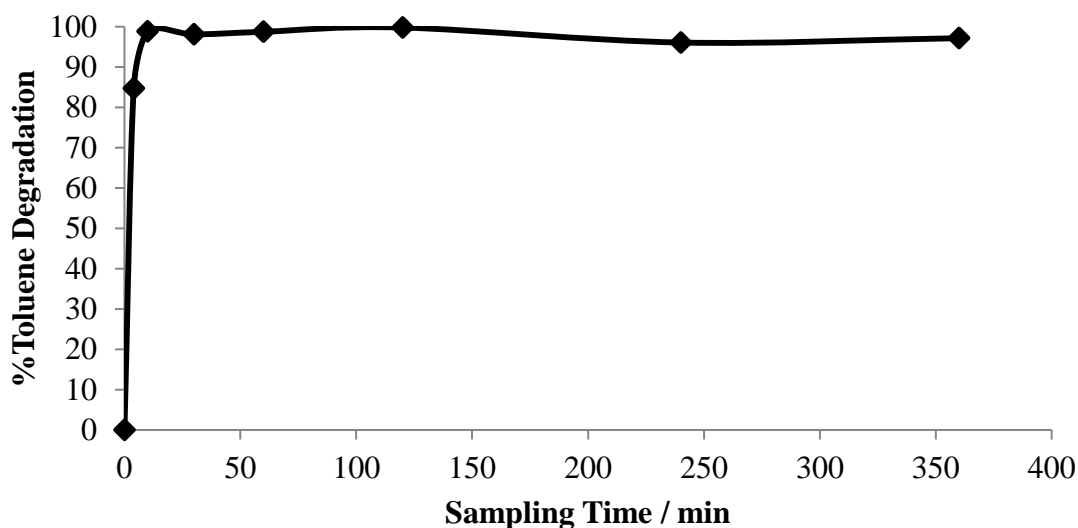
Figure 5.8: Long-term toluene degradation.

The results illustrated in Figure 5.8 and Table 5.6 further demonstrate the ability of the photocatalyst to maintain a high degradation efficiency of toluene over long-term operation. With the % RSD values less than 5 % for the 4 min timepoint and less than 2 % for 10 through to 360 mins, it can be noted that toluene degradation was lowest for the 4 min time

point. It is known that the recombination process of a photogenerated electron hole pair within the photocatalyst is very fast (picoseconds) therefore for electron transfer and hence the PCO reaction to occur the reactant VOC must be adsorbed onto the catalyst surface. This would suggest that at 4 min, insufficient time had elapsed for the adsorption of the substrates onto the TiO_2 to reach saturation and hence the degradation was lower.

The initial 84.7 % average toluene degradation at 4 min was shown to increase with time, quickly reaching a steady level of around 100 % toluene degradation within, suggesting that an operation time of as little as 10 min is required for the photocatalyst to operating at full efficiency. It was noted that a slight decrease, outside error, in photocatalytic activity was observed for the additional 4 h and 6 h time points. An explanation for this can be found by examining the chromatograms of each sampling time. Figure 5.9 shows the chromatograms of the 4 min – 2 h samples and Figure 5.10 shows the chromatograms of the 4 and 6 h samples along with an additional 4 min sample analysed after a further cool down period.
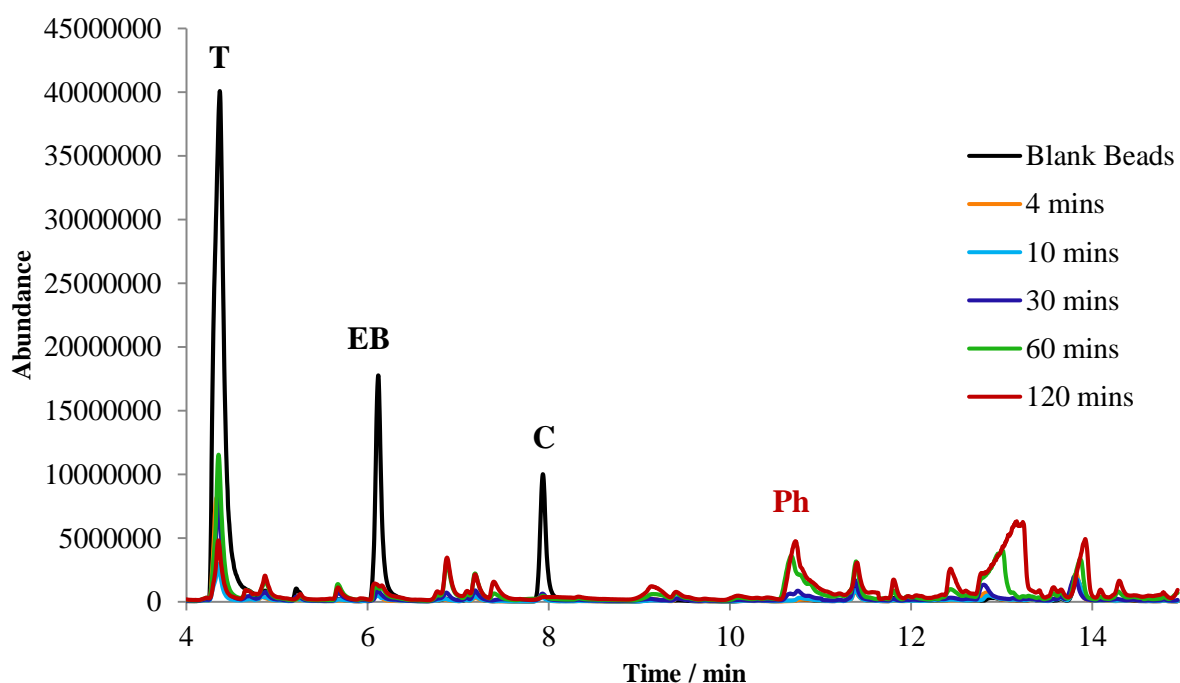
Figure 5.9: Chromatograms for VOC photodegradation 4 min to 2 h samples.
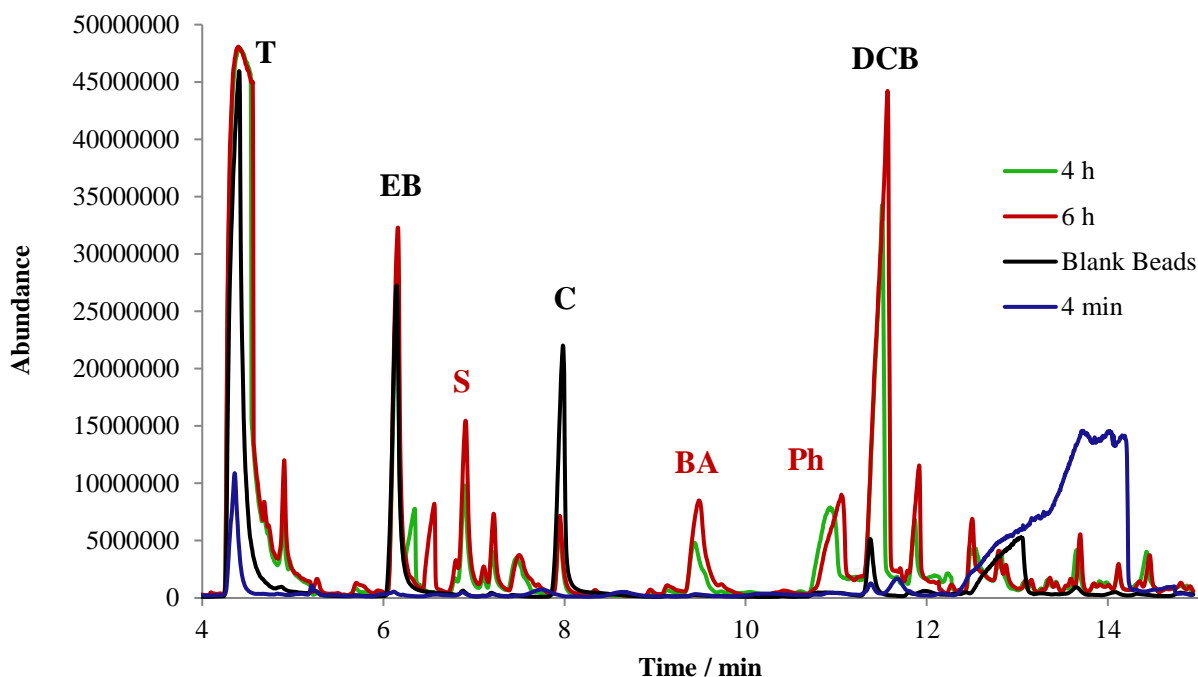
Figure 5.10: Chromatograms for VOC photodegradation 4 and 6 h samples.

Although a continuously high photodegradation performance was observed during these PCO experiments, reaction intermediates begin to appear in the 2 h sample after 3 h 44 min of continuous operation. It is well recognised that PCO reactions of VOCs proceed in a stepwise fashion with the reaction products of each step known as intermediates. These unintended intermediates can be toxic or irritating and may be less acceptable for human health and comfort than their precursors. These intermediates may also be strongly adsorbed on the surface of the photocatalyst and deteriorate its photoreactivity by blocking reaction sites.[244] This is known as photocatalyst deactivation and is a common problem experienced when the photoreaction is operational for long time periods. It is, therefore, necessary to identify the intermediates formed during the photocatalytic reaction. The use of GC-MS for VOC analysis made it possible to identify unknown intermediates using NIST software.

Figure 5.9 showing the chromatograms from the 4 min to 2 h samples appears consistent with Figure 5.7 which shows the chromatograms of the same samples obtained from the first experiment. Similar to the first experiment, reaction intermediate, phenol (Ph) is present in the 2 h sample. As the operation of the photocatalyst is continued for a further 4 h and then 6 h, a greater number of intermediates appear in the chromatograms, see Figure 5.10. The most abundant intermediates produced were identified using the NIST software and are listed in Table 5.7 with the increasing abundance of each illustrated in Figure 5.11.

Table 5.7: Intermediates produced from PCO reaction of target VOCs.

RT / min	Intermediate Compound
6.9	Styrene (S)
9.4	Benzaldehyde (BA)
11.0	Phenol (Ph)
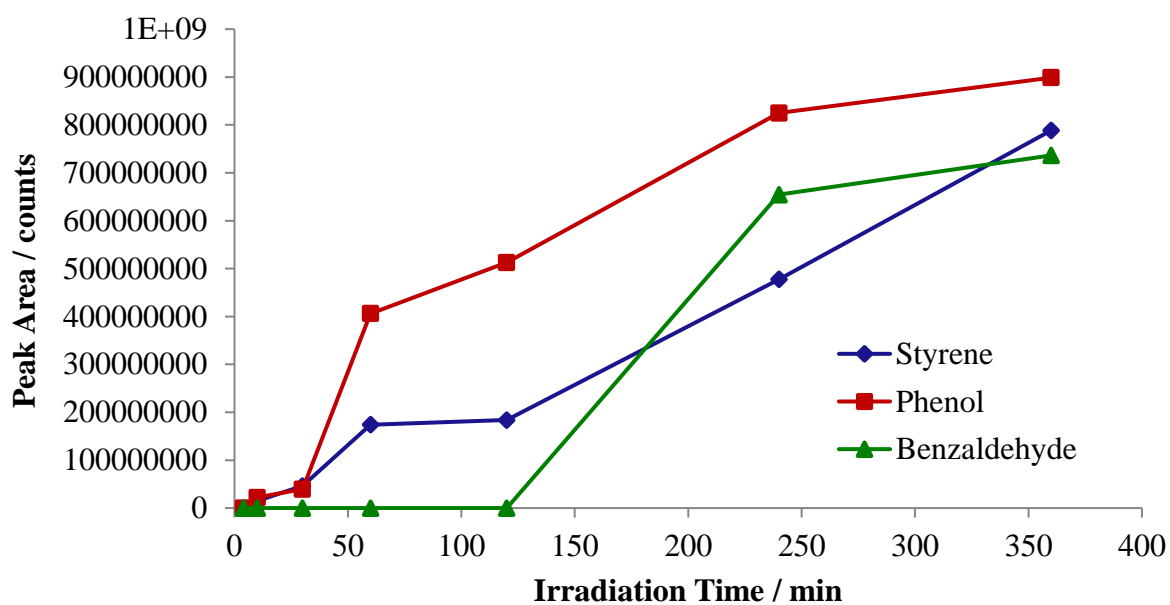
Figure 5.11: Photocatalytic oxidation intermediates.

As a result of the mix of VOCs present in the chamber atmosphere being sampled (toluene, ethylbenzene, cumene and dichlorobenzene) and their similar chemical structures (shown in Figure 5.12), it is not possible to determine reaction pathways for each VOC photodegradation based on the intermediates produced as they could be a result of more than one target VOC photodegradation or from the photodegradation of another intermediate.
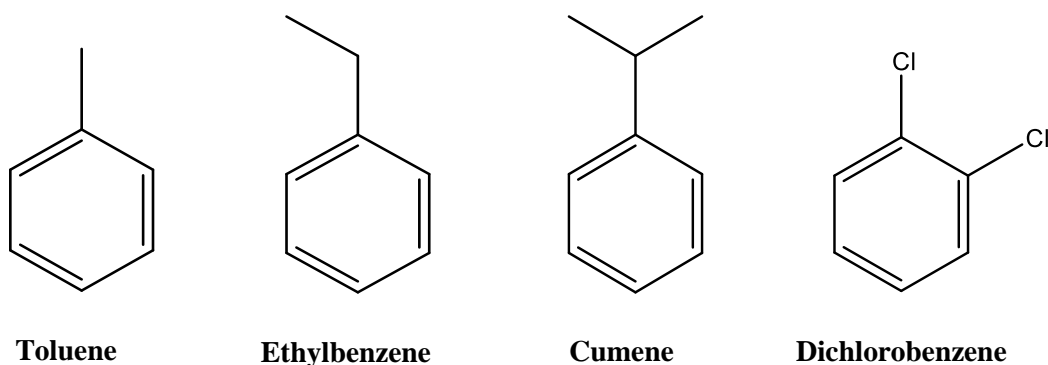
Figure 5.12: Chemical Structures of the four VOCs sampled.

However, the sources of the intermediates can be postulated. Styrene is widely produced by the catalytic dehydrogenation of ethylbenzene. Phenol is most commonly generated from the partial oxidation of cumene, however, it can also be produced from the oxidation of toluene. Benzaldehyde can be generated from the selective oxidation of styrene and the oxidation of phenol and also from the oxidation of toluene. Benzaldehyde, although being the intermediate in lowest abundance, is the most widely documented product from the photocatalytic oxidation of toluene. It has been reported that the formation of benzaldehyde during the PCO of toluene leads to the deactivation of the photocatalyst.[244-246]

To assess whether the presence of the intermediates had hindered the photocatalytic performance of the catalyst, the TiO_2 tube was removed from the system and left to cool down for 20 min and then an additional 4 min sample was analysed. As shown in Figure 5.10, the peak area of toluene was small, corresponding to a toluene degradation of 86 % and the disappearance of the intermediate peaks should also be noted. Both of these findings indicated that a simple cool down procedure of the photocatalyst tube was sufficient for regeneration of the photocatalyst. The only non-target VOC peak that was prevalent in the chromatogram could be seen over a retention time of 13 – 14 min. This peak was identified as 2-(2-butoxyethoxy)ethanol which is a common plasticiser found in plastic materials such as the tubing that connected the photocatalyst to the Tenax TA tube. It is thought that exposure to the UV light for the extensive period of time caused the plastic tubing to degrade, the plasticiser to leach out and be carried in the air stream into the Tenax tube where it was detected. If this photoreactor set up is used for further studies involving long-term operation, then alternative connecting materials should be investigated. The presence of intermediates during PCO usually indicates catalyst deactivation; however, their presence on the Tenax tube and the continued high photocatalytic performance observed would suggest that they were not irreversibly adsorbed onto the catalyst surface.

As previously mentioned, dichlorobenzene was omitted from earlier results due to its small (~15 ng) and sometimes unquantifiable masses trapped when sampling using blank tubes for 4 min at 50 cm^3 min^{-1}. However, from the examination of Figure 5.10, an additional observation that should be noted is the presence of substantial dichlorobenzene (DCB) peaks in the chromatograms of later sampling times. The corresponding dichlorobenzene masses and percent degradation are recorded in Table 5.8 and illustrated in Figure 5.13.

Table 5.8: % degradation of dichlorobenzene for each sampling time period.

Sampling Time / min	Mass Expected / ng	Average Calculated Mass of Dichlorobenzene / ng	% Degradation
4	15	0	100.0
10	37	0	100.0
30	112	2	97.9
60	224	8	96.5
120	448	22	95.1
240	896	488	45.5
360	1344	831	38.2
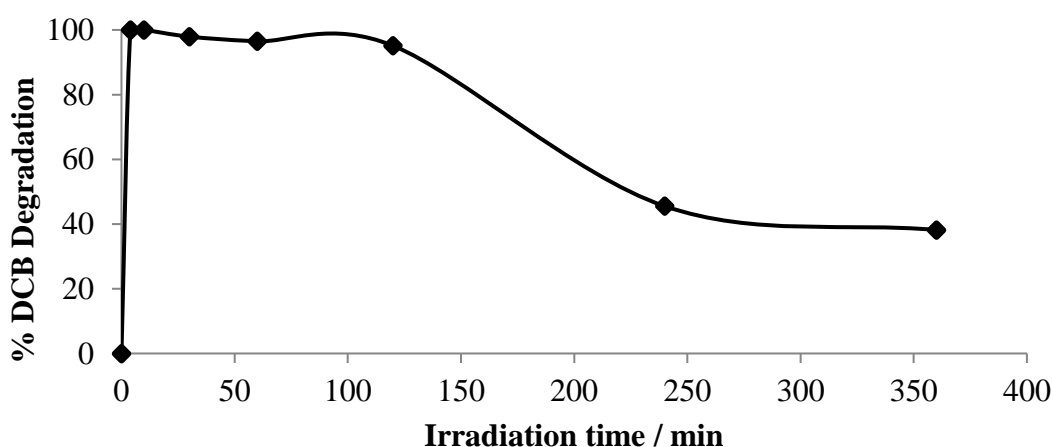
Figure 5.13: Long-term dichlorobenzene degradation.

In comparison to the other three target VOCs for which the TiO_2 photocatalyst showed excellent long-term degradation, the dichlorobenzene degradation decreases significantly with extended operational periods. Although dichlorobenzene conversion was initially 100 % up until the 10 min irradiation time point, the degradation yield dropped to an average of 38.2 % after the 6 h sampling time point. The % RSD values calculated for each timepoint increases (from less than 1 % for 4 - 10 min to less than 2 % for 30 - 120 min to around 5 and 8 % for 240 and 360 min, respectively) as dichlorobenzene degradation decreases thereby suggesting that the photocatalytic oxidation of dichlorobenzene becomes more unreliable as the reaction time increase. In addition, the dichlorobenzene degradation decreases as the intermediates produced increases. This implies that the intermediates, along with the other target VOCs, were more strongly adsorbed on the catalyst surface than dichlorobenzene and, thereby, the intermediates were deactivating the catalyst in respect to its photocatalytic ability to degrade dichlorobenzene. A possible explanation for the weaker adsorption of

dichlorobenzene on the catalyst surface and hence a lower percent degradation, may lie in the differences between the aromatic structures. As previously mentioned, the chlorine groups present on the dichlorobenzene molecule withdraw electron density away from the aromatic π–system thereby weakening the interaction of the molecule with the TiO_2 surface. This would cause dichlorobenzene to pass through the photocatalyst tube unreacted when in competition for active sites with intermediate molecules, explaining the high masses observed at longer sampling time periods.

5.4 Conclusion

The process of photocatalytic oxidation, using TiO_2 as a photocatalyst, was assessed for the degradation of indoor air VOCs. The study revealed that for optimum photocatalytic activity, the photocatalyst support material required five coatings of TiO_2 film, successfully achieving an average toluene degradation of 94.1 %. The investigation into the long-term performance of the photocatalyst showed high photocatalytic activity with respect to the degradation of toluene, ethylbenzene and cumene (96 – 100 %). However, the presence of reaction intermediates at longer operational times was found to hinder the degradation of dichlorobenzene; the degradation yield falling from 100 % to around 38 % over an operational time period of 13 h 44 min. Regeneration of the photocatalyst proved to be a simple process, achieved by cooling down the system. This feature is extremely promising for the potential industrial application of the photocatalyst tubes where, to avoid any downtime in the running of the photocatalytic process, a cooling system could be installed to ensure continuous high photocatalytic activity without the accumulation of degradation products. A second, perhaps more cost effective, option would be to have two photocatalyst tubes running in parallel; the regeneration cool down procedure occurring in one reactor tube simultaneously to the photodegradation of VOCs in the other and vice versa. Further work in this area could involve the characterisation of the TiO_2 films: X-ray diffraction (XRD) used to study the morphology of the TiO_2 crystalline phase, film thickness measured using both scanning and transmission electron microscopy (SEM, TEM) and surface area and pore sizes determined using nitrogen sorption analysis. Additionally, characterisation methods could be used to assess the adsorption of both the target VOC molecules and the intermediate molecules on the TiO_2 surface.

Part B – Water remediation

6. Adsorption as a technique for aqueous environmental remediation

6.1 Introduction

6.1.1 Pharmaceuticals in the environment

The presence of pharmaceuticals in drinking water sources is a long recognised concern,[247] however, it is in recent years that the relevance of these molecules as environmental contaminants has gained increasing attention. A wide range of pharmaceuticals have been detected in surface and ground waters[248-253] at trace levels (ng or low µg L^{-1});[254] their detection largely attributable to the advances in analytical techniques and instrumentation.[255-257] The introduction of these compounds into the environment is a consequence of a combination of manufacturing processes, improper disposal of unused drugs leading to their presence in landfill effluent[258, 259] and human excretion from both hospitals[260, 261] and private households[262, 263] leading to their presence in sewage effluent. Pharmaceutical concentrations in water bodies are not currently regulated meaning sewage treatment plants (STPs) are not designed for their removal. As a result, the treatment of sewage effluent has been shown to be inefficient in the degradation of some pharmaceuticals, causing parent drug residues and metabolites to be released into the environment via wastewater effluent.[264-268]

Pharmaceuticals are used in vast quantities, in everyday life, all over the world and as a consequence, unlike some other pollutants, they are constantly released into the environment. This means that even if they do not display persistent behaviour in water systems, their continuous introduction offsets transformation and removal rates leading to their accumulation.

The active ingredients contained within pharmaceuticals have been tailored to have very specific pharmacological effects upon biological systems. The detection of these contaminants in water bodies raises concern because of the potential to cause adverse effects to the health of humans or aquatic organisms.[269, 270] Pharmaceuticals are governed by stringent regulatory processes and require rigorous preclinical and clinical studies to assess their efficacy and safety before commercialisation, making them characterised better than other environmental contaminants. The very low concentration at which pharmaceuticals are commonly found in the environment means that the potential indirect daily exposure to pharmaceuticals in drinking water is generally more than 1000-fold below the minimum therapeutic dose (MTD), which is the lowest clinically active dosage. Current risk assessments indicate that any considerable risks to human health arising from exposure to

these very low concentrations of pharmaceuticals in drinking water are unlikely. However, there is little known about the human health effects associated with long-term, low level ingestion of pharmaceuticals through the consumption of drinking water[271-273] as well as the possible synergistic/antagonistic effects of chemical mixtures,[274-277] in addition to the increased risk to subpopulations that have a lower tolerance to certain pharmaceuticals. Although the effects on humans remain uncertain and disputable, it has been shown that trace levels of pharmaceutically active compounds can have chronic effects on the development, reproduction and behaviour of a number of animal species in aquatic environments.[257, 278-281]

The uncertainty surrounding the effects on humans should not be an excuse for allowing this group of environmental contaminants to remain in drinking water supplies. Although pharmaceutically active compounds are not currently regulated, it would be wise to apply precautionary measures in order to reduce the levels of these compounds in drinking water as much as possible. Therefore, from a conservative perspective, drinking water should be as clean as possible and thus the effective removal of pharmaceuticals from water systems it is an emerging issue.[274, 282, 283]

Re-evaluation of current adsorptive water treatment technologies and the development of potential new sorbents should be investigated to assess their capability to remove low concentrations of pharmaceutically active compounds.

6.1.2 Nitrobenzene as a priority pollutant

Nitrobenzene is widely used in industry, mainly during the production of aniline. It is also used as an intermediate in the preparation of explosives, pesticides and dyes.[284-286] The presence of nitrobenzene in surface and ground waters has long been recognised as a serious environmental issue.[287]

As a result of its hazardous carcinogenic effects on humans, as well as its bio-toxicity and persistent behaviour in the environment,[288, 289] nitrobenzene is regarded as a "pollutant of main concern" by environmental protection agencies (EPA) in many countries and has been classified as a priority pollutant by the United States EPA.[290] The introduction of this compound into the environment is mainly a consequence of oil spills, industrial and municipal discharges.[291] Owing to the electron-deficient character of the nitro-group, mineralisation of nitrobenzene by microorganisms is prevented. Therefore, conventional

biological treatment processes have been shown to be inefficient in the degradation of nitrobenzene,[292, 293] causing parent molecule residues and metabolites to be released into the surrounding aquatic environment via wastewater effluent.[294] The abatement of nitrobenzene in wastewaters has therefore become an important challenge.

6.1.3 Adsorption for water remediation

Adsorption using high-binding sorbents provides a simple and efficient way to eliminate contaminant substances dissolved in the aqueous phase. Due to its strong adsorption affinity and relatively low cost, activated carbon (discussed in detail in Section 4.1.3) has been commonly used as an effective adsorbent for water treatment. It has been shown to have a high adsorption capacity for pharmaceuticals.[295-303] However, because commercial activated carbons predominately consist of micropores (< 2 nm in size) with irregular shaped, closed pore structures, adsorption of large organic molecules might be greatly impeded by the size-exclusion effect. Furthermore, activated carbons are known to be susceptible to pore clogging, which can be an issue in 'real' water samples where the matrix is complex and are also known to be difficult to regenerate.[304] Aside from activated carbon, adsorption of pharmaceuticals has been studied using silica gel, alumina[305], amberlite[306] and polymer resins.[307]

Mesoporous silica such as MCM-41 and SBA-15 could prove to be a promising adsorbent owing to its uniform ordered structure, high pore volume and high surface area. Bui et al have investigated the use of SBA-15[308] and functionalised SBA-15[309, 310] as adsorbents for the removal of pharmaceuticals in aqueous solutions as well as examining the influence of water characteristics such as ionic strength, the presence of anions, cations and natural organic matter (NOM)[311]. The removal of pharmaceuticals from aqueous solutions have also been investigated using magnetic MCM-48[312], Ni grafted MCM-41[313] and functionalised hexagonal mesoporous silica.[314]

6.1.4 Aims and objectives

The use of silica materials for the removal of pharmaceuticals or nitrobenzene from water has not been explored in detail in the literature and in spite of the extensive use of activated carbon for adsorption applications, the specific mechanisms by which the adsorption of these target contaminants takes place on both of these materials are still ambiguous. This study details the examination of 4 sorbent types (7 different materials) for their effectiveness to remove target contaminants, a mixture of four selected pharmaceutically active compounds or nitrobenzene, at ug mL^{-1} concentrations from water. The materials investigated were powdered activated carbon (PAC); silica materials, As-syn MCM-41 and Calc MCM-41; bioinspired silica materials, As-syn Bio-Si and Calc Bio-Si; and iron incorporated bioinspired silica, Fe As-syn Bio-Si and Calc Fe Bio-Si. The four selected pharmaceuticals were; acetaminophen (Ace), caffeine (Caff), carbamazepine (Carb) and sulfamethoxazole (Sulf). A full assessment of these sorbents performance was undertaken to provide a comprehensive understanding of the processes involved in adsorption from aqueous solution. This involved investigating the effect that solution conditions such as pH will have on the sorbent performance. For the adsorption of pharmaceutical target compounds by PAC and As-syn MCM-41, additional experiments were conducted to examine parameters such as the adsorption kinetics, to determine the mechanism and rate-limiting step of adsorption, and adsorption isotherms, to evaluate the sorbent adsorption capacity.

6.2 Adsorption theory

6.2.1 Liquid-solid adsorption

Adsorption is defined as a process where one or more solutes accumulate at the surface with which they are in contact. The term adsorbate is used to describe a chemical substance transferred from the liquid phase to the solid one during adsorption and an adsorbent is a solid phase accumulating the adsorbate. Depending on the properties of the species involved in the adsorption, the process mechanism can be generally classified into two fundamental types; physisorption and chemisorption.

Some general features which are useful in distinguishing between physisorption and chemisorption are given in Table 6.1.

Table 6.1: General Characteristics of Physisorption and Chemisorption[315-317]

Physisorption	Chemisorption
Low heat of adsorption	High heat of adsorption
Non-specific	Highly specific
Monolayer or multilayer adsorption	Monolayer adsorption only
No dissociation of adsorbed species	May involve dissociation
No electron transfer, although polarization of sorbate may occur	Electron transfer leading to the bond formation between sorbate and surface
Rapid, reversible	May be slow and reversible only at high temperatures

Physisorption involves relatively weak intermolecular forces, such as van der Waals forces, hydrogen bonding and hydrophobic interactions. This is a non-specific weak interaction between adsorbed molecules and a solid surface. In this interaction, the adsorbed molecules are not fixed to the specific sites of the adsorbent and can move over the surface. In chemisorption, molecules adhere to the surface due to the formation of chemical, usually covalent, bonds between adsorbed molecules and a solid surface.

The adsorption of solutes on solid/liquid interface depends on many factors, such as:

- physico-chemical properties of the solid surface (porosity, surface area, presence or absences of charged or non-polar groups);
- the nature of the solute (pK_a, hydrophobicity, molecular size);
- properties of the liquid phase (pH, salt concentration, temperature, presence of the competitive solute);
- complexation in the liquid phase.

Adsorption processes are being increasingly used to perform bulk separation or purification at an industrial level. A proper understanding of the adsorption process and design of adsorption equipment demands knowledge of adsorption kinetics and equilibrium isotherms. The first determines the rate of adsorption and the latter determines the adsorption capacity.

6.2.2 Kinetic sorption mechanisms

Sorption kinetics are influenced by sorption reactions and the mass transfer steps that govern the transfer of solutes from the bulk of the solution to the sorption sites on the surface and inside adsorbent particles, i.e. external and intraparticle diffusion.

In turn, these mechanisms depend on the physical form of the sorbent, its intrinsic structure, the nature of the adsorbate and the solution as well as the process conditions (temperature and pH). By measuring the rate of change of the adsorbed mass with time, it is possible to determine the kinetic parameters and identify the rate-controlling mechanisms for the adsorption process using simplified models, the most widely used of which are the pseudo first-order, pseudo second-order and the intra-particle diffusion model.

6.2.2.1 Pseudo first-order model

A linear form of pseudo first-order model[318] is given as:

$$ln(q_e - q_t) = \frac{k_1}{2.303}t - lnq_e \qquad \textbf{Equation 6.1}$$

where q_e and q_t are the adsorption capacity (mg g^{-1}) at equilibrium and time t (min), respectively, and k_1 is the pseudo-first order rate constant (1 min^{-1}).

A linear plot of $ln(q_e - q_t)$ versus t allows k_1 and q_e to be determined from the slope and intercept of the plot, respectively.

6.2.2.2 Pseudo second-order model

In this model,[319] the rate limiting step is the surface adsorption that involves chemisorption, where the removal from a solution is due to physico-chemical interactions between two phases. The pseudo second-order adsorption kinetic rate equation is expressed as:

$$\left(\frac{t}{q_t}\right) = \frac{1}{k_2 q_e^2} + \frac{1}{q_e}t \qquad \textbf{Equation 6.2}$$

where the equilibrium adsorption capacity (q_e) and the second-order rate constant k_2 (g mg^{-1} min^{-1}) can be determined from the slope and intercept of plot t / q_t versus t.

6.2.2.3 Intraparticle diffusion model

A detailed understanding of adsorption mechanisms facilitates a determination of the rate-limiting step, which can in turn be used to optimise the design of adsorbents and adsorption conditions. The Weber-Morris[320] intraparticle diffusion model has often been used to determine if intraparticle diffusion is the rate-limiting step.

The intraparticle diffusion model can be expressed by the following equation:

$$q_t = k_{id}t^{1/2} + C \qquad\qquad \textbf{Equation 6.3}$$

where k_{id} is the intra-particle diffusion rate constant (mg g^{-1} min$^{-1/2}$). According to Weber and Morris,[320] if intraparticle diffusion is the sole rate-limiting step in the adsorption process, the graph of q_t versus $t^{1/2}$ should yield a straight line passing through the origin. However, failure of the plot to pass through the origin indicates the presence of boundary layer diffusion, represented by the intercept C. The larger the intercept value, the greater the contribution of the surface diffusion in the rate controlling step.[321]

6.2.3 Adsorption equilibrium

Adsorption is usually described by isotherms which show how much solute can be adsorbed at a given temperature. An adsorption isotherm relates the concentration of solute on the surface of the adsorbent to the concentration of the solute in the fluid with which the adsorbent is in contact. These values are usually determined experimentally, but there are also models to predict them, both for single and multi-component adsorption.

6.2.3.1 The Langmuir isotherm

The Langmuir model is based on a series of assumptions,[322, 323] these being:

i) The adsorbent has a completely uniform, homogenous surface with a series of equivalent adsorbent sites.

ii) Molecules adsorb at fixed sites, are immobile and do not migrate over the surface.

iii) Each site can accommodate only one molecule; all adsorption occurs through the same mechanism and at the point of adsorption saturation only a monolayer is formed.

iv) There are no interactions between adjacent adsorbate molecules.

The Langmuir isotherm is an empirical isotherm derived from a proposed kinetic mechanism and can be expressed by the linearised form:

$$\frac{C_e}{q_e} = \left(\frac{1}{q_m}\right) C_e + \left(\frac{1}{q_m b}\right)$$
Equation 6.4

where q_e (mg g^{-1}) and C_e (mg L^{-1}) are the equilibrium concentrations of the analyte adsorbed by the sorbent and remaining in solution, respectively. The linear plot of specific adsorption (C_e/q_e) against equilibrium concentration allows the Langmuir constants, q_m and b to be determined from the slope and intercept, respectively. q_m (mg g^{-1}) is the maximum monolayer capacity and b (L mg^{-1}) is a constant relating to the adsorption affinity of the binding sites.

To predict the favourability of an adsorption system, the Langmuir equation can be expressed in terms of a dimensionless separation factor (R_L) by using the Langmuir constant b and the lowest initial analyte concentration, C_0.

$$R_L = \frac{1}{1 + C_0 b}$$
Equation 6.5

The value of R_L indicates the shape of the isotherm to be either unfavourable ($R_L > 1$), linear ($R_L = 1$), favourable ($0 < R_L < 1$) or irreversible ($R_L = 0$).[324-326]

6.2.3.2 The Freundlich isotherm

The Freundlich equation is one of the earliest empirical equations used to describe equilibrium data. This model can be applied to non-ideal sorption. It often represents an initial surface adsorption followed by a condensation effect resulting from extremely strong solute-solute interactions. The Freundlich equation does not consider all sites in the adsorbent surface to be equal and can be employed to describe heterogeneous systems. Furthermore, it is assumed that, once the surface is covered, additional adsorbed species can still be accommodated. In other words, multilayer adsorption is predicted by this equation.

The Freundlich equation can be expressed in its linear form:

$$\ln q_e = \left(\frac{1}{n}\right) \ln C_e + \ln K_f \qquad \textbf{Equation 6.6}$$

where K_f (mg g^{-1}) and n (L mg^{-1}) are the Freundlich constants which are related to the sorption capacity and intensity, respectively and can be calculated from the slope and intercept of the plot of $\ln q_e$ against $\ln C_e$.

Larger values of n (smaller values of 1/n) imply stronger interactions between the sorbent and the analyte molecules while 1/n = 1 indicates the linear adsorption leading to identical adsorption energies for all sites.[326, 327]

6.2.4 Evaluation of experimental data

Adsorbed mass

The adsorbed amount (mg g^{-1}) at equilibrium can be determined using the following equation:

$$q_e = \frac{(C_0 - C_t)V}{W} \qquad \textbf{Equation 6.7}$$

where q_e is the mass (mg) of solute that is adsorbed onto 1 g of adsorbent at equilibrium; C_0 represents the concentration of analyte (mg mL^{-1}) initially present in solution; C_t is the

concentration of such analyte (mg mL^{-1}) at a time, t; V represents the volume of solution (mL); and W is the mass of sorbent (g) kept in contact with the solution.

Removal efficiency

The removal efficiency can be determined according to the following equation:

$$\% \ removal = \frac{(C_0 - C_e)}{C_0} \times 100 \qquad \textbf{Equation 6.8}$$

with C_e being the concentration of analyte in the solution (mg L^{-1}) once the equilibration time is elapsed.

6.3 Experimental

6.3.1 Materials and reagents

Acetaminophen ($\geq$ 99 %), carbamazepine ($\geq$ 99 %), caffeine (European Pharmacopoeia, Ph Eur, grade) and sulfamethoxazole (analytical standard grade) and nitrobenzene were all purchased from Sigma Aldrich. Hydrochloric acid (HCl, 37 %) and sodium hydroxide (NaOH 30%) were also purchased from Sigma Aldrich. Acetonitrile (MeCN) was of HPLC grade and supplied by Fisher Scientific (Loughborough, UK).

Commercially available Norit CA1 powdered activated carbon (PAC) was supplied by Sigma Aldrich. As-syn MCM-41 and Calc MCM-41 were synthesised as detailed in Section 3.2.1. As-syn Bio-Si and Calc BioSi were synthesised as detailed in Section 3.2.3. As-syn Fe Bio-Si and Calc Fe Bio-Si were synthesised as detailed in Section 3.2.4.

Nitrogen sorption isotherms were analysed using the conditions and procedure reported in Section 3.4.1

6.3.2 HPLC method development
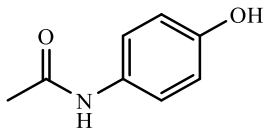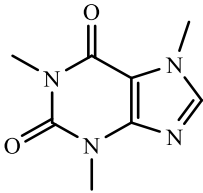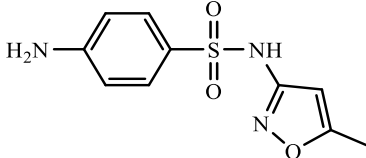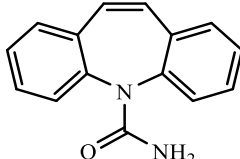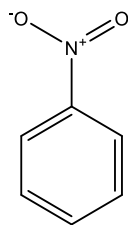
6.3.2.1 Target compounds

Four pharmaceuticals were selected in this research as targets compounds: acetaminophen (Ace), caffeine (Caff), sulfamethoxazole (Sulf) and carbamazepine (Carb). These pharmaceuticals were selected because they are widely used and detected, resilient during treatment processes, or persistent in the aqueous environment.

Nitrobenzene was selected as a target contaminant as a result of its hazardous carcinogenic effects on humans, as well as its bio-toxicity and persistent behaviour in the environment and the inefficiency of conventional treatment processes to remove it, as detailed in Section 6.1.2. Table 6.2 depicts the molecular structures of the four selected pharmaceuticals and nitrobenzene and summarises their physiochemical properties.

Table 6.2: Target pharmaceutical characteristics

Compound	Chemical Structure	Mw / g	pKa	log K_{ow}	Cs / mg/ L
Acetaminophen		151.2	9.38	0.46	1.4×10^4
Caffeine		194.2	0.5 14	-0.07	2.17×10^4
Sulfamethoxazole		253.3	(1) 1.39 (2) 5.81	0.89	600
Carbamazepine		236.3	13.94	1.89	17.7
Nitrobenzene		123.1	3.98 (0°C)	1.85	1.46×10^{-2}

6.3.2.2 UV spectra of target analytes

Solutions were scanned using a UNICAM 300 UV-Vis spectrometer. A quartz cuvette, with path length of 1 cm, was used. The spectrum was acquired, using Vision 32 computer software, over the wavelength range of 200 to 350 nm; band width of 1.5 nm; scan speed set to intelliscan and the data interval set to normal.

Aqueous solutions of the pharmaceutically active compounds: acetaminophen, caffeine, sulfamethoxazole and carbamazepine (10 μg mL^{-1}) and nitrobenzene (10 μg mL^{-1}) were prepared in 10 mL volumetric flasks. This involved an initial preparation of 1 mg mL^{-1} individual stock solutions for each analyte.

For the pharmaceutically active compounds this was carried out by accurately weighing 100 mg of each pharmaceutical into 100 mL volumetric flasks and making up to the mark with acetonitrile.

For nitrobenzene the volume of required to prepare 100 mL of a 1 mg mL^{-1} solution was calculated as follows:

Mass required in 100 mL volumetric flask = 100 mg

Liquid density of nitrobenzene = 1.196 g mL^{-1} = 1196 mg mL^{-1}

Volume of nitrobenzene = 100 mg / 1196 mg mL^{-1} = 8.36 x 10^{-2} mL = 83.6 μL

Therefore, 83.3 μL of nitrobenzene was measured into 100 mL flask and made up to the mark with acetonitrile.

Preparation of each 10 μg mL^{-1} solution was then carried out by pipetting 100 μL of each stock solution into 10 mL volumetric flasks and diluting with 50:50 acetonitrile (MeCN)/distilled water.

6.3.2.3 Chromatographic method development

Calibration solution preparation and method validation

Working solutions were prepared for calibration standards in 25 mL volumetric flasks as outlined in Table 6.3. The volumes required to prepare each working solution, given in Table 6.4, were dispensed using micropipettes. Calibrants were prepared in 10 mL volumetric flasks with the appropriate, corresponding volumes of 50:50 acetonitrile/distilled water.

Stock ID	Concentration / µg mL^{-1}	Preparation scheme
A1	100	2.5 mL of 1 mg mL^{-1} stock solution made up to 25 mL with 50:50 MeCN/water
A2	10	2.5 mL A1 + 22.5 mL 50:50 MeCN/water
A3	1	2.5 mL A2 + 22.5 mL 50:50 MeCN/water
A4	0.1	2.5 mL A3 + 22.5 mL 50:50 MeCN/water
A5	0.01	2.5 mL A4 + 22.5 mL 50:50 MeCN/water

Table 6.4 - Volumes required to prepare calibrant solutions.

Concentration µg mL^{-1}	Volume A5 mL	Volume A4 mL	Volume A3 mL	Volume A2 mL	Volume A1 mL	Volume 50:50 MeCN/water mL
Blank	-	-	-	-	-	10
0.0025	2.5	-	-	-	-	7.5
0.005	5	-	-	-	-	5
0.01	10	-	-	-	-	-
0.025	-	2.5	-	-	-	7.5
0.05	-	5	-	-	-	5
0.1	-	10	-	-	-	-
0.25	-	-	2.5	-	-	7.5
0.5	-	-	5	-	-	5
1	-	-	10	-	-	-
2.5	-	-	-	2.5	-	7.5
5	-	-	-	5	-	5
10	-	-	-	10	-	-
25	-	-	-	-	2.5	7.5
50	-	-	-	-	5	5
100	-	-	-	-	10	-

6.3.2.4 HPLC conditions

The HPLC-UV operating conditions used for analysis of target pharmaceuticals; calibration, method validation and sample analyses are outlined in Table 6.5.

Table 6.5: HPLC-UV conditions for analysis of pharmaceutical compound

Software Acquisition and processing:	PeakNet
Instrument No. / Type:	TSP HPLC system with P2000 pump, AS3000 autosampler and UV1000 detector
Wavelength:	270 nm
HPLC Column (type/size):	Zorbax SB-Phenyl 5 µm, 4.6 x 150 mm
Flow rate (mL min^{-1}):	1.4
Run time (min):	5
Injection volume (µL):	105
Elution:	Isocratic
Eluant:	Acetonitrile/distilled water (40:60, v/v)

The HPLC-UV operating conditions used for analysis of nitrobenzene; calibration, method validation and sample analyses are outlined in Table 6.6.

Table 6.6: HPLC conditions for nitrobenzene analysis

Software Acquisition and processing:	PeakNet
Instrument No. / Type:	TSP HPLC system with P2000 pump, AS3000 autosampler and UV1000 detector
Wavelength:	264 nm
HPLC Column (type/size):	Zorbax SB-Phenyl 5 µm, 4.6 x 150 mm
Flow rate (mL min^{-1}):	1.4
Run time (min):	5
Injection volume (µL):	105
Elution:	Isocratic
Eluant:	Acetonitrile/distilled water (50:50, v/v)

Prior to analysis, the acetonitrile/water mobile phases (either 40:60 or 50:50 for the pharmaceutical mixture and nitrobenzene, respectively) were placed into a sonicator for 30 min to allow the solution to degas, ensuring that air bubbles do not cause a problem with HPLC pumps or pass through the detector, resulting in spurious peaks.

6.3.4 Adsorption experiments

The adsorption performance of 4 sorbent types (7 different sorbents in total) was assessed for the removal of both the target pharmaceuticals and nitrobenzene from aqueous solutions. These included mesoporous silica without and with the removal of surfactant (As-syn MCM-41 and Calc MCM-41, respectively), bio-inspired silica without and with the removal of surfactant (As-syn Bio-Si and Calc Bio-Si, respectively), iron incorporated bioinspired silica without and with the removal of surfactant (As-syn Fe Bio-Si and Calc Fe Bio-Si) and commercially used PAC.

6.3.4.1 Batch adsorption

All batch adsorption experiments were conducted using constant volumes, 25 mL, of solution containing the pharmaceutical targets or nitrobenzene into which accurately weighed amounts of sorbent (50 mg or 5 mg of silica material and activated carbon, respectively) were suspended. Note that for the pharmaceutical experiments a mixed solution containing all 4 target compounds was used. The starting concentration of each analyte in the solutions remained fixed at 2.5 µg mL^{-1} (the assessment of adsorption capacity being the only exception). Reactions were allowed to proceed for 2 h (the study of adsorption kinetics being the only exception) at room temperature and with a stir rate of 250 rpm. The 2 h reaction time was shown to be adequate by preliminary kinetic experiments for equilibrium to be attained and stirring rates of 250 rpm were shown to be sufficient to minimise mass transfer effects.

After 2 h, the solution was filtered (Fisherbrand QL 100) and the filtrate solution subsequently analysed by HPLC-UV, using the conditions outlined in Tables 6.5 and 6.6 for the pharmaceutical mixture and nitrobenzene, respectively to establish equilibrium pharmaceutical concentration, C_e, values. Prior to analysis, samples were prepared in the same matrix as the calibration solutions (50:50 acetonitrile/water). This involved pipetting

700 μL aliquots of aqueous sample into 2 mL HPLC vials in addition to 700 μL of acetonitrile. The resulting dilution factor was taken into account in subsequent calculations. Starting pharmaceutical/nitrobenenzene solutions, prior to addition of sorbent, were analysed in parallel with every sample to obtain initial analyte concentration, C_0, values. Determination of the C_e and C_0 values allow the amount of each analyte adsorbed at equilibrium, q_e (mg g^{-1}), and the removal efficiency (% removal) to be established using Equation 6.7 and Equation 6.8, respectively.

Adsorption Kinetics

The adsorption kinetics were investigated by conducting a series of reactions, stirred for pre-determined time intervals; 5, 15, 30, 45, 60, 120, 240 and 480 min. With the aim of assessing the evolution of the adsorption process with time, the concentration of each pharmaceutical remaining in the solutions after the given time (C_t) was determined using HPLC-UV. The results collected allowed the kinetics of pharmaceutical adsorption to be analysed using pseudo first-order, pseudo second-order and intra-particle diffusion kinetics models by fitting the data to Equations 6.1, 6.2 and 6.3, respectively.

Adsorption Capacity

Adsorption isotherms were produced by varying the starting concentration of each pharmaceutical in the mixed solution; 2.5, 5, 10, 25 and 50 μg mL^{-1}. The collected experimental data was subsequently analysed using to the Langmuir and Freundlich adsorption isotherm models; which are represented mathematically in Equations 6.4 and 6.6, respectively.

Influence of solution pH

In addition to adsorption kinetics and capacity, the effect of solution pH was also investigated. The pH dependence of the adsorption process was studied by varying the pharmaceutical/nitrobenenze solution pH: pH 3, 5.5/5.3, 7 and 9. The pH of the mixed pharmaceutical and nitrobenzene solutions without adjustment were pH 5.5 and 5.3, respectively. The other solutions were adjusted using 0.1 M NaOH or HCl to the desired pH values, measured using a Jenway 3505 pH meter.

6.3.4.2 Assessment of sorbent performance in dynamic mode

Fixed bed experiments were carried out using self-made sorbent tubes containing an accurate mass, 25 mg, of either As-syn MCM-41 or PAC sorbent. Each sorbent was interdispersed with 2 g of glass beads and packed into empty solid phase extraction (SPE) polypropylene cartridges (6 mL) plugged with a modified filter paper at both ends, see Figure 6.1.
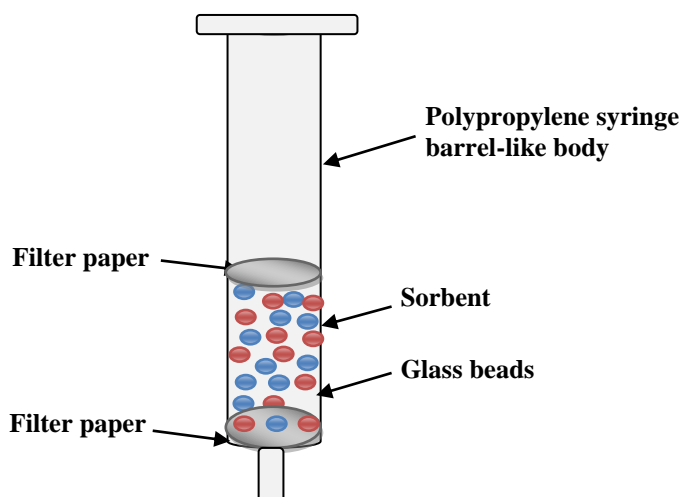
Figure 6.1: Schematic diagram for the SPE column filled with sorbent and glass beads.

The glass beads were incorporated within the sampling tubes to aid passage of the sample solution through the column, enhancing the elution efficiency and enabling higher flow rates to be used. In order to equilibrate, clean and condition the column before use, 20 mL of distilled water was passed over the sorbent bed. To determine the efficiency of each sorbent for pharmaceutical removal in dynamic mode, solutions containing 2.5 µg mL^{-1} were passed through the column, the eluates were collected and subsequently analysed by HPLC-UV. The solutions were initially passed through the column by gravity, the time taken to pass varying depending on sorbent (0.8 and 0.6 mL min^{-1} for As-syn MCM-41 and PAC, respectively) Using a Sulpelco Visiprep vacuum manifold connected to a vacuum pump (KNF Laboport), the flow rates through the individual columns were calibrated and adjusted to 5, 10, 15 and 20 mL min^{-1}.

6.4 Results and discussion

6.4.1 Adsorption of pharmaceutically active compounds in multi-solute solution

6.4.1.1 HPLC method development for pharmaceutical analysis

6.4.1.1.1 Assessment of HPLC-UV measurements

The first stage in the development of a HPLC-UV method was to determine the sensitivity of the target pharmaceuticals; acetaminophen, caffeine, sulfamethoxazole and carbamazepine, towards UV absorbance. UV spectra in the range of 200 – 350 nm of 10 μg mL^{-1} standard solutions of each pharmaceutical in 50:50 acetonitrile/water were acquired; the UV absorbance spectra are shown in Figure 6.2.
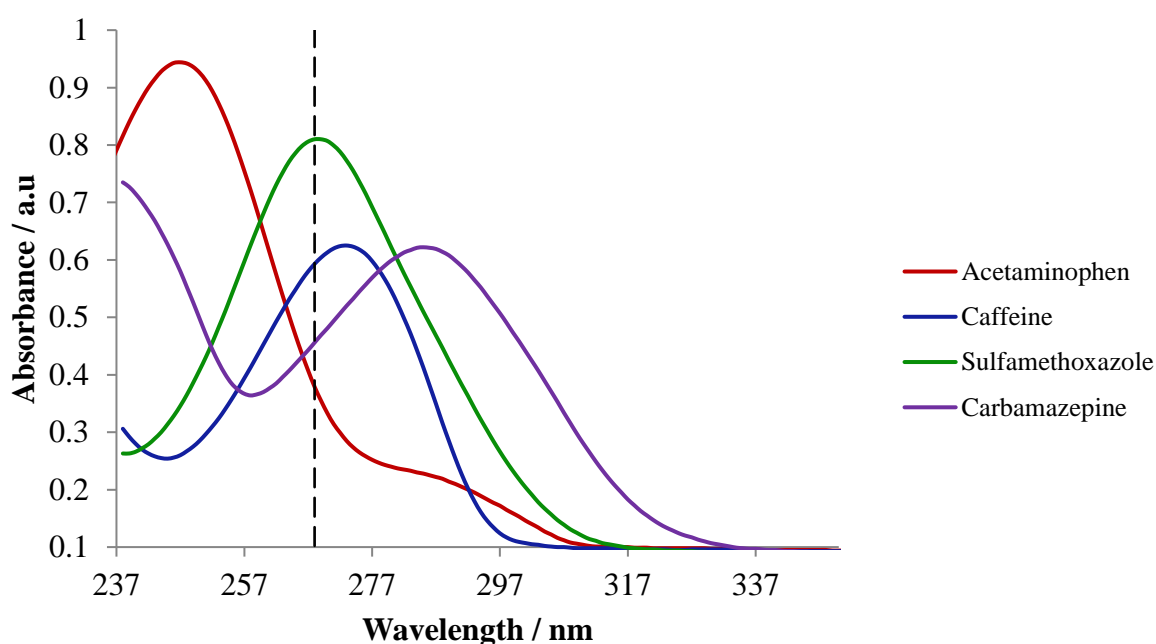
Figure 6.2 UV absorbance spectra of 10 μg mL^{-1} pharmaceutical standards.

Figure 6.2 confirmed that the target pharmaceuticals absorbed UV radiation with the UV spectra containing peaks with maximum absorbance at wavelengths of 247, 273, 268 and 285 nm for acetaminophen, caffeine, sulfamethoxazole and carbamazepine, respectively.

However, it can also be observed from Figure 6.2 that the UV spectra and wavelengths of maximum absorbance vary greatly for each compound. The difficulty when developing a

HPLC-UV method tuned for the analysis of all four pharmaceuticals was found to be selecting a wavelength that optimises the sensitivity of all compounds.

Through a trial and error process, assessing the sensitivity of peaks obtained using wavelengths ranging from 247 – 285 nm; a wavelength of 268 nm was found to produce optimum sensitivity when analysing all four compounds together.

6.4.1.1.2 Chromatographic method development

The main aim of this section of the investigation was to find chromatographic conditions that would allow the development of a simple yet reproducible, accurate and sensitive HPLC-UV method that could be used for the quantification of acetaminophen, caffeine, sulfamethoxazole and carbamazepine. There are a number of factors that play a role in the chromatography of a molecule, as discussed in detail in Section 2.2.2, and therefore, in order to achieve the ideal retention, resolution, peak shape and sensitivity these variables require optimisation.

The chromatographic variables that were investigated are as follows:

- The stationary phase
- Mobile phase composition
- Mobile phase pH
- Mobile phase flow rate

The final chromatographic conditions used throughout this investigation are outlined below:

The four target pharmaceuticals were separated on a Zorbax column (Zorbax SB-Phenyl, 4.6 x 150 mm, 5 µm). Isocratic elution was employed using the following mobile phase: 40:60 acetonitrile/distilled water. The flow rate was 1.4 mL min^{-1}. UV detection was set at a wavelength of 268 nm.

The chromatograms acquired using the chosen HPLC-UV conditions, detailed above, of 10 µg mL^{-1} standard solutions of acetaminophen, caffeine, sulfamethoxazole and carbamazepine are shown in Figure 6.3 (a), (b), (c) and (d), respectively. The chromatogram obtained from the analysis of a 10 ug mL^{-1} mixed standard solution is shown in Figure 6.4.
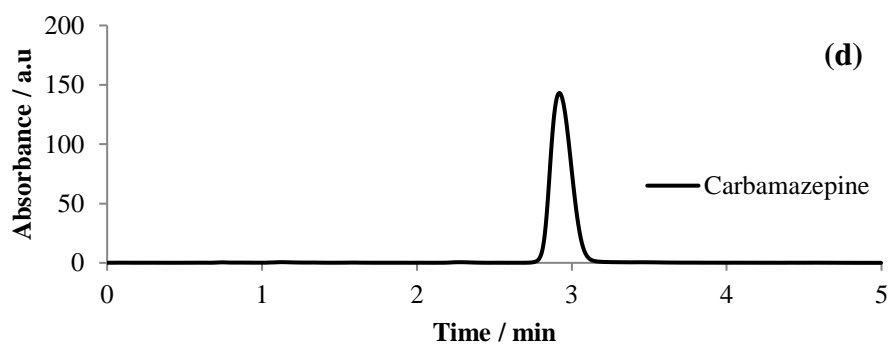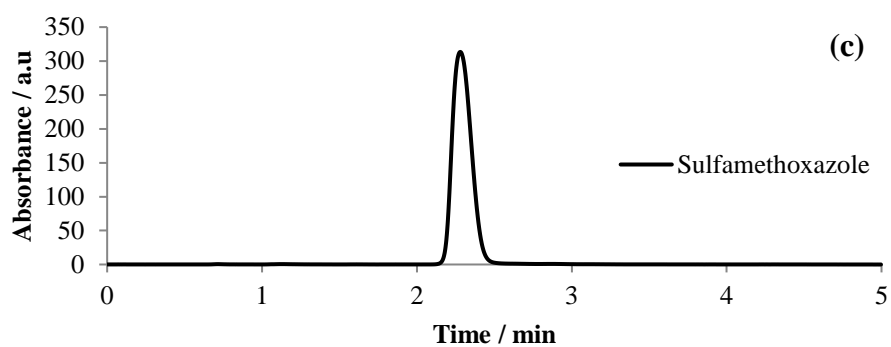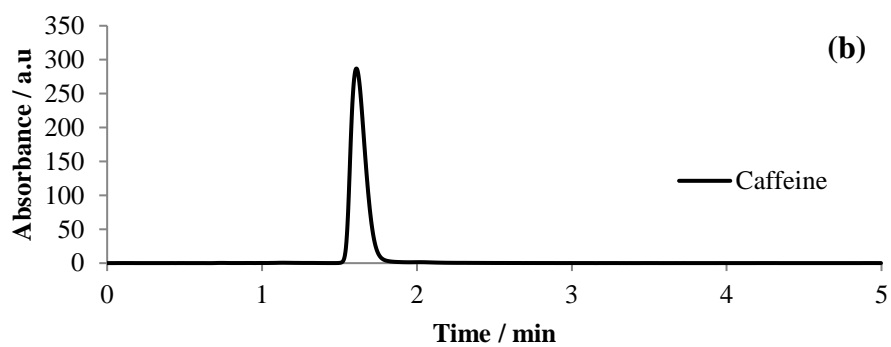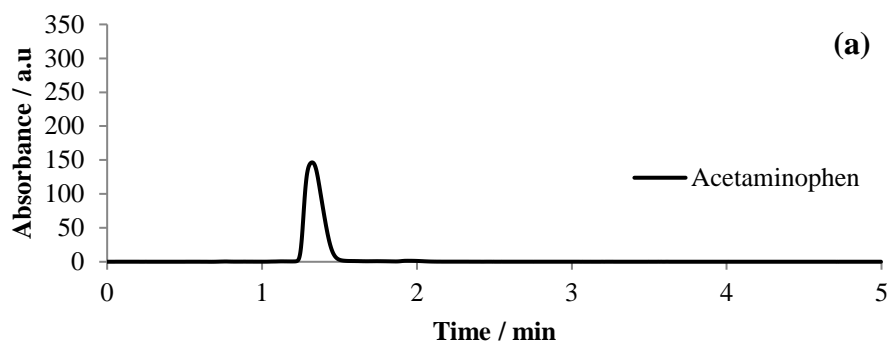
Figure 6.3: Chromatograms of 10 µg mL^{-1} standard solutions; (a) acetaminophen (b) caffeine, (c) sulfamethoxazole, (d) carbamazepine.
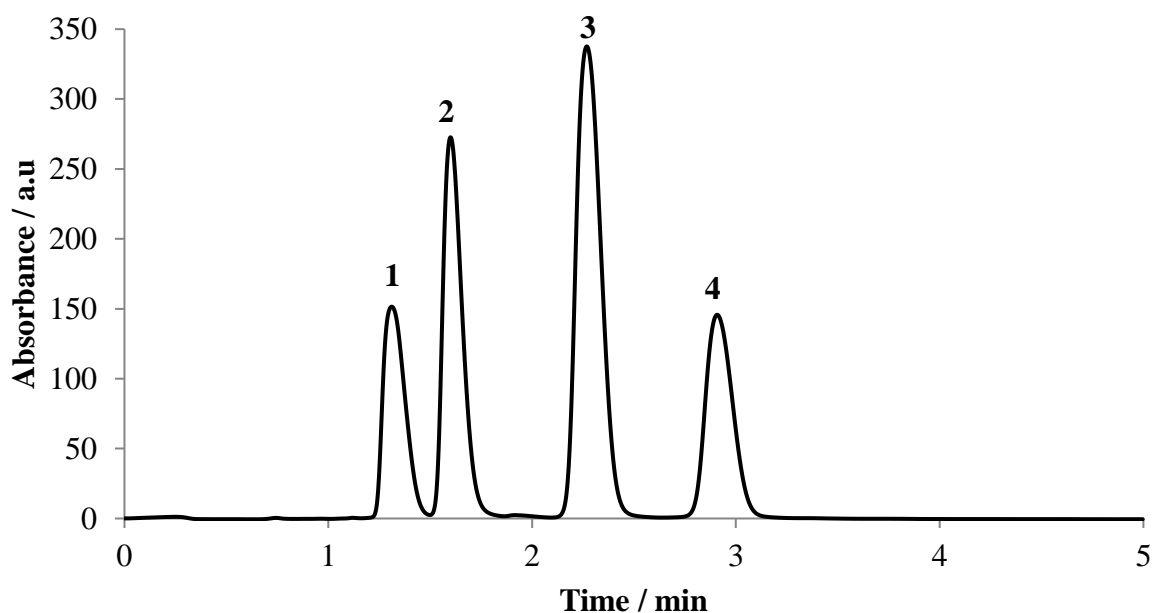
Figure 6.4: Chromatogram of a 10 μg mL^{-1} mixed standard solution where peak 1 is acetaminophen (RT = 1.32 min), peak 2 is caffeine (RT = 1.60 min), peak 3 is sulfamethoxazole (RT = 2.27 min) and peak 4 is carbamazepine (RT = 2.92 min).

The chromatogram illustrates the acetaminophen, caffeine, sulfamethoxazole and carbamazepine peaks at retention times (RT) of 1.32, 1.60, 2.27 and 2.92 min, respectively. All analytes are eluted within 3.5 min and as a result, a short analysis time of 5 min was selected, thus, producing a fast, efficient method for analysing the four target pharmaceuticals.

6.4.1.1.3 Assessment of HPLC method: calibration and validation

Before it is used in any pivotal study, a developed chromatographic method must be validated to ensure the robustness of the chromatography. This was achieved through the analysis of calibration solutions in order to establish the limit of detection, linear range, accuracy, precision and reproducibility of the chromatographic method. Calibration standard solutions (0.001 – 100 μg mL^{-1}) were prepared as outlined in Table 6.4 and analysed using the HPLC conditions listed in Table 6.5. The resulting regression lines are given in Figure 6.5 (a-d) for acetaminophen, caffeine, sulfamethoxazole and carbamazepine, respectively.
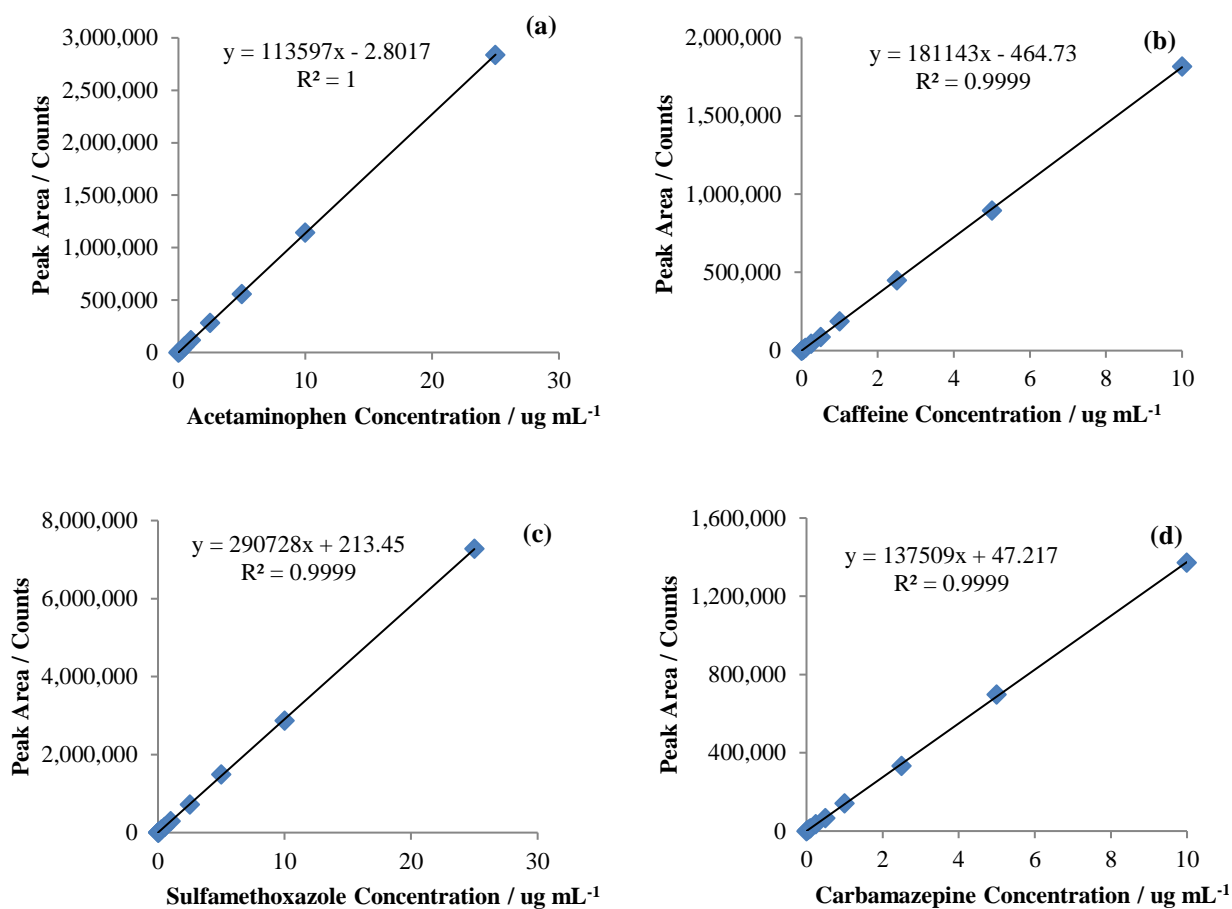
Figure 6.5: Calibration lines obtained from analysis of standard solutions using HPLC: (a) Acetaminophen (b) Caffeine (c) Sulfamethoxazole (d) Carbamazepine.

By examination of the regression lines and the correlation coefficients the method was shown to produce linear signal responses, $R^2 \geq 0.9999$ and be acceptable for quantitative analysis over the following ranges: acetaminophen from $0.05 - 25$ μg mL^{-1}; caffeine from $0.025 - 10$ μg mL^{-1}; sulfamethoxazole from $0.01 - 25$ μg mL^{-1} and carbamazepine from $0.025 - 10$ μg mL^{-1}. All standards within these ranges were within $+/- 10$ % of nominal concentrations demonstrating a high degree of accuracy for each compound. The lowest calibration standards, 0.001 and 0.0025 μg mL^{-1}, were found to be below the limit of detection, BLD, for all compounds and, therefore, were not analysed in subsequent calibrations. At higher concentrations the detector experienced saturation and the calibration line deviated from linearity, becoming curved. This is expected as the Beer-Lambert law fails to hold true for higher concentrated solutions as the analyte molecules are within close proximity, they can

influence each other's charge distribution, consequently affecting the ability of a species to absorb UV radiation.

To establish the accuracy and precision of the method mixed pharmaceutical standard solutions at three different levels; low, medium and high concentrations within the linear range of each compound, were analysed in replicates of 4. The three concentrations analysed were 0.05, 0.5 and 5 µg mL^{-1}. The variations between replicates at each concentration level are shown in Table 6.7.

Table 6.7: %RSD values for each pharmaceutical obtained from the analysis of 3 concentrations of mixed pharmaceutical solution, analysed in replicates of 4.

Concentration / ug mL^{-1}	% RSD			
	Acetaminophen	Caffeine	Sulfamethoxazole	Caffeine
0.05	2.78	3.09	3.98	4.10
0.5	2.55	2.73	0.30	1.39
5	2.86	2.04	2.14	3.26

The % relative standard deviation (RSD) values obtained across the peak areas at each compound concentration are all under 5 % which demonstrated that the peak area did not vary significantly with each replicate injection, at the three different concentrations. This suggested good precision of the chromatographic method.

6.4.1.2 Effect of pH on pharmaceutical adsorption

6.4.1.2.1 Physiochemical properties of pharmaceuticals and their behaviour in varying pH conditions

Prior to assessing the behaviour of pharmaceutical adsorption under varying solution pH, it is important to consider the effects that these conditions will have on the target molecules themselves. The different species of each pharmaceutical found under varying pH conditions are presented in Table 6.8.

Table 6.8: Acetaminophen, caffeine and sulfamethoxazole and carbamazepine species with increasing pH

Ace	
Caff	
Sulf	
Carb	

The pH dependence of the adsorption process was studied by varying the pharmaceutical solution pH: pH 3, 5.5, 7 and 9. From Table 6.8 and their pKa values reported in Table 6.2, it can be seen that for acetaminophen, in pH conditions below pKa (9.38), acetaminophen is a neutral molecule and at pH above the pKa it will exist predominately as an anion. Caffeine is a neutral molecule over a wide range of pH; it will only exist as a cationic species in very low pH conditions. Carbamazepine, with a pKa of 14, is also a neutral molecule over the entire pH range. The different species of sulfamethoxazole in varying pH conditions are also illustrated in Table 6.8. The isoelectric point of sulfamethoxazole is around pH 4.5, which means at this specific pH, the molecules carry no net electrical charge. Below the isoelectric point, sulfamethoxazole carries a net positive charge and above, it carries a net negative charge. More specifically, sulfamethoxazole exhibits two acid dissociation constants; one involving protonation of the aniline N (pK_{a1}) and the other corresponding to deprotonation of the sulphonamide NH (pK_{a2}). In acidic conditions at pH below 1.39, sulfamethoxazole exists predominately as a cationic species; between pH 1.39 and 5.81, the molecule is characterised by neutral charge; and above pH 5.81, sulfamethoxazole is negatively charged. The most acidic hydrogen is that of the $-SO_2$-NH- group, and the resulting anion is stabilised by the powerful electron-withdrawing effect of the sulfonyl substituent as well as resonance into the oxazole ring.

6.4.1.2.2 Effect of pH on sorbent performance

The effect of varying solution pH on the adsorption of pharmaceuticals from a multi-analyte solution onto 7 different sorbents: PAC, Calc MCM-41, As-syn MCM-41, Calc Bio-Si, As-syn Bio-Si, Calc Fe Bio-Si and As-syn Fe Bio-Si are shown in Figure 6.6 (a-g).
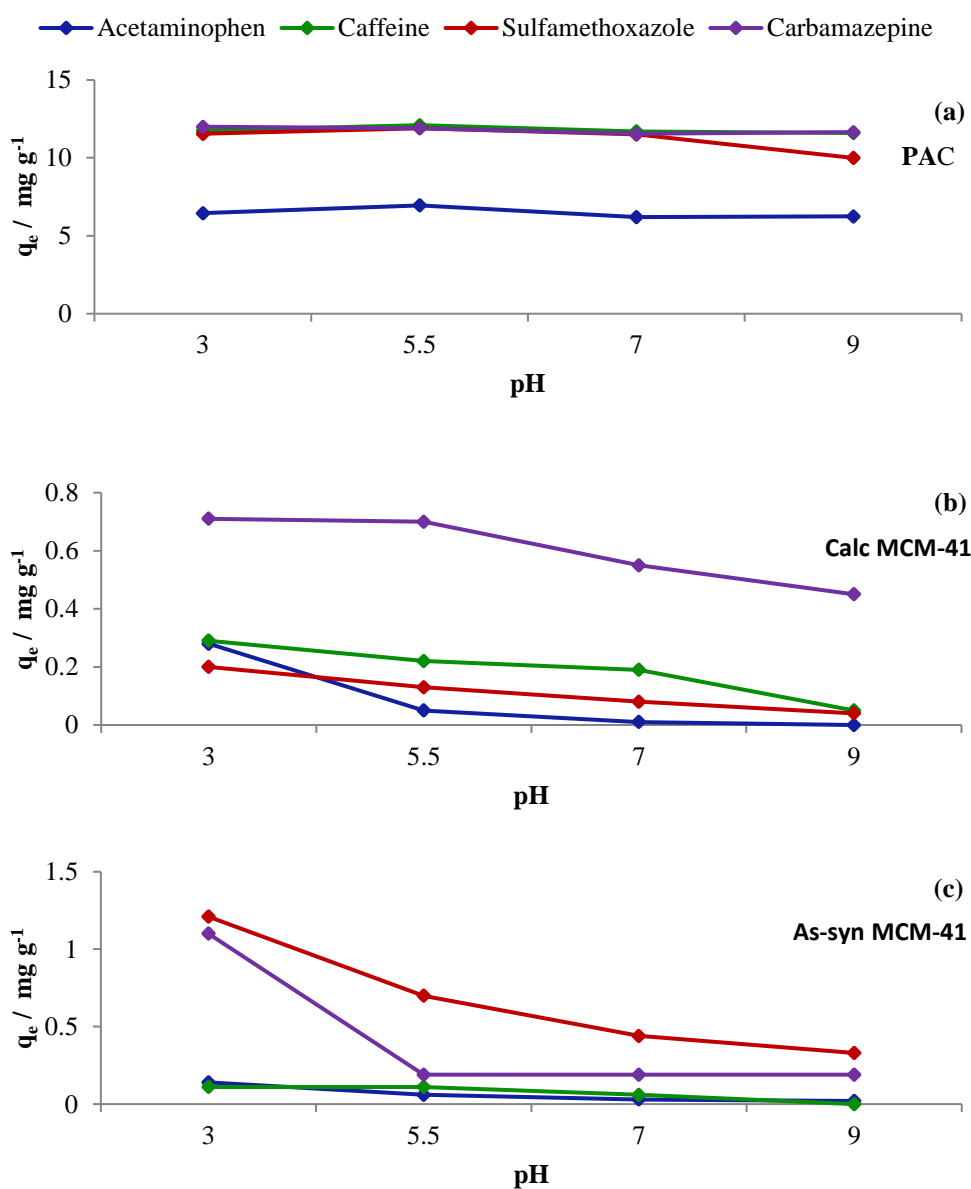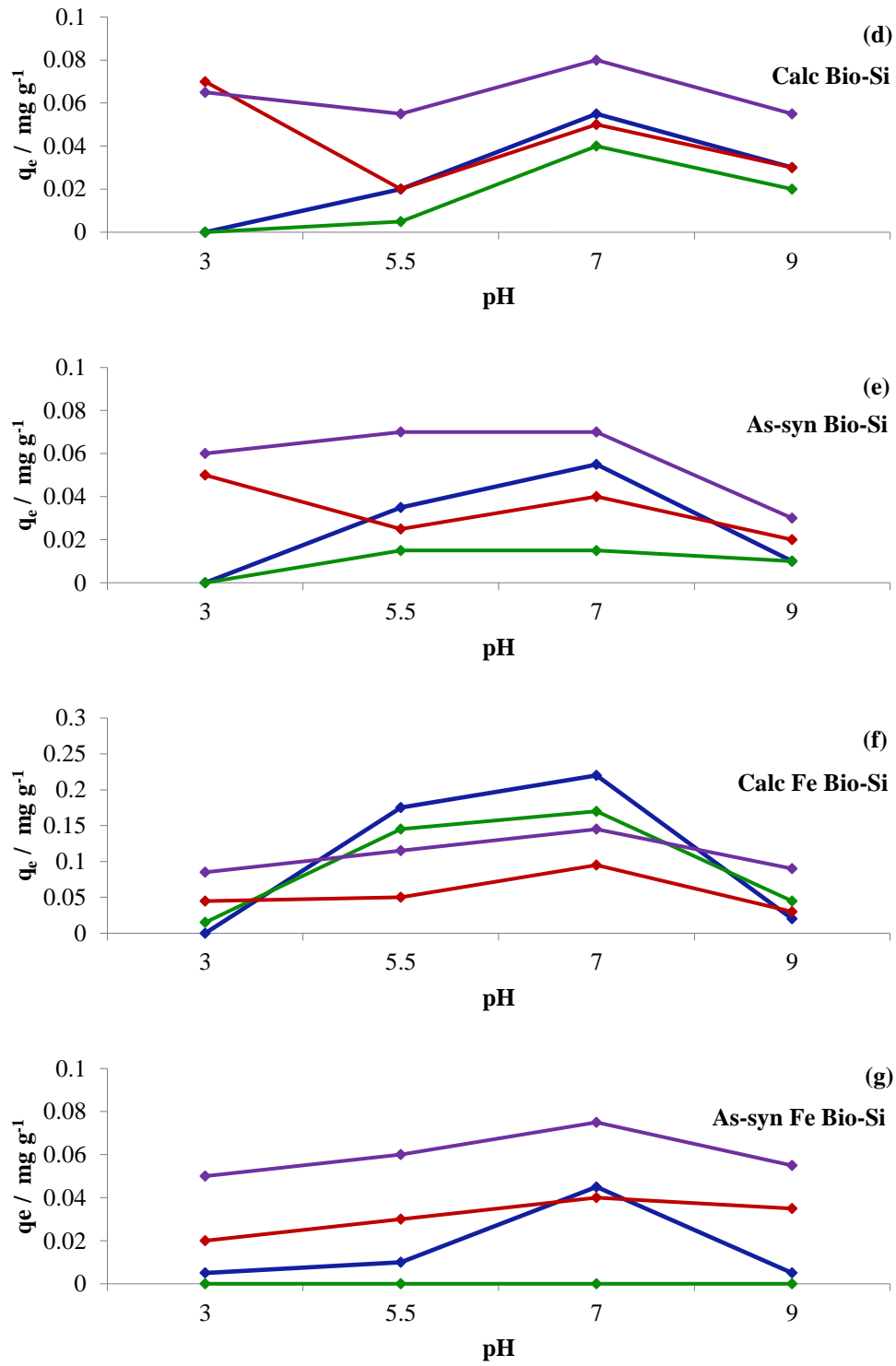
Figure 6.6. Effect of pH on pharmaceutical adsorption using PAC, Calc MCM-41, As-syn MCM-41, Calc Bio-Si, As-syn Bio-Si, Calc Fe Bio-Si and As-syn Fe Bio-Si (a-g, respectively).

The bioinspired silica materials, both with and without the incorporation of iron, were shown to be the lowest performing sorbents for the adsorption of pharmaceuticals from a mixed analyte solution. Calc Bio-Si, As-syn Bio-Si and As-syn Bio-Si all had q_e values < 0.1 mg g^{-1} for each pharmaceutical at each solution pH with the Calc Fe Bio-Si presenting similarly low q_e values of < 0.25 mg g^{-1}. In comparison, the MCM-41 materials were shown to perform better with a high q_e of 1.21 mg g^{-1} for the adsorption of sulfamethoxazole onto As-syn MCM-41. However, PAC proved to be the superior sorbent by far with q_e values between 6 and 12 mg g^{-1} for each pharmaceutical at each solution pH. With the overall order of performance following an increase in sorbent surface area (see Section 3.4.1), PAC presenting as the best sorbent with the largest surface area, it is a possibly that this sorbent property could be governing the absorption of these target analytes. As a consequence of the low performance of the bioinspired materials (with and without iron) for the adsorption of pharmaceuticals from a multi-analyte solution, the investigation using these materials was taken no further and the adsorption kinetic and isotherm results are not reported within this work.

The PAC is shown to perform well for the removal of all four pharmaceuticals and it can be seen that the adsorption of acetaminophen, caffeine and carbamazepine by PAC was not significantly affected by a change in solution pH between 3 and 9. As mentioned previously, these pharmaceutical molecules are neutral over this pH range, confirming that non-electrostatic interactions, such as van der Waals forces, hydrogen bonding, π-π dispersion or hydrophobic interactions, are largely responsible for the adsorption of these compounds by PAC. Sulfamethoxazole showed a slight decrease in adsorption at pH 9 when the molecule should be present in solution as an anion, suggesting that repulsive electrostatic interactions are established with the carbon surface at this pH. Over the pH range studied, the adsorption of acetaminophen from the mixed pharmaceutical solution was shown to be significantly lower than that of the other targets. From examination of the pharmaceutical structures (Table 6.2), the reduced adsorption of acetaminophen could be explained by the lower aromaticity of the molecule resulting in the extent of the π-π interaction being weaker in acetaminophen than in the other pharmaceutical molecules. This would suggest that the main non-electrostatic forces driving pharmaceutical adsorption is π-π dispersion interactions between the aromatic ring(s) of the pharmaceutical molecules and the aromatic structure of the graphene layers of the PAC.

In the case of Calc MCM-41, adsorption was shown to be most substantial for the molecule with greatest hydrophobicity, carbamazepine. The non-electrostatic interactions responsible for the adsorption of this molecule onto the silica surface involve hydrogen bonding which is preferred at a pH lower than 4.0 (isoelectric point of MCM-41), at which the silica surface has a net positive charge. However, it becomes less favourable on negative silica surfaces at a pH higher than 4, resulting in an inverse relationship between carbamazepine adsorption capacity and pH. Meanwhile, the adsorption of sulfamethoxazole on the silica surface can be attributed to both electrostatic and non-electrostatic interactions. At pH 3, sulfamethoxazole is a neutral molecule and thus exhibits behaviour similar to that of the other molecules where adsorption is governed by their hydrophobicity. At pH > pK_{a2} (pH 7 and 9) the sulfamethoxazole molecules exist predominately in anionic form. Under these pH conditions, the anionic sulfamethoxazole molecule would experience electrostatic repulsion from the progressively more negatively charged surface of Calc MCM-41 resulting in lower adsorption onto the material.

As-syn MCM-41 behaves like a supported-micelle material with the same solubility properties as those of the micelles themselves. The micelles allow the pores to be accessible to organic molecules at room temperature, a function attributed to their hydrophobicity. It is, therefore, expected that carbamazepine would have the highest uptake into the micelles. However, the adsorption efficiency was shown to follow the general trend sulfamethoxazole > carbamazepine > acetaminophen ≈ caffeine, which is in order of decreasing molecular weight thus suggesting that molecule size plays an important role in micelle encapsulation. The adsorption of carbamazepine is relatively constant over the pH range 5.5 to 9, however in acidic pH 3 conditions, there is a sharp increase. As mentioned previously, at pH 3 the silica surface has a net positive charge which is favourable for the hydrogen bonding involved in adsorption of the neutral molecules, resulting in the higher removal efficiencies observed under these solution conditions. This reveals that the adsorption process onto As-syn MCM-41 is governed by both the hydrophobicity of the micelles and the surface properties of the silica.

To fully understand the interactions involved in the adsorption of the four target pharmaceuticals by the As-syn MCM-41, the role the micelle plays needs to be discussed, see Section 6.4.1.2.3.

6.4.1.2.3 Role of micelle encapsulation in adsorption performance of MCM-41

To establish the contribution of micelle encapsulation to the adsorption performance of As-syn MCM-41, adsorption experiments were performed initially using only a micellar solution of cetyltrimethylammonium bromide (CTAB) to extract pharmaceuticals and then Calc MCM-41 in the presence of CTAB. 10 mg of CTAB or 10 mg of CTAB and 50 mg of Calc MCM-41 were added to 25 mL of 2.5 ppm pharmaceutical solutions (at pH 3 and pH 5.5) and stirred for 2 h. This prepared a 1.1 mM solution of CTAB, above the critical micelle concentration (cmc) of CTAB which is 0.8 mM. Figures 6.7 and 6.8 illustrate the extent of pharmaceutical removal using CTAB and the effect the cationic surfactant has on the adsorption process using Calc MCM-41 as a sorbent at pH 3 and 5.5, respectively.
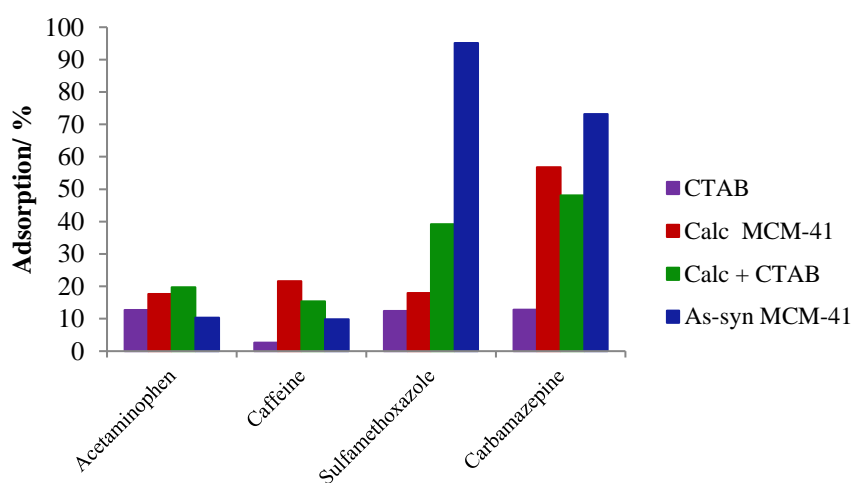
Figure 6.7: Effect of CTAB on adsorption using Calc MCM-41 at pH 3.
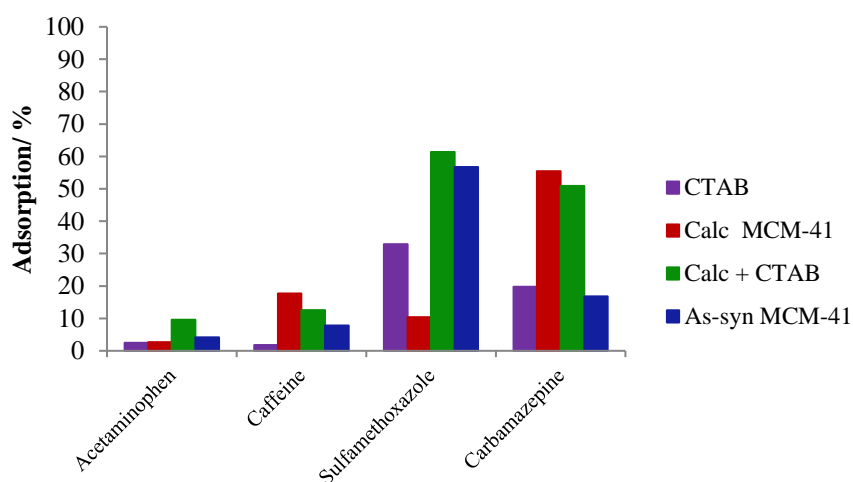
Figure 6.8: Effect of CTAB on adsorption using Calc MCM-41 at pH 5.5.

Although CTAB alone has been shown to remove the pharmaceuticals, to differing extents, from the solution, removal is low as observed in Figures 6.7 and 6.8. This is perhaps a result of the micelle size formed in the water/pharmaceutical solution being undetermined. It is likely to differ from that of the micelles found within the silica structure and could be restricting the access of pharmaceutical molecules into the micelle. These results indicate that it must be a combination of silica and surfactant that is the cause of the high removal efficiencies previously observed for As-syn MCM-41. From the pharmaceutical adsorption using Calc MCM-41 in the presence of CTAB it would appear that the sorption mechanism involved a combined adsorption onto the Calc MCM-41 of the CTAB and target drug molecules with the cationic surfactant being adsorbed onto the silica surface via electrostatic interactions. Figures 6.7 and 6.8 indicate that the CTAB enhanced the adsorption of sulfamethoxazole on Calc MCM-41 at both pH 3 and 5.5. This increase in sulfamethoxazole adsorption can be explained through hydrophobic portioning and weak physical interactions, such as Van der Waals forces, of sulfamethoxazole into the adsorbed CTAB. The increase in adsorption proved larger at pH 5.5 (51 % increase) than pH 3 (21.3 % increase). This could be a consequence of greater adsorption of CTAB onto the silica at pH 5.5, attributed to the electrostatic interactions between the positively charged ammonium groups ($[CH_3)_3NR]^+$) and the overall negatively charged silica surface at this pH. At pH 3, although the CTAB adsorbed onto the silica could increase the adsorption of sulfamethoxazole, the proportion of CTAB adsorbed was smaller as a result of the positively charged CTAB molecules experiencing repulsion from the positively charged silica.

From Figures 6.7 and 6.8 it can be seen that CTAB has lowest interaction with caffeine at both pH 5.5 and 3. The presence of CTAB in addition to the Calc-MCM-41 was shown to inhibit caffeine adsorption onto the sorbent. Caffeine is known to be a very hydrophilic molecule, see Table 6.2, and would have very little affinity for CTAB. Therefore, there could be competition between the caffeine molecules and CTAB for the limited silica adsorption active sites (silanol groups). The presence of CTAB was also shown to decrease the adsorption of carbamazepine onto the Calc MCM-41 suggesting competition between the carbamazepine and CTAB.

6.4.1.2.4 Adsorption of Individual Pharmaceuticals onto MCM-41

All previous experiments carried out throughout this study involved assessing the performance of each sorbent for the adsorption of pharmaceuticals from multi-solute solutions. In the case of As-syn MCM-41 and Calc MCM-41, it was thought that the lower adsorption capacities observed, especially for acetaminophen and caffeine, may be as a result of competitive adsorption among compounds.

To establish whether competitive adsorption was an issue, the adsorption of mixed pharmaceutical solutions was compared with adsorption of individual pharmaceutical solutions. Solutions containing the same initial pharmaceutical concentration, C_0, of 2.5 µg mL^{-1} at pH 3 were stirred in the presence of either 50 mg As-syn MCM-41 or Calc MCM-41 at 25 °C. The solutions either contained the individual pharmaceuticals or a mixture of all four. After 2 h of stirring, the solutions were filtered and the filtrate analysed by HPLC-UV. The results are compared in Figure 6.9.
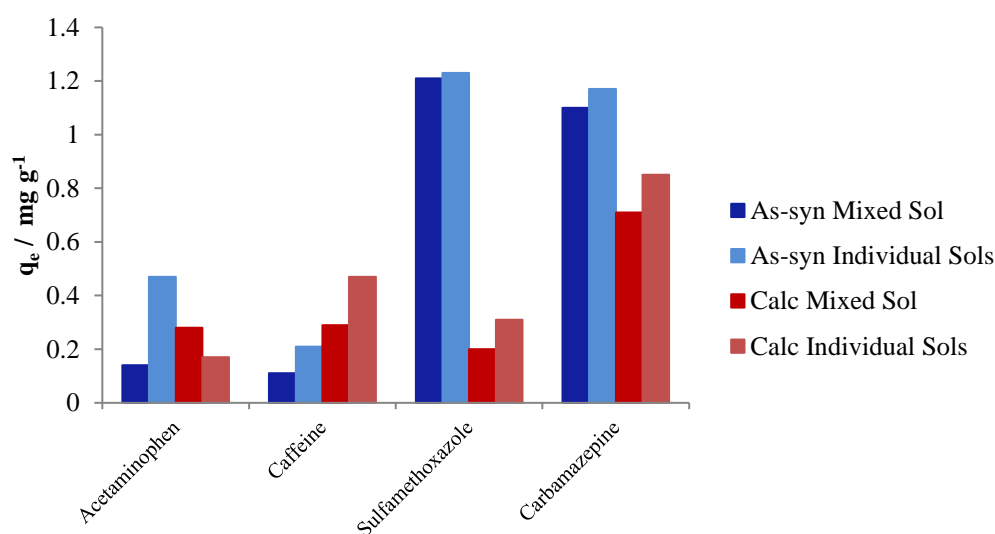
Figure 6.9: Adsorption of pharmaceuticals from mixed and individual analyte solutions using As-syn and Calc MCM-41.

It was expected that the removal of the individual pharmaceuticals would be much higher than that of the mixed solution, as a result of competitive adsorption among compounds. However, from Figure 6.9 it can be seen that this was not the case. With the exception of acetaminophen adsorption onto As-syn MCM-41, for which a reasonable increase was observed, for caffeine, sulfamethoxazole and carbamazepine there was only a small increase, if any, in the adsorption of individual compounds.

6.4.1.3 Adsorption kinetics – Adsorption mechanism and rate-limiting step determination

6.4.1.3.1 Adsorption kinetics

In order to gain insight into the mechanism and rate controlling steps affecting the adsorption process, the adsorption kinetics were investigated.

The results of the adsorption of pharmaceuticals as a function of contact time onto As-syn MCM-41 at pH 5.5 and 3 and PAC at pH 5.5 are shown in Figure 6.10 (a-c), respectively.
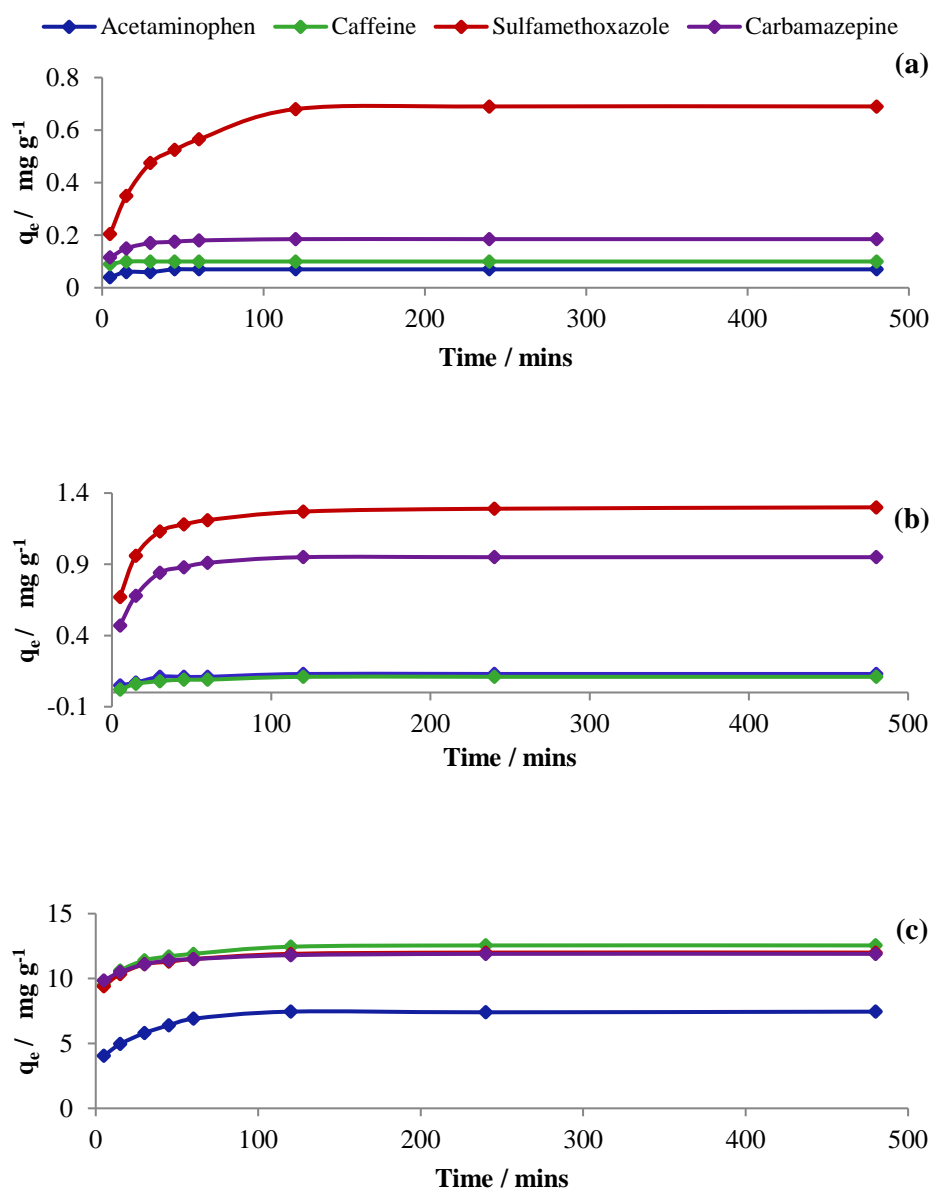
Fig. 6.10. Adsorption of pharmaceuticals from multi solute solution for varying contact times using (a) As-syn MCM-41 at pH 5.5 (b) As-syn MCM-41 at pH 3 and (c) PAC.

For each sorbent, adsorption occurred dramatically in the initial 30 min and then gradually reached equilibrium in 2 h. As-syn MCM-41 at pH 5.5 was shown to be selective in adsorption of sulfamethoxazole. At pH 3, the amount of sulfamethoxazole adsorbed almost doubled (from 0.7 to 1.2 mg g^{-1}) and, in addition, there was a significant increase in the amount of carbamazepine adsorbed (0.1 to 0.8 mg g^{-1}). Despite the increase in pharmaceutical adsorption onto As-syn MCM-41 observed at pH 3, the surfactant containing silica material only proved useful for the removal of 2 out of 4 of the target pharmaceuticals. Moreover, Figure 6.10 (c) illustrates the superior performance of PAC with q_e values of around 12 mg g^{-1} for 3 out of the 4 pharmaceuticals and 6 mg g^{-1} for acetaminophen.

Unlike the adsorption behaviour of the other sorbents, the adsorption capacity of each pharmaceutical onto Calc MCM-41 was shown decrease with time, Figure 6.11.
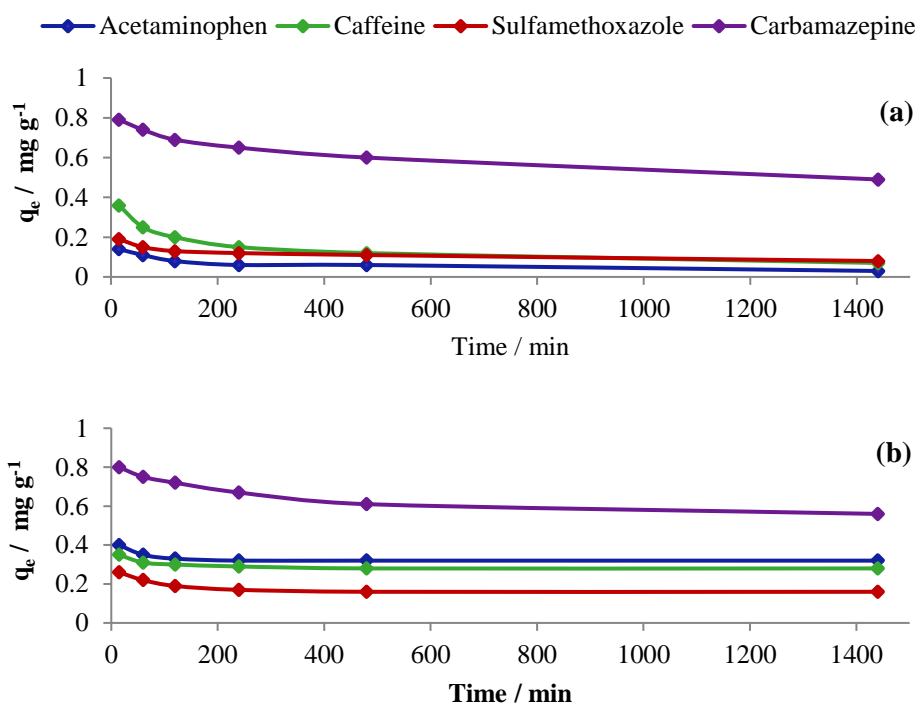
Figure 6.11: Adsorption of pharmaceuticals from multi solute solution using Calc MCM-41 at (a) pH 5.5 and (b) pH 3.

This observation could possibly be a result of the silica material being soluble over time in aqueous solutions. The interaction between the surface of the Calc MCM-41 and the water molecules may have provoked a collapse in the silica to an extent, involving rupture of pore walls and thus a reduction in the active sites available for analyte adsorption.[328] This

phenomenon was not observed in As-syn MCM-41; the hydrophobic nature of the CTAB molecule present in the material would significantly inhibit any water adsorption leading to relatively higher chemical and mechanical stability in aqueous solutions.

However, when the contact time was extended from 480 to 1440 min, the reduction in adsorption appears to plateau as equilibrium is established. Another possible cause may be as a result of an increase in solution pH during the adsorption process which, as previously mentioned, has been shown to decrease adsorption as the molecules desorb from the material surface. As a consequence of this result, the data obtained for the Calc MCM-41 was not taken any further or analysed using kinetics models.

6.4.1.3.2 Kinetic model parameters

The experimental data was analysed using the pseudo first-order and pseudo second-order kinetic models, Equations 6.1 and 6.2, respectively. In the first-order model, the time is plotted against log $(q_e - q_t)$ values, whereas in the second-order model, the time is plotted against t / q_t. The resultant plots are given in Figure 6.12 (a) and (b) for As-syn MCM-41 and Figure 6.13 (a) and (b) for PAC. The corresponding kinetic parameters and regression coefficients are outlined in Tables 6.9 and 6.10 for As-syn MCM-41 and PAC, respectively.
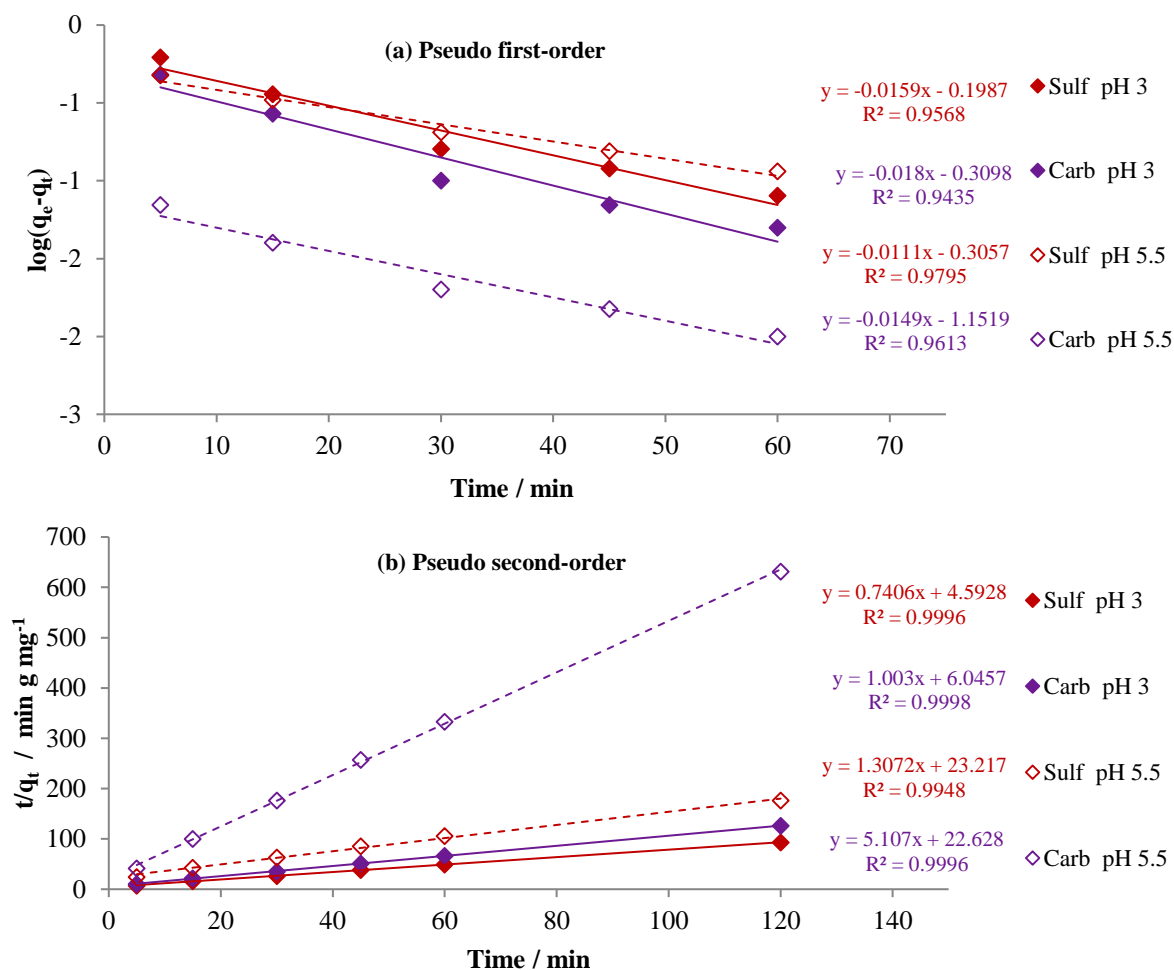
Figure 6.12: (a) Pseudo first-order and (b) Pseudo second-order kinetic models of pharmaceutical adsorption onto As-syn MCM-41 at pH 5.5 and pH 3.

Table 6.9: Kinetic parameters for pseudo first and second-order kinetic models of pharmaceutical adsorption onto As-syn MCM-41 at pH 5.5 and pH 3

Compound	Experimental value	The pseudo first order			The pseudo second order		
	q_e / mg g^{-1}	q_e / mg g^{-1}	k_1 / min^{-1}	r^2	q_e / mg g^{-1}	k_2 / g mg^{-1} min^{-1}	r^2
pH 5.5							
Sulfamethoxazole	0.68	0.50	0.03	0.9795	0.76	0.06	0.9948
Carbamazepine	0.19	0.07	0.03	0.9613	0.20	0.23	0.9996
pH 3							
Sulfamethoxazole	1.29	0.63	0.04	0.9568	1.35	0.16	0.9996
Carbamazepine	0.95	0.49	0.04	0.9435	1.00	0.17	0.9998

178
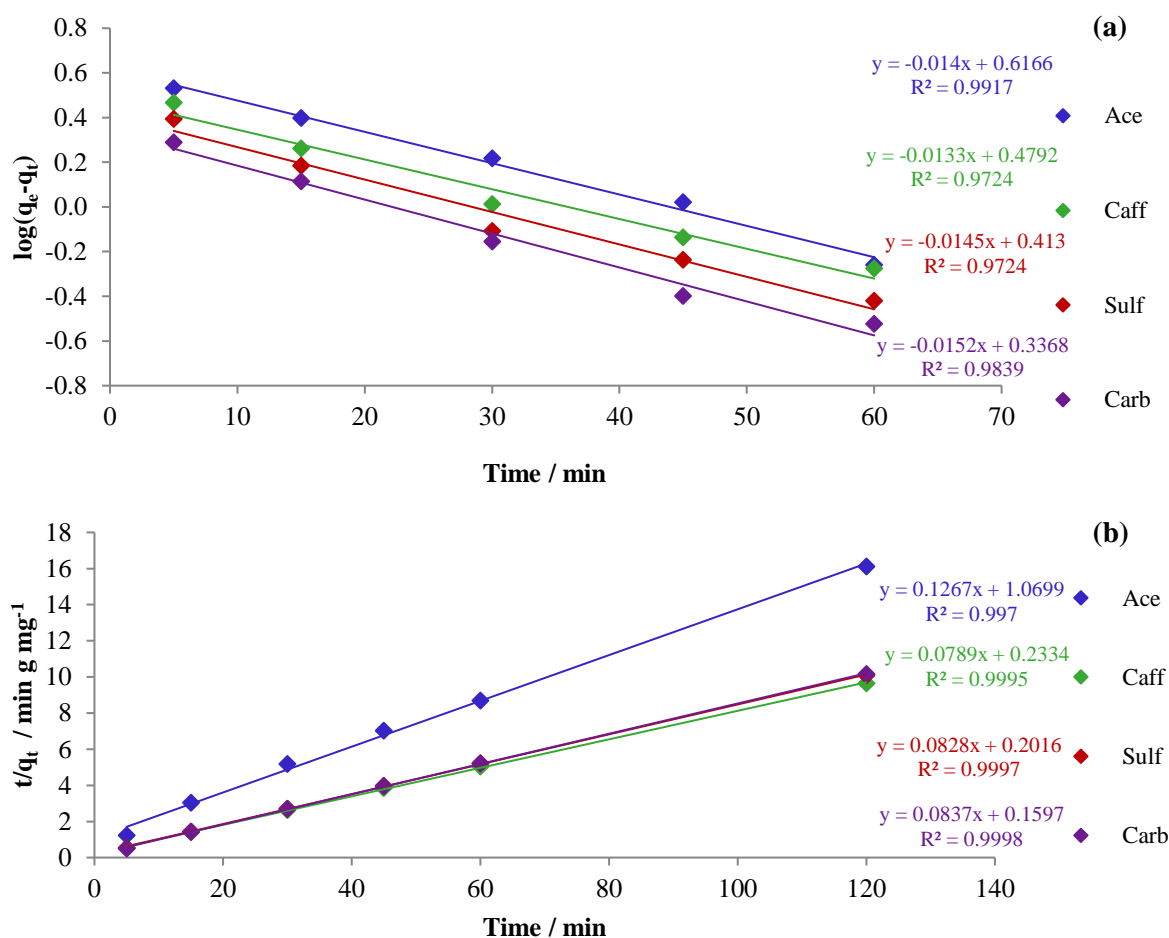
Figure 6.13: (a) Pseudo first-order and (b) Pseudo second-order kinetic models of pharmaceutical adsorption onto PAC.

Table 6.10: Kinetic parameters for pseudo first and second-order kinetic models of pharmaceutical adsorption onto PAC

Compound	Experimental Value	The pseudo first order			The pseudo second order		
	q_e / mg g^{-1}	q_e / mg g^{-1}	k_1 / min^{-1}	r^2	q_e / mg g^{-1}	k_2 / g mg^{-1} min^{-1}	r^2
Acetaminophen	7.45	4.14	0.03	0.9917	7.89	0.12	0.9970
Caffeine	12.45	3.01	0.03	0.9724	12.67	0.34	0.9995
Sulfamethoxazole	11.90	2.59	0.03	0.9724	12.08	0.41	0.9997
Carbamazepine	11.80	2.17	0.04	0.9839	11.95	0.52	0.9998

The conformity between experimental data and the model predicted values was expressed through the correlation coefficients, r^2. The pseudo second-order kinetic model proved to better describe the experimental data, attested by the higher r^2 values and good agreement between theoretical and experimental q_e values. The better fit of the data to the pseudo second-order model for both sorbents infers that chemisorption is playing a significant role in the rate-limiting step, in contrast to the first-order kinetic process which indicates the occurrence of reversible interactions. Similar trends have been reported for the adsorption of various pharmaceutical molecules from aqueous solution by activated carbon and mesoporous silica materials.[299, 308, 312, 314, 329] However, the occurrence of chemisorption contradicts the findings from Section 3.2.1 where it was proposed that non-electrostatic interactions, π-π dispersion and hydrophobic interactions in the case of PAC and As-syn MCM-41, respectively, govern the adsorption of the pharmaceutical molecules.

In order to gain further insight into the mechanisms and rate controlling steps affecting the kinetics of pharmaceutical adsorption onto As-syn MCM-41 and PAC, the kinetic experimental results were also fitted to the Weber-Morris[320] intra-particle diffusion model (Equation 6.3). The resultant plots and corresponding kinetic parameters for As-syn MCM-41 and PAC adsorption are shown in Figures 6.14 and 6.15 and Tables 6.11 and 6.12, respectively.
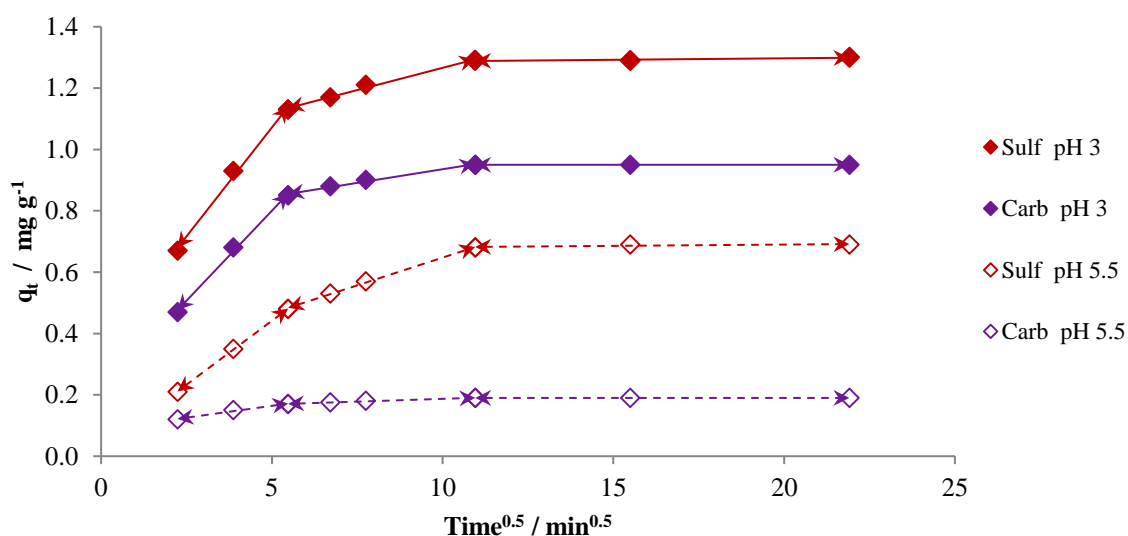
Figure 6.14: Intra-particle diffusion model of pharmaceutical adsorption onto As-syn MCM-41 at pH 5.5 and pH 3.

Table 6.11: Kinetic parameters for intraparticle diffusion model of pharmaceutical adsorption onto As-syn MCM-41 at pH 5.5 and pH 3

Compound	The intra-particle diffusion model				
	$k_{(1)}$ / g mg^{-1} min^{-1}	$k_{(2)-id}$ / g mg^{-1} min^{-1}	$r^{2\,(1)}$	$r^{2\,(2)}$	C
pH5.5					
Sulfamethoxazole	0.08	0.04	0.9998	0.9982	0.29
Carbamazepine	0.02	0.003	0.9881	0.9911	0.15
pH 3					
Sulfamethoxazole	0.14	0.03	0.9952	0.9911	0.98
Carbamazepine	0.12	0.02	0.997	0.9883	0.76
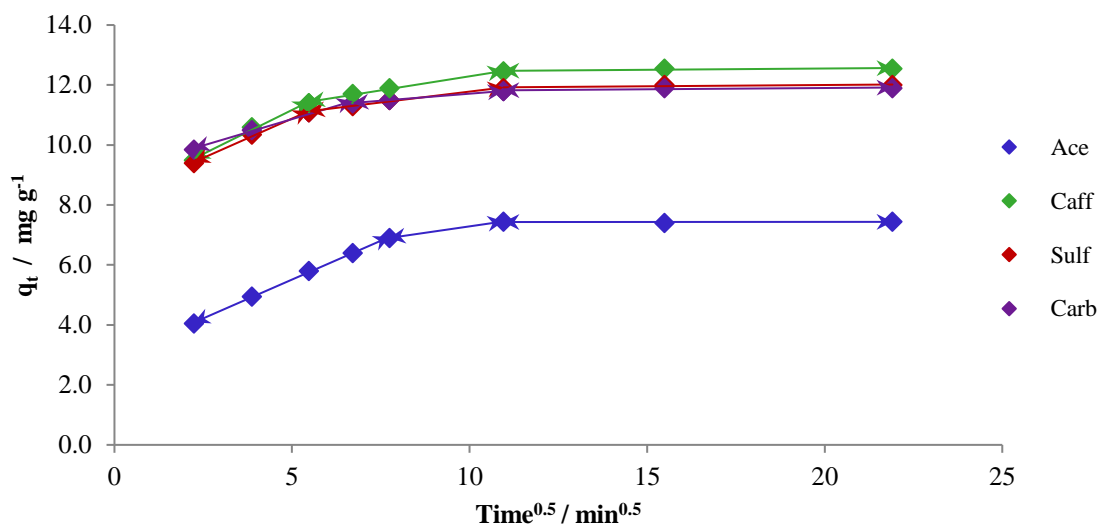
Figure 6.15: Intra-particle diffusion model of pharmaceutical adsorption onto PAC.

Table 6.12: Kinetic parameters for intraparticle diffusion model of pharmaceutical adsorption onto PAC

Compound	The intra-particle diffusion model				
	$k_{(1)}$ / g mg^{-1} min^{-1}	$k_{(2)-id}$ / g mg^{-1} min^{-1}	$r^{2\,(1)}$	$r^{2\,(2)}$	C
Acetaminophen	0.52	0.17	0.9992	1	5.57
Caffeine	0.59	0.19	0.9928	0.9933	10.41
Sulfamethoxazole	0.53	0.15	0.9962	0.9911	10.33
Carbamazepine	0.35	0.09	0.9918	1	10.77

According to the Weber-Morris intra-particle diffusion model, if a plot of q_t versus $t^{0.5}$ is linear and passes through the origin then intra-particle diffusion is the sole rate-limiting step. As the plots did not pass through the origin, intra-particle diffusion was not the only rate-limiting step. It has also been suggested that in instances when q_t versus $t^{0.5}$ is multi-linear, two or more steps govern the adsorption process. Given the multi-linearity of the plots shown in Figures 6.14 and 6.15 for the adsorption of pharmaceuticals on both As-syn MCM-41 and PAC, it can be proposed that adsorption occurred in three phases. The initial steeper section was attributed to the diffusion of pharmaceuticals through the solution to the external surface of adsorbent, or the boundary layer diffusion of solute molecules and the second linear section represents a gradual adsorption stage attributed to intra-particle or pore diffusion. In the third section, the plots are shown to plateaux representing equilibrium between the sorbents and pharmaceutical solutions and therefore this final section is not considered as rate limiting. The intra-particle diffusion rate constant k_{2-id} was calculated from the slope of the second linear section, for both sorbents it was found to be the slowest, and therefore the rate determining stage for each adsorption process. The value of the intercept C in this second section provides information related to the thickness of the boundary layer. Larger intercepts suggest that external surface diffusion has a larger role as a rate-limiting step.

In the case of As-syn MCM-41 the results recorded in Table 6.11 suggest that for sulfamethoxazole adsorption, intraparticle diffusion plays a larger role as the rate-limiting step at pH 3 in contrast to carbamazepine where it is a more significant rate-limiting factor at pH 5.5.

With regard to PAC, the intraparticle diffusion rates, shown in Table 6.12, followed the order Caff > Ace > Sulf > Carb, which is in order of increasing hydrophobicity (see Table 6.2), suggesting that there is electrostatic or hydrogen bonding interactions occurring within the micropores that are resulting in the less hydrophobic molecules diffusing into them faster.

The mechanism of pharmaceutical adsorption on As-syn MCM-41 and PAC were, therefore, shown to be complex and involve both surface and intra-particle adsorption; both reaction mechanisms contributing to the adsorption kinetics with intra-particle diffusion being the rate determining step in each process.

6.4.1.4 Adsorption isotherms – Evaluation of adsorption capacity

The results of the pharmaceutical adsorption capacity, as a function of initial pharmaceutical concentration, of As-syn MCM-41 at pH 5.5 and 3 and PAC at pH 5.5 are shown in Figure 6.16 (a-c), respectively.
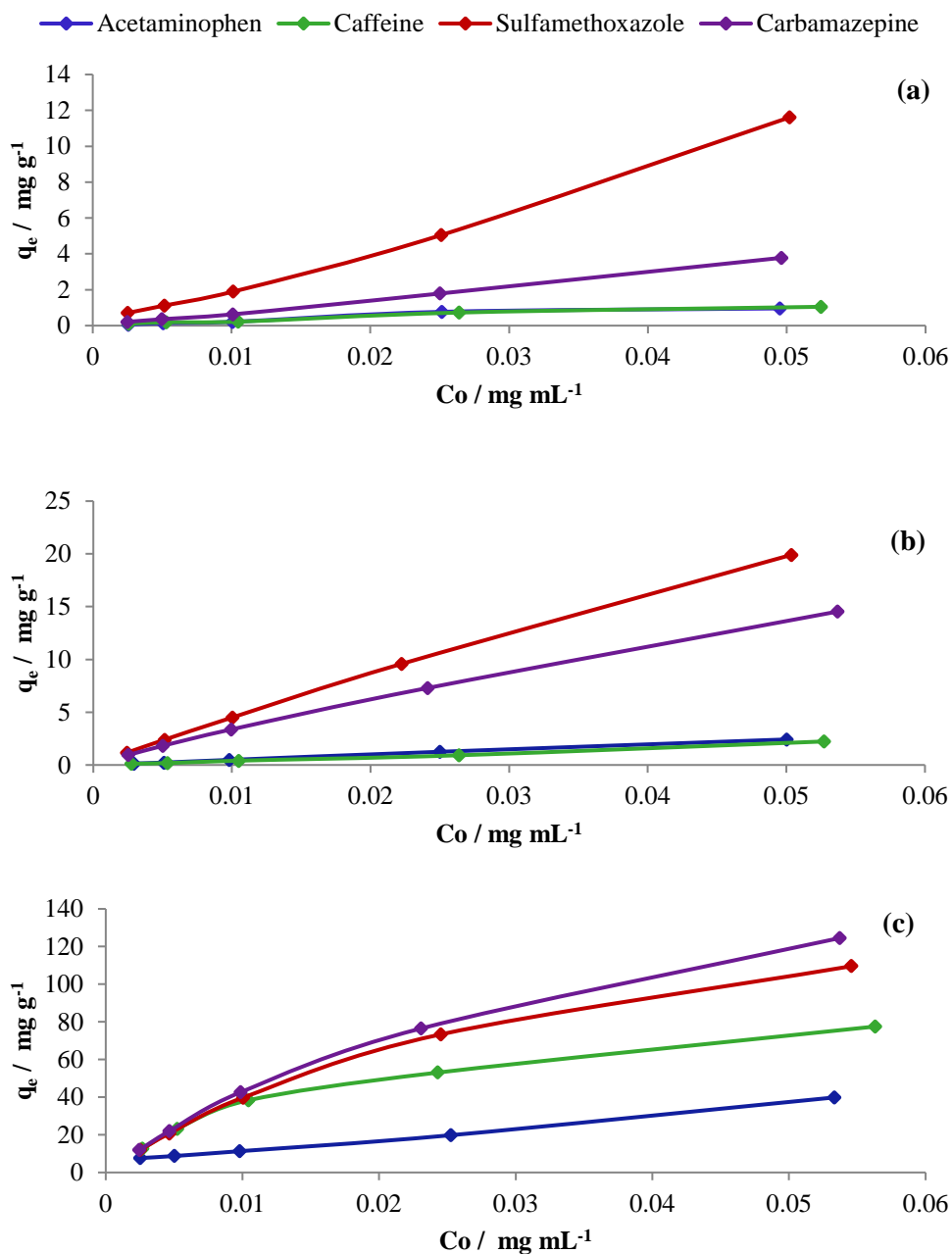
Figure 6.16: Adsorption of pharmaceuticals from multi solute solutions of increasing concentrations using (a) As-syn MCM-41 (b) As-syn MCM-41 at pH 3 and (c) PAC.

Equilibrium adsorption isotherms are important in evaluating the maximum adsorption capacity of pharmaceuticals by each sorbent and characterising the mechanism of adsorption onto a sorbent. Langmuir and Freundlich isotherm models (Equations 6.4 and 6.6) correspond to homogenous and heterogeneous adsorbent surfaces, respectively, and both were used to describe the experimental data. Isotherm parameters are outlined in Table 6.13 for As-syn MCM-41 and in Table 6.14 for PAC.

Table 6.13: Isotherm parameters for Langmuir and Freundlich models of pharmaceutical adsorption onto As-syn MCM-41 at pH 5.5 and pH 3

Compound	Langmuir				Freundlich		
	r^2	q_m (mg g^{-1})	b (L mg^{-1})	R_L	r^2	K_f (mg g^{-1})	n (L mg^{-1})
pH 5.5							
Sulfamethoxazole	0.0183	116.28	0.004	0.99	0.9539	0.51	1.15
Carbamazepine	0.0004	476.19	0.0002	1	0.9847	0.10	1.05
pH 3							
Sulfamethoxazole	0.9164	26.18	0.26	0.61	0.9989	4.65	1.63
Carbamazepine	0.9304	24.63	0.05	0.88	0.9992	1.38	1.35

Table 6.14: Isotherm parameters for Langmuir and Freundlich models of pharmaceutical adsorption onto PAC

Compound	Langmuir				Freundlich		
	r^2	q_m (mg g^{-1})	b (L mg^{-1})	R_L	r^2	K_f (mg g^{-1})	n (L mg^{-1})
Acetaminophen	0.7515	48.54	0.06	0.87	0.8839	6.12	2.37
Caffeine	0.9791	80	0.37	0.50	0.9857	25.28	3.25
Sulfamethoxazole	0.9822	117.65	0.32	0.56	0.9976	27.82	2.45
Carbamazepine	0.9747	129.87	0.44	0.49	0.9992	36.40	2.71

As previously mentioned in Section 6.2.3.1 and Equation 6.5, the Langmuir equation can be expressed in terms of a dimensionless separation factor (R_L) to predict the favourability of an adsorption system. The R_L values derived for all pharmaceuticals onto both sorbents are between 0 and 1, indicating that the adsorption is favourable. As reflected in the regression coefficients for each isotherm type, the distribution of pharmaceuticals measured between the

liquid phase and both PAC and As-syn MCM-41 sorbents at equilibrium is best described by the Freundlich model, thus implying the adsorption processes involve multilayer sorption onto heterogeneous surfaces. The Freundlich constant, n, is the empirical parameter related to the intensity of the adsorption process, if the n value is below 1 then the adsorption is a chemical process; otherwise, the adsorption is a physical process. All values of n exceed 1 suggesting the adsorption of each pharmaceutical on both PAC and MCM-41 were physical processes. This supports the hypothesis that non-electrostatic interactions govern the adsorption of the pharmaceutical molecules onto both sorbents as detailed in Section 6.4.1.2. The PAC demonstrated a higher affinity for each pharmaceutical than As-syn MCM-41 at pH 3 which in turn proved to have a higher affinity than As-syn MCM-41 at pH 5.5.

The Freundlich constant, K_f, can be used to evaluate the maximum adsorption capacity for each pharmaceutical on both sorbents as well as predicting the total pharmaceutical adsorption capacity (Table 6.15). It is evident that the commercially used PAC has a significantly greater pharmaceutical adsorption capacity than As-syn MCM-41 regardless of the pH conditions of the solution.

Table 6.15: Total pharmaceutical adsorption capacity for each sorbent

Sorbent	Total pharmaceutical adsorption capacity / mg g^{-1} (Predicted using K_f values)
As-syn pH 5.5	0.61
As-syn pH 3	6.03
PAC	96.82

6.4.1.5 Assessment of sorbent performance in packed-bed under dynamic flow

Although the batch extraction results provide the fundamental information related to sorbent behaviour and pharmaceutical sorption performance, a continuous mode of operation would be preferred in large scale water treatment applications with perceived advantages including high yields, simple operation, easy regeneration of packed bed and ease of scale up from a laboratory to industrial or environmental application. Hence, the extraction of pharmaceuticals was also studied in dynamic flow.

The results of varying solution flow rate through sorbent columns containing As-syn MCM-41 and PAC on the dynamic pharmaceutical adsorption are shown in Figures 6.17 and 6.18 (a), respectively. Figure 6.18 (b) depicts the results obtained from the additional investigation into the adsorption capacity of PAC in dynamic flow as a function of initial pharmaceutical concentration.
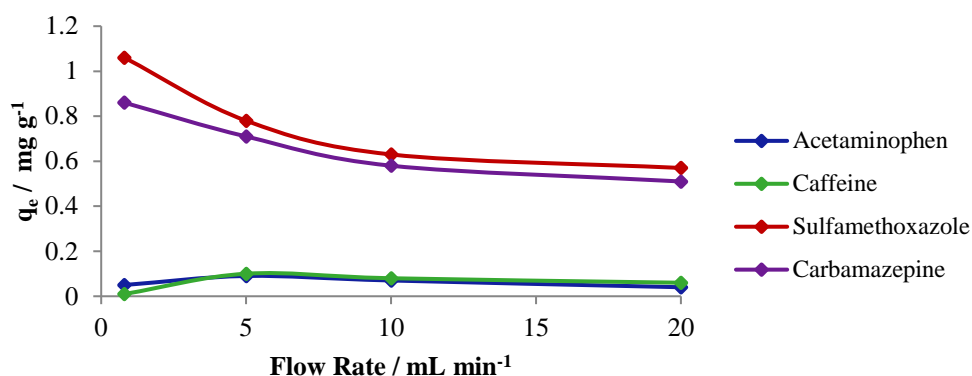
Figure 6.17: Effect of solution flow rate on dynamic adsorption of pharmaceuticals onto As-syn MCM-41.
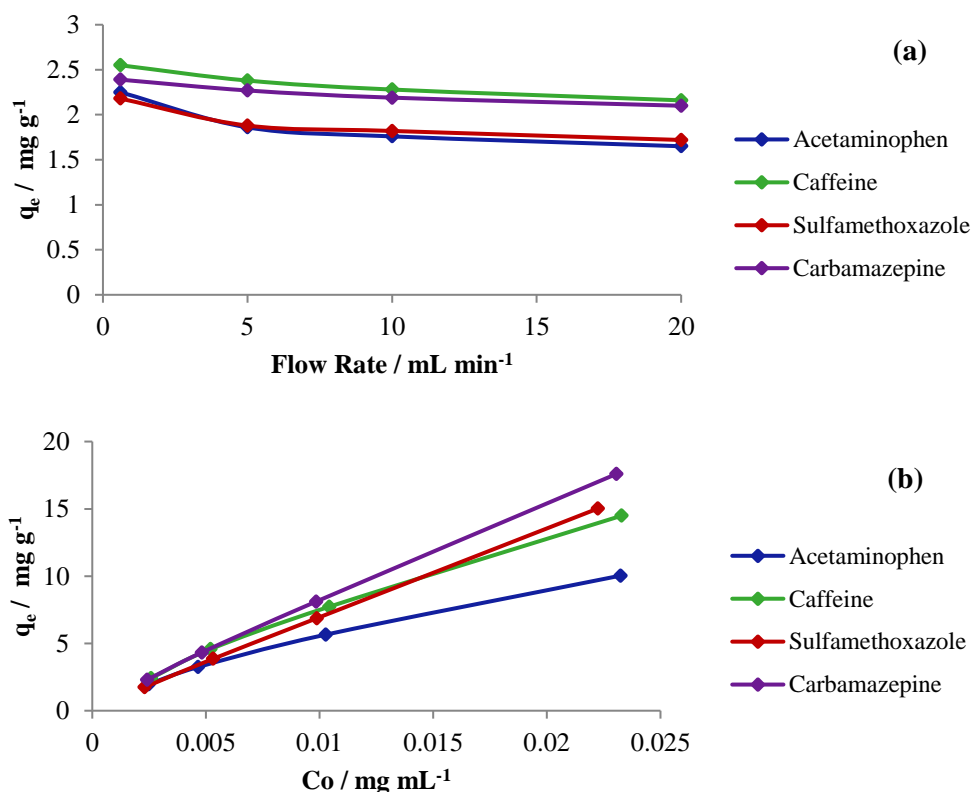
Figure 6.18: Effect of (a) solution flow rate and (b) initial pharmaceutical concentration on dynamic adsorption onto PAC.

As indicated in Figure 6.17, using As-syn MCM-41 at the lowest flow rate of around 0.8 mL min^{-1}, higher uptake values of sulfamethoxazole and carbamazepine were observed with the adsorbed quantity decreasing significantly at higher flow rates. This behaviour can be explained by insufficient residence time of the solutes in the column: the residence time decreases with the increase in the flow that leads to insufficient time for diffusion of the pharmaceuticals into the micelles of the As-syn MCM-41; thus, limiting the number of available active sites for adsorption. For the dynamic adsorption of acetaminophen and caffeine onto As-syn MCM-41 the increase in the flow appears to cause an initial increase in the quantity adsorbed which could correspond to an improvement in the kinetics of adsorption caused by a reduction of the resistance of film in the external transfer. This increase is only favourable until the flow reaches the value at which this external resistance is no longer limited. A rise in the flow beyond this value, localised in these conditions towards 5 mL min^{-1}, causes a fall in the adsorbed quantity since the residence time decreases and the acetaminophen and caffeine molecules do not penetrate deeply in the micelle pores.

As shown in Figures 6.18 (a), the dynamic adsorption of all four pharmaceutical molecules onto PAC, in comparison to the As-syn MCM-41, does not appear to be as significantly affected by an increase in flow rate. A slightly higher uptake value, most notably for acetaminophen and caffeine, is observed for the lowest flow rate of around 0.6 mL min^{-1}. Overall the decreasing residence time of solutes in the column with increasing flow rate does not greatly hinder pharmaceutical diffusion into the micropores of PAC.

Figure 6.18 (b) shows the pharmaceutical dynamic adsorption capacity of PAC, as a function of initial pharmaceutical concentration. The collected experimental data was subsequently analysed using the Langmuir and Freundlich adsorption isotherm models given by Equations 6.4 and 6.6, respectively. From examination of the isotherms and regression coefficients, the distribution of pharmaceuticals between the liquid phase and the solid adsorbent phase during dynamic flow at 10 mL min^{-1} was best described by the Freundlich model. The resultant Freundlich isotherm plots and corresponding Freundlich isotherm parameters and are given in Figure 6.19 and Table 6.16, respectively.
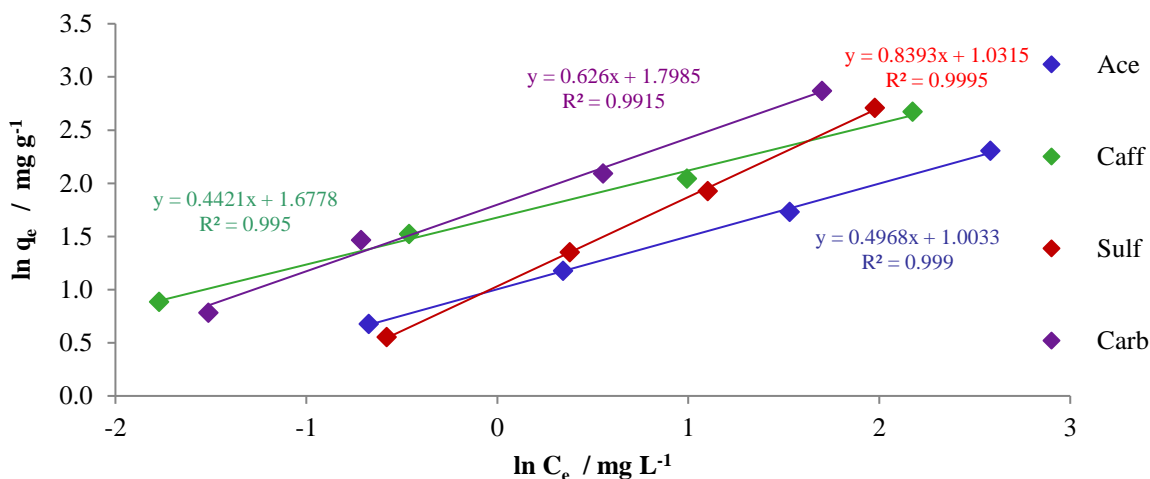
Figure 6.19: Freundlich isotherm model of pharmaceutical adsorption onto PAC in dynamic mode.

Table 6.16: Isotherm parameters for Langmuir and Freundlich models of pharmaceutical adsorption onto PAC

Compound	Freundlich			Total pharmaceutical adsorption capacity / mg g^{-1}
	r^2	K_f (mg g^{-1})	n (L mg^{-1})	
Acetaminophen	0.9990	2.73	2.01	
Caffeine	0.9950	5.35	2.26	16.92
Sulfamethoxazole	0.9995	2.80	1.19	
Carbamazepine	0.9915	6.04	1.59	

This result was similarly observed in the batch adsorption experiments, supporting the proposal that the mechanism of adsorption onto PAC was multilayer sorption via a heterogeneous surface. As previously mentioned, the Freundlich constant, n, is related to the intensity of the adsorption process, with n >1 suggesting the adsorption of each pharmaceutical on PAC was a physical process. As observed with the batch experiments the PAC demonstrated a higher affinity for each pharmaceutical in the order of caffeine > carbamazepine > acetaminophen > sulfamethoxazole. The Freundlich constant, K_f, was used to evaluate the adsorption capacity for each pharmaceutical on each sorbent as well as predicting the total pharmaceutical adsorption capacity for PAC in dynamic mode.

6.4.2 Adsorptive removal of nitrobenzene from aqueous solutions – A study of the effect of solution pH on adsorption performance

6.4.2.1 HPLC method development for nitrobenzene analysis

6.4.2.1.1 Chromatographic method development

The first stage in the development of a HPLC-UV method for nitrobenzene was to determine the sensitivity of the molecule towards UV absorbance. A UV spectrum in the range of 200 – 350 nm of a 10 µg mL^{-1} standard solution nitrobenzene in 50:50 acetonitrile/water was acquired; the UV absorbance spectrum is shown in Figure 6.20.
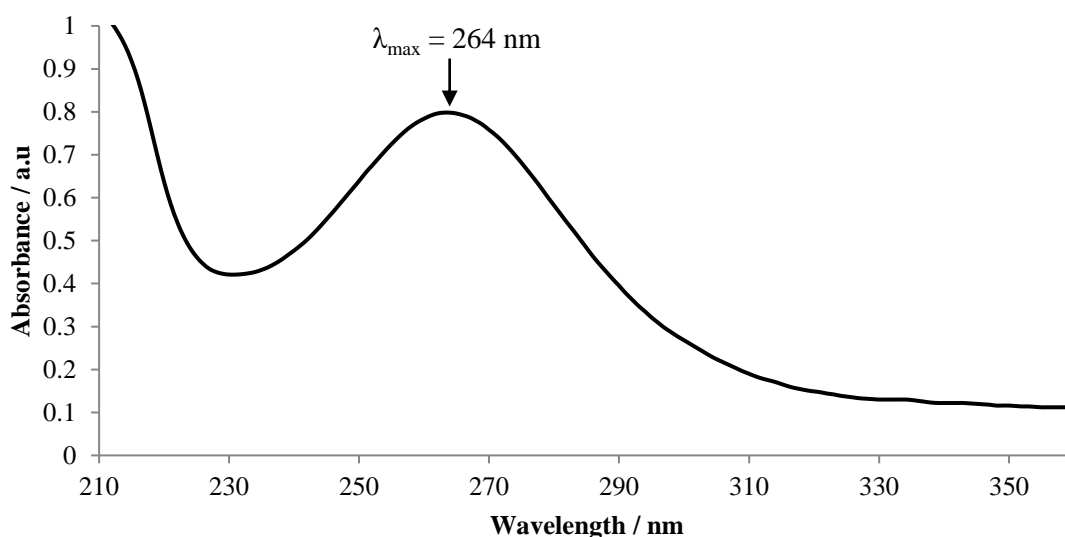
Figure 6.20: UV absorbance spectrum of 10 µg mL^{-1} nitrobenzene standard.

Figure 6.20 confirmed that nitrobenzene absorbed UV radiation with the UV spectrum containing a peak with a maximum absorbance at a wavelength of 264 nm.

The development of a simple and efficient yet reproducible, accurate and sensitive HPLC-UV method is key for the quantification of nitrobenzene. As discussed in detail in Section 2.2.2 and Section 3.4.1.1, there are a number of factors that play an important role in the chromatography of a molecule and thus variables that require optimisation. After investigations into stationary phase, mobile phase composition, pH and flow rate the final chromatographic conditions, used throughout this investigation are outlined as follows:

Nitrobenzene was separated on a Zorbax C18 column (Zorbax SB-Phenyl, 4.6 x 150 mm, 5 μm). Isocratic elution was employed using the following mobile phase: 40:60 acetonitrile/distilled water. The flow rate was 1.4 mL min^{-1}. UV detection was set at a wavelength of 268 nm.

Acquired using the chosen HPLC-UV conditions, detailed above, the chromatogram obtained from analysis of a 5 ug mL^{-1} standard solution of nitrobenzene is shown in Figure 6.21.
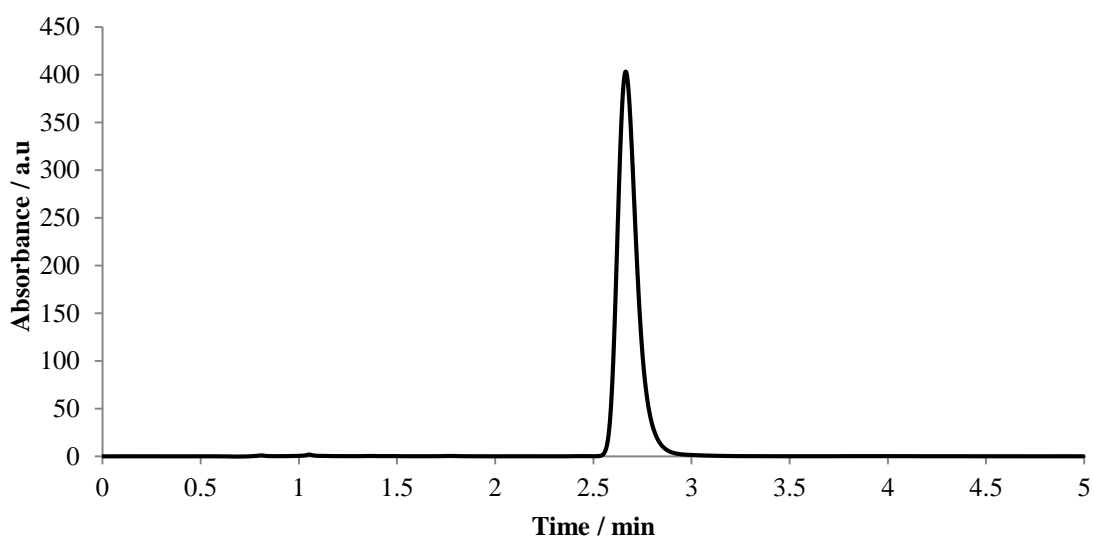
Figure 6.21: Chromatogram of 5 μg mL^{-1} nitrobenzene standard solution (RT = 2.68 min).

The chromatogram illustrates the nitrobenzene peak at a retention time (RT) of 2.68 min. As a result, a short analysis time of 5 min was selected thus producing an efficient method.

6.4.2.1.1 Assessment of HPLC method: calibration and validation

The chromatographic method for nitrobenzene was validated by establishing the limit of detection, linear range, accuracy, precision and reproducibility of the method through the analysis of calibration solutions. Calibration standard solutions (0.001 – 100 μg mL^{-1}) were prepared as outlined in Table 6.4 and analysed using the HPLC conditions listed in Table 6.6. This was performed regularly, for each new set of samples that were analysed. An example of the resulting regression line for nitrobenzene is given in Figure 6.22.
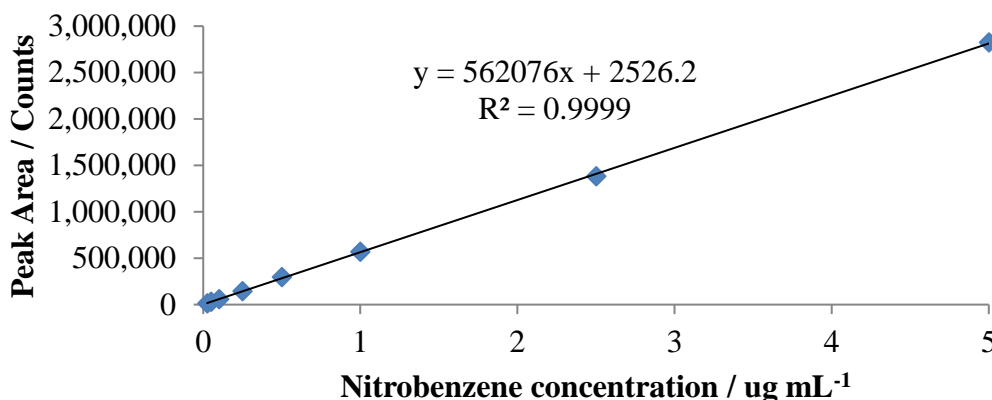
Figure 6.22: Calibration line obtained from analysis of nitrobenzene standard solutions using HPLC.

By examination of the regression line and the correlation coefficient the method was shown to produce a linear signal response, $R^2 \geq 0.9998$ and be acceptable for quantitative analysis over a range from 0.025 – 5 µg mL^{-1}. All standards within these ranges were within +/- 10 % of nominal concentrations demonstrating a high degree of accuracy for nitrobenzene. The lower concentration calibration standards, 0.001 - 0.01 µg mL^{-1}, were found to be below the limit of detection, BLD, or outside +/- 10 % of nominal concentrations and therefore were not analysed in subsequent calibrations. At higher concentrations the detector experienced saturation and the calibration line deviated from linearity, becoming curved.

To establish the accuracy and precision of the method nitrobenzene standard solutions at three different levels, low, medium and high concentrations within the linear range of each compound, were analysed in replicates of 4. The three concentrations analysed were 0.05, 0.5 and 5 µg mL^{-1}. The variations between replicates at each concentration level are shown in Table 6.17.

Table 6.17: %RSD values obtained from the analysis of 3 concentrations of nitrobenzene solution, analysed in replicates of 4.

Concentration / ug mL^{-1}	%RSD
0.05	1.84
0.5	0.24
5	0.22

The % relative standard deviation (RSD) values obtained across the peak areas at each compound concentration are all under 5 % which demonstrated that the peak area did not vary significantly with each replicate injection, at the three different concentrations. This suggested excellent precision of the chromatographic method.

6.4.2.2 Effect of pH on nitrobenzene adsorption

The performance of 7 different sorbents: PAC, Calc MCM-41, As-syn MCM-41, Calc Bio-Si, As-syn Bio-Si, Calc Fe Bio-Si and As-syn Fe Bio-Si for the adsorption of nitrobenzene from aqueous solutions was assessed. The effect of varying solution pH on sorbent performance is shown in Figures 6.23 (a) and (b) for PAC and all silica material, respectively.
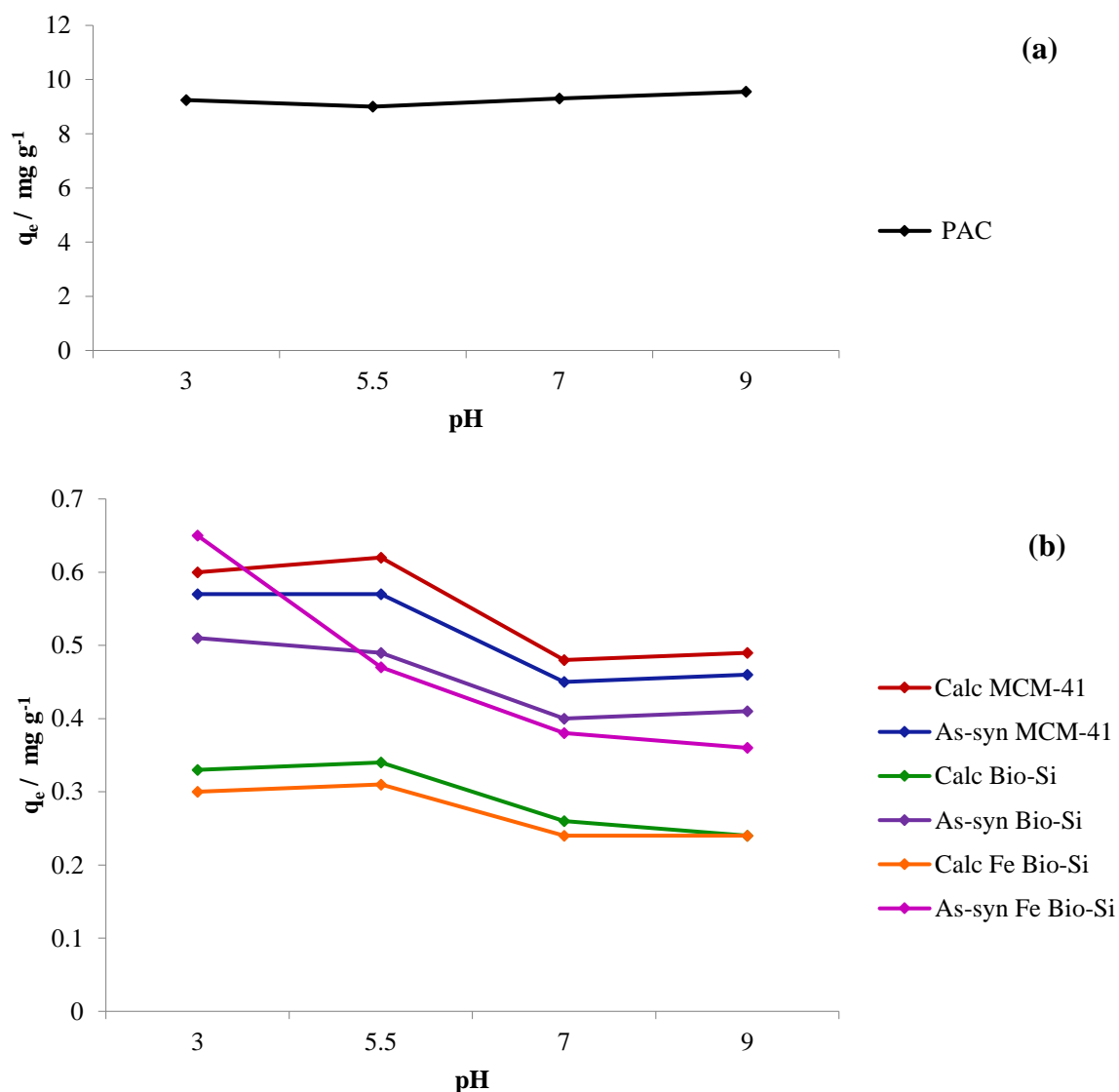
Figure 6.23: Effect of pH on nitrobenzene adsorption using (a) PAC and (b) Calc MCM-41, As-syn MCM-41, Calc Bio-Si, As-syn Bio-Si, Calc Fe Bio-Si and As-syn Fe Bio-Si.

As observed with the investigation into the adsorption of pharmaceuticals, the activated carbon material (PAC) was shown to be the superior performing sorbent with the highest affinity for nitrobenzene. From examination of the nitrobenzene structure (Table 6.2), the

increased adsorption observed using PAC could be explained by the aromaticity of the molecule. It would suggest that the main non-electrostatic forces driving nitrobenzene adsorption is π-π dispersion interactions between the aromatic ring of the target molecule and the aromatic structure of the graphene layers of the PAC.

Nitrobenzene adsorption using the silica containing materials appeared to follow the general pattern: MCM-41 materials > As-syn Bio-Si and Fe Bio-Si materials > Calc Bio-Si and Fe Bio-Si materials. Calc MCM-41 exhibits the highest adsorption performance, which could be governed by the high surface area of the material. However, the performance of the remaining sorbents do not appear to be related to material surface area, with the As-syn MCM-41 and As-syn Bio-Si sorbents displaying the smallest surface areas. This indicates the possibility that the surfactant template and amine additive are playing a key role in the adsorption of nitrobenzene. The exception to the general adsorption pattern is As-syn Fe Bio-Si at pH 3 which demonstrated the highest nitrobenzene adsorption with a q_e value of 0.65 mg g^{-1}. This signifies that the presence iron was a dominating factor in nitrobenzene removal and suggests of the possibility of co-operative effects from the amine additive, PEHA, and iron enhancing the adsorption. This is in combination with the increase in surface area observed for as-synthesised bioinspired materials when iron is incorporated.

Lower adsorption of nitrobenzene was observed for each silica material at pH 5.5 and 9. Nitrobenzene is regarded as a non-ionisable compound over the pH range, however, the deactivating nitro group on the molecule withdraws electron density from the aromatic ring, leaving it with a partially positive charge. With an isoelectric point of 4, the silica surface has a net positive charge at pH less than this value and negative above this. Attractive forces would therefore be expected between the partially positive charge on the nitrobenzene and negative charge on the adsorbent surface thus increasing adsorption interaction, however, this is not the case. The variation observed in nitrobenzene adsorption by the silica materials with pH may therefore be as a result of changes in the stability of the silica structure under different pH conditions.[330] It is well documented that MCM-41 material is relatively stable with high acid resistance, whereas degradation is observed in basic solutions due to dissolution.[331, 332] Therefore, raising the pH would lead to a decrease in the surface area available for adsorption and as well as a decrease in the hydrophobic character, which ultimately results in a decrease in nitrobenzene adsorption observed for the silica materials at higher pHs.

6.5 Conclusion

The performance of 7 different sorbents: PAC, Calc MCM-41, As-syn MCM-41, Calc Bio-Si, As-syn Bio-Si, Calc Fe Bio-Si and As-syn Fe Bio-Si, was assessed for the adsorption of pharmaceuticals from multi-analyte aqueous solution. The target pharmaceutically active compounds were acetaminophen, sulfamethoxazole, caffeine and carbamazepine. The bioinspired silica materials, both with and without the incorporation of iron, were shown to be the lowest performing sorbents for the adsorption of the target pharmaceuticals. Calc Bio-Si, As-syn Bio-Si and As-syn Fe Bio-Si all had q_e values < 0.1 mg g^{-1} for each pharmaceutical at each solution pH with the Calc Fe Bio-Si presenting similarly low q_e values of less than 0.25 mg g^{-1}. In comparison, the MCM-41 materials were shown to perform better with a high q_e of 1.21 mg g^{-1} for the adsorption of sulfamethoxazole onto As-syn MCM-41. However, PAC proved to be the superior sorbent by far with q_e values between 6 and 12 mg g^{-1} for each pharmaceutical at each solution pH. These results indicate that sorbent performance improves with increasing material surface area.

Batch adsorption experiments were carried out using the 3 best performing sorbents, varying contact time, initial pharmaceutical concentration and solution pH. As-syn MCM-41 and Calc MCM-41 were shown to perform more efficiently under acidic conditions with the adsorption shown to decrease with an increase in pH, predominately as a result of changes in silica surface chemistry. The pH of the solution failed to have a significant effect on PAC adsorption. It was proposed that non-electrostatic interactions including π-π dispersion and hydrophobic interactions govern the adsorption of the pharmaceutical molecules onto the sorbents.

In terms of adsorption kinetics, it was demonstrated that adsorption of pharmaceuticals onto both sorbents, As-syn MCM-41 and PAC, best fitted the pseudo second order model. This would infer that chemisorption was playing a significant role in the rate-limiting step which contradicted the previous hypothesis and therefore the process was investigated further by fitting the data to the Weber-Morris intra-particle diffusion model. Both sorbents were shown to share a common adsorption mechanism and a two-stage process was proposed involving an initial steeper step, representing the boundary layer diffusion of solute molecules, and secondly a gradual adsorption stage attributed to intra-particle diffusion. Each mechanism was found to contribute to the adsorption kinetics with intra-particle diffusion being the rate determining step in both adsorption processes. Adsorption isotherm data was shown to be

better described by the Freundlich isotherm model than the Langmuir isotherm model, indicating that both sorbent surfaces were heterogeneous. The corresponding Freundlich constants (K_f and n) also revealed the superior performance, in terms of adsorption capacity, of PAC in comparison to As-syn MCM-41 for pharmaceutical adsorption. PAC proved to not only have a higher affinity for each pharmaceutical (greater n values) but also a significantly higher total adsorption capacity, successfully adsorbing ~16 times the mass of pharmaceuticals adsorbed by As-syn MCM-41.

As observed with the investigation into the adsorption of pharmaceuticals, PAC was shown to be the superior performing sorbent with the highest affinity for nitrobenzene. Nitrobenzene adsorption using the silica containing materials appeared to follow the general pattern: MCM-41 materials > As-syn Bio-Si and Fe Bio-Si materials > Calc Bio-Si and Fe Bio-Si materials. Calc MCM-41 exhibited the highest adsorption performance, possibly governed by the high surface area of the material. The surfactant template and amine additive in As-syn MCM-41 and As-syn Bio-Si, respectively, were thought to play a key role in the adsorption of nitrobenzene by these materials. The high nitrobenzene adsorption performance observed by As-syn Fe Bio-Si at pH 3 demonstrated that the presence of iron was a dominating factor in nitrobenzene removal and indicates the possibility of co-operative effects from the amine additive, PEHA, and iron enhancing the sorbent performance.

Both investigations into adsorption of target contaminants in aqueous solutions have shown PAC to be the dominant sorbent which supports the, already extensive, use of activated carbon in water purification and wastewater treatments. This material is known to exhibit a heterogeneous pore structure in which micropores and mesopores are present.[333, 334] In particular, the micropore surface area in activated carbon has been shown to contribute approximately 60 to 80 % of the total surface area,[333, 334] thus, providing predominant adsorptive sites with higher adsorption energies for the removal of organic contaminants from aqueous solutions. In addition, the smaller particle size of powdered activated carbon in comparison to other commercially available granular activated carbons is advantageous as the adsorption rate of analytes from solution is improved due to a shorter travel distance for intraparticle diffusion and the larger surface area generated.[335]

However, there are drawbacks with using activated carbon as a sorbent for water remediation. The micropores that contribute to the majority of the activated carbon surface area, as well as increasing the total surface area, can have irregular shaped, closed pore structures. Therefore, adsorption of larger organic molecules might be significantly impeded by the size-exclusion

effect. Furthermore, activated carbons are known to be susceptible to pore clogging, which can be an issue in 'real' water samples where the matrix is complex. In addition, they have been reported to be difficult to separate from aqueous systems when they become exhausted and are also known to be difficult to regenerate,[304] with chemical and thermal regeneration procedures proving expensive and reporting loss of sorbent.[336]

The development of novel processes for water purification and the abatement of contaminants in wastewaters has become an important challenge with attention being drawn to techniques such as photocatalysis and chemical oxidation processes to reliably remove the pollutant molecules.[337]

7. Advanced oxidation technologies for the abatement of water contaminants.

7.1 Introduction

In the previous chapter powdered activated carbon (PAC) was shown to be the superior performing sorbent for the adsorptive removal of both sets of target contaminants, pharmaceutically active compounds and nitrobenzene, from aqueous solutions. However, this traditional adsorption technique using activated carbon is restricted in application because of several inherent drawbacks. Firstly, the process of adsorption fails to destroy the contaminants but merely transfers them from solution to a sorbent which, after a certain concentration is reached, requires regeneration and a further treatment of the adsorbates. The surface area of activated carbon is primarily composed of micropores which can be irregular shaped, closed pore structures and thus might impede the adsorption of larger organic molecules. In addition, the use of activated carbons in 'real' water samples where the matrix is complex can be problematic as they are known to be susceptible to pore clogging. Furthermore, they have been reported to be difficult to separate from aqueous systems when they become exhausted and are also known to be difficult to regenerate,[304] with chemical and thermal regeneration procedures proving expensive and reporting loss of sorbent.[336]

Therefore, alternative abatement methods are needed to overcome this disadvantage. In this Chapter the use of advanced oxidation techniques are investigated through the application of the photo-Fenton process and visible-light initiated photocatalytic oxidation. These techniques will be assessed for the removal of the same contaminant target sets as examined in Chapter 6: pharmaceutically active compounds and nitrobenzene. The pharmaceuticals examined are acetaminophen, carbamazepine, sulfamethoxazole and carbamazepine.

7.1.1 The Fenton process for water remediation

The application of advanced oxidation technologies (AOTs) has emerged as an important alternative for the efficient treatment of organic pollutants through the generation of very reactive and non-selective hydroxyl radicals.[338-341] Among these technologies, the Fenton process, which can generate •OH through the catalytic reaction of Fe^{2+}/ Fe^{3+} in the presence of H_2O_2, has been regarded as one of the most economical alternatives. It is long believed[342] that the mechanism of the Fenton oxidation system (Fe^{3+}/H_2O_2) involves the reduction of Fe^{3+} to Fe^{2+} (Equation 7.1). The Fe^{2+} formed then reacts with H_2O_2 to generate •OH radicals

(Equation 7.2), which are capable of oxidising and degrading organic compounds to smaller, less polluting molecules or even mineralising them[343] (Equation 7.3).

$$Fe^{3+} + H_2O_2 \rightarrow Fe^{2+} + \bullet OOH + H^+ \qquad \textbf{Equation 7.1}$$

$$Fe^{2+} + H_2O_2 \rightarrow Fe^{3+} + \bullet OH + OH^- \qquad \textbf{Equation 7.2}$$

$$\bullet OH + \text{organic compounds} \rightarrow \text{oxidised products} \qquad \textbf{Equation 7.3}$$
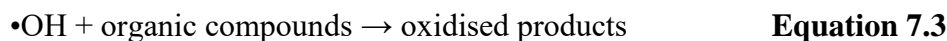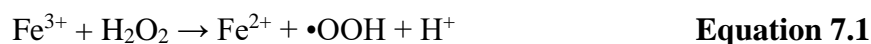
The oxidation efficiency of the Fenton reagent can be greatly enhanced by light irradiation (photo-Fenton reaction) due to the regeneration of Fe^{2+}, which in turn promotes additional generation of $\bullet OH$ radicals (Equation 7.4).

$$Fe(OH)^{2+} + hv \rightarrow Fe^{2+} + \bullet OH \qquad \textbf{Equation 7.4}$$

It is an attractive method for the effective degradation of pollutants because of its low cost, Fe is widely available, hydrogen peroxide is easily handled, the operating conditions are usually mild and the excess reagents can be decomposed into environmentally safe products. However, the application of homogeneous Fenton systems has disadvantages; commonly up to 50 - 80 mg L^{-1} of iron ions in solution are required, a concentration significantly higher than the European Union (EU) directive which permits only 2 mg L^{-1} of iron in treated water to be released directly into the environment. In order to remove the iron ions from solution and treated sludge, separation and recovery techniques are necessary with additional operational costs. Furthermore, homogeneous Fenton catalysts are difficult to recycle[344, 345] and the reaction is limited by the narrow, acidic working pH, preferably between 2.5 and 3.5, required for efficient catalytic performance. To overcome these drawbacks[346] and extend the working pH range, many efforts have been made to develop heterogeneous Fenton and photo-Fenton catalysts, including immobilisation of Fe ions, Fe clusters or iron oxides on solid supports. It is well accepted that the most important factors in the development of a heterogeneous Fenton catalyst are a combination of high catalytic activity and long-term stability at reasonable cost as well as the possibility of employing the system in pH environments near neutrality. Most work refers to iron catalysts supported on zeolites[347, 348] and activated carbon.[349-352] However, silica materials such as silica gels[353] and mesoporous silica including SBA-15[354-356]and MCM-41[357] have also been used. Recently the development of bio-inspired methods for the synthesis of 'green' nanomaterials has received more attention in the literature.[90, 104, 358] Through understanding the mechanism of biological silica

formation in organisms, porous silica materials can be prepared using green routes that mimic the biomineralisation process.[84, 92] The use of a bio-inspired method for the synthesis of a heterogeneous Fenton catalyst proves attractive due to the ease of synthesis, the use of less toxic reagents and environmentally friendly conditions with waste of neutral pH which can be easily disposed of and the cost effectiveness resulting from the process requiring little energy input. Also a high level of control over the product is maintained through the use of synthetic 'additives' to produce silica under rapid and mild conditions.[359]

7.1.2 Visible-light photocatalysis using iron incorporated titanium dioxide for water remediation

Photocatalytic oxidation has been an active area of research for several years as a technique of water pollution abatement. TiO_2 is one of the most commonly used photocatalysts for pollutant degradation.[360-365] Owing to its advantageous properties;[366, 367] the stability of its chemical structure, biocompatibility, strong oxidizing power, non-toxicity, low cost and capability of mineralising pollutants completely, it has been largely applied as a catalyst for water decontamination.[368, 369] However, its application is limited and technological use restricted by the need for UV excitation source for photocatalytic activity. For widespread applications, development of TiO_2 photocatalysts that are effective under visible radiation or solar light is essential in order to harvest maximum energy from the sunlight. TiO_2 adsorbs only 3-5 % of energy from the solar spectrum[370, 371], hence, in an attempt to extend the photo-response and to enhance the photocatalytic activity of TiO_2, studies have focussed on modifying its surface structure, surface properties and composition to sensitise the TiO_2 material for absorption of light in the visible region.[372-376] Surface modification by doping with metal ions,[377-382] and non-metals[383-386] has proven to be an efficient route to improve the photocatalytic activity of TiO_2. Doping iron, the Fe^{3+} ion, into the titania structure is a promising candidate to modify the optical properties of TiO_2 and has been found to be successful in shifting the adsorption into the visible region.[387-395] With narrow band gap energy (1.9 eV) it has the potential to enhance the photocatalytic features of titania due to its half-filled electronic configuration and the similarity of the ionic radii of Fe^{3+} (0.64 A) and Ti^{4+} (0.68 A).[396] Several authors claim that the incorporation of Fe^{3+} into titania improves the

photocatalytic features of the sample by reducing the band gap energy by about 2 eV and extending the photoexcitation response to the visible region.[397-401]

Design of a TiO$_2$ synthesis method that is capable of producing a material with a well-defined mesoporous structure is also a promising way to achieve high photocatalytic activity since mesopore channels can facilitate rapid intraparticle molecular transfer.[402-404] Synthesis of mesoporous TiO$_2$ has been documented in the literature.[405-407] Such a method was previously used in Chapter 5 to synthesise mesoporous TiO$_2$ thin film coated glass beads which proved successful for the degradation of VOCs from indoor air.

Since mesoporous TiO$_2$ is not photocatalytically active in the visible-light region without the presence of a photosensitiser, this study investigates the introduction of iron oxide (Fe$_2$O$_3$) to this mesoporous material and examines the effect it has on its performance under visible or solar irradiation. In previously discussed studies, it is common for the photosensitiser to be added to the already prepared TiO$_2$ catalyst in a separate synthesis step. In contrast to such a technique, the synthesis method reported in this work demonstrates the in-situ synthesis of mesoporous iron oxide (Fe$_2$O$_3$)-TiO$_2$ composite photocatalyst, prepared using a sol-gel and self-assembly approach. The advantage of such a method is that the technique demonstrates a uniform dispersion of iron throughout the composite. With the addition of iron oxide to the reaction mixture, Fe ions can be inserted into the TiO$_2$ structure located in interstices or replacing Ti ions in the Ti-O-Ti network[408] since Fe^{3+} has an ionic radius of 0.69 A while that of Ti^{4+} is 0.64 A, thus, it is possible to form a solid solution in the TiO$_2$ matrix. In comparison to materials prepared by doping the TiO$_2$ catalyst with Fe ions in a subsequent reaction step where the Fe is largely confined to the surface and pore openings of TiO$_2$, the surfactant templated, sol-gel approach allows an even distribution of Fe from the exterior to the interior of the TiO$_2$ framework thereby enhancing the interfacial interaction in addition to charge transfer. Localised bands are formed near the bottom of the conduction band thereby decreasing the band gap energy and extending light absorbance to the visible region.

In view of the features exhibited by this preparation technique, the presented study reports the synthesis, using P123 tri-block copolymer by the sol-gel method, and the coating of this composite solution onto glass bead supports to produce mesoporous Fe-TiO$_2$ thin films. These thin film catalysts are then examined for the photocatalytic degradation of nitrobenzene in solar light.

7.1.3 Aims and objectives

In this study the versatility of iron incorporated bio-inspired silica (Fe Bio-Si) as a heterogeneous Fenton catalyst for water remediation is examined using the same target sets investigated in Chapter 6: pharmaceutically active compounds and nitrobenzene. In addition, the degradation of nitrobenzene is briefly examined through the application of UV and visible-light photocatalysis using TiO_2 and $Fe-TiO_2$ as photocatalysts, respectively.

7.2. Experimental

7.2.1 Materials and reagents

Hydrochloric acid (HCl, 37 %) and HPLC grade acetonitrile (MeCN) were supplied by Fisher Scientific. Titanium (IV) isopropoxide (97 %), absolute ethanol, hydrogen peroxide (H_2O_2, 30 %) and iron (III) nitrate nonahydrate ($\geq$ 99 %) were purchased from Sigma Aldrich. Pluronic P123 block copolymer was supplied by the BASF Corporation. Glass beads (600 – 800 μm) were purchased from Sigma Aldrich.

Acetaminophen ($\geq$ 99 %), carbamazepine ($\geq$ 99 %), caffeine (European Pharmacopoeia, Ph Eur, grade), sulfamethoxazole (analytical standard grade) and nitrobenzene were all purchased from Sigma Aldrich. As-syn Fe Bio-Si and Calc Fe Bio-Si were synthesised as detailed in Section 3.2.4.

TiO_2 thin film coated glass beads were prepared as outlined in Section 5.2.2.

7.2.2 Determination of nitrobenzene and pharmaceuticals in aqueous samples using HPLC-UV

The concentration of nitrobenzene and each pharmaceutically active compound in solution before and after adsorption was determined using a TSP HPLC system combined with P2000 pump, AS3000 autosampler and UV1000 detector. The HPLC-UV operating conditions used for the analysis of nitrobenzene and the target pharmaceuticals are outlined in Table 6.6 and 6.5, respectively. In brief, for both sets of analytes chromatographic separation was achieved

isocratically on a C18 column (Zorbax SB-Phenyl 5 µm, 4.6 x 150 mm). For nitrobenzene a mobile phase of acetonitrile/water (50:50, v/v) was used at a flow rate of 1.4 ml min^{-1} with UV detection at 264 nm. For the pharmaceutical mixture, a mobile phase of acetonitrile/ water (40:60, v/v) was used at a flow rate of 1.4 ml min^{-1} with UV detection at 270 nm. The calibration lines produced for each were found to be reproducible and linear ($R^2 > 0.999$) over the concentration range used in this work, examples of which are displayed in Figures 6.5 and 6.22 for the pharmaceutical compounds and nitrobenzene, respectively.

7.2.3 Photo-Fenton reactions

It is well known that the efficiency of Fe based Fenton-like systems can be substantially enhanced in the presence of UV ($\lambda > 250$ nm) light irradiation. This enhancement is due to regeneration of the consumed Fe^{2+} ions (i.e. reduction of Fe^{3+} to Fe^{2+}), as shown in Equation 7.4. In addition, depending on the irradiation wavelength, photochemical processes such as H_2O_2 photolysis and substrate photolysis may also play some role in the photo-enhanced systems.[409] The heterogeneous Fenton-like reaction was initiated by the addition of H_2O_2 to the solution. The effect of these parameters on the performance of the As-syn and Calc Fe Bio-Si materials as heterogeneous Fenton catalysts were investigated.

7.2.3.1 Photo-Fenton reactor

Experiments assessing the performance of the As-syn and Calc Fe Bio-Si materials as heterogeneous photo-Fenton catalysts were performed using a photoreactor set-up. The reaction took place inside a 30 mL cylindrical quartz vessel, containing either the pharmaceutical mixture or nitrobenzene solution and the catalyst being examined. The heterogeneous Fenton-like reaction was initiated by the addition of H_2O_2 to the solution. Illumination was provided by two near UV/Vis light sources: a 2 x 4 W blacklight blue, BLB, lamp (UVITEC, Cambridge, UK) and a 4 W BLB lamp (UVP Ltd, Cambridge, UK). Both emit photons with wavelengths in the region of 300 – 425 nm with a maximum light intensity output at 365 nm. Light was focused onto the quartz vessel; positioned at either side, approximately 40 mm away.

7.2.3.2 Batch photo-Fenton reactions

Batch photo-Fenton catalytic experiments were conducted in cylindrical quartz vessels using constant volumes, 25 mL, of nitrobenzene or mixed pharmaceutical solution at pH 3 into which accurately weighed amounts of catalyst (50 mg) were suspended. For both target sets, the starting concentration of either nitrobenzene or mixed pharmaceutical solution remained fixed at 2.5 µg mL^{-1}. Reactions were initialised with the addition of 100 mM H_2O_2 and allowed to proceed for 2 h at room temperature, under UV irradiation and a stirring rate of 300 rpm. A stirring rate of 300 rpm was shown to be sufficient to ensure good dispersion and minimise mass transfer effects. After 2 h, the solution was filtered (Fisherbrand QL 100) and the filtrate solution subsequently analysed by HPLC-UV, using the conditions outlined in Section 7.2.2, to establish the concentration of unreacted target compound remaining after the photo-Fenton reaction (C_1). The concentration of each starting solution was also determined (C_0) and the photocatalytic efficiency of each material was calculated, in terms of degradation percentage, using Equation 7.5.

$$\text{Degradation (\%)} = C_1 / C_0 \times 100 \qquad \textbf{Equation 7.5}$$

For assessing nitrobenzene degradation, preliminary experiments were conducted to determine the optimum hydrogen peroxide concentration required for maximum catalytic efficiency by varying the concentration added to the reaction mixture; 5, 10, 50, 100 and 200 mM.

For both target set, nitrobenzene and the pharmaceutically active compounds, control experiments were performed to evaluate the contribution made to the reaction by adsorption onto the catalyst, direct photolysis of H_2O_2 under UV irradiation and to assess the activity of the catalyst under dark-Fenton reaction conditions. This involved carrying out three sets of experiments where either the catalyst, 100 mM H_2O_2 and UV irradiation, or the catalyst and H_2O_2, were present.

All reactions were repeated in triplicate and analysed using the conditions detailed in Section 7.2.2. Results are reported as the average of these replicates.

7.2.3.3 Heterogeneous Fenton catalyst re-use

One of the most important advantages of heterogeneous catalysts is their capability of reuse.[410-413] Previous experiments showed that for nitrobenzene degradation, the Calc Fe Bio-Si material was the better performing catalyst under the optimised H_2O_2 concentration of 100 mM. To estimate the long-term performance of this catalyst for the degradation of nitrobenzene, the reuse of Calc Fe Bio-Si was assessed in 15 consecutive reaction cycles. The experimental procedure detailed in Section 7.2.3.2 was used, however in between each reaction, the catalyst was separated from the solution by filtration and introduced to a new 2.5 $\mu g \; mL^{-1}$ nitrobenzene solution at pH 3 with fresh H_2O_2 added to initiate the reaction. This procedure was carried out 15 times. The re-use of Calc Fe Bio-Si was also performed at pH 7 to assess the catalyst performance under neutral conditions.

Investigation into the long-term performance of both As-syn Fe Bio-Si and Calc Fe Bio-Si was conducted for the degradation of the pharmaceutically active compound mixture. The re-use of each catalyst was assessed in 6 consecutive reaction cycles at a solution pH of 3 and 7. As with the nitrobenzene study, reactions were initialised with 100 mM H_2O_2, the catalyst separated from solution by filtration and introduced to a new 2.5 $\mu g \; mL^{-1}$ pharmaceutical mixture solution with fresh H_2O_2 added to reinitialise the reaction.

7.2.4 Visible-light photocatalysis reactions

The process of photocatalytic oxidation and the use of titanium dioxide (TiO_2) as the photocatalyst of choice are discussed in detail in Section 5.1. The TiO_2 thin film coated glass beads used in Chapter 5 for the investigation of photocatalysis as an air remediation technique were used further in the assessment of nitrobenzene degradation in water. In view of increasing the photocatalytic activity of TiO_2 and enhancing the application of this photocatalyst for use in the visible-light region, mesoporous iron incorporated TiO_2 (Fe-TiO_2) was synthesised using a sol-gel and self-assembly approach.

The photocatalytic activity of the Fe-TiO_2 material in the visible light region, using sunlight as the energy source, was then evaluated for the photodegradation of nitrobenzene in aqueous solutions. In addition, as a set of control experiments, pure mesoporous TiO_2 was also

assessed under the same conditions. This allowed the incorporation of iron as a photosensitiser to be evaluated.

7.2.4.1 Preparation of iron incorporated titanium dioxide (Fe-TiO$_2$) thin film photocatalyst

Mesoporous titanium dioxide coated glass beads were previously synthesised as detailed in Section 5.2.2.

Mesoporous iron incorporated titanium dioxide was prepared via the same surfactant templated, sol gel synthesis method. In brief, a triblock copolymer, P123, was employed as a structure directing agent, titanium (IV) isopropoxide as a Ti source and iron (III) nitrate as the iron source. Removal of the organic template from the catalyst was carried out by calcination. Two batches of iron incorporated titanium dioxide were produced with differing weight percentages of 20 % and 50 % iron. In a typical synthesis 1.01 g or 2.57 g (for 20 % and 50 % iron, respectively) iron (III) nitrate was added to 4.2 g of titanium (IV) isoproxide, this mixture subsequently dissolved in 3 cm^3 of concentrated HCl and stirred at room temperature for 10 min. A separate solution was then prepared where 1.3 g of P123 co-polymer was dissolved, under slight heating, in 12 g of ethanol. Both solutions were then mixed and stirred for a further 15 min. Glass beads (600 – 800 µm) were coated with the resulting Fe-TiO$_2$ gel and left overnight in the fridge. Beads were then calcined at 400 °C for 10 min (heated at 25 °C min^{-1} to 400 °C and held at for 10 min). This technique generated a mesoporous Fe-TiO$_2$ thin film on the surface of the support materials. The procedure was repeated daily until glass beads with 1 to 5 coatings of Fe-TiO$_2$ thin film were prepared.

7.2.3.2 Batch TiO$_2$ and Fe-TiO$_2$ photocatalysis reactions

Batch photocatalytic experiments were conducted in glass beakers or quartz vessels (for the application of visible-light and UV irradiation, respectively) using constant volumes, 25 mL, of nitrobenzene at pH 5.3 (no pH adjustment to nitrobenzene solution) into which accurately weighed amounts of Fe-TiO$_2$ catalyst (100 mg) were suspended. The starting concentration of nitrobenzene solution remained fixed at 2.5 µg mL^{-1}. Reactions were allowed to proceed for 2

h at room temperature, under natural visible-light conditions, and a stirring rate of 300 rpm. A stirring rate of 300 rpm was shown to be sufficient to ensure good dispersion and minimise mass transfer effects. After 2 h, the solution was filtered (Fisherbrand QL 100) and the filtrate solution subsequently analysed by HPLC-UV, using the conditions for nitrobenzene outlined in Section 7.2.2, to establish the concentration of unreacted target compound remaining after the photocatalytic reaction (C_1). The concentration of each starting solution was also determined (C_0) and the photocatalytic efficiency of each material was calculated, in terms of degradation percentage, for nitrobenzene using Equation 7.5.

These reactions were conducted using Fe-TiO$_2$ thin film glass beads coated 1-5 times with the catalyst material to assess the optimum number of coatings required to obtain the highest photocatalytic activity in terms of nitrobenzene degradation.

Analogous experiments were conducted in quartz vessels using TiO$_2$ coated glass beads under UV irradiation.

7.3. Results and discussion

7.3.1 Photo-Fenton reactions

7.3.1.1 Optimum H_2O_2 concentration for nitrobenzene degradation

The H_2O_2 concentration required for maximum catalytic activity for nitrobenzene degradation was investigated using both As-syn and Calc Fe Bio-Si materials. Figure 7.1 shows the photo-assisted Fenton degradation of nitrobenzene with different H_2O_2 concentrations. With increasing H_2O_2 concentrations, from 5 mM to 100 mM, the average degradation efficiency of nitrobenzene (% RSD values less than 2 %) was shown to increase from 37 to 67 % for Calc Fe Bio-Si and from 30 to 52 % for As-syn Fe Bio-Si. This is a consequence of the formation of more hydroxyl radicals generated by the reaction of the formed Fe^{2+} with H$_2$O$_2$ as discussed previously in Section 7.1.1 and Equation 7.2 (shown again below). These are subsequently available to oxidise and degrade organic compounds such as nitrobenzene as shown in Figure 7.6.

$$Fe^{2+} + H_2O_2 \rightarrow Fe^{3+} + \bullet OH + OH^- \qquad \textbf{Equation 7.2}$$
$$RH + \bullet OH \rightarrow H_2O + R\bullet \rightarrow \text{further oxidation} \qquad \textbf{Equation 7.6}$$
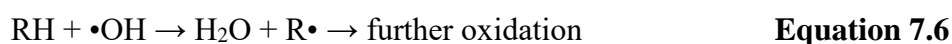
A H_2O_2 concentration of 100 mM was found to promote the highest performance for Calc Fe Bio-Si however a lower concentration of 10 mM was shown to be sufficient for As-syn Fe Bio-Si to reach a maximum efficiency of 52 % where the % degradation subsequently plateaued. Literature indicates that at high concentrations, the excessive H_2O_2 may act as a hydroxyl radical 'scavenger', with the hydroperoxyl radical ($HO_2\bullet$) being less effective in the degradation of nitrobenzene than $\bullet OH$ thus causing a detrimental effect on degradation process. However, as shown in Figure 7.1, this was not found to be the case with a higher H_2O_2 concentration of 200 mM making no further change to the performance of the systems.
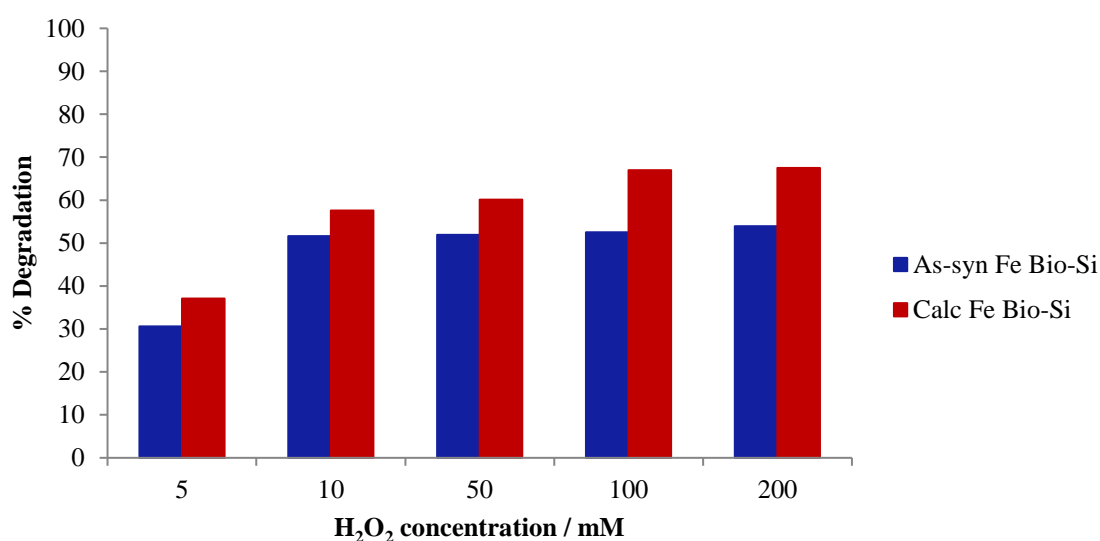
Figure 7.1: % degradation of nitrobenzene with varying H_2O_2 concentration.

7.3.1.2 Contribution of individual parameters – catalyst adsorption, UV irradiation and H_2O_2

For both target sets, nitrobenzene and the pharmaceutically active compounds, control experiments were performed to evaluate the contribution made to the reaction by adsorption onto the catalyst, direct photolysis of H_2O_2 under UV irradiation and to assess the activity of the catalyst under dark-Fenton reaction conditions. This involved carrying out three sets of experiments where only the catalyst, 100 mM H_2O_2 and UV irradiation; and the catalyst and H_2O_2, were present. Both As-syn Fe Bio-Si and Calc Fe Bio-Si catalysts were examined. The results of which are reported in Figure 7.2 for the degradation of nitrobenzene at pH 3 and in

Figure 7.3 (a) and (b) for the degradation of the pharmaceutical mixture at pH 3 and 7 using As-syn Fe Bio-Si and Calc Fe Bio-Si, respectively.

7.3.1.2.1 Nitrobenzene

The photo-Fenton reaction using 50 mg catalyst, UV irradiation and 100 mM H_2O_2 successfully produced nitrobenzene degradations, on average, of 50.5 and 67 % for As-syn Fe Bio-Si and Calc Fe Bio-Si, respectively.

The contribution of adsorption onto each catalyst to the nitrobenzene removal was examined through the reaction without the presence of UV irradiation or H_2O_2. The effect that these conditions had separately on the degradation of nitrobenzene was also investigated. As shown in Figure 7.2, around 10 % nitrobenzene was removed via adsorption onto each material at pH 3.

An enhancement in degradation percentages are observed in analogous experiments which were carried out in the absence of UV light and the presence of catalyst and hydrogen peroxide, 36 and 32 % degradation for As-syn and Calc Fe Bio-Si, respectively. This demonstrates the production of hydroxyl radicals by catalytic dark-Fenton reactions under these particular conditions.

UV light in the absence of catalyst and the presence of hydrogen peroxide yielded a substantial degradation percentage (47 %) which reveals that hydroxyl radical production by the direct photolysis of H_2O_2 under UV irradiation was significant (see Equation 7.7).

$$H_2O_2 + h\nu \rightarrow 2HO\bullet \qquad \qquad \textbf{Equation 7.7}$$

In the case of assessing the performance of each catalyst in the presence of H_2O_2 under light irradiation, Calc Fe Bio-Si exhibited moderate activity with around a 20 % enhancement in nitrobenzene degradation in comparison to H_2O_2 and UV alone. However little change in degradation was observed using As-syn Fe Bio-Si; thus, it would appear that the As-syn material exhibited no activity for photo-Fenton reactions and the sole factor controlling the degradation was direct photolysis of H_2O_2. These results would raise the question whether, for the degradation of nitrobenzene, the use of a catalyst is necessary. This finding, contrary from being a drawback, proves promising for nitrobenzene degradation from an industrial perspective. UV irradiation is already an advanced technique currently available, as a

disinfecting method, in water treatment plants, thereby, its implementation for nitrobenzene degradation and possibly the degradation of other organic pollutants would be easy and cost effective.
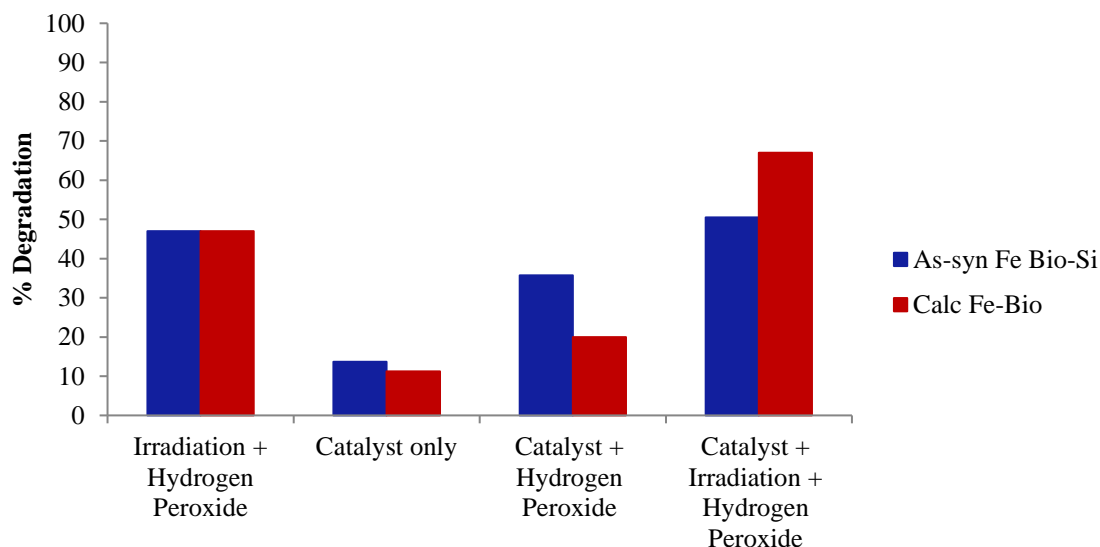
Figure 7.2: Nitrobenzene % degradation under varying reaction conditions at pH 3.

7.3.1.2.2 Pharmaceutically active compounds

Using As-syn Fe Bio-Si as a catalyst, the photo-Fenton reaction under UV irradiation and 10 mM H_2O_2 successfully degraded, on average, 100, 86.6, 97.5 and 100 % (% RSD values less than 2 %) of acetaminophen, caffeine, sulfamethoxazole and carbamazepine from the pharmaceutical mixture, respectively, at a solution pH of 3. At neutral solution pH, a significant decrease in the performance of the photo-Fenton reaction was observed with average degradations of 17.3, 4, 25.8 and 31.8 % (% RSD values less than 5 %) reported for acetaminophen, caffeine, sulfamethoxazole and carbamazepine, respectively.

Using Calc Fe Bio-Si as a catalyst, the photo-Fenton reaction under UV irradiation and 10 mM H_2O_2 successfully degraded 100, 94.3, 96.6 and 100 % (% RSD values less than 1 %) of acetaminophen, caffeine, sulfamethoxazole and carbamazepine from the pharmaceutical mixture, respectively, at a solution pH of 3. As observed with the as-synthesised material, at neutral solution pH a significant decrease in the performance of the photo-Fenton reaction was observed with avaerge degradations of 27.4, 33.3, 32.9 and 48.7 % (% RSD values less

than 5 %) reported for acetaminophen, caffeine, sulfamethoxazole and carbamazepine, respectively.

Both catalysts were shown to perform extremely well with 100 % or nearly complete degradation of each of the four target pharmaceuticals in the solution mixture under acidic conditions. The superior performance of the photo-Fenton reaction at pH 3 highlights the importance of solution pH to the degradation efficiency and is explained in detail in the ensuing Section 7.3.1.3.

The contribution of adsorption onto each catalyst material to the removal of pharmaceuticals from the solution was examined through the reaction without the presence of UV light irradiation or H_2O_2. As shown in Figure 7.3 (a) and (b) for As-syn Fe Bio-Si and Calc Fe Bio-Si, respectively, less than 20 % of each pharmaceutically active compound was removed via adsorption onto each material at pH 3 and pH 7 for both catalyst materials.

In analogous experiments, which were carried out in the absence of UV light and the presence of catalyst and hydrogen peroxide, only a small enhancement in degradation percentages from that of the adsorption efficiencies are observed for each pharmaceutical using As-syn and Calc Fe Bio-Si at pH 3 and 7. This demonstrates that the production of hydroxyl radicals by catalytic dark-Fenton reactions were not significant under these particular conditions.

UV light in the absence of catalyst and the presence of hydrogen peroxide yielded substantial degradation percentages; 70 – 89 % and 50 – 66 % for all pharmaceutically active compounds at pH 3 and 7, respectively, with % RSD values less and 2 %. This reveals that hydroxyl radical production by the direct photolysis of H_2O_2 under UV irradiation was significant as illustrated in Equation 7.8.

In the case of assessing the performance of each catalyst in the presence of H_2O_2 under light irradiation, both catalyst materials exhibited moderate activity at pH 3 with 9 – 30 % enhancement in pharmaceutical degradation in comparison to H_2O_2 and UV alone.

However, a decrease in degradation was observed at a solution pH 7; thus, it would appear that both catalyst materials exhibited no activity for photo-Fenton reactions at neutral pH and in fact, surprisingly, would appear to inhibit the degradation caused by direct photolysis of H_2O_2. These results show that for the degradation of the four pharmaceutically active compounds at pH 7, the use of a catalyst is detrimental to the degradation process.

Figure 7.3: % degradation of each pharmaceutically active compound using (a) As-syn Fe Bio-Si and (b) Calc Fe Bio-Si as a photocatalyst under varying reaction conditions at pH 3 and pH 7.

7.3.1.3 Catalyst Re-use

7.3.1.3.1 Nitrobenzene

Despite the results reported in the previous section, which would suggest that nitrobenzene could be degraded to a great extent using the application of H_2O_2 and UV irradiation alone, the use of a catalyst was further investigated. The reusability and stability of the photocatalyst are two of the key factors for industrial applications therefore the catalytic ability of Calc Fe Bio-Si with repeat usage was determined for the degradation of nitrobenzene. The assessment

of the As-syn material performance discontinued at this stage due to its apparent inactivity towards the degradation process. To this end, the Calc Fe Bio-Si catalyst was used in 15 consecutive photo-Fenton reaction cycles; the catalyst filtered in between reactions, introduced to a new 2.5 μg mL^{-1} nitrobenzene solution at pH 3 or 7 and fresh H_2O_2 added to reinitiate the reaction. The ensuing profiles at both pH 3 and pH 7 are shown in Figure 7.4.

Under acidic conditions, the degradation percentage initially increased (70 to 95 %) then remained stable during the 15 cycles (% RSD values less than 2 %). Around 50 % of the degradation obtained during the initial cycle can be assumed to be a consequence of the direct photolysis of H_2O_2 under UV irradiation. The increase in average degradation efficiency to around 95 % observed in successive applications indicates that the catalyst exhibited good activity for photo-Fenton reactions at pH 3 and could be explained by the surface of the catalyst being activated during the initial cycle. Accordingly, with repeated usage, there was an obvious synergistic effect between the photocatalysis of Calc Fe Bio-Si and H_2O_2 oxidation which significantly accelerates the degradation of nitrobenzene.

The extent of direct UV photolysis of H_2O_2 on the degradation of nitrobenzene at pH 7 was also evaluated, giving rise to 40 % degradation. Even under neutral pH conditions Calc Fe Bio-Si showed good catalytic activity, 53 % degradation was achieved which subsequently increased to around 85 % (% RSD values less than 1 %). The activity was again shown to be very stable for successive cycles.
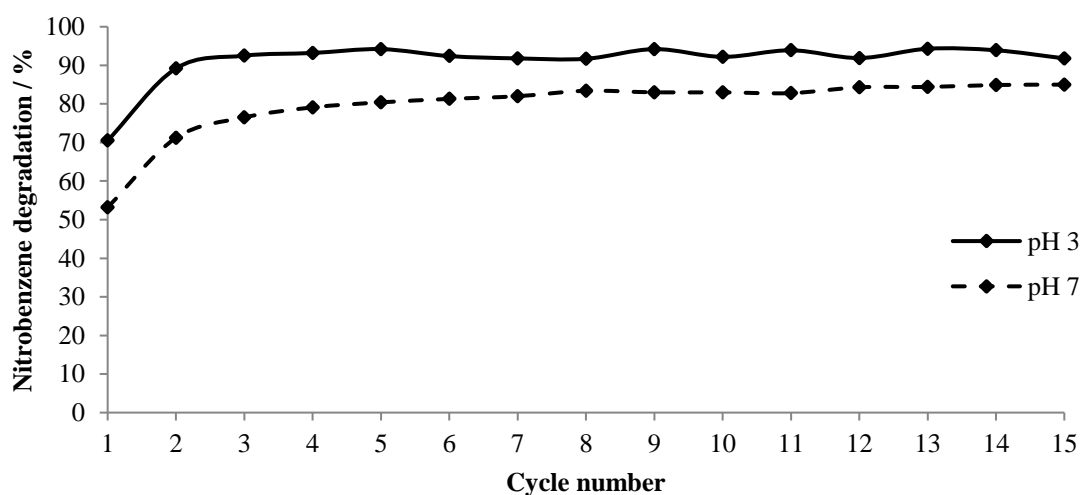
Figure 7.4: % degradation nitrobenzene using Calc Fe Bio-Si as a photocatalyst in 15 consecutive reaction cycles at pH 3 and pH 7.

7.3.1.3.2 Pharmaceutically active compounds

In the previous section, results indicated that the application of H_2O_2 and UV irradiation alone to the pharmaceutical mixture had a significant impact on the degradation of the four target compounds, successfully removing 70 – 89 % and 50 – 66 % at pH 3 and 7, respectively. However, both catalysts were shown to moderately enhance this degradation by 9 – 30 % at pH 3 thus the use of a catalyst in the complete photo-Fenton reaction was further investigated. Despite the apparent inhibition of pharmaceutical degradation observed with the use of a catalyst at neutral solution pH, examination of the performance of the catalysts was continued. The reusability and stability of the photocatalysts were investigated by assessing the catalytic ability of As-syn and Calc Fe Bio-Si with repeat usage for the degradation of the pharmaceutical mixture at pH 3 and 7. Both materials were used in 6 consecutive photo-Fenton reaction cycles; the catalyst filtered in between reactions, introduced to a new 2.5 μg mL^{-1} pharmaceutical mixture solution at pH 3 or 7 and fresh H_2O_2 added to reinitiate the reaction. The ensuing profiles for each of the four pharmaceutically active compounds at both pH 3 and pH 7 are shown in Figure 7.5 (a) and (b) for As-syn and Calc Fe Bio-Si, respectively.
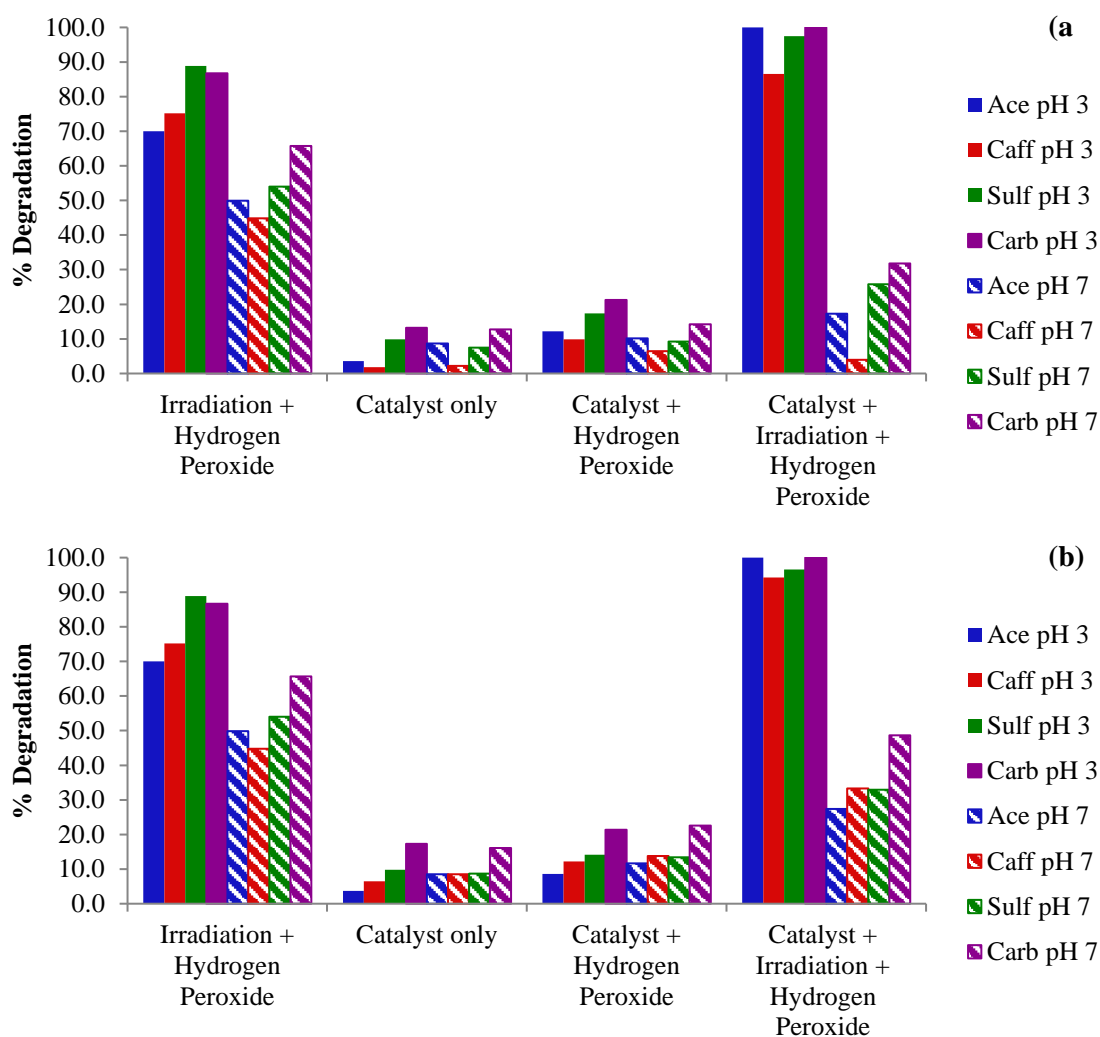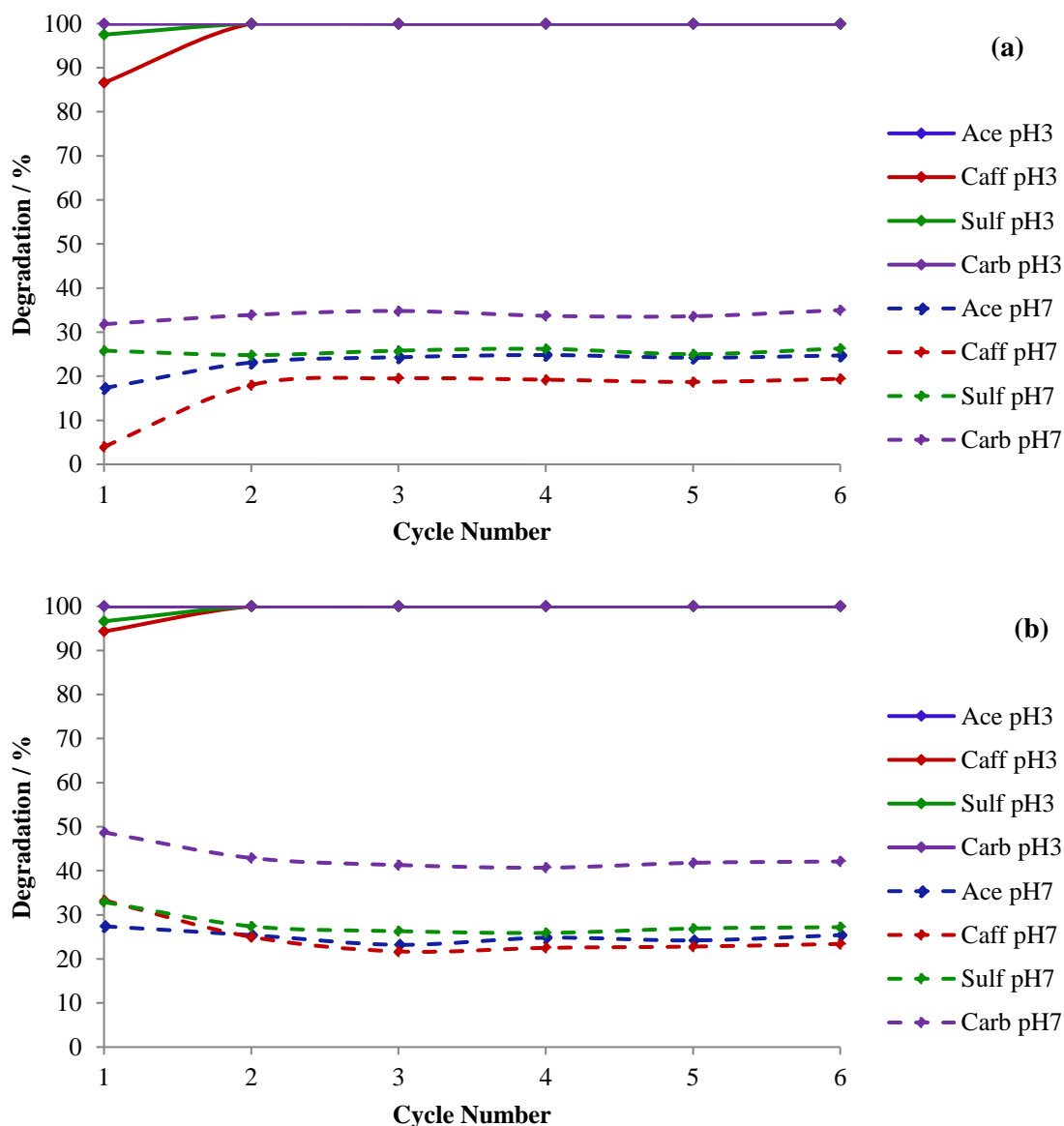
Figure 7.5: % degradation of each pharmaceutically active compound using (a) As-syn Fe Bio-Si and (b) Calc Fe Bio-Si as a photocatalyst in 6 consecutive reaction cycles at pH 3 and pH 7.

Under acidic conditions the degradation percentage for each compound using both catalyst materials remained at or increased to 100 % by the second cycle and continued to demonstrate stability during the 6 cycles. Around 70 - 89 % of the degradation obtained during the initial cycle can assumed to be a consequence of the direct photolysis of H_2O_2 under UV irradiation.

The increase in degradation efficiency to 100 % observed in successive applications indicates that the catalyst exhibited good activity for photo-Fenton reactions at pH 3 and could be explained by the surface of the catalyst being activated during the initial cycle. As observed with the nitrobenzene investigation, with repeated usage, there was an apparent synergistic

effect between the photocatalysis of Calc Fe Bio-Si and H_2O_2 oxidation which enhances the degradation of the pharmaceutically active compounds.

The extent of direct UV photolysis of H_2O_2 on the degradation of the pharmaceutical mixture at pH 7 gave rise to 50 - 66 % degradation. Under neutral pH conditions, both catalysts failed to show catalytic activity, and instead proved to be detrimental to the degradation process by inhibiting the direct photolysis. It was thought that with repeated usage, similar to the results demonstrated when nitrobenzene was studied, that the catalyst surface might be activated during successive cycles. However, this was not the case, with the application of the As-syn Fe Bio-Si demonstrating an initial increase in pharmaceutical degradation but subsequently plateauing at values less than that contributed by direct photolysis. Performance of the Calc Fe Bio-Si in successive cycles at neutral pH was shown to initially inhibit the direct photolysis further before plateauing at this lower degradation percentage.

The results indicate the catalysts (Calc Fe Bio-Si for nitrobenzene and both As-syn and Calc Fe Bio-Si for the degradation of pharmaceutically active compounds) can remain active for long-term service without a detrimental effect on catalyst performance under the given conditions. This good performance could be attributed to the structural aspects of the silica as well as the stability of the iron species under both acidic and neutral conditions. The stability of the catalyst's high activity implies that there is little or no iron leaching from the catalyst as this would cause a reduction in active sites with subsequent loss in activity. It would also suggest that the porous system is not blocked by adsorption, allowing nitrobenzene molecules to easily enter the active sites. Due to the repeated filtration steps, a small mass of catalyst was lost with each cycle, however, this does not appear to affect the degradation efficiency of the target contaminants. This can be explained by the scavenging of hydroxyl radicals being accelerated by the development of parallel reactions between excess catalyst and hydroxyl radicals. Another advantage made evident from the ability to reuse the catalyst is that there is no requirement for a catalyst regeneration method.

For both pharmaceutical and nitrobenzene degradation, the chosen catalysts and photo-Fenton process were shown to perform better under acidic conditions. This is expected with the maximum catalytic activity in Fenton reactions typically found at a pH around 3. Under these conditions, a large amount of •OH can be efficiently produced by Fenton reactions according to Equation 7.8 below. Thus, the reaction system has high oxidisability with the oxidation rates of the Fe^{3+} / H_2O_2 system known to decrease dramatically at pH values larger

than 3,[416] where the Fe^{3+} begins to precipitate as $Fe(OH)_3$ and H_2O_2 is preferentially decomposed into O_2 and H_2O.

$$Fe^{2+} + H_2O_2 \rightarrow Fe^{3+} + HO^- + HO^\bullet \qquad \textbf{Equation 7.8}$$

Despite this, a high catalytic activity towards the degradation of nitrobenzene is observed under neutral conditions, without the acidification process. This observation is very important since it is well known that one of the major drawbacks of Fenton like reactions is the costly acidification process, which limits its practical industrial application in wastewater treatment.

7.3.2 Photocatalysis reactions using TiO_2 and Fe-TiO_2 as photocatalysts

Photocatalyst thin films were prepared on glass supports using the sol-gel method as described in Section 5.2.2 and 7.2.4.1 for TiO_2 and Fe-TiO_2, respectively. In brief, glass beads were coated with either TiO_2 or Fe-TiO_2 (20 or 50 % iron) gel before being calcined, to generate a mesoporous photocatalyst thin film on the surface of the support materials. This process was repeated to produce glass beads with 1 to 5 coatings of photocatalyst film. The coated beads were then submerged in the contaminated water solution under UV or visible–light irradiation for TiO_2 and Fe-TiO_2, respectively, and stirred for 2 h. In addition, the TiO_2 photocatalyst was also examined under visible–light irradiation as a control. Table 7.1 and Figure 7.9 show the percent degradation of nitrobenzene obtained using the TiO_2, 20 % and 50 % Fe-TiO_2 beads, coated 1 to 5 times under UV or visible–light irradiation. As a result of the variation in visible-light intensity that might be experienced while the study proceeds under the exposure of sunlight on the lab bench, all experiments were conducted in triplicate and the % degradations recorded are an average of these results.

Table 7.1: % degradation of nitrobenzene using 1 – 5 coats of TiO$_2$ or Fe-TiO$_2$ film.

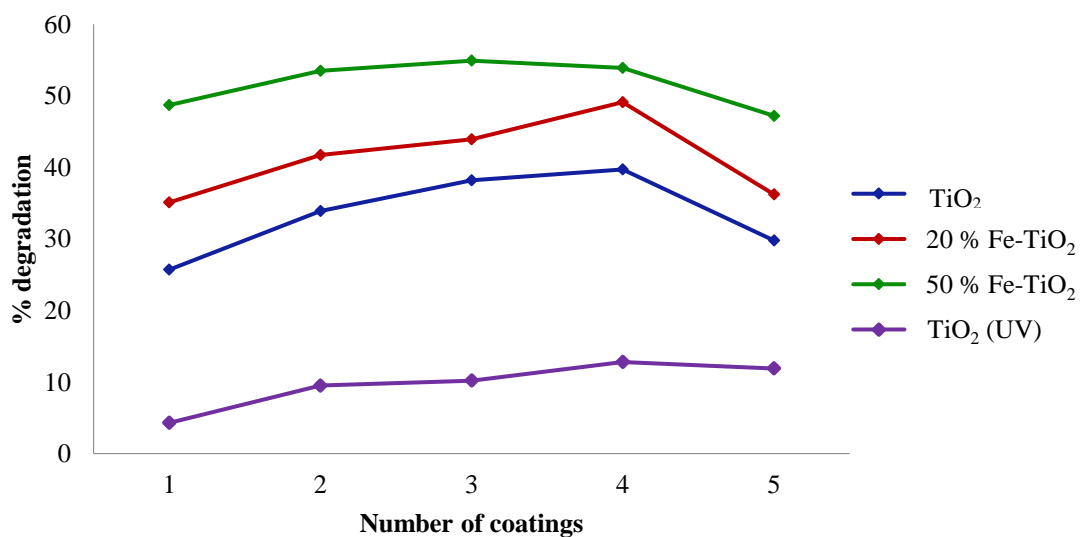| Material	Coat Number	% Degradation
TiO$_2$	1	25.7
	2	38.2
	3	33.9
	4	39.7
	5	29.8
20 % Fe-TiO$_2$	1	35.1
	2	43.9
	3	41.7
	4	49.1
	5	36.2
50 % Fe-TiO$_2$	1	48.7
	2	53.5
	3	54.9
	4	53.9
	5	47.2
TiO$_2$ (UV Irradiation)	1	4.3
	2	9.5
	3	10.2
	4	13.1
	5	12.4

Figure 7.5: % degradation of nitrobenzene using 1 – 5 coats of TiO$_2$, 20 % or 50 % Fe-TiO$_2$ film.

For visible-light photocatalysis, using Fe-TiO$_2$ thin film as a photocatalyst, it can be seen from Table 7.1 and Figure 7.5 that the % degradation of nitrobenzene steadily increases with each catalyst film coating (% RSD values for all materials were less than 2 % and less than 1 %). This trend was observed up to 4 or 2 coatings for 20 % and 50 % iron, respectively, (degradation plateaued, within error, for coatings 2 – 4 of 50% Fe-TiO$_2$) although photocatalytic performance was subsequently reduced with application of the 5th coat. This suggests that photocatalytic activity was initially enhanced by an increase in film thickness; a result which is expected and could be simply explained by an increase in the Fe-TiO$_2$ photocatalyst available to participate in the photocatalytic reaction.

The decrease in photocatalytic activity observed with coatings higher than 4 or 2 for 20 % and 50 % Fe-TiO$_2$, respectively, was thought to be as a result of several factors. The photocatalytic reactions might occur predominantly on the surface active sites of photocatalyst thin films as a consequence of Fe-TiO$_2$ in the interior region of the films being less accessible to reactant nitrobenzene molecules. Also, an increase in opacity is observed with Fe-TiO$_2$ film above a certain thickness, this in addition to the possibility of increased light scattering would lead to a decrease in the passage of visible-light irradiation through the film. Therefore, once an optimum thickness is reached, the photocatalytic activity will remain constant despite additional TiO$_2$ film coatings.

Independent of the number of catalyst coatings, the 50 % Fe-TiO$_2$ was shown to perform better than the 20 % Fe-TiO$_2$ material. In addition, the material with higher iron content required fewer coatings to achieve an optimum photocatalytic activity for nitrobenzene degradation. This is thought to be as a result of a greater incorporation of Fe into the framework of TiO$_2$ in the 50 % Fe-TiO$_2$. As discussed in Section 7.1.2, iron is incorporated into the TiO$_2$ structure in the form of Fe^{3+}, the similarity of the ionic radii of Fe^{3+} (0.64 A) and Ti^{4+} (0.68 A) allows Fe ions to replace Ti ions in the Ti-O-Ti network in addition to being incorporated into structure interstices. As a consequence, the excitation band gap is reduced and the photoexcitation response is shifted to a longer wavelength. Under visible-light irradiation, once the electron is band gap excited it may be immediately picked up by Fe^{3+} and reduced to Fe^{2+}. Since Fe^{2+} is not stable, it is rapidly oxidised to Fe^{3+} by dissolved oxygen. As a result, the electron hole recombination is supressed and the degradation efficiency of nitrobenzene increased by the hole. The level of Fe^{3+} incorporation in the lattice of TiO$_2$ is thereby important for light adsorption in the visible region and subsequently a higher photocatalytic activity under solar light exposure is demonstrated by 50 % Fe-TiO$_2$ in comparison to 20 % Fe-TiO$_2$ or TiO$_2$.

The extent of adsorption onto the catalyst on the observed degradation percentages was examined by conducting analogous reactions in the absence of sunlight (in a dark box). Average adsorption efficiencies of 14.2 and 9.3 % (% RSD values less than 1 %) were obtained for 20 % and 50 % Fe-TiO$_2$, respectively. Around 35 and 46 % increase in nitrobenzene removal is observed when the reaction is exposed to sunlight, indicating that visible-light irradiation plays a significant role in nitrobenzene removal and indicates that the contaminant is indeed being photocatalytically degraded during the reaction process. This would suggest that the surfactant templated, sol-gel synthesis approach used in the preparation of the iron incorporated titania materials was successful in distributing iron ions uniformly through the titania structure from exterior to interior with Fe^{3+} evenly incorporated into the titania framework to form a titanium-iron solid solution.[417] However, in depth characterisation of the material is required to reinforce this deduction, possibly through the use of X-ray diffraction (XRD), Fourier transform infra-red (FTIR), scanning and transmission electron microscope (SEM, TEM) and nitrogen sorption analysis.

Although the Fe-TiO$_2$ catalysts demonstrated good photocatalytic activity for the degradation of nitrobenzene, the reaction efficiency could possibly be improved further by ensuring there is sufficient oxygen available for the reaction to proceed. A constant supply of oxygen in the form of air could be bubbled through the nitrobenzene solution.

The TiO$_2$ film coated glass beads were also investigated for the degradation of nitrobenzene in visible-light (as a control) and under UV irradiation. When exposed to visible light, the TiO$_2$ photocatalyst followed the same trend as the 20 % Fe-TiO$_2$ material, increasing in nitrobenzene removal to an optimum performance of around 38 % removal at 4 coatings. As TiO$_2$ is not photocatalytically active under visible-light irradiation, it can be presumed that the nitrobenzene removal is solely a consequence of adsorption onto the material. To confirm this presumption, an analogous experiment was conducted in the absence of sunlight using beads coated 4 times in the TiO$_2$ material where similar nitrobenzene removal was demonstrated. The surface area available for adsorption increases with each coat of TiO$_2$ up to an optimum of 4 coatings, after which it is possible that the mesopores in the material were blocked by subsequent layering.

Surprisingly, under UV irradiation, nitrobenzene removal was significantly reduced with an average maximum performance of 12.8 % observed for beads coated 4 times with the TiO$_2$ material. It would appear that exposure of the TiO$_2$ to UV irradiation, instead of initiating photocatalytic activity of the material and enhancing removal efficiency like expected, instead proved to be detrimental to the removal process, even inhibiting nitrobenzene

adsorption. A possible explanation for this observation is overheating of the experimental set-up during the 2 h time frame in which the reaction is exposed to constant UV irradiation. This might cause the adsorbed nitrobenzene molecules to desorb back off the catalyst and into solution. This observation could prove to be useful in the search for a method of regenerating the catalyst once it had reached capacity with the adsorbed molecules being removed simply by heating the catalyst and surrounding solution. However, for the purpose of this study and the photocatalytic degradation of nitrobenzene, a potential solution would be the introduction of a cooling system or jacket to the experimental set-up to control the reaction temperature.

The reaction was followed using HPLC and the chromatograms produced after the 2 h reaction time showed a single nitrobenzene peak with reduced height and area, no other peaks were observed. This suggests that there were no intermediate molecules present and that the catalyst was successful in completely mineralising the pollutant molecules. In order to investigate the degradation mechanism, the reaction and transformation of nitrobenzene could be monitored over time using LC-MS or GC-MS to identify any intermediates and deduce a possible mechanism of reaction.

7.4. Conclusion

The application of As-syn and Calc Fe Bio-Si as heterogeneous Fenton catalysts for water remediation was examined using the same target sets investigated in Chapter 6: pharmaceutically active compounds and nitrobenzene.

For the degradation of nitrobenzene, it can be reported that a major factor controlling the degradation was direct photolysis of H_2O_2, with the Calc material yielding a further enhancement in degradation of around 20 % and the As-syn material showing little activity in the photo-Fenton reaction. This raised the question whether, for the degradation of nitrobenzene, the use of a catalyst is truly necessary. A finding which proves, in itself, promising for nitrobenzene degradation from an industrial perspective as UV irradiation is already an advanced technique currently available in wastewater treatment plants and would, therefore, be easy and cost effective to implement. However, an increase in catalyst performance was observed when the Calc Fe Bio-Si was used in successive cycles. The catalyst was shown to effectively activate H_2O_2 to successfully degrade nitrobenzene under UV light irradiation at pH 3, reaching around 95 % degradation after the initial cycle, thus

displaying a high catalytic activity towards the degradation of nitrobenzene. In particular, this process was found to possess superior degradation efficiency due to a synergistic effect between the photocatalysis of Calc Fe Bio-Si and H_2O_2 oxidation. Furthermore, and what is perhaps key to the use of this material in industrial applications, is the ability to repeatedly use the Calc Fe Bio-Si to degrade nitrobenzene in aqueous solutions. The material exhibited excellent photocatalytic stability and can be reused for long-term service with no loss of activity observed after 15 repeated applications (with the potential to go further) even without the acidification process. These results are promising in the development of a highly active heterogeneous photo-Fenton catalyst with good recycling behaviour as Calc Fe Bio-Si shows the potential to be effective in the oxidative treatment of nitrobenzene solutions at circumneutral pH values.

From the investigation into the removal of pharmaceutically active compounds: acetaminophen, caffeine, sulfamethoxazole and carbamazepine it can be reported that the main factor contributing to the degradation was direct photolysis of H_2O_2, successfully mineralising 70 – 89 % and 50 – 66 % at pH 3 and 7, respectively. Both the As-syn and Calc material were shown to enhance the degradation by 9 – 30 % at pH 3. However, the use of a catalyst at neutral solution pH was shown to be detrimental to the performance of the photo-Fenton reaction, inhibiting the breakdown of the pharmaceuticals by H_2O_2 and UV irradiation. The use of a catalyst proved necessary to achieve 100 or near 100 % degradation of all pharmaceutically active compounds in the mixed solution. Similar to the nitrobenzene degradation, when used in successive cycles both catalysts were shown to effectively activate H_2O_2 to successfully mineralise the pharmaceuticals under UV light irradiation at pH 3, reaching 100 % degradation for all compounds after the initial cycle, thus displaying a high catalytic activity towards the degradation of these pharmaceutical compounds. The process was once again found to possess superior degradation efficiency due to a synergistic effect between the photocatalysis of Calc Fe Bio-Si and H_2O_2 oxidation.

The potential to use these materials in industrial applications is highlighted in the ability to repeatedly use the As-syn and Calc Fe Bio-Si catalysts to degrade both the pharmaceutical target compounds and nitrobenzene in aqueous solutions. The long-term performance of the catalyst removes the requirement for the development of a regeneration method as the catalyst is self-regenerating and can be used in multiple subsequent extractions without any signs of deactivation. The excellent photocatalytic stability and long-term activity of the catalysts in addition to the diversity in the contaminant targets that can be mineralised demonstrates that this study was successful in developing active heterogeneous photo-Fenton

catalysts with good recycling behaviour that play a key role in what proved to be a highly effective photo-Fenton process for the oxidative treatment of contaminants in water.

The preparation of these materials also possesses the advantages of using neutral pH, room temperature conditions, rapid synthesis and a substantial reduction in secondary pollution by the elimination of the need for organic solvents from the preparation method. The environmentally friendly catalyst synthesis, as well as the absence of a pH adjustment step during the reaction, minimal waste production and low potential for production of toxic by-products may provide benefits over other remediation approaches. Additional research is needed to further enhance the understanding of the mechanism of the catalyst activity and assess the scaling up of the treatment systems employing the catalyst.

The process of visible-light induced photocatalytic oxidation, using $Fe-TiO_2$ thin film as a photocatalyst, was assessed for the degradation of nitrobenzene in aqueous solutions. In addition, the performance of TiO_2 thin film for the photodegradation of nitrobenzene was also evaluated under both UV and visible–light irradiation.

For the application of the iron incorporated TiO_2 material, the study revealed that for optimum photocatalytic activity, the photocatalyst support material required 4 or 2 coatings of film for 20 % and 50 % $Fe-TiO_2$, respectively, successfully achieving nitrobenzene degradations, on average, of around 50 and 55 %. The 50 % $Fe-TiO_2$, with greater iron content, showed superior photocatalytic activity with fewer film coatings, thought to be as a result of a greater incorporation of Fe into the framework of TiO_2. Average adsorption efficiencies of 14.2 and 9.3 % were obtained for 20 % and 50 % $Fe-TiO_2$, respectively, indicating that exposure to visible-light plays a significant role in nitrobenzene removal and that the contaminant is indeed being photodegraded during the reaction process by the iron incorporated titanium dioxide catalysts. The performances observed for the $Fe-TiO_2$ catalysts suggested that the surfactant templated, sol-gel synthesis approach used in the preparation of the iron incorporated titania materials was successful in distributing iron ions uniformly through the titania structure from exterior to interior with Fe^{3+} evenly incorporated into the titania framework to form a titanium-iron solid solution. Further work in this area could involve the characterisation of the $Fe-TiO_2$ films to support this deduction: X-ray diffraction (XRD) used to study the morphology of the TiO_2 crystalline phase, film thickness measured using both scanning and transmission electron microscopy (SEM, TEM) and surface area and pore sizes determined using nitrogen sorption analysis. Additionally, characterisation

methods could be used to assess the adsorption of the target nitrobenzene molecule and any intermediate molecules on the Fe-TiO$_2$ surface.

Without the presence of iron in the material, the TiO$_2$ thin film photocatalyst, when exposed to solar light, achieved an optimum performance of around 38 % removal at 4 coatings. It can be presumed that adsorption onto the material is the main factor contributing to the observed decrease in nitrobenzene solution concentration. Surprisingly, exposure to UV irradiation, instead of initiating photocatalytic activity of the material and enhancing degradation efficiency like expected, proved to be detrimental to the removal process and was even found to inhibit nitrobenzene adsorption. This was thought to be a result of the constant UV irradiation overheating the reaction set-up, causing the nitrobenzene molecules to desorb from the TiO$_2$ surface, which could be easily resolved through the introduction of a cooling system to control the reaction temperature. Such an observation could prove advantageous to the long-term application of this technique for water remediation as it suggests that regeneration of the photocatalyst would be a simple process, achieved by heating the catalyst or surrounding solution to remove adsorbed contaminants.

Further improvement of the experimental set-up could be made to potentially increase the reaction efficiency and photodegradation performance of the catalyst by ensuring there is sufficient oxygen available for the reaction to proceed. A constant supply of oxygen in the form of air could be bubbled through the nitrobenzene solution.

Additional work in this area could merge the two advanced oxidation techniques examined in this Chapter by investigating the use of the iron incorporated TiO$_2$ for the application as a catalyst in a photo-Fenton reaction, through the addition of H$_2$O$_2$, for the degradation of nitrobenzene in aqueous solutions.

8. Concluding Remarks

8.1 Adsorption Vs. Advanced oxidation techniques

The results acquired from Part A of this work allow a comparison to be made between the application of adsorption and the use of photocatalytic reactions for the removal of VOCs from indoor air. The silica sorbents and commercially available, Tenax TA, used in this investigation have proved to be efficient as scavengers for reducing VOC concentrations in air, however this technique fails to destroy the pollutants but merely transfers them from air to sorbent which, after a certain concentration is reached, requires regeneration by thermal desorption and a further treatment of the pollutants.

Alternatively, the process of photocatalytic oxidation has revealed excellent potential for not only removing VOCs from indoor air but also efficiently degrading them in the process. The research presented in this Section of the thesis was successful in producing mesoporous TiO_2 thin film photocatalyst tubes that, when coupled with UV irradiation, have proved to be a very simple yet extremely effective technique for air remediation. The only downside with this technique is that while the photocatalytic degradation of VOCs is very high (~ 90 %), it is not complete, allowing unreacted VOCs to pass through the system. Additionally, the use of the PCO technique in VOC removal applications where long-term sampling is required would generate undesirable intermediate compounds, some of which can be more harmful to human health than their precursors. However, the solution to this problem proved simple with regeneration of the photocatalyst easily achieved by cooling down the system. This feature is extremely promising for the potential industrial application of the photocatalyst tubes where, to avoid any downtime in the running of the photocatalytic process, a cooling system could be installed to ensure continuous high photocatalytic activity without the accumulation of degradation products. A second, perhaps more cost effective, option would be to have two photocatalyst tubes running in parallel; the regeneration cool down procedure occurring in one reactor tube simultaneously to the photodegradation of VOCs in the other and vice versa. As both techniques have their drawbacks, further work could also investigate bringing these methods together to resolve the issues. A long-term VOC removal method could involve the PCO reactions to degrade the majority of the indoor air VOCs with sorbents used in line to capture any unreacted VOCs along with any intermediate compounds produced.

From the investigations conducted throughout Part B of this work a comparison can be made between the application of adsorption and the use of advanced oxidation techniques for the

removal of target contaminants, pharmaceutically active compounds and nitrobenzene, from aqueous solutions.

The mesoporous silica sorbents have proved that they can be used as scavengers for reducing concentrations of both pharmaceutically active compounds and nitrobenzene in water, however, their ability is largely inefficient as they fail to compare to the far superior performance of the commercially available and, industrially used activated carbon. The inability of mesoporous silica to meet the performance levels attained by materials already available is perhaps one of the reasons for the decline in the number of papers and citations on the subject area in recent years (See Figure 1.2). It is possible that research surrounding the materials has decreased as they have proved not to have the abilities of the materials originally strived for and investigations have begun to focus on new materials. In addition, as shown through the work carried out in this thesis, bench top synthesis produces mesoporous silica in very small quantities. In order to realise the technological impact of these materials and if they are to be applied industrially then a large scale-up process would require investigation and development, from laboratory syntheses to pilot-plant and subsequently plant scale production. However, there doesn't appear to be a lot of focus in the literature or drive in research around this area, perhaps as a result of difficulties encountered with performing the synthesis on a large scale. The inability to produce larger quantities of mesoporous silica for applications such as environmental remediation would also be a reason for this notable decline in interest investigating these materials.

The application of activated carbon as an adsorption technique also has its limitation as it fails to destroy the pollutants but merely transfers them from water to sorbent which, after a certain concentration is reached, requires regeneration and a further treatment of the pollutants. Difficulties have been reported in the separation of activated carbon materials from aqueous solutions and their regeneration with chemical and thermal procedures proving expensive and reporting loss of sorbent. In addition, the use of activated carbons in 'real' water samples where the matrix is complex can be problematic as they are known to be susceptible to pore clogging.

Alternatively, the application of advanced oxidation techniques has revealed their potential for not only removing target contaminants from aqueous solutions but also efficiently degrading them in the process. The development of iron incorporated bioinspired silica material as a heterogeneous catalyst and the application of this catalyst as part of the photo-Fenton process proved to be an excellent technique for water remediation. The process demonstrated excellent potential for use in large scale waste water treatment with high

efficiency, long-term performance and the complete mineralisation of a range of target compounds, in addition to a cheap, environmentally friendly catalyst synthesis method. The only downside to this technique is that while the photocatalytic degradation of both pharmaceutically active compounds and nitrobenzene is very high (> 90 %), the system relies on H_2O_2 and UV light to operate successfully. The constant exposure to light in this wavelength might be thought of as being costly from an industrial perspective, however UV irradiation is already an advanced technique currently available in wastewater treatment plants and would, therefore, be easy and cost effective to implement.

An alternative solution, which would require investigation in future work, could be the application of the developed iron incorporated TiO_2 thin films as a catalyst in a visible light initiated photo-Fenton reaction.

8.2 Material highlights and future work

Perhaps one of the most thought-provoking, exciting discoveries made in this thesis are the remarkable features presented by the synthesised iron incorporated bioinspired silica.

The surface areas are significantly higher, for As-syn Fe Bio-Si, and lower, for Calc Fe Bio-Si, than their non-iron incorporated equivalents. Interestingly, and unlike the As-syn and Calc Bio-Si, both materials produced type IV N_2 sorption isotherms suggesting that they are mesoporous, unlike the type I/II isotherm obtained for the Calc Bio-Si. Both As-syn and Calc Fe Bio-Si were shown to have larger pore volumes than the original bioinspired materials and average pore sizes of around 8.8 nm, larger than than any other mesoporous material synthesised in this thesis. With the amine additive template remaining intact within the As-syn Fe Bio-Si material, a low surface area and lack of porosity would be expected. However, surprisingly, the material has a surface area and pore volume similar to that of the Calc Fe Bio-Si. These observations indicate that the silica framework of the bioinspired material was greatly altered when iron was incorporated into the synthesis mixture. Both materials were shown to have broad pore size distributions, indicating that they contain pores of different shape and size. Most interestingly, however, steps or shoulder peaks on the curve were revealed that at around 6, 8 and 10-12 nm that reached a maximum at 14 nm. These are common to both As-syn and Calc Fe Bio-Si, with the step at 10-12 nm decreasing in volume and when the amine additive is removed by calcination. These steps indicate groups of pores

within the structure with distinct size that perhaps correspond to different, yet controlled arrangements of the silica, iron and additive to produce a framework that possesses a remarkable multimodal pore system. The features of these iron incorporated bioinspired silica materials, to the authors best knowledge, have not been reported in literature. The exact mechanism by which they are formed and the role of iron on the framework assembly are of great interest and are owed further investigation. The final structure requires full characterisation to establish whether, as believed, a fascinating novel material has been produced.

Future work would involve fully characterising, not only the Fe Bio-Si materials, but all materials used in this thesis. For the silica-based materials the presence of the structure directing compound (surfactant, amine additive) can be examined using Fourier transform infrared spectroscopy (FTIR) and (C, H, N) elemental analysis. Structural information, can be obtained through a combination of X-ray diffraction (XRD), scanning and transmission electron microscopy (SEM and TEM, respectively) and nitrogen sorption analysis (already performed). SEM is useful for examining particle morphology and size and TEM for investigating the internal structure of the material, the framework and pore arrangements and, thus, the properties of the pore channels.

For the TiO_2 thin film photocatalysts, XRD can be used to study the morphology of the TiO_2 crystalline phase (anatase or rutile), the film thickness measured using both SEM and transmission electron microscopy (TEM) and surface area and pore properties determined using nitrogen sorption analysis.

In addition, for the iron incorporated materials, SEM and TEM are useful for examining the distribution of iron within the material. The composition of inorganic components and the oxidation state of iron can be investigated by performing X-ray photoelectron spectroscopy (XPS) analysis. Mössbauer spectroscopy can also be used to provide additional information on the chemical nature of iron in the materials.

9. References

1. J. Rouquerol, *Pure and applied chemistry*, 1994, **66**, 1739.
2. A. F. Cronstedt, *Academy of Handlingar. Stockholm*, 1756, **17**, 120-123.
3. R. M. Barrer and D. W. Brook, *Transactions of the Faraday Society*, 1953, **49**, 940-948.
4. J. W. MacBain, *The sorption of gases and vapours by solids*, Routledge, London, 1932.
5. D. W. Breck, W. G. Eversole, R. M. Milton, T. B. Reed and T. L. Thomas, *Journal of the American Chemical Society*, 1956, **78**, 5963-5972.
6. M. G. Rimoli, M. R. Rabaioli, D. Melisi, A. Curcio, S. Mondello, R. Mirabelli and E. Abignente, *Journal of Biomedical Materials Research Part A*, 2008, **87A**, 156-164.
7. A. Corma, *Chemical Reviews*, 1997, **97**, 2373-2419.
8. T. J. Pinnavaia, *Science*, 1983, **220**, 365-371.
9. J. S. Beck, J. C. Vartuli, W. J. Roth, M. E. Leonowicz, C. T. Kresge, K. D. Schmitt, C. T. W. Chu, D. H. Olson and E. W. Sheppard, *Journal of the American Chemical Society*, 1992, **114**, 10834-10843.
10. C. T. Kresge, *Nature*, 1992, **359**, 710.
11. C. T. Kresge and W. J. Roth, *Chemical Society Reviews*, 2013, **42**, 3663-3670.
12. V. Chiola, J. E. Ritsko and C. D. Vanderpool, *US Patent*, 1971, No: 3,556,725.
13. F. Di Renzo, H. Cambon and R. Dutartre, *Microporous Materials*, 1997, **10**, 283-286.
14. T. Yanagisawa, T. Shimizu, K. Kuroda and C. Kato, *Bulletin of the Chemical Society of Japan*, 1990, **63**, 988-992.
15. F. Hoffmann, M. Cornelius, J. Morell and M. Fröba, *Angewandte Chemie International Edition*, 2006, **45**, 3216-3251.
16. V. Alfredsson and M. W. Anderson, *Chemistry of Materials*, 1996, **8**, 1141-1146.
17. J. Man Kim and R. Ryoo, *Chemical communications*, 1998, **0**, 259-260.
18. A. Monnier, F. Schüth, Q. Huo, D. Kumar, D. Margolese, R. S. Maxwell, G. D. Stucky, M. Krishnamurty, P. Petroff, A. Firouzi, M. Janicke and B. F. Chmelka, *Science*, 1993, **261**, 1299-1303.
19. R. Ryoo, S. H. Joo and J. M. Kim, *The Journal of Physical Chemistry B*, 1999, **103**, 7435-7440.
20. J. C. Vartuli, K. D. Schmitt, C. T. Kresge, W. J. Roth, M. E. Leonowicz, S. B. McCullen, S. D. Hellring, J. S. Beck and J. L. Schlenker, *Chemistry of Materials*, 1994, **6**, 2317-2326.
21. Q. Huo, D. I. Margolese and G. D. Stucky, *Chemistry of Materials*, 1996, **8**, 1147-1160.
22. D. Zhao, J. Feng, Q. Huo, N. Melosh, G. H. Fredrickson, B. F. Chmelka and G. D. Stucky, *Science*, 1998, **279**, 548-552.
23. M. Impéror-Clerc, P. Davidson and A. Davidson, *Journal of the American Chemical Society*, 2000, **122**, 11925-11933.
24. M. Kruk, M. Jaroniec, C. H. Ko and R. Ryoo, *Chemistry of Materials*, 2000, **12**, 1961-1968.
25. J. Liu, X. Zhang, Y. Han and F. S. Xiao, *Chemistry of Materials*, 2002, **14**, 2536-2540.
26. C.-M. Yang, B. Zibrowius, W. Schmidt and F. Schüth, *Chemistry of Materials*, 2004, **16**, 2918-2925.
27. K.-K. Kang and H.-K. Rhee, *Microporous and Mesoporous Materials*, 2005, **84**, 34-40.
28. P. F. Fulvio, S. Pikus and M. Jaroniec, *Journal of Materials Chemistry*, 2005, **15**, 5049-5053.
29. J. M. Kim and G. D. Stucky, *Chemical Communications*, 2000, **0**, 1159-1160.

30.	J. Liu, Q. Yang, X. S. Zhao and L. Zhang, *Microporous and Mesoporous Materials*, 2007, **106**, 62-67.

31.	C. J. Brinker and G. W. Scherer, *Sol-gel science: the physics and chemistry of sol-gel processing*, Academic Pr, 1990.

32.	C. C. Egger, M. W. Anderson, G. J. T. Tiddy and J. L. Casci, *Physical Chemistry Chemical Physics*, 2005, **7**, 1845-1855.

33.	R. K. Iler, *The chemistry of silica: solubility, polymerization, colloid and surface properties, and biochemistry*, Wiley New York, 1979.

34.	H. B. S. Chan, P. M. Budd and T. d. Naylor, *Journal of Materials Chemistry*, 2001, **11**, 951-957.

35.	C.-Y. Mou and H.-P. Lin, *Pure and Applied Chemistry*, 2000, **72**, 137-146.

36.	G. A. Ozin, H. Yang, I. Sokolov and N. Coombs, *Advanced Materials*, 1997, **9**, 662-667.

37.	H. Yang, N. Coombs and G. A. Ozin, *Nature*, 1997, **386**, 692-695.

38.	K. Holmberg, B. Jönsson, B. Kronberg and B. Lindman, *Surfactants and Polymers in Aqueous Solution: Novel Surfactants*, Second edn., John Wiley & Sons Ltd, Chichester UK, 2003.

39.	X. S. Zhao, G. Q. Lu and G. J. Millar, *Industrial & Engineering Chemistry Research*, 1996, **35**, 2075-2090.

40.	D. Myers, *Surfactant science and technology*, Third edn., John Wiley & Sons Ltd, Hoboken New Jersey, 2006.

41.	J. N. Israelachvili, D. J. Mitchell and B. W. Ninham, *Journal of the Chemical Society, Faraday Transactions 2: Molecular and Chemical Physics*, 1976, **72**, 1525-1568.

42.	C. Liu, X. Wang, S. Lee, L. D. Pfefferle and G. L. Haller, *Microporous and Mesoporous Materials*, 2012, **147**, 242-251.

43.	M. C. A. Stuart and E. J. Boekema, *Biochimica et Biophysica Acta (BBA) - Biomembranes*, 2007, **1768**, 2681-2689.

44.	A. M. Lapeña, A. F. Gross and S. H. Tolbert, *Langmuir*, 2004, **21**, 470-480.

45.	F. Kleitz, W. Schmidt and F. Schüth, *Microporous and Mesoporous Materials*, 2003, **65**, 1-29.

46.	P. T. Tanev and T. J. Pinnavaia, *Science*, 1995, **267**, 865-867.

47.	J. Goworek, A. Kierys, W. Gac, A. Borówka and R. Kusak, *Journal of Thermal Analysis and Calorimetry*, 2009, **96**, 375-382.

48.	M. T. Keene, R. D. Gougeon, R. Denoyel, R. K. Harris, J. Rouquerol and P. L. Llewellyn, *Journal of Materials Chemistry*, 1999, **9**, 2843-2849.

49.	R. Kusak, *Journal of Thermal Analysis and Calorimetry*, 2005, **79**, 555-560.

50.	F. Bérubé and S. Kaliaguine, *Microporous and Mesoporous Materials*, 2008, **115**, 469-479.

51.	C.-Y. Chen, H.-X. Li and M. E. Davis, *Microporous Materials*, 1993, **2**, 17-26.

52.	J. Blanchard, F. Schüth, P. Trens and M. Hudson, *Microporous and Mesoporous Materials*, 2000, **39**, 163-170.

53.	F. Schüth, U. Ciesla, S. Schacht, M. Thieme, Q. Huo and G. Stucky, *Materials research bulletin*, 1999, **34**, 483-494.

54.	W. A. Gomes Jr, L. A. M. Cardoso, A. R. E. Gonzaga, L. G. Aguiar and H. M. C. Andrade, *Materials Chemistry and Physics*, 2005, **93**, 133-137.

55.	S. Hitz and R. Prins, *Journal of Catalysis*, 1997, **168**, 194-206.

56.	Z. Liu, O. Terasaki, T. Ohsuna, K. Hiraga, H. J. Shin and R. Ryoo, *ChemPhysChem*, 2001, **2**, 229-231.

57.	M. Benjelloun, P. Van Der Voort, P. Cool, O. Collart and E. F. Vansant, *Physical Chemistry Chemical Physics*, 2001, **3**, 127-131.

58. B. Tian, X. Lui, C. Yu, F. Gao, Q. Luo, S. Xie, B. Tu and D. Zhao, *Chemical Communications*, 2002, 1186-1187.
59. T. Maschmeyer, *Current Opinion in Solid State and Materials Science*, 1998, **3**, 71-78.
60. A. Sayari and S. Hamoudi, *Chemistry of Materials*, 2001, **13**, 3151-3168.
61. A. Stein, B. J. Melde and R. C. Schroden, *Advanced Materials*, 2000, **12**, 1403-1419.
62. T. Asefa, M. J. MacLachlan, N. Coombs and G. A. Ozin, *Nature*, 1999, **402**, 867-871.
63. A. S. Maria Chong and X. S. Zhao, *The Journal of Physical Chemistry B*, 2003, **107**, 12650-12657.
64. B. G. Trewyn, I. I. Slowing, S. Giri, H.-T. Chen and V. S. Y. Lin, *Accounts of Chemical Research*, 2007, **40**, 846-853.
65. M. Vallet-Regí, *Chemistry – A European Journal*, 2006, **12**, 5934-5943.
66. M. H. Lim and A. Stein, *Chemistry of Materials*, 1999, **11**, 3285-3295.
67. F. Cagnol, D. Grosso and C. Sanchez, *Chemical Communications*, 2004, **0**, 1742-1743.
68. S. L. Burkett, S. D. Sims and S. Mann, *Chemical Communications*, 1996, **0**, 1367-1368.
69. D. J. Macquarrie, *Chemical Communications*, 1996, **0**, 1961-1962.
70. S. Huh, J. W. Wiench, J.-C. Yoo, M. Pruski and V. S. Y. Lin, *Chemistry of Materials*, 2003, **15**, 4247-4256.
71. R. M. Grudzien, S. Pikus and M. Jaroniec, *The Journal of Physical Chemistry B*, 2006, **110**, 2972-2975.
72. O. Olkhovyk and M. Jaroniec, *Journal of the American Chemical Society*, 2004, **127**, 60-61.
73. Y.-T. Hsu, W.-L. Chen and C.-M. Yang, *The Journal of Physical Chemistry C*, 2009, **113**, 2777-2783.
74. N. Linares, E. Serrano, M. Rico, A. Mariana Balu, E. Losada, R. Luque and J. Garcia-Martinez, *Chemical Communications*, 2011, **47**, 9024-9035.
75. C.-F. Cheng, Z. Luan and J. Klinowski, *Langmuir*, 1995, **11**, 2815-2819.
76. C.-Y. Chen, S. L. Burkett, H.-X. Li and M. E. Davis, *Microporous Materials*, 1993, **2**, 27-34.
77. D. W. Bruce, D. O'Hare and R. I. Walton, *Porous Materials*, First edn., John Wiley and Sons Ltd, 2011.
78. A. Firouzi, D. Kumar, L. Bull, T. Besier, P. Sieger, Q. Huo, S. Walker, J. Zasadzinski, C. Glinka, J. Nicol and a. et, *Science*, 1995, **267**, 1138-1143.
79. Q. Huo, D. I. Margolese, U. Ciesla, D. G. Demuth, P. Feng, T. E. Gier, P. Sieger, A. Firouzi and B. F. Chmelka, *Chemistry of Materials*, 1994, **6**, 1176-1191.
80. G. D. Stucky, A. Monnier, F. Schüth, Q. Huo, D. Margolese, D. Kumar, M. Krishnamurty, P. Petroff, A. Firouzi, M. Janicke and B. F. Chmelka, *Molecular Crystals and Liquid Crystals Science and Technology. Section A. Molecular Crystals and Liquid Crystals*, 1994, **240**, 187-200.
81. Q. Huo, D. I. Margolese, U. Ciesla, P. Feng, T. E. Gier, P. Sieger, R. Leon, P. M. Petroff, F. Schuth and G. D. Stucky, *Nature*, 1994, **368**, 317-321.
82. S. A. Bagshaw, E. Prouzet and T. J. Pinnavaia, *Science*, 1995, **269**, 1242-1244.
83. P. Treguer, D. M. Nelson, A. J. Van Bennekom, D. J. DeMaster, A. Leynaert and B. Quéguiner, *Science*, 1995, **268**, 375-379.
84. M. Hildebrand, *Chemical Reviews*, 2008, **108**, 4855-4874.
85. C. Exley, in *Biosilica in evolution, morphogenesis, and nanobiotechnology*, Springer, Editon edn., 2009, pp. 173-184.

86.	F. E. Round, R. M. Crawford and D. G. Mann, *Diatoms: biology and morphology of the genera*, Cambridge University Press, 1990.

87.	E. G. Vrieling, W. Gieskes and T. P. Beelen, *Journal of Phycology*, 1999, **35**, 548-559.

88.	C. J. Brinker and G. W. Scherer, *The physics and chemistry of sol–gel processing*, 1990.

89.	L. L. Hench, *Journal of the American Ceramic Society*, 1991, **74**, 1487-1510.

90.	S. V. Patwardhan, *Chemical Communications*, 2011, **47**, 7567-7582.

91.	D. Belton, S. V. Patwardhan and C. C. Perry, *Chemical Communications*, 2005, 3475-3477.

92.	R. L. Brutchey and D. E. Morse, *Chemical Reviews*, 2008, **108**, 4915-4934.

93.	N. Kröger, R. Deutzmann, C. Bergsdorf and M. Sumper, *Proceedings of the National Academy of Sciences*, 2000, **97**, 14133-14138.

94.	N. Kröger, R. Deutzmann and M. Sumper, *Science*, 1999, **286**, 1129-1132.

95.	S. V. Patwardhan and S. J. Clarson, *Polymer Bulletin*, 2002, **48**, 367-371.

96.	S. V. Patwardhan, S. J. Clarson and C. C. Perry, *Chemical Communications*, 2005, 1113-1121.

97.	N. Poulsen and N. Kröger, *Journal of Biological Chemistry*, 2004, **279**, 42993-42999.

98.	N. Poulsen, M. Sumper and N. Kröger, *Proceedings of the National Academy of Sciences*, 2003, **100**, 12075-12080.

99.	T. Coradin, O. Durupthy and J. Livage, *Langmuir*, 2002, **18**, 2331-2336.

100.	C. C. Perry and T. Keeling-Tucker, *JBIC Journal of Biological Inorganic Chemistry*, 2000, **5**, 537-550.

101.	J. N. Cha, G. D. Stucky, D. E. Morse and T. J. Deming, *Nature*, 2000, **403**, 289.

102.	K. Shimizu and D. E. Morse, *Biomineralization: from biology to biotechnology and medical application. Wiley-VCH, Weinheim*, 2000, 207-219.

103.	S. V. Patwardhan and S. J. Clarson, *Materials Science and Engineering: C*, 2003, **23**, 495-499.

104.	D. J. Belton, S. V. Patwardhan, V. V. Annenkov, E. N. Danilovtseva and C. C. Perry, *Proceedings of the National Academy of Sciences*, 2008, **105**, 5963-5968.

105.	M. Sumper, E. Brunner and G. Lehmann, *FEBS letters*, 2005, **579**, 3765-3769.

106.	D. J. Belton, S. V. Patwardhan and C. C. Perry, *Journal of Materials Chemistry*, 2005, **15**, 4629-4638.

107.	T. Coradin and J. Livage, *Colloids and Surfaces B: Biointerfaces*, 2001, **21**, 329-336.

108.	M. R. Knecht and D. W. Wright, *Chemistry of Materials*, 2004, **16**, 4890-4895.

109.	V. V. Annenkov, S. V. Patwardhan, D. Belton, E. N. Danilovtseva and C. C. Perry, *Chemical Communications*, 2006, 1521-1523.

110.	T. Mizutani, H. Nagase, N. Fujiwara and H. Ogoshi, *Bulletin of the Chemical Society of Japan*, 1998, **71**, 2017-2022.

111.	F. Noll, M. Sumper and N. Hampp, *Nano Letters*, 2002, **2**, 91-95.

112.	D. M. Ruthven, *Principles of adsorption and adsorption processes*, John Wiley & Sons, 1984.

113.	M. Suzuki, *Adsorption engineering: Chemical engineering monographs. Elsevier, Amsterdam*, 1990, **25**, 97-99.

114.	F. Roquerol, J. Rouquerol and K. Sing, *Academic Press, London*, 1999, **54**, 15893-15899.

115.	J. Rouquerol, D. Avnir, C. Fairbridge, D. Everett, J. Haynes, N. Pernicone, J. Ramsay, K. Sing and K. Unger, *Pure and Applied Chemistry*, 1994, **66**, 1739-1758.

116.	K. S. Sing, *Pure and Applied Chemistry*, 1985, **57**, 603-619.

117.	K. Sing, D. Everett, R. Haul, L. Moscou, R. Pierotti, J. Rouquerol and T. Siemieniewska, *Pure and Applied Chemistry*, 1982, **54**, 2201.
118.	S. Brunauer, P. H. Emmett and E. Teller, *Journal of the American Chemical Society*, 1938, **60**, 309-319.
119.	J. De Boer, B. Lippens, B. Linsen, J. Broekhoff, A. Van den Heuvel and T. J. Osinga, *Journal of Colloid and Interface Science*, 1966, **21**, 405-414.
120.	B. C. Lippens and J. De Boer, *Journal of Catalysis*, 1965, **4**, 319-323.
121.	W. D. Harkins and G. Jura, *Journal of the American Chemical Society*, 1944, **66**, 1366-1373.
122.	E. P. Barrett, L. G. Joyner and P. P. Halenda, *Journal of the American Chemical Society*, 1951, **73**, 373-380.
123.	D. C. Harris, *Quantitative chemical analysis*, Macmillan, 2010.
124.	F. Rouessac and A. Rouessac, *Chemical analysis: modern instrumentation methods and techniques*, John Wiley & Sons, 2013.
125.	D. A. Skoog, F. J. Holler and S. R. Crouch, *Principles of instrumental analysis*, Cengage learning, 2017.
126.	E. Heftmann, *Chromatography: Fundamentals and applications of chromatography and related differential migration methods*, Elsevier, 2004.
127.	B. M. Tissue, *Basics of analytical chemistry and chemical equilibria*, John Wiley & Sons, 2013.
128.	H. M. McNair and J. M. Miller, *Basic gas chromatography*, John Wiley & Sons, 2011.
129.	G. M. Message, *Practical aspects of gas chromatography/mass spectrometry*, Wiley, 1984.
130.	M. Harper, *Journal of Chromatography A*, 2000, **885**, 129-151.
131.	S. Ahuja and M. Dong, *Handbook of pharmaceutical analysis by HPLC*, Elsevier, 2005.
132.	R. J. Hamilton and P. A. Sewell, in *Introduction to high performance liquid chromatography*, Springer, Editon edn., 1982, pp. 1-12.
133.	L. R. Snyder, J. J. Kirkland and J. L. Glajch, *Practical HPLC method development*, John Wiley & Sons, 2012.
134.	K. Töppner, D. Hansen and E. Herbig, *Técnicas de laboratorio*, 2014, 32-37.
135.	F. W. Fifield and D. Kealey, *Principles and practise of analytical chemistry*, Fifth edn., Blackwell Science, 2000.
136.	R. K. Boyd, C. Basic and R. A. Bethem, *Trace Quantitative Analysis by Mass Spectroscopy*, Wiley, 2008.
137.	M. C. McMaster, *HPLC a practical users guide*, Second edn., Wiley, 2007.
138.	J. J. van Deemter, F. J. Zuiderweg and A. Klinkenberg, *Chem. Eng. Sci.*, 1956, **5**, 271-289.
139.	L. Kirkup, M. Foot and M. Mulholland, *J. Chromatogr. A*, 2004, **1030**, 25-31.
140.	P. E. Stackelberg, J. Gibs, E. T. Furlong, M. T. Meyer, S. D. Zaugg and R. L. Lippincott, *Science of The Total Environment*, 2007, **377**, 255-272.
141.	E. De Hoffmann, *Mass spectrometry*, Encyclopedia of Chemical Technology, 2000.
142.	E. d. Hoffmann and V. Stroobant, *Mass Spectrometry: Principles and Applications*, Third edn., John WIley & Sons Ltd, 2007.
143.	*Quadrupole mass analyser*, https://attic.gsfc.nasa.gov/huygensgcms/MS_Analyzer_1.htm, Accessed October 2018.
144.	R. Bilhorn, P. Epperson, J. Sweedler and M. B. Denton, *Applied Spectroscopy*, 1987, **41**, 1125-1136.

145. R. Bilhorn, J. Sweedler, P. Epperson and M. B. Denton, *Applied Spectroscopy*, 1987, **41**, 1114-1125.
146. H.-H. Perkampus, *UV-VIS Spectroscopy and its Applications*, Springer Science & Business Media, 2013.
147. F. C. Strong, *Analytical Chemistry*, 1952, **24**, 338-342.
148. R. J. Anderson, D. J. Bendell and P. W. Groundwater, *Organic Spectroscopic Analysis*, Royal Societyof Chemistry, 2004.
149. N. Pounds, S. Maclean, M. Webley, D. Pascoe and T. Hutchinson, *Ecotoxicology and Environmental Safety*, 2008, **70**, 47-52.
150. E. Heftmann, *Chromatography: Fundamentals and applications of chromatography*, Sixth edn., Elsevier, 2004.
151. L. R. Snyder, J. J. Kirkland and J. W. Dolan, *Introduction to Modern Liquid Chromatography*, Third edn., Wiley, 2011.
152. S. A. Idris, C. Robertson, M. Morris and L. T. Gibson, *Analytical Methods*, 2010, **2**, 1803-1809.
153. A. M. Ewlad-Ahmed, M. A. Morris, S. V. Patwardhan and L. T. Gibson, *Environmental Science & Technology*, 2012, **46**, 13354-13360.
154. M. Grün, K. K. Unger, A. Matsumoto and K. Tsutsumi, *Microporous and Mesoporous Materials*, 1999, **27**, 207-216.
155. S.-Y. Park, M. Barton and P. Pendleton, *Colloids and Surfaces A: Physicochemical and Engineering Aspects*, 2011, **385**, 256-261.
156. C. Jia, S. Batterman and C. Godwin, *Atmospheric Environment*, 2008, **42**, 2083-2100.
157. W. Chan, S.-C. Lee, Y. Chen, B. Mak, K. Wong, C.-S. Chan, C. Zheng and X. Guo, *International Journal of Hospitality Management*, 2009, **28**, 26-32.
158. J. Van Durme, J. Dewulf, W. Sysmans, C. Leys and H. Van Langenhove, *Chemosphere*, 2007, **68**, 1821-1829.
159. H. Yu, S. C. Lee, J. Yu and C. H. Ao, *Journal of Molecular Catalysis A: Chemical*, 2006, **246**, 206-211.
160. J. L. Adgate, T. R. Church, A. D. Ryan, G. Ramachandran, A. L. Fredrickson, T. H. Stock, M. T. Morandi and K. Sexton, *Environmental Health Perspectives*, 2004, **112**, 1386.
161. H. S. Koren, D. E. Graham and R. B. Devlin, *Archives of Environmental Health: An International Journal*, 1992, **47**, 39-44.
162. G. Viegi, M. Simoni, A. Scognamiglio, S. Baldacci, F. Pistelli, L. Carrozzi and I. Annesi-Maesano, *The International Journal of Tuberculosis and Lung Disease*, 2004, **8**, 1401-1415.
163. R. Kostiainen, *Atmospheric Environment*, 1995, **29**, 693-702.
164. L. A. Wallace, *Annual review of energy and the environment*, 2001, **26**, 269-301.
165. S. M. Rappaport and L. L. Kupper, *Journal of Exposure Analysis and Environmental Epidemiology*, 2004, **14**, 92-107.
166. S. K. Brown, M. R. Sim, M. J. Abramson and C. N. Gray, *Indoor Air*, 1994, **4**, 123-134.
167. B. Horemans, A. Worobiec, A. Buczynska, K. Van Meel and R. Van Grieken, *Journal of Environmental Monitoring*, 2008, **10**, 867-876.
168. K. Patja, S. Vainiotalo, T. Laatikainen, L. Kuusimäki, K. Peltonen and E. Vartiainen, *Nicotine & Tobacco Research*, 2008, **10**, 1327-1333.
169. S. Batterman, G. Hatzivasilis and C. Jia, *Atmospheric Environment*, 2006, **40**, 1828-1844.
170. R. E. Dodson, J. I. Levy, J. D. Spengler, J. P. Shine and D. H. Bennett, *Atmospheric Environment*, 2008, **42**, 1569-1581.

171. E. Gallego, F. X. Roca, X. Guardino and M. G. Rosell, *Journal of Environmental Sciences*, 2008, **20**, 1063-1069.
172. C. Y. Chao and G. Y. Chan, *Atmospheric Environment*, 2001, **35**, 5895-5913.
173. R. D. Edwards, J. Jurvelin, K. Saarela and M. Jantunen, *Atmospheric Environment*, 2001, **35**, 4531-4543.
174. S. C. Lee, S. Lam and H. Kin Fai, *Building and Environment*, 2001, **36**, 837-842.
175. E. Ilgen, N. Karfich, K. Levsen, J. Angerer, P. Schneider, J. Heinrich, H. E. Wichmann, L. Dunemann and J. Begerow, *Atmospheric Environment*, 2001, **35**, 1235-1252.
176. K. Demeestere, J. Dewulf, B. De Witte and H. Van Langenhove, *Journal of Chromatography A*, 2007, **1153**, 130-144.
177. P. Bruno, M. Caselli, G. De Gennaro, S. Iacobellis and M. Tutino, *Indoor Air*, 2008, **18**, 250-256.
178. C. Walgraeve, K. Demeestere, J. Dewulf, K. Van Huffel and H. Van Langenhove, *Atmospheric Environment*, 2011, **45**, 5828-5836.
179. R. N. Reeve, *Introduction to environmental analysis*, John Wiley & Sons Ltd, 2002.
180. P. Bruno, M. Caputi, M. Caselli, G. De Gennaro and M. De Rienzo, *Atmospheric Environment*, 2005, **39**, 1347-1355.
181. M. R. Ras, F. Borrull and R. M. Marcé, *TrAC Trends in Analytical Chemistry*, 2009, **28**, 347-361.
182. S. Król, B. Zabiegała and J. Namieśnik, *TrAC Trends in Analytical Chemistry*, 2010, **29**, 1101-1112.
183. A. Kumar and I. Víden, *Environmental Monitoring and Assessment*, 2007, **131**, 301-321.
184. B. Seifert and D. Ullrich, *Atmospheric Environment (1967)*, 1987, **21**, 395-404.
185. S. Solomon, G. Schade, J. Kuttippurath, A. Ladstätter-Weissenmayer and J. Burrows, *Indoor and Built Environment*, 2008, **17**, 260-268.
186. K. D. Dettmer and W. E. Engewald, *Analytical and Bioanalytical Chemistry*, 2002, **373**, 490-500.
187. A. J. Fletcher, M. J. Benham and K. M. Thomas, *The Journal of Physical Chemistry B*, 2002, **106**, 7474-7482.
188. A. Ahmadpour and D. Do, *Carbon*, 1996, **34**, 471-479.
189. J. Pis, M. Mahamud, J. Pajares, J. Parra and R. Bansal, *Fuel processing technology*, 1998, **57**, 149-161.
190. J. Rudling, *Journal of Chromatography A*, 1990, **503**, 33-40.
191. C. Jia, S. Batterman and C. Godwin, *Journal of Environmental Monitoring*, 2007, **9**, 1220-1230.
192. M. Guillemot, J. Mijoin, S. Mignard and P. Magnoux, *Applied Catalysis B: Environmental*, 2007, **75**, 249-255.
193. Q. Hu, J. J. Li, Z. P. Hao, L. D. Li and S. Z. Qiao, *Chemical Engineering Journal*, 2009, **149**, 281-288.
194. D. P. Serrano, G. Calleja, J. A. Botas and F. J. Gutierrez, *Industrial & Engineering Chemistry Research*, 2004, **43**, 7010-7018.
195. R. Serna-Guerrero and A. Sayari, *Environmental Science & Technology*, 2007, **41**, 4761-4766.
196. P. Russo, M. M. Ribeiro Carrott and P. M. Carrott, *Adsorption*, 2008, **14**, 367-375.
197. T.-M. Wu, G.-R. Wu, H.-M. Kao and J.-L. Wang, *Journal of Chromatography A*, 2006, **1105**, 168-175.
198. B. L. Newalkar, N. V. Choudary, U. T. Turaga, R. P. Vijayalakshmi, P. Kumar, S. Komarneni and T. S. G. Bhat, *Chemistry of Materials*, 2003, **15**, 1474-1479.

199. Y. Ueno, A. Tate, O. Niwa, H.-s. Zhou, T. Yamada and I. Honma, *Chemical Communications*, 2004, **0**, 746-747.
200. H. Vinh-Thang, Q. Huang, M. Eić, D. Trong-On and S. Kaliaguine, *Langmuir*, 2005, **21**, 5094-5101.
201. B. Dou, Q. Hu, J. Li, S. Qiao and Z. Hao, *Journal of Hazardous Materials*, 2011, **186**, 1615-1624.
202. M. Hartmann and C. Bischof, *The Journal of Physical Chemistry B*, 1999, **103**, 6230-6235.
203. K. Kosuge, S. Kubo, N. Kikukawa and M. Takemori, *Langmuir*, 2007, **23**, 3095-3102.
204. S. Z. Qiao, S. K. Bhatia and D. Nicholson, *Langmuir*, 2003, **20**, 389-395.
205. V. Kocherbitov and V. Alfredsson, *The Journal of Physical Chemistry C*, 2007, **111**, 12906-12913.
206. A. Matsumoto, K. Tsutsumi, K. Schumacher and K. K. Unger, *Langmuir*, 2002, **18**, 4014-4019.
207. X. Hu, S. Qiao, X. S. Zhao and G. Q. Lu, *Industrial & Engineering Chemistry Research*, 2001, **40**, 862-867.
208. J. W. Lee, W. G. Shim and H. Moon, *Microporous and Mesoporous Materials*, 2004, **73**, 109-119.
209. Y.-H. Chu, H.-J. Kim, K.-Y. Song, Y.-G. Shul, K.-T. Jung, K. Lee and M.-H. Han, *Catalysis today*, 2002, **74**, 249-256.
210. M. B. Ray, *Developments in Chemical Engineering and Mineral Processing*, 2000, **8**, 405-439.
211. I. Fujishima and K. Honda, *Nature*, 1972, **238**, 38.
212. O. Carp, C. L. Huisman and A. Reller, *Progress in Solid State Chemistry*, 2004, **32**, 33-177.
213. J. Zhao and X. Yang, *Building and Environment*, 2003, **38**, 645-654.
214. A. J. Maira, K. Yeung, J. Soria, J. Coronado, C. Belver, C. Lee and V. Augugliaro, *Applied Catalysis B: Environmental*, 2001, **29**, 327-336.
215. J. Mo, Y. Zhang, Q. Xu, J. J. Lamson and R. Zhao, *Atmospheric Environment*, 2009, **43**, 2229-2246.
216. A. Fujishima, X. Zhang and D. A. Tryk, *Surface Science Reports*, 2008, **63**, 515-582.
217. J.-M. Herrmann, *Catalysis today*, 1999, **53**, 115-129.
218. M. Anpo and M. Takeuchi, *Journal of Catalysis*, 2003, **216**, 505-516.
219. C. Ao and S. Lee, *Chemical engineering science*, 2005, **60**, 103-109.
220. C. Lin, Y. Song, L. Cao and S. Chen, *Nanoscale*, 2013.
221. I. K. Konstantinou, V. A. Sakkas and T. A. Albanis, *Water research*, 2002, **36**, 2733-2742.
222. F. Bosc, D. Edwards, N. Keller, V. Keller and A. Ayral, *Thin Solid Films*, 2006, **495**, 272-279.
223. M. Sleiman, P. Conchon, C. Ferronato and J.-M. Chovelon, *Applied Catalysis B: Environmental*, 2009, **86**, 159-165.
224. J. Yu, M. Zhou, B. Cheng, H. Yu and X. Zhao, *Journal of Molecular Catalysis A: Chemical*, 2005, **227**, 75-80.
225. K. Rajeshwar, C. Chenthamarakshan, S. Goeringer and M. Djukic, *Pure and Applied Chemistry*, 2001, **73**, 1849-1860.
226. U. I. Gaya and A. H. Abdullah, *Journal of Photochemistry and Photobiology C: Photochemistry Reviews*, 2008, **9**, 1-12.
227. D. A. Hanaor and C. C. Sorrell, *Journal of Materials Science*, 2011, **46**, 855-874.

228. A. Sclafani and J. Herrmann, *The Journal of Physical Chemistry*, 1996, **100**, 13655-13661.
229. S. Watson, D. Beydoun, J. Scott and R. Amal, *Journal of Nanoparticle Research*, 2004, **6**, 193-207.
230. C. Ooka, S. Akita, Y. Ohashi, T. Horiuchi, K. Suzuki, S.-i. Komai, H. Yoshida and T. Hattori, *J. Mater. Chem.*, 1999, **9**, 2943-2952.
231. S. J. Kim, S. D. Park, Y. H. Jeong and S. Park, *Journal of the American Ceramic Society*, 1999, **82**, 927-932.
232. R. Wang, N. Sakai, A. Fujishima, T. Watanabe and K. Hashimoto, *The Journal of Physical Chemistry B*, 1999, **103**, 2188-2194.
233. T. Alapi, P. Sipos, I. Ilisz, G. Wittmann, Z. Ambrus, I. Kiricsi, K. Mogyorósi and A. Dombi, *Applied Catalysis A: General*, 2006, **303**, 1-8.
234. H. Luo, C. Wang and Y. Yan, *Chemistry of Materials*, 2003, **15**, 3841-3846.
235. J. Yu, X. Zhao and Q. Zhao, *Thin Solid Films*, 2000, **379**, 7-14.
236. C. Chaibundit, N. g. M. Ricardo, N. d. M. Ricardo, F. v. d. M. Costa, M. G. Wong, D. Hermida-Merino, J. Rodriguez-Perez, I. W. Hamley, S. G. Yeates and C. Booth, *Langmuir*, 2008, **24**, 12260-12266.
237. A. Denkova, E. Mendes and M.-O. Coppens, *The Journal of Physical Chemistry B*, 2008, **112**, 793-801.
238. K. Cassiers, T. Linssen, V. Meynen, P. Van Der Voort, P. Cool and E. Vansant, *Chemical Communications*, 2003, 1178-1179.
239. Q. Dai, L. Shi, Y. Luo, J. Blin, D. Li, C. Yuan and B. Su, *Journal of Photochemistry and Photobiology A: Chemistry*, 2002, **148**, 295-301.
240. Y. K. Hwang, K.-C. Lee and Y.-U. Kwon, *Chemical Communications*, 2001, 1738-1739.
241. I. Kartini, P. Meredith, X. Zhao, J. D. da Costa and G. Lu, *Journal of nanoscience and nanotechnology*, 2004, **4**, 270-274.
242. H. S. Yun, K. C. Miyazawa, I. Honma, H. Zhou and M. Kuwabara, *Materials Science and Engineering: C*, 2003, **23**, 487-494.
243. L. A. Dibble and G. B. Raupp, *Catalysis letters*, 1990, **4**, 345-354.
244. Y. Feng, L. Li, M. Ge, C. Guo, J. Wang and L. Liu, *ACS Applied Materials & Interfaces*, 2010, **2**, 3134-3140.
245. L. Cao, Z. Gao, S. L. Suib, T. N. Obee, S. O. Hay and J. D. Freihaut, *Journal of Catalysis*, 2000, **196**, 253-261.
246. J.-H. Park, Y.-S. Seo, J.-K. Lee and I.-K. Kim, *Journal of Chemical Engineering of Japan*, 2009, **42**, 139-146.
247. M. L. Richardson and J. M. Bowron, *Journal of Pharmacy and Pharmacology*, 1985, **37**, 1-12.
248. K. K. Barnes, D. W. Kolpin, E. T. Furlong, S. D. Zaugg, M. T. Meyer and L. B. Barber, *Science of The Total Environment*, 2008, **402**, 192-200.
249. G. R. Boyd, H. Reemtsma, D. A. Grimm and S. Mitra, *Science of The Total Environment*, 2003, **311**, 135-149.
250. J. E. Drewes, T. Heberer, T. Rauch and K. Reddersen, *Ground Water Monitoring & Remediation*, 2003, **23**, 64-72.
251. A. Nikolaou, S. Meric and D. Fatta, *Analytical and Bioanalytical Chemistry*, 2007, **387**, 1225-1234.
252. E. Vulliet and C. Cren-Olivé, *Environmental Pollution*, 2011, **159**, 2929-2934.
253. A. Watkinson, E. Murby, D. Kolpin and S. Costanzo, *Science of The Total Environment*, 2009, **407**, 2711-2723.

254. D. W. Kolpin, E. T. Furlong, M. T. Meyer, E. M. Thurman, S. D. Zaugg, L. B. Barber and H. T. Buxton, *Environmental Science & Technology*, 2002, **36**, 1202-1211.
255. F. Hernández, J. V. Sancho, M. Ibáñez and C. Guerrero, *TrAC Trends in Analytical Chemistry*, 2007, **26**, 466-485.
256. S. Pérez and D. Barceló, *TrAC Trends in Analytical Chemistry*, 2007, **26**, 494-514.
257. S. D. Richardson and T. A. Ternes, *Analytical Chemistry*, 2011, **83**, 4614-4648.
258. K. K. Barnes, S. C. Christenson, D. W. Kolpin, M. J. Focazio, E. T. Furlong, S. D. Zaugg, M. T. Meyer and L. B. Barber, *Groundwater Monitoring & Remediation*, 2004, **24**, 119-126.
259. J. Metzger, in *Pharmaceuticals in the Environment*, Springer, Editon edn., 2004, pp. 133-137.
260. K. D. Brown, J. Kulis, B. Thomson, T. H. Chapman and D. B. Mawhinney, *Science of The Total Environment*, 2006, **366**, 772-783.
261. K. Kümmerer, *Journal of Environmental Management*, 2009, **90**, 2354-2366.
262. J. P. Bound, K. Kitsou and N. Voulvoulis, *Environmental Toxicology and Pharmacology*, 2006, **21**, 301-307.
263. J. P. Bound and N. Voulvoulis, *Environmental Health Perspectives*, 2005, 1705-1711.
264. R. Andreozzi, M. Raffaele and P. Nicklas, *Chemosphere*, 2003, **50**, 1319-1330.
265. M. Carballa, F. Omil, J. M. Lema, M. a. Llompart, C. García-Jares, I. Rodríguez, M. Gomez and T. Ternes, *Water Research*, 2004, **38**, 2918-2926.
266. M. J. Gómez, M. Martínez Bueno, S. Lacorte, A. Fernández-Alba and A. Agüera, *Chemosphere*, 2007, **66**, 993-1002.
267. T. Heberer, *Journal of Hydrology*, 2002, **266**, 175-189.
268. T. A. Ternes, *Water Research*, 1998, **32**, 3245-3260.
269. K. Fent, A. A. Weston and D. Caminada, *Aquatic Toxicology*, 2006, **76**, 122-159.
270. H. C. Poynton and C. D. Vulpe, *JAWRA Journal of the American Water Resources Association*, 2009, **45**, 83-96.
271. O. A. Jones, J. N. Lester and N. Voulvoulis, *Trends in Biotechnology*, 2005, **23**, 163-167.
272. O. A. H. Jones, N. Voulvoulis and J. N. Lester, *Water research*, 2002, **36**, 5013-5022.
273. S. Webb, T. Ternes, M. Gibert and K. Olejniczak, *Toxicology Letters*, 2003, **142**, 157-167.
274. C. G. Daughton and T. A. Ternes, *Environmental Health Perspectives*, 1999, **107**, 907.
275. P. E. Stackelberg, E. T. Furlong, M. T. Meyer, S. D. Zaugg, A. K. Henderson and D. B. Reissman, *Science of The Total Environment*, 2004, **329**, 99-113.
276. M. Cleuvers, *Chemosphere*, 2005, **59**, 199-205.
277. D. Huggett, J. Cook, J. Ericson and R. Williams, *Human and Ecological Risk Assessment*, 2003, **9**, 1789-1799.
278. T. Brodin, J. Fick, M. Jonsson and J. Klaminder, *Science*, 2013, **339**, 814-815.
279. J.-M. Brozinski, M. Lahti, A. Oikari and L. Kronberg, *Chemosphere*, 2013, **93**, 1789-1795.
280. S. Jobling, R. Williams, A. Johnson, A. Taylor, M. Gross-Sorokin, M. Nolan, C. R. Tyler, R. Aerle, E. Santos and G. Brighty, *Environmental Health Perspectives*, 2006, **114**, 1.
281. L. J. Mills and C. Chichester, *Science of The Total Environment*, 2005, **343**, 1-34.
282. N. Kemper, *Ecological Indicators*, 2008, **8**, 1-13.
283. S. K. Khetan and T. J. Collins, *Chemical Reviews*, 2007, **107**, 2319-2364.
284. S. Contreras, M. Rodríguez, E. Chamarro and S. Esplugas, *Journal of Photochemistry and Photobiology A: Chemistry*, 2001, **142**, 79-83.

285. M. Rodriguez, V. Timokhin, F. Michl, S. Contreras, J. Gimenez and S. Esplugas, *Catalysis today*, 2002, **76**, 291-300.

286. J. Sarasa, M. Roche, M. Ormad, E. Gimeno, A. Puig and J. Ovelleiro, *Water Research*, 1998, **32**, 2721-2727.

287. D. S. Bhatkhande, V. G. Pangarkar and A. A. Beenackers, *Water Research*, 2003, **37**, 1223-1230.

288. D. T. Sponza and Ö. S. Kuscu, *Journal of Hazardous Materials*, 2011, **185**, 1187-1197.

289. Z.-g. Yan, Z.-s. Zhang, H. Wang, F. Liang, J. Li, H.-l. Liu, C. Sun, L.-j. Liang and Z.-t. Liu, *Environmental Pollution*, 2012, **162**, 86-90.

290. *United States Environmental Protection Agency - Priority Pollutants*, http://water.epa.gov/scitech/methods/cwa/pollutants.cfm, Accessed June 2015.

291. A. Wang, C. Hu, J. Qu, M. Yang, H. Liu, J. Ru, R. Qi and J. Sun, *Journal of Environmental Sciences*, 2008, **20**, 787-795.

292. P. H. Nielsen and T. H. Christensen, *Journal of Contaminant Hydrology*, 1994, **17**, 55-67.

293. J. D. Rodgers and N. J. Bunce, *Water research*, 2001, **35**, 2101-2111.

294. C. Wang, Y. Feng, S. Zhao and B.-L. Li, *Chemosphere*, 2012, **88**, 69-76.

295. C. Adams, Y. Wang, K. Loftin and M. Meyer, *Journal of Environmental Engineering*, 2002, **128**, 253-260.

296. K.-J. Choi, S.-G. Kim and S.-H. Kim, *Journal of Hazardous Materials*, 2008, **151**, 38-43.

297. M. Dutta, N. Dutta and K. Bhattacharya, *Separation and Purification Technology*, 1999, **16**, 213-224.

298. M. Fuerhacker, A. Dürauer and A. Jungbauer, *Chemosphere*, 2001, **44**, 1573-1579.

299. E. K. Putra, R. Pranowo, J. Sunarso, N. Indraswati and S. Ismadji, *Water research*, 2009, **43**, 2419-2430.

300. J. Rivera-Utrilla, G. Prados-Joya, M. Sánchez-Polo, M. Ferro-García and I. Bautista-Toledo, *Journal of Hazardous Materials*, 2009, **170**, 298-305.

301. S. A. Snyder, S. Adham, A. M. Redding, F. S. Cannon, J. DeCarolis, J. Oppenheimer, E. C. Wert and Y. Yoon, *Desalination*, 2007, **202**, 156-181.

302. T. A. Ternes, M. Meisenheimer, D. McDowell, F. Sacher, H.-J. Brauch, B. Haist-Gulde, G. Preuss, U. Wilme and N. Zulei-Seibert, *Environmental Science & Technology*, 2002, **36**, 3855-3863.

303. Z. Yu, S. Peldszus and P. M. Huck, *Environmental Science & Technology*, 2009, **43**, 1467-1473.

304. M. Purkait, A. Maiti, S. DasGupta and S. De, *Journal of Hazardous Materials*, 2007, **145**, 287-295.

305. O. Lorphensri, J. Intravijit, D. A. Sabatini, T. C. Kibbey, K. Osathaphan and C. Saiwan, *Water research*, 2006, **40**, 1481-1491.

306. J. R. Domínguez‑Vargas, T. Gonzalez, P. Palo and E. M. Cuerda‑Correa, *CLEAN‑Soil, Air, Water*, 2013, **41**, 1052-1061.

307. I. Vergili and H. Barlas, *Journal of Scientific & Industrial Research*, 2009, **68**, 417-425.

308. T. X. Bui and H. Choi, *Journal of Hazardous Materials*, 2009, **168**, 602-608.

309. T. X. Bui, S.-Y. Kang, S.-H. Lee and H. Choi, *Journal of Hazardous Materials*, 2011, **193**, 156-163.

310. T. X. Bui, V. H. Pham, S. T. Le and H. Choi, *Journal of Hazardous Materials*, 2013, **254**, 345-353.

311. T. X. Bui and H. Choi, *Chemosphere*, 2010, **80**, 681-686.

312. Z. Qiang, X. Bao and W. Ben, *Water Research*, 2013, **47**, 4107-4114.
313. S. M. Rivera-Jiménez and A. J. Hernández-Maldonado, *Microporous and Mesoporous Materials*, 2008, **116**, 246-252.
314. N. Suriyanon, P. Punyapalakul and C. Ngamcharussrivichai, *Chemical Engineering Journal*, 2013, **214**, 208-218.
315. C. R. Brundle, C. A. Evans and S. Wilson, *Encyclopedia of materials characterization: surfaces, interfaces, thin films*, Gulf Professional Publishing, 1992.
316. J.-G. Choi, D. Do and H. Do, *Industrial & Engineering Chemistry Research*, 2001, **40**, 4005-4031.
317. P. Webb, January, Editon edn., 2003.
318. Y. Ho and G. McKay, *Adsorption Science & Technology*, 2002, **20**, 797-815.
319. Y.-S. Ho, *Water Research*, 2006, **40**, 119-125.
320. W. Weber and J. Morris, *Journal of the Sanitary Engineering Division American Society of Cival Engineers*, 1963, **89**, 31-60.
321. S. S. Gupta and K. G. Bhattacharyya, *Advances in Colloid and Interface Science*, 2011, **162**, 39-58.
322. A. Ince, G. Bayramoglu, B. Karagoz, B. Altintas, N. Bicak and M. Y. Arica, *Chemical Engineering Journal*, 2012, **189**, 404-412.
323. P. Atkins and J. De Paula, Oxford: Oxford University Press, Editon edn., 2006.
324. T. Guo, Y. Xia, G. Hao, M. Song and B. Zhang, *Biomaterials*, 2004, **25**, 5905-5912.
325. J. Pan, X. Zou, X. Wang, W. Guan, Y. Yan and J. Han, *Chemical Engineering Journal*, 2010, **162**, 910-918.
326. R. H. Krishna and A. Swamy, *International Journal of Engineering Research and Development*, 2012, **4**, 29-38.
327. F. Haghseresht and G. Lu, *Energy & Fuels*, 1998, **12**, 1100-1107.
328. M. Ribeiro Carrott, A. Estêvão Candeias, P. Carrott and K. Unger, *Langmuir*, 1999, **15**, 8895-8901.
329. A. Mestre, J. Pires, J. Nogueira and A. Carvalho, *Carbon*, 2007, **45**, 1979-1988.
330. Q. Qin, J. Ma and K. Liu, *Journal of Colloid and Interface Science*, 2007, **315**, 80-86.
331. M. Broyer, S. Valange, J. Bellat, O. Bertrand, G. Weber and Z. Gabelica, *Langmuir*, 2002, **18**, 5083-5091.
332. X. Zhao and G. Lu, *The Journal of Physical Chemistry B*, 1998, **102**, 1556-1561.
333. J. Li, Y. Li, Y. Wu and M. Zheng, *Journal of Hazardous Materials*, 2014, **280**, 450-457.
334. F. Villacañas, M. F. R. Pereira, J. J. Órfão and J. L. Figueiredo, *Journal of Colloid and Interface Science*, 2006, **293**, 128-136.
335. Y. Matsui, N. Ando, H. Sasaki, T. Matsushita and K. Ohno, *Water Research*, 2009, **43**, 3095-3103.
336. Q. Jiuhui, *Journal of Environmental Sciences*, 2008, **20**, 1-13.
337. E. Lipczynska-Kochany, *Chemosphere*, 1991, **22**, 529-536.
338. A. Aleboyeh, H. Aleboyeh and Y. Moussa, *Environmental Chemistry Letters*, 2003, **1**, 161-164.
339. R. Andreozzi, V. Caprio, A. Insola and R. Marotta, *Catalysis today*, 1999, **53**, 51-59.
340. E. Brillas, I. Sirés and M. A. Oturan, *Chemical Reviews*, 2009, **109**, 6570-6631.
341. P. R. Gogate and A. B. Pandit, *Advances in Environmental Research*, 2004, **8**, 501-551.
342. C. Walling and A. Goosen, *Journal of the American Chemical Society*, 1973, **95**, 2987-2991.
343. I. Oller, S. Malato and J. Sánchez-Pérez, *Science of The Total Environment*, 2011, **409**, 4141-4166.

344. J. Deng, J. Jiang, Y. Zhang, X. Lin, C. Du and Y. Xiong, *Applied Catalysis B: Environmental*, 2008, **84**, 468-473.
345. S.-P. Sun, X. Zeng and A. T. Lemley, *Journal of Molecular Catalysis A: Chemical*, 2013, **371**, 94-103.
346. S. Perathoner and G. Centi, *Topics in Catalysis*, 2005, **33**, 207-224.
347. H. Decolatti, B. Dalla Costa and C. Querini, *Microporous and Mesoporous Materials*, 2015, **204**, 180-189.
348. O. Makhotkina, E. Kuznetsova and S. Preis, *Applied Catalysis B: Environmental*, 2006, **68**, 85-91.
349. T. Dantas, V. Mendonca, H. Jose, A. Rodrigues and R. Moreira, *Chemical Engineering Journal*, 2006, **118**, 77-82.
350. Q. Liao, J. Sun and L. Gao, *Colloids and Surfaces A: Physicochemical and Engineering Aspects*, 2009, **345**, 95-100.
351. M. C. Pereira, F. S. Coelho, C. C. Nascentes, J. D. Fabris, M. H. Araújo, K. Sapag, L. C. Oliveira and R. M. Lago, *Chemosphere*, 2010, **81**, 7-12.
352. J. Ramirez, F. Maldonado-Hódar, A. Pérez-Cadenas, C. Moreno-Castilla, C. Costa and L. Madeira, *Applied Catalysis B: Environmental*, 2007, **75**, 312-323.
353. G. Satishkumar, M. Landau, T. Buzaglo, L. Frimet, M. Ferentz, R. Vidruk, F. Wagner, Y. Gal and M. Herskowitz, *Applied Catalysis B: Environmental*, 2013, **138**, 276-284.
354. F. Martínez, G. Calleja, J. Melero and R. Molina, *Applied Catalysis B: Environmental*, 2005, **60**, 181-190.
355. P. Shukla, S. Wang, H. Sun, H.-M. Ang and M. Tadé, *Chemical Engineering Journal*, 2010, **164**, 255-260.
356. X. Zhong, S. Royer, H. Zhang, Q. Huang, L. Xiang, S. Valange and J. Barrault, *Separation and Purification Technology*, 2011, **80**, 163-171.
357. N. Gokulakrishnan, A. Pandurangan and P. K. Sinha, *Industrial & Engineering Chemistry Research*, 2008, **48**, 1556-1561.
358. M. Tomczak, J. Slocik, M. Stone and R. Naik, *Biochemical Society Transactions*, 2007, **35**, 512-515.
359. S. V. Patwardhan, S. J. Clarson and C. C. Perry, *Chemical Communications*, 2005, 1113-1121.
360. M. Addamo, M. Bellardita, D. Carriazo, A. Di Paola, S. Milioto, L. Palmisano and V. Rives, *Applied Catalysis B: Environmental*, 2008, **84**, 742-748.
361. W. Choi, *Catalysis Surveys from Asia*, 2006, **10**, 16-28.
362. M. Ghezzar, F. Abdelmalek, M. Belhadj, N. Benderdouche and A. Addou, *Journal of Hazardous Materials*, 2009, **164**, 1266-1274.
363. J. R. Peller, R. L. Whitman, S. Griffith, P. Harris, C. Peller and J. Scalzitti, *Journal of Photochemistry and Photobiology A: Chemistry*, 2007, **186**, 212-217.
364. F. L. Toma, G. Bertrand, S. Begin, C. Meunier, O. Barres, D. Klein and C. Coddet, *Applied Catalysis B: Environmental*, 2006, **68**, 74-84.
365. J. Zhu, J. Zhang, F. Chen and M. Anpo, *Materials Letters*, 2005, **59**, 3378-3381.
366. G. L. Puma, A. Bono, D. Krishnaiah and J. G. Collin, *Journal of Hazardous Materials*, 2008, **157**, 209-219.
367. W. Zhao, Z. Bai, A. Ren, B. Guo and C. Wu, *Applied Surface Science*, 2010, **256**, 3493-3498.
368. T. Berger, T. Lana-Villarreal, D. Monllor-Satoca and R. Gómez, *Electrochemistry Communications*, 2006, **8**, 1713-1718.
369. N. Venkatachalam, A. Vinu, S. Anandan, B. Arabindoo and V. Murugesan, *Journal of Nanoscience and Nanotechnology*, 2006, **6**, 2499-2507.

370. M. Anpo and M. Takeuchi, *Journal of Catalysis*, 2003, **216**, 505-516.
371. B. Neppolian, S. Kanel, H. Choi, M. Shankar, B. Arabindoo and V. Murugesan, *International Journal of Photoenergy*, 2003, **5**, 45-49.
372. M. Anpo, *Catalysis Surveys from Asia*, 1997, **1**, 169-179.
373. M. Anpo, Y. Ichihashi, M. Takeuchi and H. Yamashita, *Research on Chemical Intermediates*, 1998, **24**, 143-149.
374. M. Anpo, Y. Ichihashi, M. Takeuchi and H. Yamashita, in *Studies in Surface Science and Catalysis*, Elsevier, Editon edn., 1999, vol. 121, pp. 305-310.
375. A. Kudo and M. Sekizawa, *Chemical Communications*, 2000, 1371-1372.
376. K. Sayama and H. Arakawa, *Journal of the Chemical Society, Faraday Transactions*, 1997, **93**, 1647-1654.
377. J. N. Clifford, E. Palomares, M. K. Nazeeruddin, M. Grätzel and J. R. Durrant, *The Journal of Physical Chemistry C*, 2007, **111**, 6561-6567.
378. F. De Angelis, S. Fantacci, A. Selloni, M. K. Nazeeruddin and M. Grätzel, *Journal of the American Chemical Society*, 2007, **129**, 14156-14157.
379. T. Morikawa, T. Ohwaki, K.-i. Suzuki, S. Moribe and S. Tero-Kubota, *Applied Catalysis B: Environmental*, 2008, **83**, 56-62.
380. V. Subramanian, E. Wolf and P. V. Kamat, *The Journal of Physical Chemistry B*, 2001, **105**, 11439-11446.
381. F. Boccuzzi, A. Chiorino, M. Manzoli, D. Andreeva, T. Tabakova, L. Ilieva and V. Iadakiev, *Catalysis today*, 2002, **75**, 169-175.
382. M. Date, Y. Ichihashi, T. Yamashita, A. Chiorino, F. Boccuzzi and M. Haruta, *Catalysis Today*, 2002, **72**, 89-94.
383. K. Lv, B. Cheng, J. Yu and G. Liu, *Physical Chemistry Chemical Physics*, 2012, **14**, 5349-5362.
384. D. Mitoraj and H. Kisch, *Angewandte Chemie International Edition*, 2008, **47**, 9975-9978.
385. G. Veréb, L. Manczinger, A. Oszkó, A. Sienkiewicz, L. Forró, K. Mogyorósi, A. Dombi and K. Hernádi, *Applied Catalysis B: Environmental*, 2013, **129**, 194-201.
386. M. Takeuchi, M. Matsuoka, H. Yamashita and M. Anpo, *Journal of Synchrotron Radiation*, 2001, **8**, 643-644.
387. M. Ahmed, E. E. El-Katori and Z. H. Gharni, *Journal of Alloys and Compounds*, 2013, **553**, 19-29.
388. A. Kay, I. Cesar and M. Grätzel, *Journal of the American Chemical Society*, 2006, **128**, 15714-15721.
389. Q. Sun, W. Leng, Z. Li and Y. Xu, *Journal of Hazardous Materials*, 2012, **229**, 224-232.
390. P. Vijayan, C. Mahendiran, C. Suresh and K. Shanthi, *Catalysis Today*, 2009, **141**, 220-224.
391. Y. Zhang and Q. Li, *Solid State Sciences*, 2013, **16**, 16-20.
392. B. Palanisamy, C. Babu, B. Sundaravel, S. Anandan and V. Murugesan, *Journal of Hazardous Materials*, 2013, **252**, 233-242.
393. R. Sonawane, B. Kale and M. Dongare, *Materials Chemistry and Physics*, 2004, **85**, 52-57.
394. N. A. Jamalluddin and A. Z. Abdullah, *Ultrasonics Sonochemistry*, 2011, **18**, 669-678.
395. H. Zhao, W. Fu, H. Yang, Y. Xu, W. Zhao, Y. Zhang, H. Chen, Q. Jing, X. Qi and J. Cao, *Applied Surface Science*, 2011, **257**, 8778-8783.
396. J. Maier, *Physical chemistry of ionic materials: ions and electrons in solids*, John Wiley & Sons, 2004.

397. T. K. Ghorai, M. Chakraborty and P. Pramanik, *Journal of Alloys and Compounds*, 2011, **509**, 8158-8164.
398. Y. Liu, J. Wei, R. Xiong, C. Pan and J. Shi, *Applied Surface Science*, 2011, **257**, 8121-8126.
399. S. Sun, J. Ding, J. Bao, C. Gao, Z. Qi, X. Yang, B. He and C. Li, *Applied Surface Science*, 2012, **258**, 5031-5037.
400. S. Tieng, A. Kanaev and K. Chhor, *Applied Catalysis A: General*, 2011, **399**, 191-197.
401. D. V. Wellia, Q. C. Xu, M. A. Sk, K. H. Lim, T. M. Lim and T. T. Y. Tan, *Applied Catalysis A: General*, 2011, **401**, 98-105.
402. C. Y. Jimmy, G. Li, X. Wang, X. Hu, C. W. Leung and Z. Zhang, *Chemical Communications*, 2006, 2717-2719.
403. H. Li, Z. Bian, J. Zhu, Y. Huo, H. Li and Y. Lu, *Journal of the American Chemical Society*, 2007, **129**, 4538-4539.
404. J. C. Yu, X. Wang and X. Fu, *Chemistry of Materials*, 2004, **16**, 1523-1530.
405. D. M. Antonelli and J. Y. Ying, *Angewandte Chemie International Edition in English*, 1995, **34**, 2014-2017.
406. E. L. Crepaldi, G. J. d. A. Soler-Illia, D. Grosso, F. Cagnol, F. Ribot and C. Sanchez, *Journal of the American Chemical Society*, 2003, **125**, 9770-9786.
407. P. Yang, D. Zhao, D. I. Margolese, B. F. Chmelka and G. D. Stucky, *Nature*, 1998, **396**, 152.
408. M. Asiltürk, F. Sayılkan and E. Arpaç, *Journal of Photochemistry and Photobiology A: Chemistry*, 2009, **203**, 64-71.
409. G. Ruppert, R. Bauer and G. Heisler, *Journal of Photochemistry and Photobiology A: Chemistry*, 1993, **73**, 75-78.
410. S. Fukuchi, R. Nishimoto, M. Fukushima and Q. Zhu, *Applied Catalysis B: Environmental*, 2014, **147**, 411-419.
411. S. Sharma, M. Mukhopadhyay and Z. Murthy, *Separation & Purification Reviews*, 2013, **42**, 263-295.
412. V. K. Sharma, T. M. Triantis, M. G. Antoniou, X. He, M. Pelaez, C. Han, W. Song, K. E. O'Shea, A. Armah and T. Kaloudis, *Separation and Purification Technology*, 2012, **91**, 3-17.
413. J. L. Wang and L. J. Xu, *Critical Reviews in Environmental Science and Technology*, 2012, **42**, 251-325.
414. J. De Laat and T. G. Le, *Applied Catalysis B: Environmental*, 2006, **66**, 137-146.
415. S. Tian, Y. Tu, D. Chen, X. Chen and Y. Xiong, *Chemical Engineering Journal*, 2011, **169**, 31-37.
416. J. De Laat and H. Gallard, *Environmental Science & Technology*, 1999, **33**, 2726-2732.
417. J. Wang, R. Limas-Ballesteros, T. Lopez, A. Moreno, R. Gomez, O. Novaro and X. Bokhimi, *The Journal of Physical Chemistry B*, 2001, **105**, 9692-9698.